Gowdy, Stephen J. (1987) *Position sensitive detectors in GaAs.* PhD thesis.

http://theses.gla.ac.uk/1625/

Copyright and moral rights for this thesis are retained by the author

A copy can be downloaded for personal non-commercial research or study, without prior permission or charge

This thesis cannot be reproduced or quoted extensively from without first obtaining permission in writing from the Author

The content must not be changed in any way or sold commercially in any format or medium without the formal permission of the Author

When referring to this work, full bibliographic details including the author, title, awarding institution and date of the thesis must be given

Glasgow Theses Service
http://theses.gla.ac.uk/
theses@gla.ac.uk

Position Sensitive Detectors in GaAs

Stephen J. Gowdy

Department of Physics & Astronomy
University of Glasgow
Glasgow
G12 8QQ

Thesis submitted for the degree of Doctor of Philosophy

June 1997

©1997 Stephen J. Gowdy

Abstract

Presented in this thesis is a summary of the development of gallium arsenide position sensitive detectors. These are aimed at various applications with the original motivation being experimental particle physics. An account is given of basic semiconductor physics relevant to particle detectors. A review of electronics applicable to reading out charged signals from semiconductor detectors is included. Applications of gallium arsenide X-ray detectors are described together with results from a Monte-Carlo simulation of the spectrum obtained from an X-ray source. The design, fabrication and laboratory testing of detectors is presented for pixel and microstrip detectors and other test structures. Test beam results are also presented for pixel and microstrip detectors. An introduction to ATLAS detector simulation is also given, with examples of detector descriptions for the GaAs Forward Semiconductor Tracker. Results from a generator level study of b-jets from the process $H \rightarrow b\bar{b}$ and predictions of fluences in the Forward Tracker are also given.

Contents

1 Introduction **1**
1.1 Overview 1
1.2 Semiconductor Detectors 1
1.3 Why choose GaAs? 3
1.4 X-ray Absorption Simulation 4
1.5 Detectors 6

2 Theory of Semiconductor Detectors **9**
2.1 Basic Semiconductor Physics 9
2.1.1 Atomic Bonding 10
2.1.2 Energy Bands in a Periodic Structure 11
2.1.3 Charged Carriers Distribution in Energy Bands 15
2.1.4 Charge Transport 18
2.2 Detector Contacts 22
2.2.1 p-n Junctions 22
2.2.2 Schottky Contacts 26
2.3 Signal Generation in GaAs Detectors 30
2.4 Noise Sources in Semiconductor Detectors 31

3 Read-out Electronics **34**
3.1 Introduction 34
3.2 Microstrip Detectors 35
3.2.1 MX7-RH 35
3.2.2 Viking 37
3.2.3 APV5-RH 37
3.2.4 FELIX 38
3.2.5 AROW 38
3.2.6 The Binary Chip 38
3.3 Pixel Detectors 39
3.3.1 The PAC Family 39
3.3.2 The Omega Family 41
3.3.3 Other types 43
3.4 Connecting to Detectors 44
3.4.1 Ultrasonic Wire Bonding 44
3.4.2 Flip Chip Bonding 45
3.5 Conclusion 46

4 X-ray Applications of GaAs Detectors **48**
4.1 Introduction 48
4.2 X-ray Astronomy 48
4.3 Synchrotron Radiation 49
4.4 Medical & Dental Imaging 50
4.5 Simulation of an X-ray Spectrum in GaAs 51
4.5.1 The Model 52
4.5.2 Physics Processes in GEANT 52
4.5.3 Simulation Input 56
4.5.4 Generation Of Signal 57
4.5.5 Results 59
4.5.6 Actual Spectrum 68
4.6 Summary & Conclusion 71

5 Design, Fabrication & Testing of GaAs Devices **73**
5.1 Introduction 73
5.2 Design of devices 73
5.2.1 Design tools 73
5.2.2 Design of Pixel Detectors 74
5.2.3 Design of Microstrip Detectors 75
5.2.4 Test Structures 77
5.3 Fabrication 79
5.3.1 Substrate Choice & Preparation 79
5.3.2 Photo-lithography 80
5.3.3 Metal Deposition 81
5.3.4 Passivation & Etch 82
5.3.5 Commercial Prototypes 82
5.4 Testing 83
5.4.1 Detector Tests 83
5.4.2 Test Structures 87
5.4.3 Radiation Damage Tests 88

6 Test Beam Results **96**
6.1 Introduction 96
6.2 Detectors Used in Test Beam 96
6.3 Microstrip Detector 98
6.3.1 Test Beam Setup 98
6.3.2 Off-line Analysis 99
6.3.3 Results 102
6.3.4 Simulation 104
6.3.5 Conclusion 105
6.4 Pixel Detector 106
6.4.1 Test Beam Setup 106
6.4.2 Detection Efficiency 106
6.4.3 Conclusion 108
6.4.4 GaAs Pixel Telescope 109
6.5 Overall Conclusions 109

7 Study of ATLAS Forward Region **113**
7.1 Introduction 113
7.2 DICE 114
7.3 b-jet Analysis 116
7.4 Particle Flux Analysis 121
7.5 Conclusion 127

8 Conclusions **128**

List of Figures

1.1 Principle of operation of a semiconductor detector 3
1.2 Ratio in percentages of absorption($\frac{GaAs}{Si}$) 5
1.3 Picture of a wafer fabricated in Glasgow 8
1.4 Picture of a biasing structure 8

2.1 Gallium arsenide lattice structure: zincblende 10
2.2 Fermi-Dirac distribution 13
2.3 Coulomb Potential in a periodic lattice 14
2.4 Relationship between E and k 16
2.5 Electron concentration versus distance 19
2.6 Band configurations in p- and n-type material forming a p-n junction 23
2.7 Band configurations in a p-n junction 24
2.8 Current-voltage characteristics of an ideal diode 26
2.9 Band configurations in a metal and n-type material forming a Schottky Contact 27
2.10 Noise Spectrum from a GaAs Detector 33

3.1 Basic MX Read-out Schematic 35
3.2 MX read-out sequence 36
3.3 Viking read-out sequence 37
3.4 Pixel Array Chip 1 40
3.5 PAC3-Detector Readout Board 42
3.6 Omega pixel schematic 43
3.7 Omega read-out sequence 43
3.8 The z-axis glue principle 45

4.1 GaAs X-ray Image of Mouse 51
4.2 GaAs X-ray Image of Fish 51
4.3 Toporowsky's model 53
4.4 Diagram of Compton scattering event 53
4.5 Assumed angular distribution of photoelectrons for a 60keV and 14keV incident photon 58
4.6 Simulated signal, measured in keV, with 34keV photons and no noise 60
4.7 Simulated signal, measured in keV, with 34keV photons and 500 electrons ENC noise 61
4.8 Simulated signal, measured in keV, with 34keV photons and 1000 electrons ENC noise 62
4.9 Simulated signal, measured in keV, with 60keV photons and no noise 63

4.10 Simulated signal, measured in keV, with 60keV photons and 500 electrons ENC noise 64
4.11 Simulated signal, measured in keV, with 60keV photons and 1000 electrons ENC noise 65
4.12 Simulated signal size verses event depth for 300μm detector with 280μm active and 60keV incident photon 66
4.13 CCE(%) against active thickness for 60keV photons 67
4.14 Fraction of photon interactions against active thickness for 60keV photons 68
4.15 Variation in simulated signal from a 300μm detector. 69
4.16 60keV ^{241}Am Spectrum from 300 μm GaAs detector biased at 300V 70
4.17 60keV Spectrum simulation for a 300 μm GaAs detector biased at 300V 70
4.18 60keV Spectrum simulation for a 300 μm GaAs detector biased at 300V without electronic noise 72

5.1 Pixel Detector bond pad cross-section 74
5.2 Corner of Omega 2 Detector Layout 75
5.3 Section of Omega2 Detector Ladder 75
5.4 Omega3 Detector Layout 76
5.5 Strip Detector Layout 77
5.6 Strip Capacitance Test Structures 78
5.7 Photo-lithography Process 81
5.8 Metal Deposition and Lift-off Process 82
5.9 LabView Application for IV Tests 84
5.10 Current-Voltage Characterisation of AL-W3-7 84
5.11 Current-Voltage Characteristics of AL-W3-6AC 85
5.12 Current-Voltage characterisation of GS196 86
5.13 Schematic of VV Circuit 86
5.14 Voltage on detector strip vs voltage on back contact 87
5.15 Signal measured in a gallium arsenide detector 88
5.16 Signal measured in a silicon detector 89
5.17 LabView Application for CV Tests 89
5.18 Inter-strip capacitance measurement for GSD185 device 90
5.19 Variation of CCE with neutron dose for Glasgow Detectors 91
5.20 Variation of Collected Charge with Neutron Dose for Tomsk Detectors 91
5.21 Proton Effect on Leakage Current of GaAs Detectors 92
5.22 Effect of Bias during Irradiation with Protons 93
5.23 Variation of CCE with Proton Dose 93
5.24 Variation of CCE with Pion Dose 94
5.25 Flash Lamp Annealing Effect on CCE 95

6.1 Representation of an Alenia AC-coupled detector 97
6.2 Strasbourg Telescope Layout 98
6.3 η distributions in a silicon detector 100
6.4 Variations along strip 101
6.5 HOLD delay 101
6.6 Results for detector AL-W3-6AC 103
6.7 DAQ Clocking Problem 104

6.8 Asymmetric η distributions in test beam 105
6.9 Results of test beam simulation 106
6.10 Pixel Detector Telescope Setup 107
6.11 Detection efficiency versus discriminator threshold 108
6.12 Beam profile in GaAs Pixel Detector 109
6.13 Hits in GaAs which are part of a reconstructed track 110
6.14 Beam profiles in gallium arsenide pixel telescope 111
6.15 Single event in gallium arsenide pixel telescope 112

7.1 Data Banks of GaAs Detector in DICE 115
7.2 Tree Display of DICE Elements 117
7.3 Module Information from **atlsim** 118
7.4 Pythia Event Used for b-jet study 119
7.5 P_T of stiffest track from $H \rightarrow b\bar{b}$ 119
7.6 Angle of track in radians from parent quark 120
7.7 ΔR for each track with B as parent 121
7.8 ΔR required to select % of tracks from B meson 122
7.9 Proton momentum spectra from pp collisions at 14TeV 123
7.10 Charged particle momentum spectra from pp collisions at 14TeV . . 124
7.11 Variation of fluence across first wheel in ATLAS 126

8.1 Optimum resolution of GaAs microstrip detector achieved to date . 129

List of Tables

1.1 Physical Properties of GaAs and other materials at 300K 4
1.2 Percentage X-ray Absorption in Silicon 6
1.3 Percentage X-ray Absorption in GaAs 6
1.4 Dimensions of pixel electronics 7

3.1 SCT Electronics Forecast Costs for ATLAS 47

4.1 Source data for ^{241}Am 71

6.1 $\frac{S}{N}$ cuts used in offline analysis for silicon and gallium arsenide microstrip detectors 100

7.1 P_T cut (GeV) to select jet from B 118
7.2 b-jet size in δR for tracks from B 120
7.3 Number (and percentage) of undecayed charged particles listed by type from 10000 events 125
7.4 Dimensions and radiation levels in first and last wheels of ATLAS very forward tracker 126

Preface

The development of position sensitive detectors fabricated on a gallium arsenide substrate is described in this thesis. This work has contributed to two distinct fields, experimental particle physics and medical imaging. These developments have been within the RD8[1] collaboration and, in the case of pixel detectors, the RD19[2] collaboration. In addition, work carried out within the ATLAS collaboration is also reported.

X-ray images in Figures 4.1 and 4.2 are by courtesy of Mario Caria and Paolo Randaccio, University of Cagliari, from the thesis work of Nando Romeo. Results on inter-strip capacitances presented in Section 5.4.2 were produced by Richard Bates.

Measurements of the radiation hardness of gallium arsenide to protons and pions, presented in Section 5.4.3, were carried out largely by Saverio D'Auria and Richard Bates.

The work described in Chapters 4 and 7 was solely by the author. The analysis presented in Chapter 6 was also done by the author.

The author also carried out the procedures described in Chapter 5 with the exception of passivating and etching.

No portion of the research by the author referred to in this thesis has been submitted in support of an application for another degree or qualification in this, or any other institute of learning.

Acknowledgements

I received a CASE award for this research from the Particle Physics & Astronomy Research Council, (originally the Science & Engineering Research Council), and the Rutherford Appleton Laboratory, Didcot, for which I am indebted. At RAL I would like to thank Peter Sharp, Paul Seller and Martin Lovell for allowing my work there to be exciting and interesting.

I'd like to thank Sarah for many years of support. Gizmo is a funny cat with a funny name who never fails to amaze me. Antonia has brought me fresh inspiration.

My family have been invaluable in helping me along the road, especially mum, dad and I guess I should mention Grant. My "extended" family are *keenly* interested in my work, at least that's what they tell me.

Friends, there's been a few... Allan and Stephen have been there for the duration, Allan even before. Richard came along later but was just as welcome. Craig deserves a large pat on the back, even although he was really late.

There are lots of "Astronomers" who are still trying their best to keep in touch, Andrew, Allan (again), Gavin, Peter, Sarah, Elaine, Alison, Aidan and David.

Some friends who date back to pre-university time (remember that?) are Peter, Ross, Steven and Robert.

The technicians and staff of the PPE Group have provided excellent support. David Martin, Alan Flavell, Mary Shearer and Brian Swann have kept the computers running, whereas Fred Doherty, Andrew Meikle and Frank McDevitt have kept the semiconductor laboratory running. Catherine MacIntyre kept everybody running smoothly (well, flying at least).

In addition, the members of the Department of Electronic & Electrical Engineering have been invaluable, most notably in the Ultra Small Structures Laboratory. Without their support and guidance many developments would not have been possible. Prof S Beaumont and Dr J Marsh have facilitated this use, and I thank both them and their staff.

Alan Poppleton and Stephen Haywood have aided greatly in my attempt at doing some semi-"real" physics, and I thank them.

I'm very grateful to my supervisor Prof K Smith for advice and guidance and for reading just about everything I've produced in the last three/four years. Also Prof I Skillicorn who very kindly proof read chapters of my thesis for me. And my "alternative" supervisor, Dr A Doyle, for running off to Hamburg for two years; he still managed to show interest in my work. Dr S D'Auria, V O'Shea and Dr C Raine have provided support and assistance for which I am very grateful.

Prof Saxon has also provided enough enthusiasm for the entire group, and still smiles. I think some of it has *probably* rubbed off on me.

Chapter 1

Introduction

1.1 Overview

In the development of a new solid state detector there are many different issues that must be dealt with in very different fashions. My research is divided into two different but very closely related parts, strip and pixel detectors. Each has its respective regions of use and parameters that dictate that area.

For example, pixel detectors will give two coordinates for hits and strips have only one. However, for a large area detector, with strips the number of channels will be proportional to the $\sqrt{area}$ and for pixel detectors to the area. The design of detectors is discussed in Section 5.2.

One area common to both is the need to understand the processes involved in the generation of the measured charge signal. To this end a simple model has been developed to simulate interactions of photons and charged particles inside our detectors.

In addition to this type of study, simulations are also done for entire detector systems. This is reviewed for the ATLAS experiment.

1.2 Semiconductor Detectors

The need for semiconductor detectors came about from a desire to resolve the decays of very short lived particles. These decay within millimetres of their production so that it was required to reconstruct their position to a very high resolution.

Semiconductor detectors offer this capability, offering position resolutions measured in microns rather than millimetres. Using the information of where the track passed through allows extrapolation to the vertex where it was created.

In addition to position measurements, by employing a magnetic field, momentum measurements also become possible. This requires multiple layers of semiconductor detectors to reconstruct the helical paths followed by charged particles. For ATLAS a $\frac{\Delta p}{p}$ of less than 30% is required (for tracks with a momentum of 500 GeV c^{-1}) in the central region of the detector ($\eta < 2$). Due to the large number of tracks many layers are also required to do efficient pattern recognition. To meet these criteria ATLAS has used six layers of semiconductor detectors, the innermost two being pixels.

Other benefits are gained from using semiconductor detectors. These include high time resolution, electronic read-out and the ability to self-trigger. The time resolution is determined from the variation in arrival time of the signal after the particle has passed through the detector. Typically the variation of this quantity is less than a nanosecond. When reading-out a detector electronically it is possible to transfer the data to a computer very easily. This aids a great deal in analysis, since no off-line digitisation is required.

The ability to self-trigger is also important, especially for X-ray detection where the particle is stopped and cannot interact with another detector to provide a trigger. Using semiconductor detectors for medical applications also allows faster treatment, with an "instant" image. There is also no degradation of the image over time.

Semiconductor detectors work by pulling apart the generated charge using a large electric field. The substrate is a reversed biased diode. Figure 1.1 illustrates the basis for semiconductor detector operation. As the particle passes through the detector it deposits energy which creates electron-hole pairs. These electrons and holes are pulled in opposite directions by the electric field which - if large enough - prevents them from recombining. As they move through the detector they induce a current in an external circuit. This is usually a pre-amplifier which shapes and amplifies the signal before further processing.

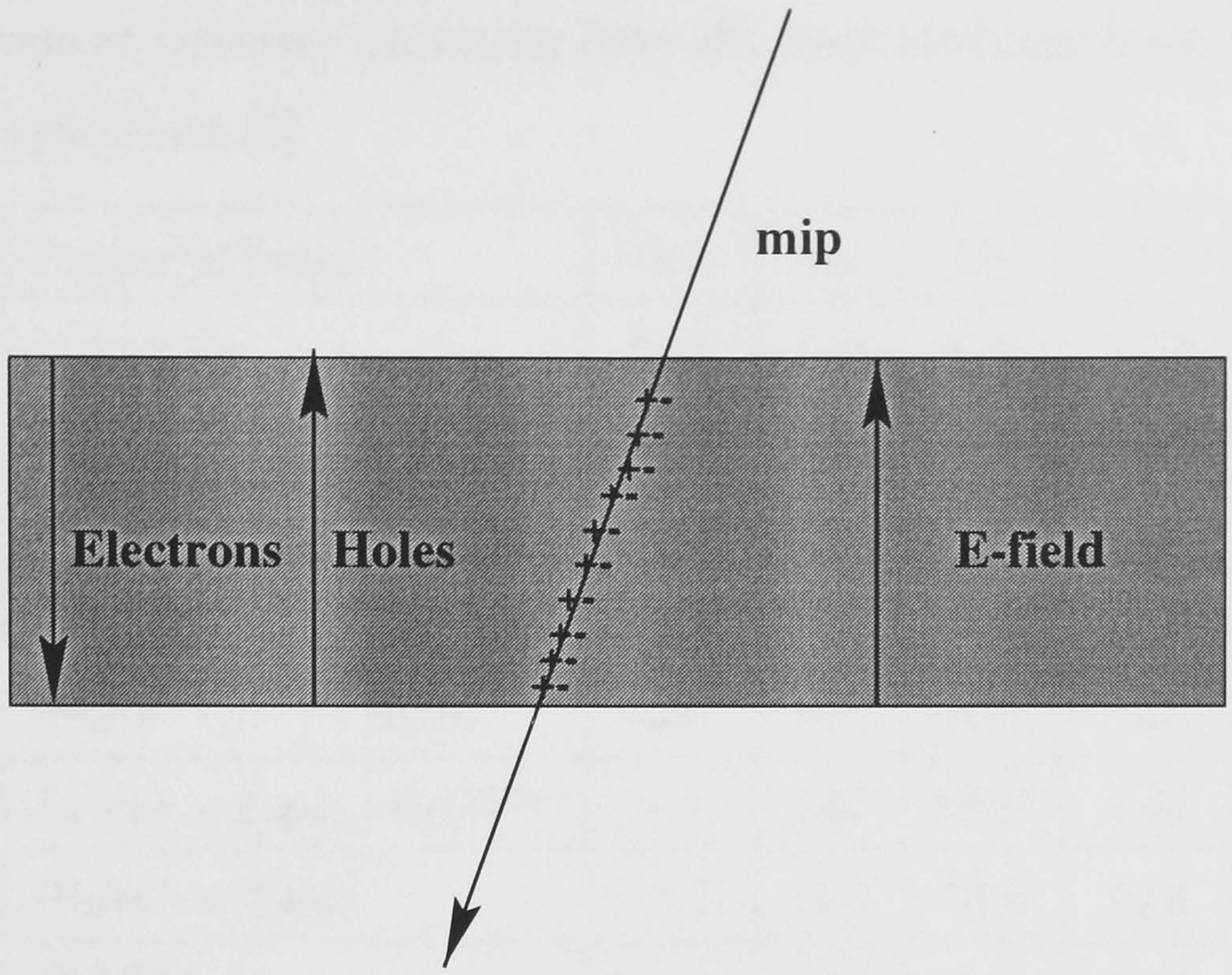

Figure 1.1: Principle of operation of a semiconductor detector

1.3 Why choose GaAs?

The main reason for using gallium arsenide in High Energy Physics applications is its radiation hardness. It has shown tolerance to doses equivalent to 10 years running at the LHC. This dose is expected to be around 10^{14} neutrons cm^{-2} in the region of the ATLAS forward tracker. Other parts of the Semiconductor Tracker are fabricated from silicon which has many problems before reaching this dose. The effect of radiation on gallium arsenide detectors is examined in Section 5.4.3.

Recent studies [3] have predicted that the silicon devices in other regions of the inner detector should survive the 10 years required, through progressive increase of their bias voltages and maintaining the detectors at -10°C to avoid "reverse annealing".

In another application - as an X-ray detector - the main advantage of gallium arsenide is its radiation length. Due to the relatively large atomic number of gallium and arsenic it has a high photoelectric absorption cross-section. Many physical properties of gallium arsenide are shown in Table 1.1 together with those for other semiconductors.

When compared to silicon it has a much higher X-ray absorption efficiency below 100keV [4]. This has been studied through simulation described in Chapter 4.5. X-

ray astronomers at Leicester University have also been studying X-ray detectors for astronomy applications [5].

Property(Units)		GaAs	Si	Ge	CdTe
$\rho(gcm^{-3})$		5.31	2.33	5.32	5.86
Z		31,33	14	32	48,52
Band Gap[1](eV)		1.43	1.12	0.66	1.47
Mobility	Electrons	8500	1450	3900	1000
$(cm^2V^{-1}s^{-1})$	Holes	400	450	1900	80
Energy per e-h pair(eV)		4.2	3.61	2.98[2]	4.43
Dielectric Cons.		13.1	11.9	16.0	10.0
$\frac{dE}{dx}(\frac{MeV}{g/cm^2})$		1.4	1.66	1.4	1.26
X_0(cm)		2.3	9.36	2.3	1.21

Table 1.1: Physical Properties of GaAs and other materials at 300K

1.4 X-ray Absorption Simulation

A calculation was made using data[4] from the simulation package EGS4[6] to show the difference in absorption rate of silicon and gallium arsenide as an X-ray detector.

This was done for various thicknesses of detector at various X-ray energies within the range of medical interest. The results for silicon and gallium arsenide are tabulated in Tables 1.2 and 1.3 respectively. The numbers presented are the percentage of the X-ray beam photons which will interact with the detector.

These results include absorption through Compton scattering. The lower energy Compton electrons would not be as easily measured so the results are a lower bound on the relative gain of using gallium arsenide. This is due to the Compton interactions providing a much larger proportion of the events in silicon than in gallium arsenide at these energies. At 60keV more than half of the events in silicon are Compton, to be compared with less than 7% in gallium arsenide. The ratio of efficiency in gallium arsenide divided by that in silicon is shown in Figure 1.2.

[1] It should be noted that Si and Ge have indirect band gaps.

[2] At 77K

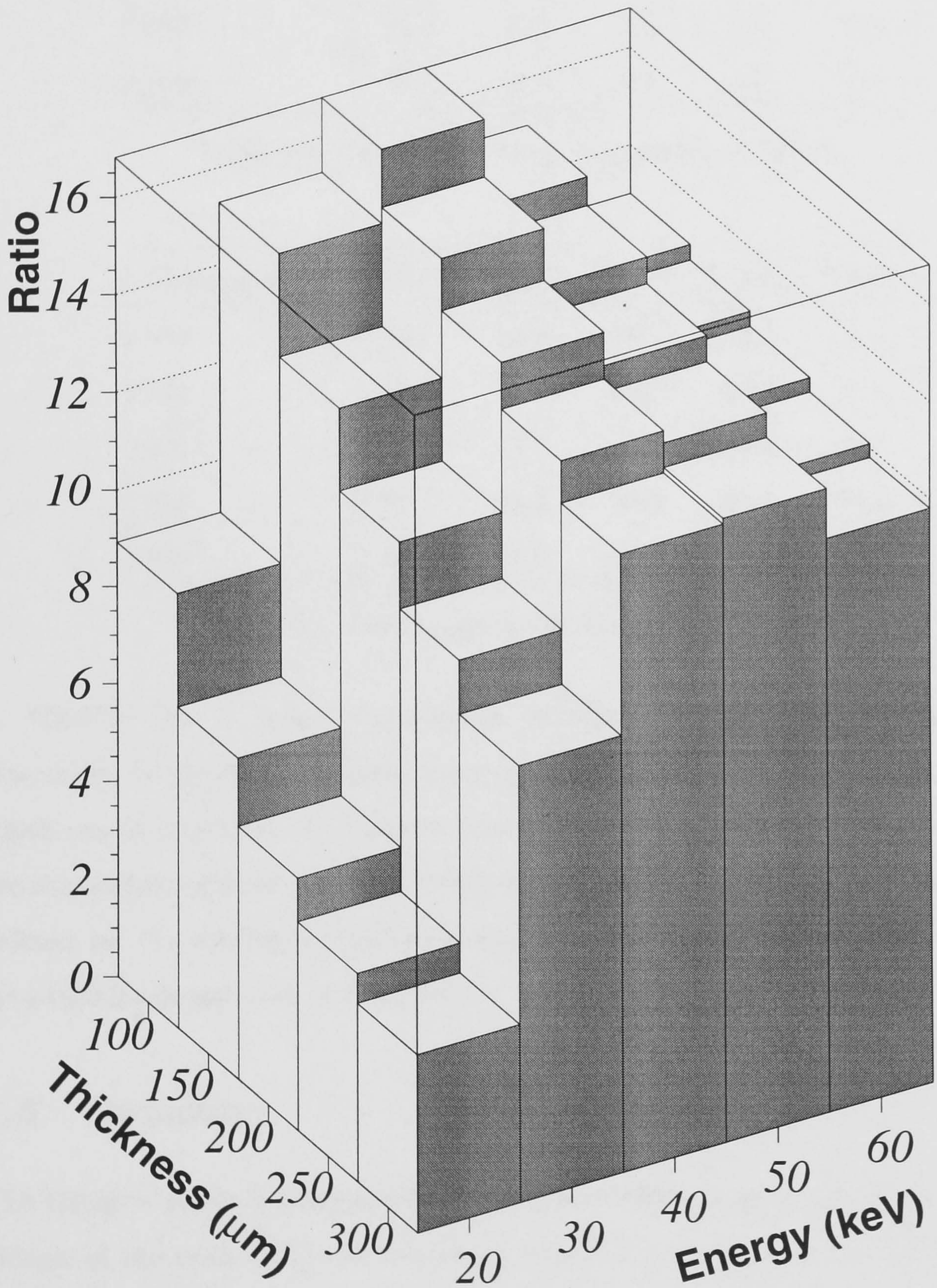

Figure 1.2: Ratio in percentages of absorption($\frac{GaAs}{Si}$)

Thickness(μm)	20keV	30keV	40keV	50keV	60keV
100	10.1	3.4	1.7	1.1	0.8
150	14.7	5.1	2.5	1.6	1.2
200	19.1	6.8	3.3	2.2	1.6
250	23.3	8.4	4.2	2.7	2.0
300	27.2	10.0	5.0	3.2	2.4

Table 1.2: Percentage X-ray Absorption in Silicon

Thickness(μm)	20keV	30keV	40keV	50keV	60keV
100	89.7	52.6	28.3	16.4	10.4
150	96.7	67.4	39.3	23.6	15.1
200	98.9	77.5	48.7	30.2	19.7
250	99.7	84.5	56.5	36.2	23.9
300	99.9	89.3	63.2	41.6	28.0

Table 1.3: Percentage X-ray Absorption in GaAs

GEANT [7] - a detector simulation package - has been used to simulate the interaction of photons in gallium arsenide and to predict the pulse height spectrum which can be measured. This allows us to investigate the properties used as inputs to the simulation, of which the most pertinent is probably the electric field distribution, defined by the applied reverse bias and by traps in the gallium arsenide. This investigation is reported in Chapter 4.5.

1.5 Detectors

The Glasgow group has fabricated many types of detectors on a common wafer. A picture of one such wafer can be seen in Figure 1.3. In addition to simple pad and microstrip detectors and test structures, two versions of pixel detectors are included on this wafer. (A third version is also under study.) They are all slightly different due to the electronics that will be used to read them out. Table 1.4 shows their relevant pixel dimensions.

The strip detectors have a "punch-through" biasing strip on the top which is

Design	Version	Array	Length(μm)	Width(μm)
Omega(CERN ECP) [8]	1,2	16×64	500	75
	3	16×128	500	50
PAC(DRAL) [9]	1	32×16	200	200
	2,3	8×8	300	300
Marseilles(CPPM)		12×24	330	330

Table 1.4: Dimensions of pixel electronics

used to reduce the voltage at which the detector strips float. Built-in capacitors have also been included with a design voltage of 10 volts to de-couple the detector from the electronics. This is required as many of the read-out chips would not work with the large leakage currents produced by our detectors.

A close-up picture of one detector that has these strips can be seen in Figure 1.4. This particular detector was fabricated by Alenia Spa. in Rome, Italy.

In the largest strip detector in Figure 1.3 the brighter and darker parts are caused by the varying ratio of metallised width to gap width. The detector has a 50μm pitch and there are three regions with different gap to metal ratios. The first has 40μm of metal with 10μm gap, the second 25μm of each and the third 10μm of metal with 40μm gap.

The laboratory testing of these detectors is described in Section 5.4 and test beam results are reported in Sections 6.3 and 6.4.

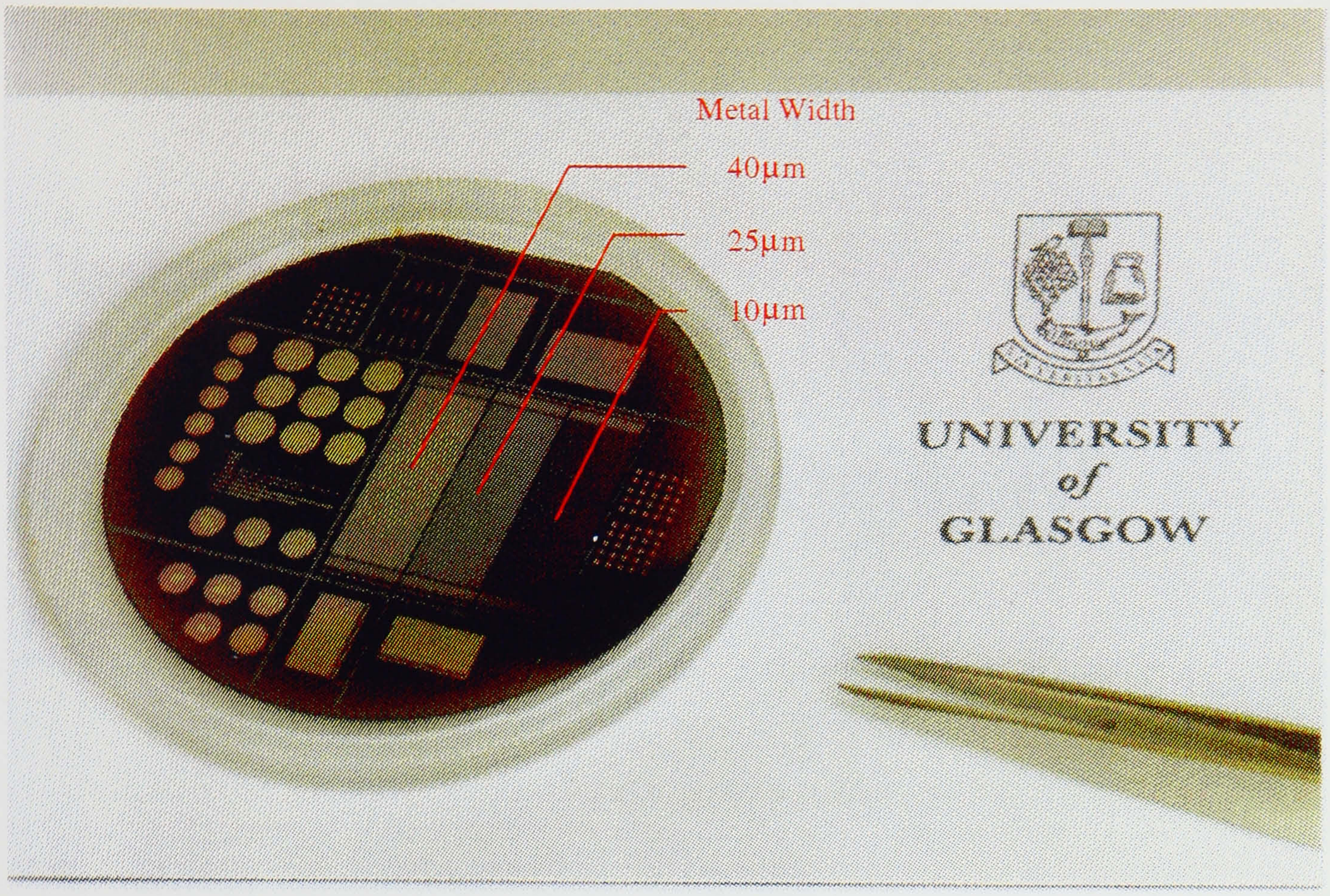

Figure 1.3: Picture of a wafer fabricated in Glasgow

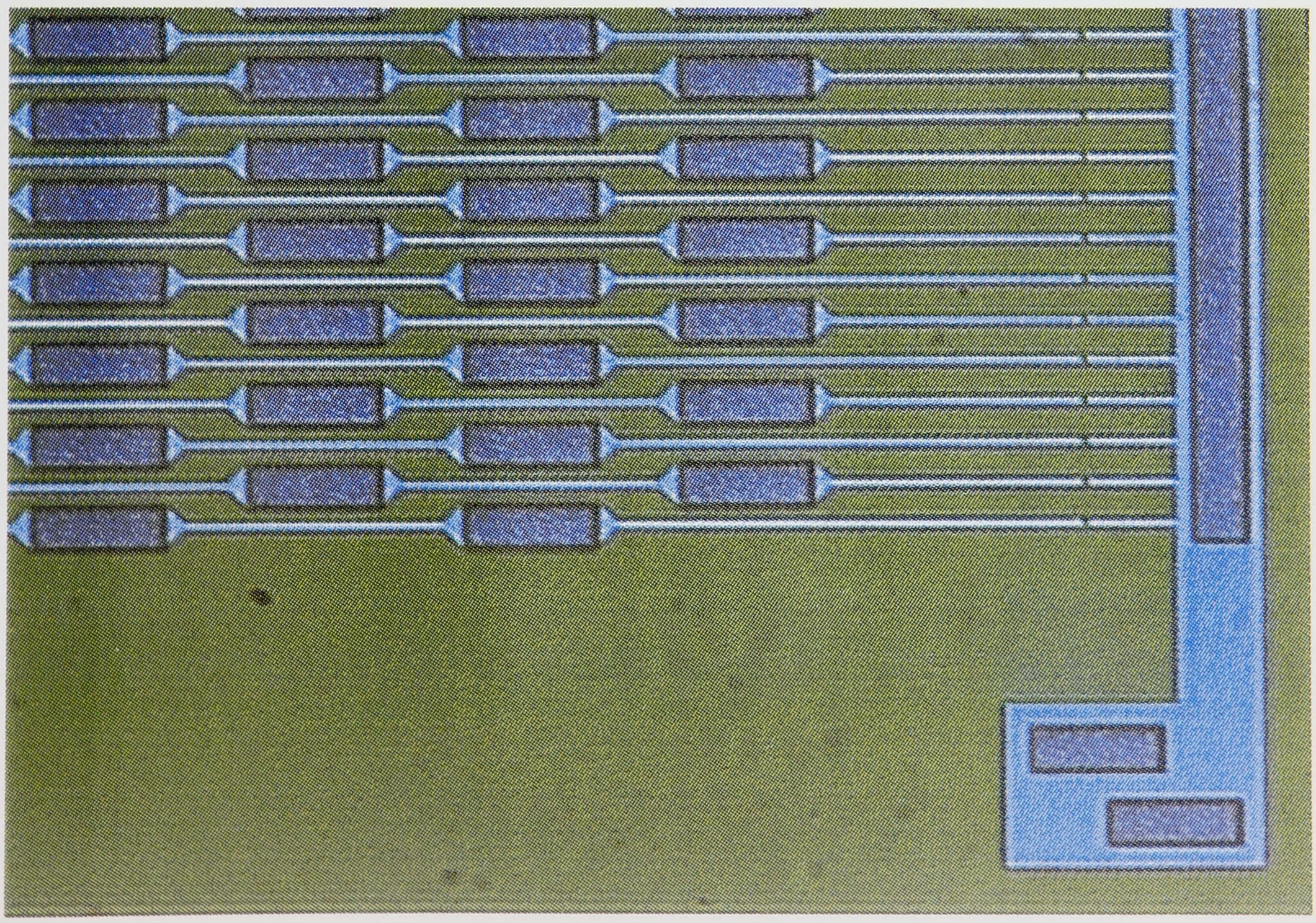

Figure 1.4: Picture of a biasing structure

Chapter 2

Theory of Semiconductor Detectors

2.1 Basic Semiconductor Physics

One of the characteristic properties of certain materials with a periodic structure is that they act as semiconductors. These crystalline materials have one of fourteen geometric configurations of their atoms described by the Bravais lattices. This property is evident as a band gap. In this region there are no energy levels for electrons. If this gap is large the material is an insulator, if the gap does not exist it is a conductor and intermediate between these extremes lie semiconductors (the Fermi level - which will be described later - must also be taken into consideration in this division of materials).

Most elemental and III-V semiconductors are formed in the face centred cubic (fcc) lattice. The basis of this lattice has two atoms, one on the lattice point and the other at $\left(\frac{1}{4}, \frac{1}{4}, \frac{1}{4}\right)$ in terms of the unit cell. If the atoms are identical it is known as a diamond lattice, otherwise as zincblende. A pictorial representation of this is shown in Figure 2.1[10] for a gallium arsenide crystal, which is of the zincblende type.

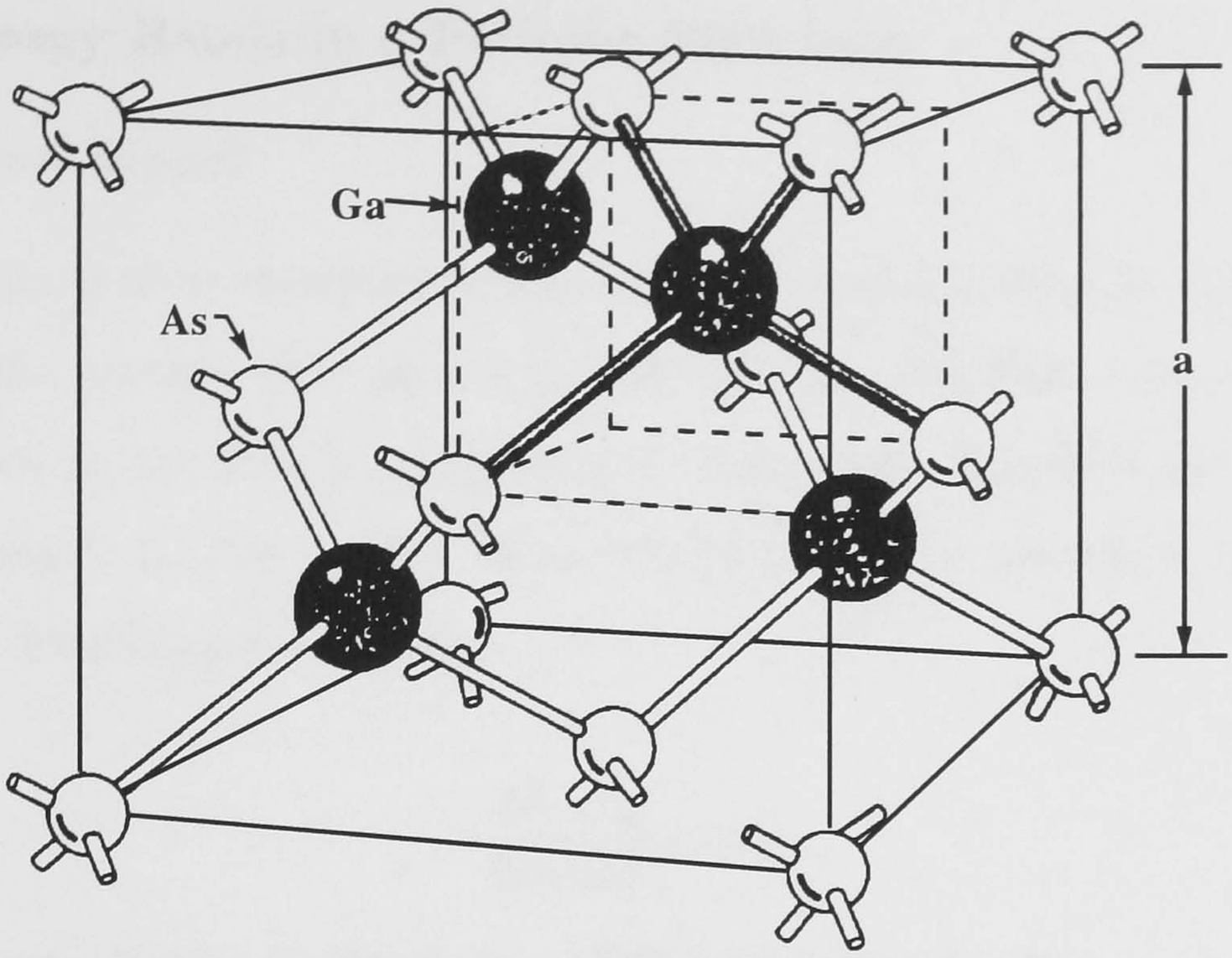

Figure 2.1: Gallium arsenide lattice structure: zincblende

2.1.1 Atomic Bonding

The atoms in the lattice have covalent bonds with each other, that is they share valence electrons with their neighbours. Most of the valence electron's time is spent in the region between the atoms which it is binding together.

This is the case for both silicon (an elemental semiconductor) and gallium arsenide (a III-V semiconductor). However, in addition to this covalent bonding there is a slight attraction between the Ga^- ions and the As^+ ions in gallium arsenide.

At low temperature the valence electrons are bound to the atoms but at higher temperature the thermal energy may be enough for them to escape from the region of the atoms. The electrons will then be available for conduction. They will also leave behind vacancies in the shells of the two atoms. A neighbouring bond may lose an electron which will then fill such a vacancy and create another. Under an applied electric field this vacancy, or "hole" will behave as a positively charged particle.

2.1.2 Energy Bands in a Periodic Structure

Free Electron Model

The behaviour of these electrons needs to be described quantum mechanically. The simplest model assumes that all valence electrons are free from their atomic cores. This is known as the Free Electron Model. Assuming initially a one dimensional crystal of length L, the motion of an electron can be described by the time-independent Schrödinger equation;

$$-\frac{\hbar^2}{2m}\frac{d^2\psi}{dx^2} = E\psi \tag{2.1}$$

The general solution to this form of differential equation is;

$$\psi = A\cos kx + B\sin kx \text{ where } k = \sqrt{\frac{2mE}{\hbar^2}} \tag{2.2}$$

If we impose the boundary conditions that the wave function vanishes at the boundary of the crystal (ie the electrons must remain inside the crystal) then $A = 0$ and $k = \frac{n\pi}{L}$. Therefore, the solution will be;

$$\psi = B\sin\frac{n\pi x}{L} \tag{2.3}$$

By substituting Equation 2.3 into 2.1 we determine the energy levels available for electrons. According to the Pauli Exclusion principle for fermions only two electrons can occupy each state. Therefore for a crystal with N electrons the energy states fill up to a certain level, known as the Fermi level, given by;

$$E_F = \frac{\hbar^2}{2m}\left(\frac{N\pi}{2L}\right)^2 \tag{2.4}$$

At absolute zero all energy levels up to this energy are filled with two electrons. As the temperature of the semiconductor rises some electrons will gain thermal energy and move to empty states above.

If we now generalise this to a three dimensional crystal Equation 2.1 becomes[11];

$$-\frac{\hbar^2}{2m}\nabla^2\psi(\mathbf{x}) = E\psi(\mathbf{x}) \tag{2.5}$$

Rather than limit the size of the crystal to L we now require only that the wave function be periodic over a distance L. This allows the wave function to be non-vanishing at the boundaries. A solution to this equation is a travelling wave of the form;

$$\psi(\mathbf{x}) = A\exp(i\mathbf{k}.\mathbf{x}) \text{ where } \mathbf{k} = \frac{2\mathbf{n}\pi}{L} \tag{2.6}$$

In Equation 2.6 $\mathbf{n}$ is a vector containing three integers denoting the order of the energy level. The energy levels are now given by;

$$E = \frac{\hbar^2}{2m}|\mathbf{k}|^2 \tag{2.7}$$

We must now consider that there may be more than two electrons at a given energy level, but there must only be two at any point in a quantised momentum space ($\mathbf{k}$). Therefore, the filled electron states occupy a sphere of states centred on the origin in this momentum space. The radius of this sphere (k_F) is known as the Fermi wave vector;

$$k_F = \sqrt{\frac{2mE_F}{\hbar^2}} \tag{2.8}$$

The number of electrons in the crystal must equate with the number of available states within this radius, so that;

$$\underbrace{\frac{N}{2}}_{\text{Two electrons per state}} = \overbrace{\left(\frac{4}{3}\pi k_F^3\right)}^{\text{Volume of Sphere}} \cdot \underbrace{\left(\frac{L}{2\pi}\right)^3}_{\text{Reciprocal Volume per state}} \tag{2.9}$$

From this equation the number of states in a shell from k to $k + \mathrm{d}k$ is;

$$\frac{\mathrm{d}N}{2} = \frac{V}{8\pi^3}4\pi k^2 \mathrm{d}k \tag{2.10}$$

By change of variable from $\mathrm{d}k$ to $\mathrm{d}E$ we have;

$$\mathrm{d}N = \frac{V}{\pi^2\hbar^3}\sqrt{2m^3E}\mathrm{d}E \tag{2.11}$$

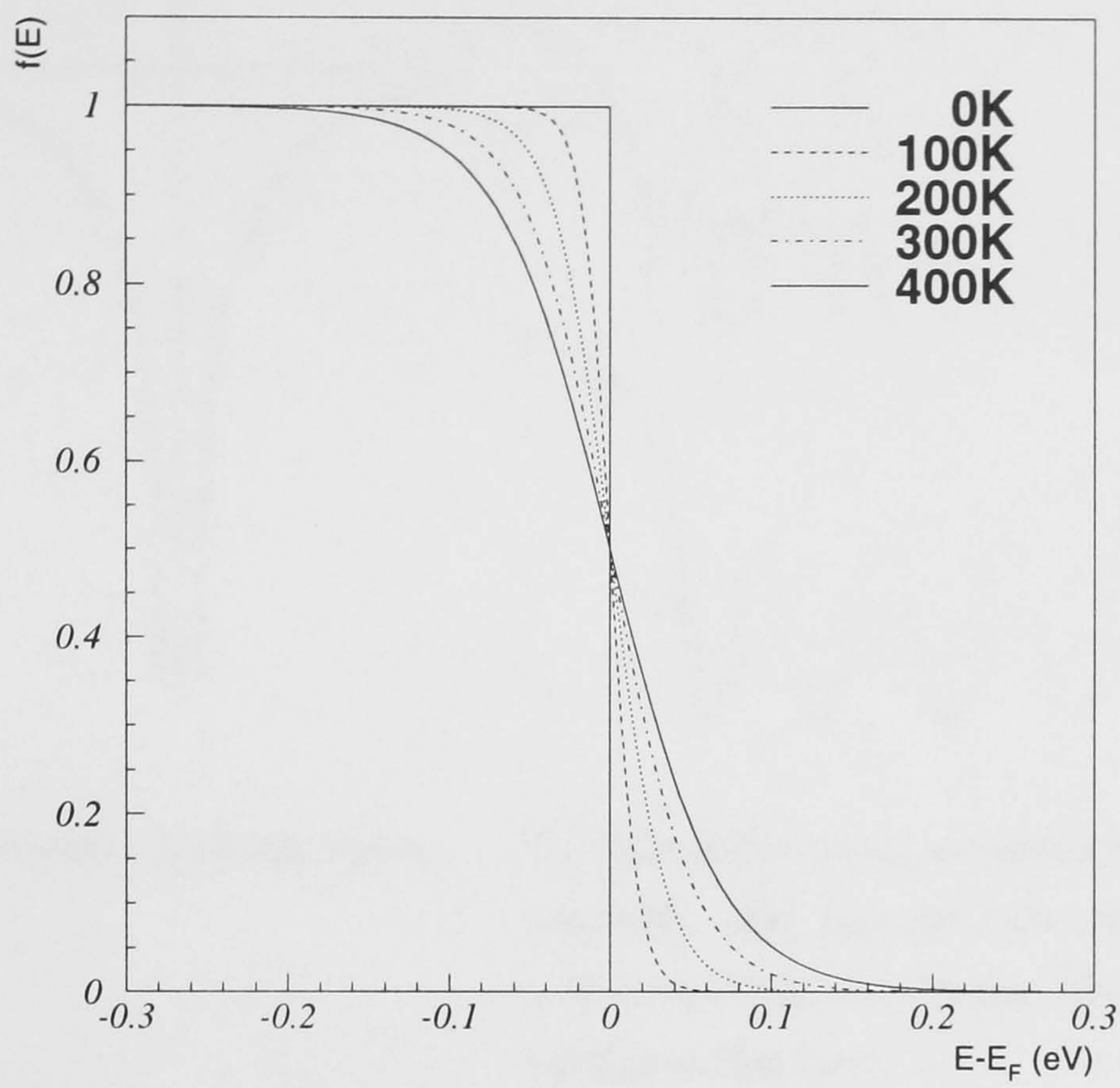

Figure 2.2: Fermi-Dirac distribution

If we now consider the density of states, $D(E)$, which is defined as the number of states available in an energy range $\mathrm{d}E$ per unit crystal volume;

$$D(E) \equiv \frac{\mathrm{d}N}{\mathrm{d}E} = \frac{\sqrt{2m^3}}{\pi^2\hbar^3}\sqrt{E} \tag{2.12}$$

If some electrons gain thermal energy they will begin to fill states higher than E_F. As electrons are fermions they must obey the Pauli Exclusion Principle and so are distributed over energy levels in a Fermi-Dirac manner. The probability of finding an electron within an interval dE of E for a given temperature T is

$$f(E)\mathrm{d}E = \frac{1}{1 + \exp\frac{E-E_F}{k_B T}}\mathrm{d}E \tag{2.13}$$

This distribution is shown in Figure 2.2.

In this model there is an energy state for each allowed value of $\mathbf{k}$. However, for semiconductors or insulators which have a forbidden energy gap, we must adopt a slightly more complicated model.

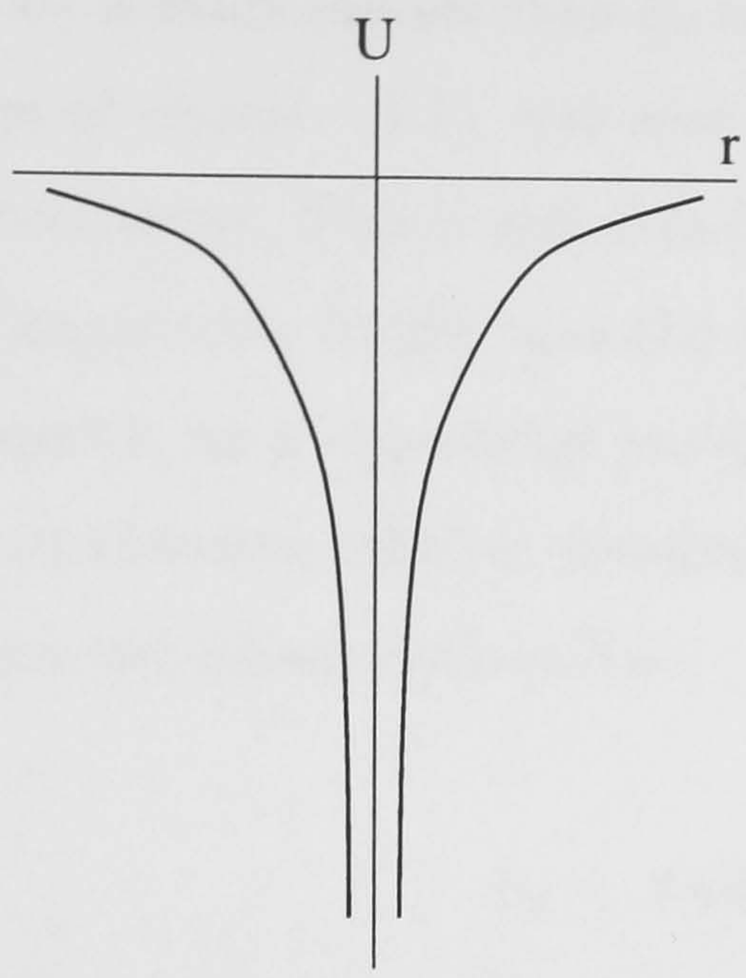

(a) Atomic Coulomb potential

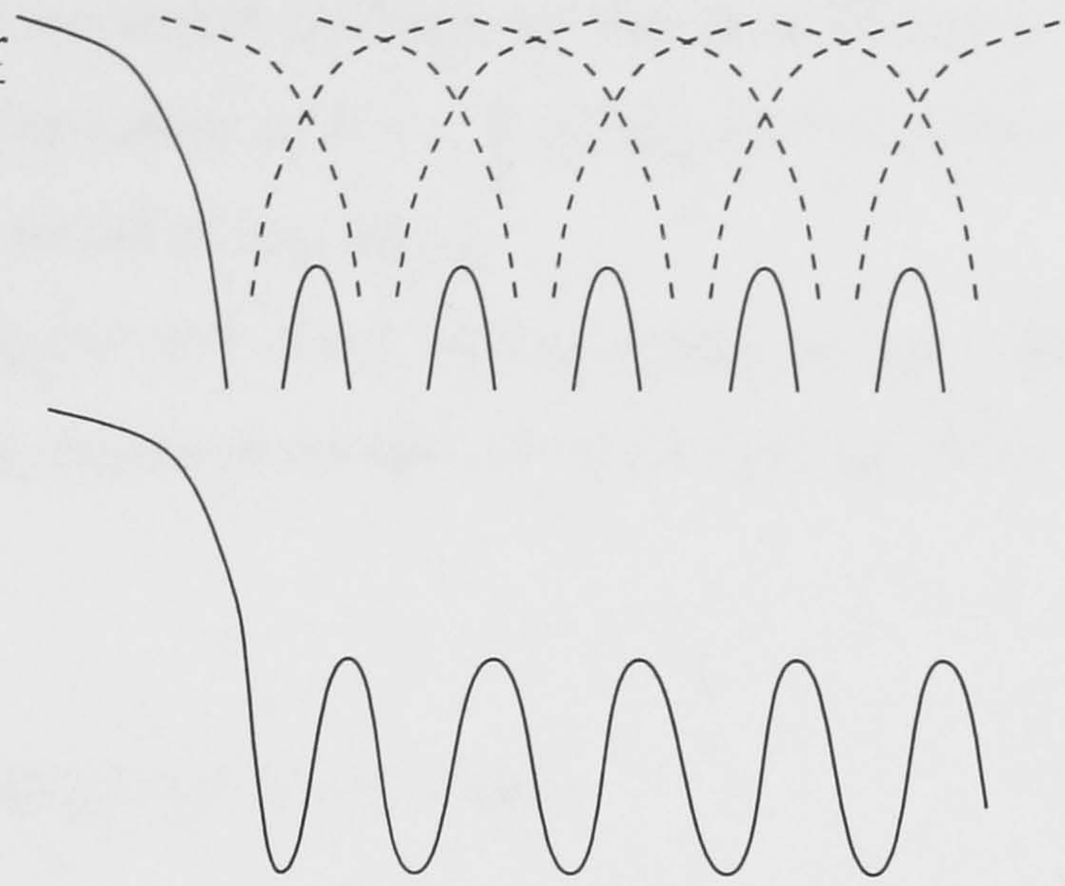

(b) Dashed line shows the individual atom's potential, solid line the potential through a line of atoms and, below, the potential parallel to this line

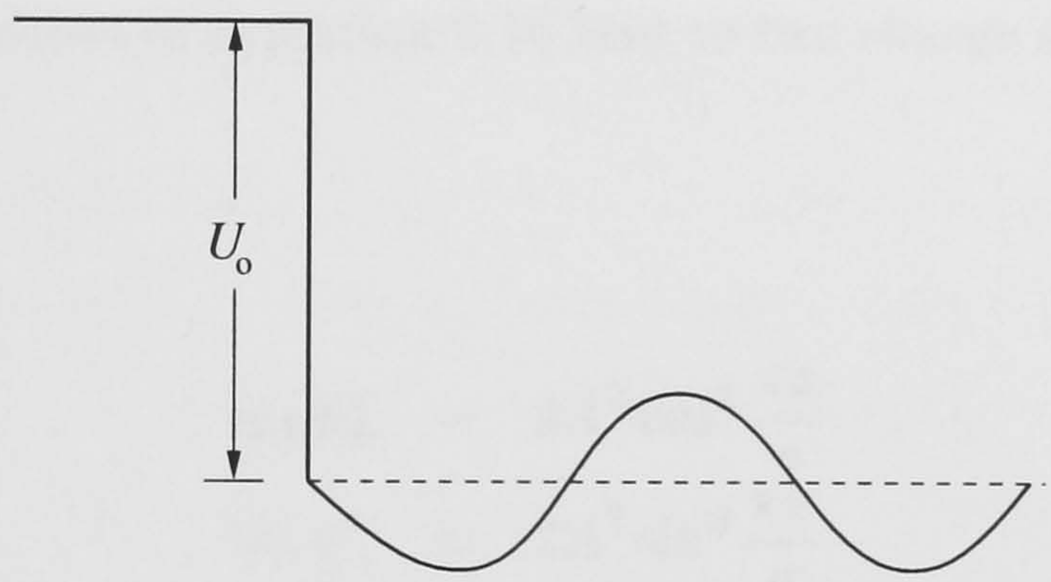

(c) A simplified representation

Figure 2.3: Coulomb Potential in a periodic lattice

Nearly-Free Electron Model

The origin of the forbidden energy gaps is the Bragg reflection of the plane electron waves.

The Coulomb potential due to the atomic cores may be assumed to have a periodic structure, as illustrated in Figure 2.3(c).

This potential can be described by the function;

$$U = U_0 + U_1 \cos \frac{2\pi x}{a} \tag{2.14}$$

where U_1 is much smaller than U_0 and a is the lattice parameter. U_0 is the potential at edge of crystal. If U_1 was zero we would be back at the Free Electron Model described above. This is also true for values of $k << \frac{\pi}{a}$ as the wave function has a much longer wave length than the period of the lattice.

However, as k approaches multiples of $\frac{\pi}{a}$ there will be strong Bragg reflection. We must therefore consider standing waves comprised of two travelling waves which can have two linear combinations;

$$\psi_{\pm} = A \exp(ikx) \pm B \exp(-ikx) \tag{2.15}$$

At the boundary of the lattice this must reduce to zero, leading to equal and opposite forward and backward components there. Therefore $A = B$;

$$\psi_{\pm} = \frac{A}{\sqrt{2}} (\exp(ikx) \pm \exp(-ikx)) \tag{2.16}$$

The two combinations of Equation 2.16 lead to two charge densities proportional to;

$$\psi_{+}\psi_{+}^{*} = 2A^2 \cos^2 \frac{\pi x}{a} \tag{2.17}$$

$$\psi_{-}\psi_{-}^{*} = 2A^2 \sin^2 \frac{\pi x}{a} \tag{2.18}$$

One is concentrated around the ion cores and the other concentrated at the mid-point between them. This clearly means that the two combinations will have very different potential energies due to the Coulomb potential of the ion cores. It is this difference which is the band gap energy, E_g.

The relationships between E and k are shown for the Free Electron Model and the Nearly Free Electron Model in Figures 2.4(a) and 2.4(b) respectively.

2.1.3 Charged Carriers Distribution in Energy Bands

We can determine the number of carriers in each band using the fact that the number of carriers per unit volume $n(E)$ at an Energy E is the density of states per unit volume $D(E)$ multiplied by the probability of that state being filled, $f(E)$. This can be integrated to find the total number of electrons in the conduction band:

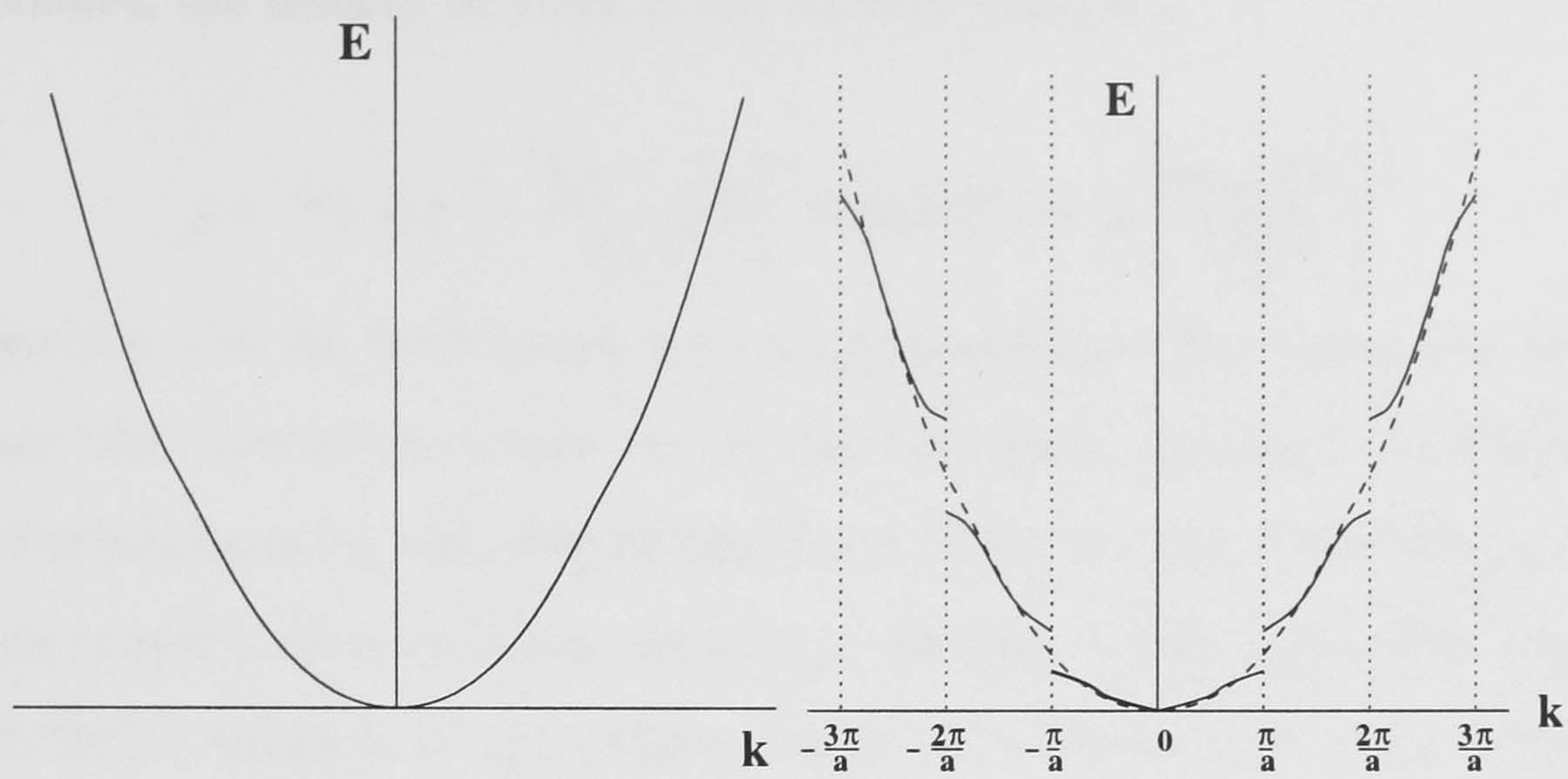

(a) Free Electron Model (b) Nearly Free Electron Model

Figure 2.4: Relationship between E and k

$$n = \int_{E_C}^{\infty} n(E)\mathrm{d}E = \int_{E_C}^{\infty} D(E)\, f(E)\, \mathrm{d}E \tag{2.19}$$

In this equation E_C is the energy of the bottom of the conduction band. The kinetic energy of a hole is taken to be zero at the top of the valence band and increases downwards, and for an electron its kinetic energy is zero at the bottom of the conduction band and increases upward. Due to differences in electrons and holes and the desire to treat them by essentially the same mathematical formalism an effective mass is used, denoted by a subscript n or p. We can use the approximation for Equation 2.13;

$$f(E) = \frac{1}{1 + \exp\frac{E-E_F}{k_B T}} \simeq \exp\frac{-(E - E_F)}{k_B T} \text{ for } (E - E_F) > 3k_B T \tag{2.20}$$

By substituting Equations 2.12 and 2.20 in Equation 2.19, then;

$$n = N_C \exp\left[-\frac{E_C - E_F}{k_B T}\right] \text{ where } N_C \equiv 2\left[\frac{m_n k_B T}{2\pi\hbar^2}\right]^{\frac{3}{2}} \tag{2.21}$$

The probability of a hole filling a state in the valence band is equivalent to an electron **not** filling it, hence

$$f_{\text{holes}}(E) = 1 - f(E) \simeq \exp\left[-\frac{E_F - E}{k_B T}\right] \tag{2.22}$$

Therefore, the density of holes in the valence band is

$$p = N_V \exp\left[-\frac{E_F - E_V}{k_B T}\right] \text{ where } N_V \equiv 2\left[\frac{m_p k_B T}{2\pi\hbar^2}\right]^{\frac{3}{2}} \tag{2.23}$$

Impurities can be introduced into a semiconductor to change its behaviour. There are two types of impurities donors and acceptors. Donors donate electrons to the conduction band by replacing an element with fewer valance electrons. Similarly, acceptors create a vacancy which can accept electrons. This vacancy is a positively charged "hole" which is in the valance band. A semiconductor with impurities is extrinsic.

Equation 2.21 and 2.23, which hold for intrinsic semiconductors must be modified, however, if dopants are present. A dopant will alter the Fermi Level from the intrinsic position E_i. We can therefore re-write these equations as;

$$\begin{aligned} n &= N_C \exp -\frac{E_C - E_i}{k_B T} \exp \frac{E_F - E_i}{k_B T} \\ &= n_i \exp \frac{E_F - E_i}{k_B T} \end{aligned} \tag{2.24}$$

$$\begin{aligned} p &= N_V \exp -\frac{E_i - E_V}{k_B T} \exp \frac{E_i - E_F}{k_B T} \\ &= n_i \exp \frac{E_i - E_F}{k_B T} \end{aligned} \tag{2.25}$$

The amount that the Fermi level moves is determined from charge neutrality. The density of acceptor dopants (or impurities) is denoted N_A and of donors N_D. The simple formula assumes that only donors are present and all of these will be ionised;

$$n = p + N_D \tag{2.26}$$

Now allowing acceptors to be present and taking account of unionised impurities we have

$$n + N_A^- = p + N_D^+ \tag{2.27}$$

where N_A^-, the number of ionised acceptors, is given in Equation 2.28 and similarly N_D^+ is given in Equation 2.29[12].

$$N_A^- = \frac{N_A}{1 + g\exp\left(\frac{E_A - E_F}{k_B T}\right)} \tag{2.28}$$

$$N_D^+ = N_D\left[1 - \frac{1}{1 + \frac{1}{g}\exp\left(\frac{E_D - E_F}{k_B T}\right)}\right] \tag{2.29}$$

In these equations E_A and E_D are the energy levels of the acceptor and donor impurities respectively. The g factor in each equation is the ground state degeneracy and is 2 for N_D^+ because the donor level can accept two spin states of the electron and 4 for N_A^- due to the two spin states of the hole and two degenerate valence bands at $\mathbf{k} = \mathbf{0}$.

Using Equation 2.27, 2.28 and 2.29 it is possible to determine the new Fermi level given N_A, N_D, E_A, E_D, E_V, E_C and T.

2.1.4 Charge Transport

In the absence of an external electric field, conduction band electrons have an average velocity, v_{th}, due to their thermal motion given by

$$\frac{1}{2}m_n v_{th}^2 = \frac{3}{2}k_B T \tag{2.30}$$

This motion is random and in general there is no overall charge transport. However, an applied external electric field gives rise to a drift component which is added to this thermal motion. The overall drift velocity is proportional to the applied electric field for low fields. The constant of proportionality is called the mobility and electrons and holes have their own values (μ_n and μ_p) in different materials,

$$v_n = -\mu_n \mathcal{E} \tag{2.31}$$

$$v_p = \mu_p \mathcal{E} \tag{2.32}$$

The current density (J) due to an external applied field is the number of carriers per unit volume multiplied by their charge and drift velocity. By combining both hole and electron current densities and using Equations 2.31 and 2.32 we can argue;

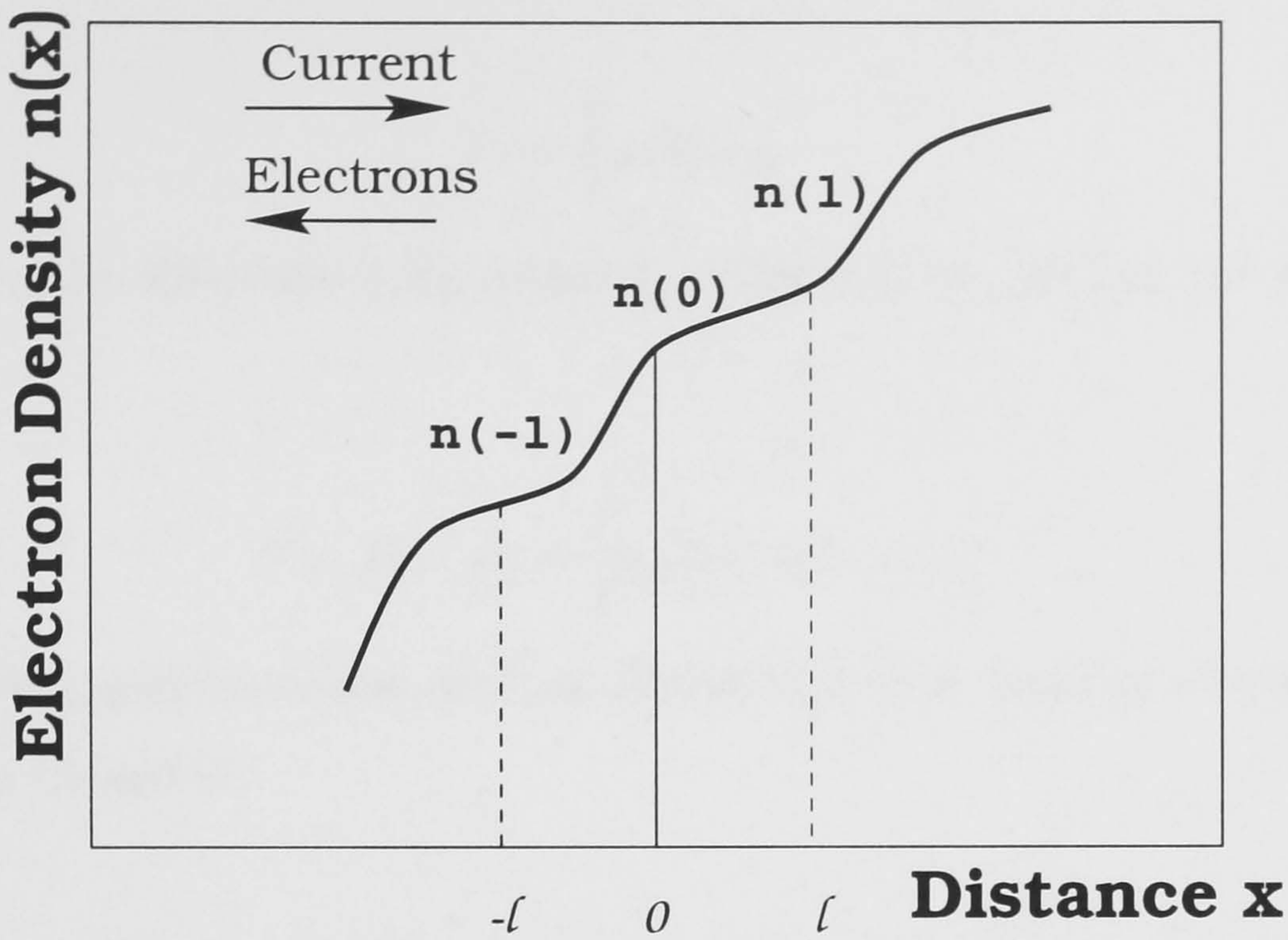

Figure 2.5: Electron concentration versus distance

$$
\begin{aligned}
J &= J_p + J_n \\
&= pev_p - nev_n \\
&= pe\mu_p\mathcal{E} + ne\mu_n\mathcal{E} \\
&= (pe\mu_p + ne\mu_n)\,\mathcal{E} \qquad (2.33) \\
&= \sigma\mathcal{E}
\end{aligned}
$$

where σ is the conductivity of the semiconductor.

A current can also arise from a gradient in carrier concentration. Figure 2.5 illustrates this process.

If we consider the electron distribution shown in Figure 2.5 we can note that the number of electrons crossing $x = 0$ from the left per unit area and time is;

$$F_1 = \frac{\frac{1}{2}n\,(-l)\,.l}{\tau_c} = \frac{1}{2}n\,(-l)\,.v_{th} \qquad (2.34)$$

In this equation n is the density of electrons at x, l is the mean free path of the electron and τ_c is the mean free time. It should be noted that $l = \tau_c v_{th}$. Similarly, for electrons moving from the right the equation is;

$$F_2 = \frac{1}{2} n(l) . v_{th} \tag{2.35}$$

By taking the difference of Equations 2.34 and 2.35 we can find the net carrier movement;

$$F = F_1 - F_2 = \frac{1}{2} v_{th} [n(-l) - n(l)] \tag{2.36}$$

If we now approximate the electron distribution with the first two terms of a Taylor series expansion;

$$\begin{aligned} F &= \frac{1}{2} v_{th} \left\{ \left[n(0) - l \frac{dn}{dx} \right] - \left[n(0) + l \frac{dn}{dx} \right] \right\} \\ &= -v_{th} l \frac{dn}{dx} \equiv -D_n \frac{dn}{dx} \end{aligned} \tag{2.37}$$

where D is the Diffusivity of the semiconductor.

As this is the number of carriers crossing a plane per unit time per unit area, we can multiply this by the charge on an electron to have a current density. This is known as diffusion current and in one dimension for both electrons and holes is given by;

$$J_n = eD_n \frac{\mathrm{d}n}{\mathrm{d}x} \tag{2.38}$$

$$J_p = -eD_p \frac{\mathrm{d}p}{\mathrm{d}x} \tag{2.39}$$

For non-degenerate semiconductors (n much smaller than N_c) an approximation can made called the Einstein relation. This is given by;

$$\mu_n = \frac{e}{k_B T} D_n \tag{2.40}$$

$$\mu_p = \frac{e}{k_B T} D_p \tag{2.41}$$

The total current density is the sum of these two components for both electrons and holes. We can therefore rewrite Equation 2.33 taking into account the diffusion current as;

$$\begin{aligned} J &= J_{\text{drift}} + J_{\text{diffusion}} \\ &= (pe\mu_p + ne\mu_n)\,\mathcal{E} + eD_n\frac{\mathrm{d}n}{\mathrm{d}x} - eD_p\frac{\mathrm{d}p}{\mathrm{d}x} \\ &= (pe\mu_p + ne\mu_n)\,\mathcal{E} + k_BT\mu_n\frac{\mathrm{d}n}{\mathrm{d}x} - k_BT\mu_p\frac{\mathrm{d}p}{\mathrm{d}x} \\ &= e\left[\mu_n\left(n\mathcal{E} + \frac{k_BT}{e}\frac{dn}{dx}\right) + \mu_p\left(p\mathcal{E} - \frac{k_BT}{e}\frac{dp}{dx}\right)\right] \end{aligned} \tag{2.42}$$

By considering a final source of current, generation or recombination of carriers we can find the Continuity Equation. The number of electrons in a portion of semiconductor delimited at x and $x + dx$ with a cross section area of A is the sum of four sources. The number of electrons entering and leaving at each end, the number of electrons generated in the block and the number recombining. The first of these is derived from the currents in Equation 2.42 divided by the electronic charge. The generation and recombination rates are denoted by G_n and R_n respectively for electrons. We can now write the rate of change of the number of electrons in the block as;

$$\frac{\partial n}{\partial t}A.dx = \left[\frac{J_n(x)A}{-q} - \frac{J_n(x+dx)A}{-q}\right] + (G_n - R_n)\,Adx \tag{2.43}$$

There is also a similar equation for the holes. If we use the Taylor expansion for $J_n(x + dx)$ and neglect terms beyond $\frac{\partial^2 J_n}{\partial x^2}dx^2$, as dx is small, we can find the equations;

$$\frac{\partial n}{\partial t} = \frac{1}{q}\frac{\partial J_n}{\partial x} + (G_n - R_n) \tag{2.44}$$

$$\frac{\partial p}{\partial t} = -\frac{1}{q}\frac{\partial J_p}{\partial x} + (G_p - R_p) \tag{2.45}$$

By substituting in Equation 2.42 and using the relations[10];

$$R_n = \frac{n_p - n_{po}}{\tau_n} \tag{2.46}$$

$$R_p = \frac{p_n - p_{no}}{\tau_p} \tag{2.47}$$

we can derive the Continuity Equations for minority carriers;

$$\frac{\partial n_p}{\partial t} = n_p\mu_n\frac{\partial \mathcal{E}}{\partial x} + \mu_n\mathcal{E}\frac{\partial n_p}{\partial x} + D_n\frac{\partial^2 n_p}{\partial x^2} + G_n - \frac{n_p - n_{po}}{\tau_n} \tag{2.48}$$

$$\frac{\partial p_n}{\partial t} = -p_n\mu_p\frac{\partial \mathcal{E}}{\partial x} - \mu_p\mathcal{E}\frac{\partial p_n}{\partial x} + D_p\frac{\partial^2 p_n}{\partial x^2} + G_p - \frac{p_n - p_{no}}{\tau_p} \tag{2.49}$$

In these equations the subscript o denotes the equilibrium value and the values $\tau_{n|p}$ are the minority carrier lifetimes.

2.2 Detector Contacts

2.2.1 p-n Junctions

The basic characteristic of a p-n junction is that it rectifies, that is, it will allow current to pass easily in one direction but not in the other. The physical properties of such a junction are the basis of many facets of semiconductor physics.

It is formed when two pieces of semiconductor are brought together in thermal equilibrium, one of p-type and the other n-type material. In thermal equilibrium there will be no net charge movement across the junction, so from Equation 2.42 and the relation $\mathcal{E} = \frac{1}{e}\frac{dE_i}{dx}$[10] we have, for holes;

$$\begin{aligned} J_p &= e\mu_p\left(p\mathcal{E} - \frac{k_BT}{e}\frac{dp}{dx}\right) \\ &= \mu_p\left(p\frac{dE_i}{dx} - k_BT\frac{dp}{dx}\right) = 0 \end{aligned} \tag{2.50}$$

By using the hole concentration defined in Equation 2.25 and taking its derivative this equation becomes;

$$\begin{aligned} J_p &= \mu_p\left[p\frac{dE_i}{dx} - k_BT\left(\frac{p}{k_BT}\left\{\frac{dE_i}{dx} - \frac{dE_F}{dx}\right\}\right)\right] \\ &= \mu_p p\left(\frac{dE_i}{dx} - \frac{dE_i}{dx} + \frac{dE_F}{dx}\right) \\ &= \mu_p p\frac{dE_F}{dx} = 0 \\ \text{therefore } \frac{dE_F}{dx} &= 0 \end{aligned} \tag{2.51}$$

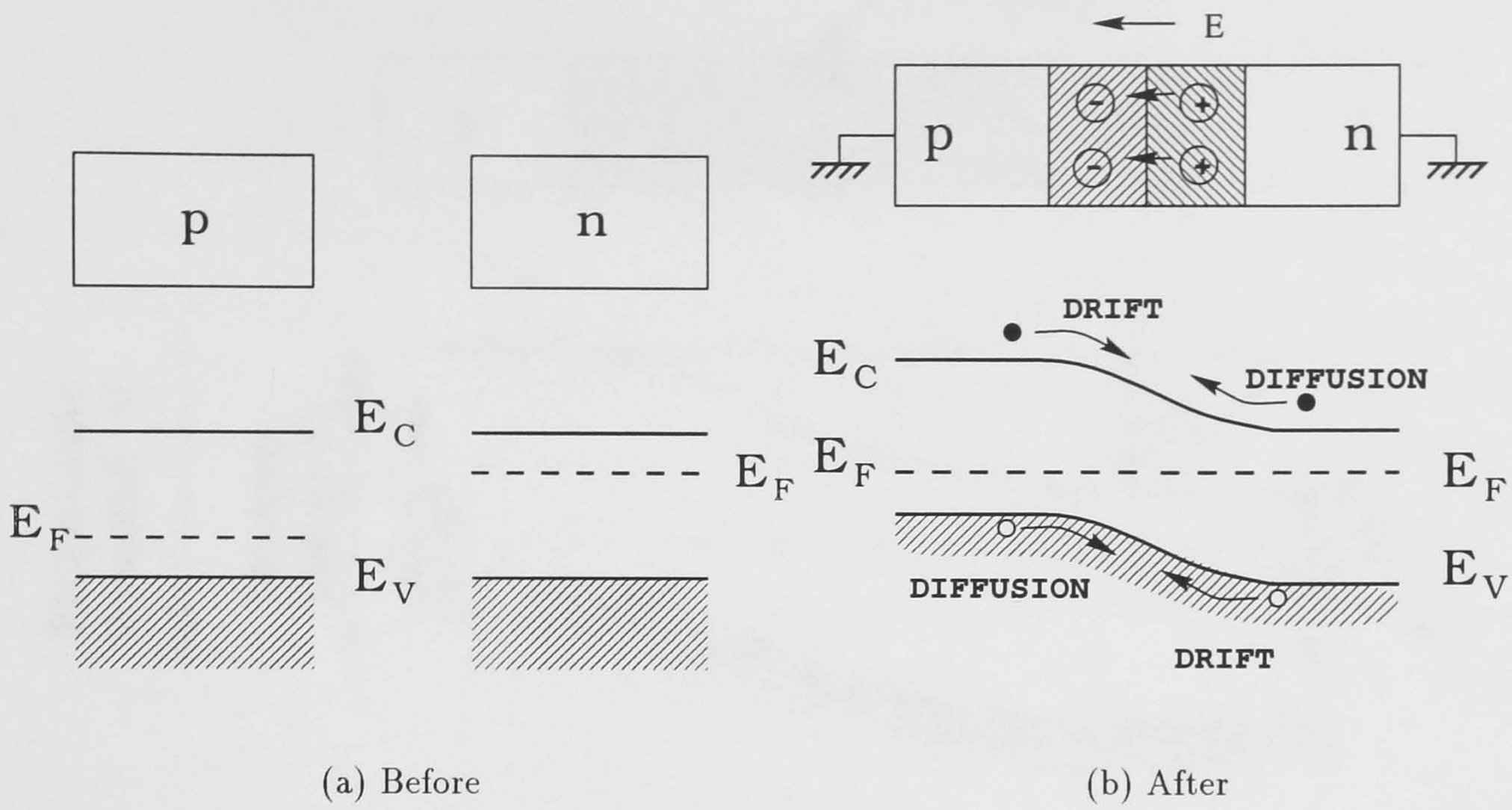

(a) Before (b) After

Figure 2.6: Band configurations in p- and n-type material forming a p-n junction

With a similar argument for electrons this requires, therefore, that the Fermi level on both sides of the barrier be equal. Figure 2.6 shows the consequence of bringing the two types of semiconductor into contact.

The restriction on having a constant Fermi level leads to a unique charge distribution about the barrier. This distribution is found from Poisson's equation,

$$\frac{d^2\psi}{dx^2} \equiv -\frac{d\mathcal{E}}{dx} = -\frac{\rho_s}{\epsilon_s} = -\frac{q}{\epsilon_s}\left(N_D - N_A + p - n\right) \tag{2.52}$$

where ψ is the electrostatic potential. This equation assumes that all donors and acceptors are ionised. At a distance from the junction there will be no net charge and therefore Equation 2.52 reduces to;

$$\frac{d^2\psi}{dx^2} = 0 \tag{2.53}$$

$$N_D - N_A + p - n = 0 \tag{2.54}$$

By assuming that N_D is zero and $p \gg n$ in the neutral p-type region in Equation 2.54 we have $p = N_A$. If we define ψ_p to be the electrostatic potential of the p-type neutral region with respect to the Fermi level (cf Figure 2.7) and by using $p = N_A$ and Equation 2.25;

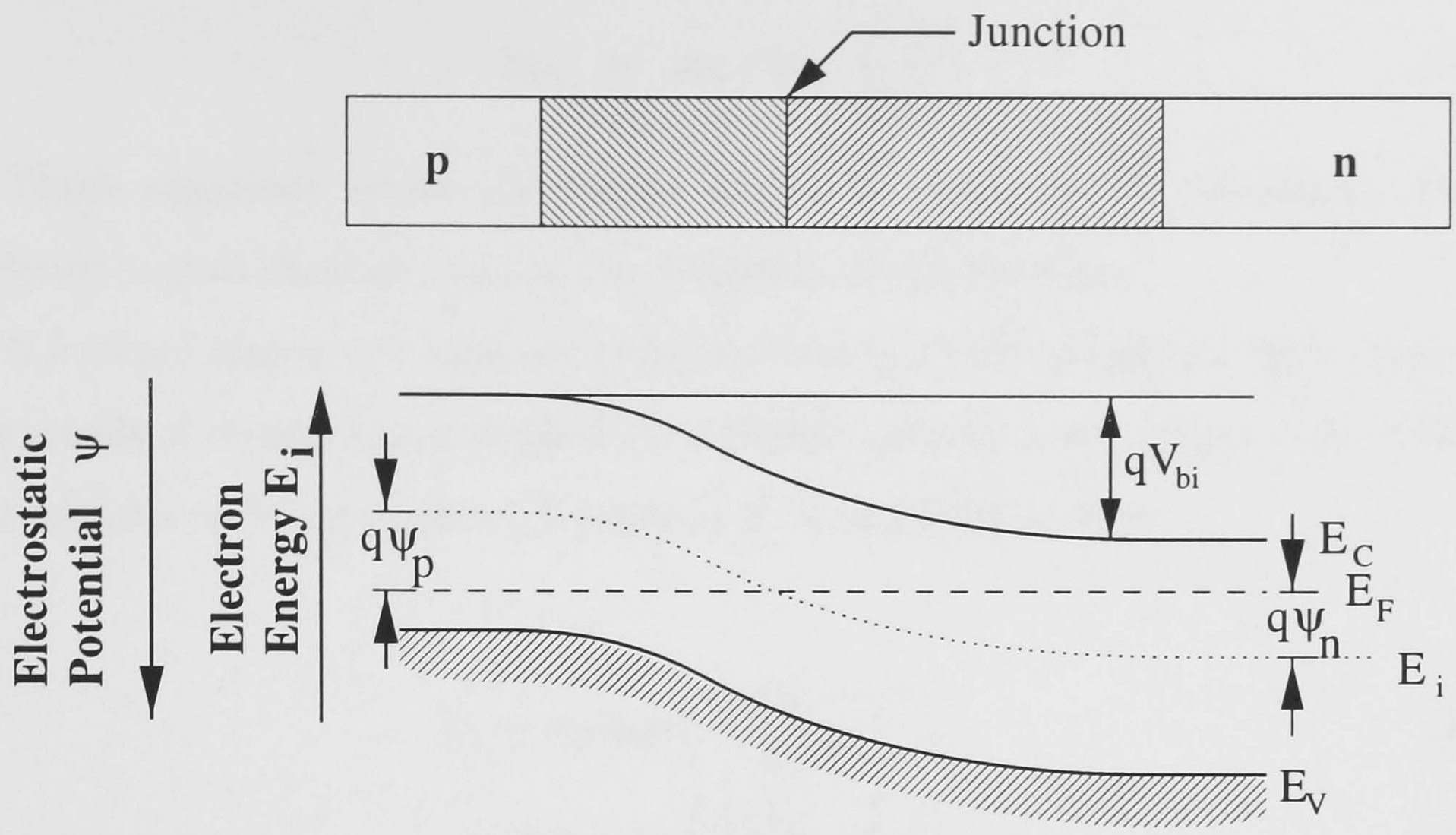

Figure 2.7: Band configurations in a p-n junction

$$\psi_p \equiv -\frac{1}{q}\left(E_i - E_F\right)\big|_{x \leq -x_p} = -\frac{k_B T}{q} \ln \frac{N_A}{n_i} \tag{2.55}$$

and similarly for the n-type region;

$$\psi_n \equiv -\frac{1}{q}\left(E_i - E_F\right)\big|_{x \geq x_n} = \frac{k_B T}{q} \ln \frac{N_D}{n_i} \tag{2.56}$$

The total electrostatic potential across the junction is called the *built-in potential* V_{bi};

$$V_{bi} = \psi_n - \psi_p = \frac{k_B T}{q} \ln \frac{N_A N_D}{n_i^2} \tag{2.57}$$

Using subscripts n or p to denote the substrate type and a subscript o to show the equilibrium value (which will be the relevant dopant concentration), this equation becomes;

$$V_{bi} = \frac{k_B T}{q} \ln \frac{p_{po} n_{no}}{n_i^2} \tag{2.58}$$

By using the relation $n_o p_o = n_i^2$ for both substrates we derive the relationships;

$$n_{no} \quad = \quad n_{po} \exp\left(\frac{qV_{bi}}{k_B T}\right) \tag{2.59}$$

$$p_{po} = p_{no} \exp\left(\frac{qV_{bi}}{k_B T}\right) \tag{2.60}$$

These equations relate the charge carrier densities at the boundaries of the depletion region through the built-in potential of the junction.

If forward bias is now applied to the junction the built-in voltage will be reduced. Conversely, if reverse bias is applied the potential difference will increase. If we define forward bias as being positive, Equations 2.59 and 2.60 become

$$n_n = n_p \exp\left(\frac{q\left(V_{bi} - V\right)}{k_B T}\right) \tag{2.61}$$

$$p_p = p_n \exp\left(\frac{q\left(V_{bi} - V\right)}{k_B T}\right) \tag{2.62}$$

The subscript o has been dropped as now the junction is no longer in equilibrium. If we assume that there is no generation or recombination in the depletion region all current must come from the neutral regions. As there is no electric field in these regions the continuity equation (Equation 2.49) for the n-type region reduces to;

$$\frac{d^2 p}{dx^2} - \frac{p_n - p_{no}}{D_p \tau_p} = 0 \tag{2.63}$$

By using Equation 2.62 and $p_n(\infty) = p_{no}$ as boundary conditions of Equation 2.63 we get;

$$p_n - p_{no} = p_{no}\left[\exp\left(\frac{qV}{k_B T}\right) - 1\right] \exp\left(-\frac{x - x_n}{L_p}\right) \tag{2.64}$$

where $L_p = \sqrt{D_p \tau_p}$ and is called the diffusion length of holes in the n-region. Therefore, at $x = x_n$;

$$J_p\left(x_n\right) = -qD_p \left.\frac{dp_n}{dx}\right|_{x_n} = \frac{qD_p p_{no}}{L_p}\left[\exp\left(\frac{qV}{k_B T}\right) - 1\right] \tag{2.65}$$

Similarly we can derive the current at the p-type end of the depletion region;

$$J_n\left(-x_p\right) = qD_n \left.\frac{dn_p}{dx}\right|_{-x_p} = \frac{qD_n n_{po}}{L_n}\left[\exp\left(\frac{qV}{k_B T}\right) - 1\right] \tag{2.66}$$

The current through the entire device must be constant and is the sum of Equations 2.65 and 2.66;

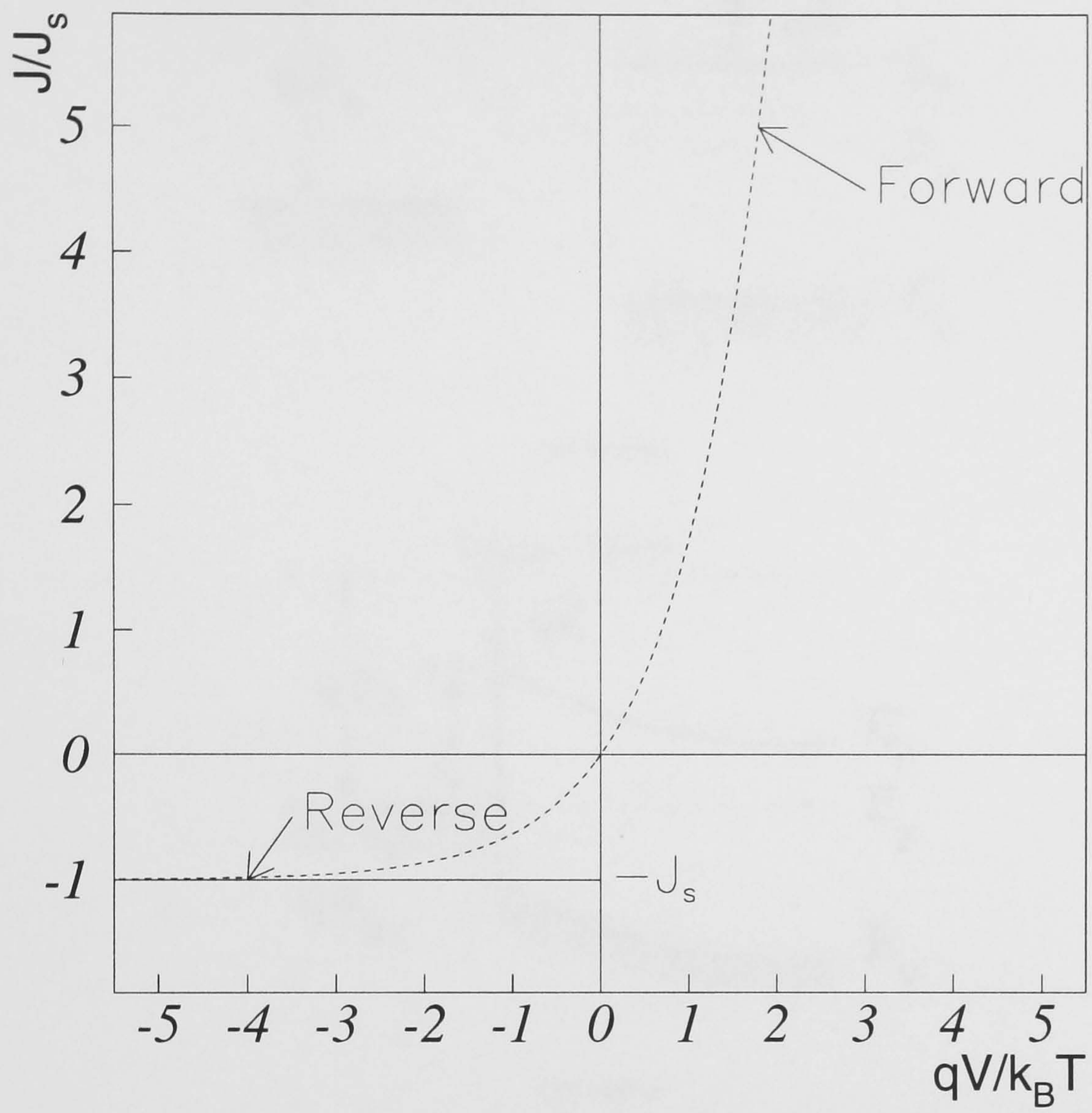

Figure 2.8: Current-voltage characteristics of an ideal diode

$$J = J_s\left[\exp\left(\frac{qV}{k_BT}\right) - 1\right] \tag{2.67}$$

$$J_s \equiv \frac{qD_p p_{no}}{L_p} + \frac{qD_n n_{po}}{L_n} \tag{2.68}$$

J_s is the saturation current and is the maximum current through the device in reverse bias. This equation shows the ideal diode current-voltage characteristics as shown in Figure 2.8.

2.2.2 Schottky Contacts

A Schottky contact is made when certain types of metal are brought into contact with a semiconductor. The factor which determines which type of contact will be

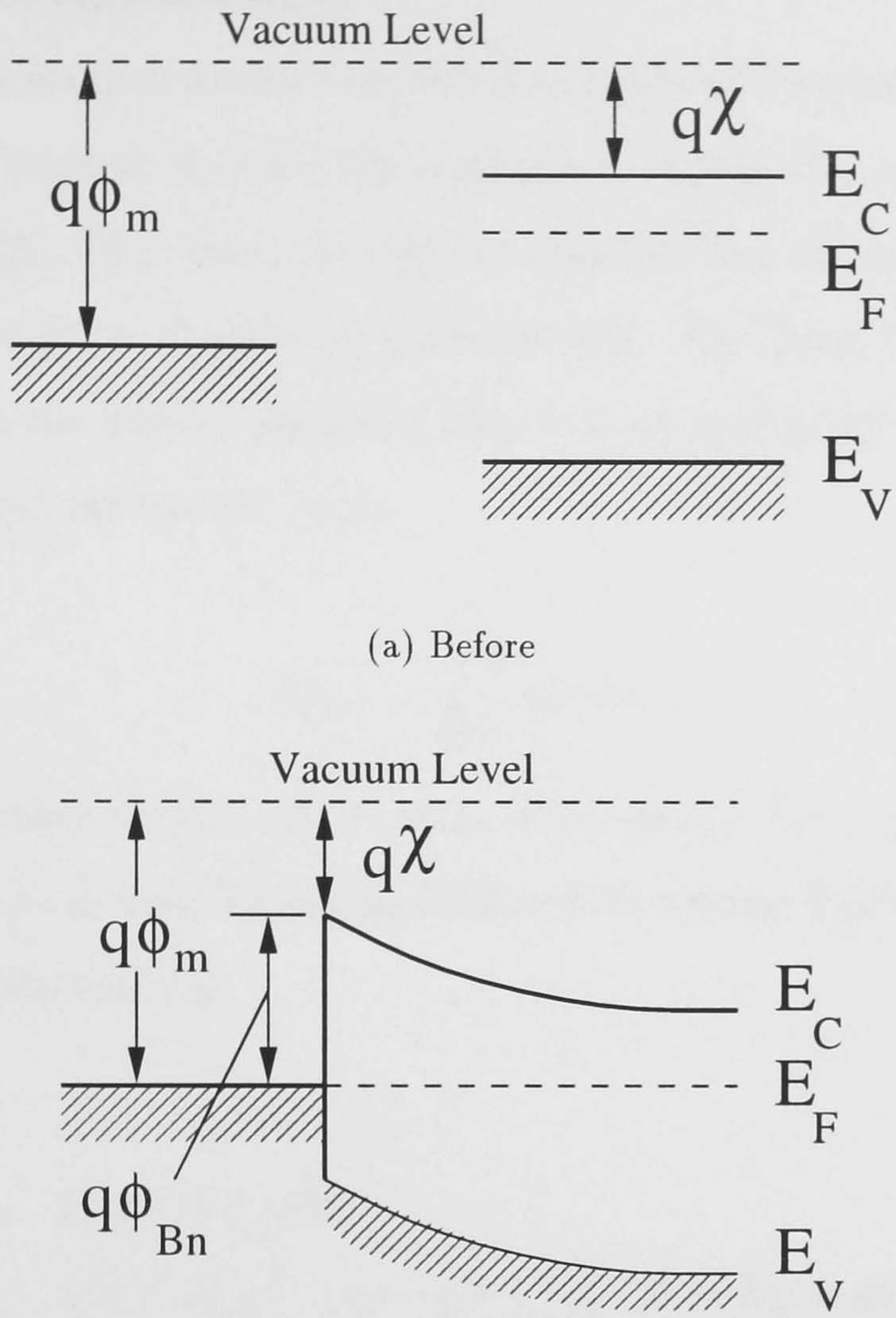

(a) Before

(b) After

Figure 2.9: Band configurations in a metal and n-type material forming a Schottky Contact

formed is the metal's work function, or the energy required to remove an electron from the metal.

Figure 2.9 shows the band structure in the metal and semiconductor before and after contact has been made.

The barrier height for n- and p-type semiconductors will be;

$$q\phi_{Bn} = q(\phi_m - \chi) \tag{2.69}$$

$$q\phi_{Bp} = E_g - q(\phi_m - \chi) \tag{2.70}$$

where χ is the electron affinity of the semiconductor. Therefore, the sum of the barrier heights for any metal on n- and p-type substrates is expected to be equal to

the band gap of that semiconductor.

In high mobility semiconductors operated at moderate temperatures (e.g. 300K) the main source of current in Schottky contacts is thermionic emission of electrons across the barrier[12]. Therefore, the current density from the semiconductor to the metal will be the number density of electrons (c.f. Equation 2.19) with sufficient energy to overcome the barrier potential ($E_F + q\phi_B$) multiplied by their velocity in the direction towards the barrier (v_x);

$$J_{s\rightarrow m} = \int_{n_x}^{\infty} q v_x dn \tag{2.71}$$

where n_x is the number density of electrons with energy $E_F + q\phi_B$.

We know what dn is from Equation 2.19 and also using Equations 2.12 and 2.20 we can derive the relationship;

$$\begin{aligned} dn &= D(E)F(E)dE \\ &= \frac{\sqrt{2}}{\pi^2}\left(\frac{m^*}{\hbar^2}\right)^{\frac{3}{2}} \sqrt{E - E_C} \exp\left[-\frac{E - E_C + qV_n}{k_B T}\right] dE \end{aligned} \tag{2.72}$$

where $qV_n = E_C - E_F$. If we assume that all of the energy of electrons in the conduction band is kinetic we have the formulae;

$$E - E_C = \frac{1}{2} m^* v^2 \tag{2.73}$$

$$dE = m^* v dv \tag{2.74}$$

$$\sqrt{E - E_C} = v\sqrt{\frac{m^*}{2}} \tag{2.75}$$

By using these equations and the transformation $4\pi v^2 dv = dv_x dv_y dv_z$ on Equation 2.72 and then using the result in Equation 2.71 we can find the current from the semiconductor to the metal;

$$\begin{aligned} J_{s\rightarrow m} &= \frac{q}{4}\left(\frac{m^*}{\pi\hbar}\right)^3 \exp\left(-\frac{qV_n}{k_B T}\right) \\ &\int_{v_{ox}}^{\infty} v_x \exp\left(-\frac{m^* v_x^2}{2k_B T}\right) dv_x \int_{-\infty}^{\infty} \exp\left(-\frac{m^* v_y^2}{2k_B T}\right) dv_y \end{aligned}$$

$$\times \int_{-\infty}^{\infty} \exp\left(-\frac{m^* v_z^2}{2k_B T}\right) dv_z$$

$$= \left(\frac{qm^*}{2\pi^2\hbar^3}\right) \{k_B T\}^2 \exp\left(-\frac{qV_n}{k_B T}\right) \exp\left(-\frac{m^* v_{ox}^2}{2k_B T}\right) \tag{2.76}$$

In this equation v_{ox} is the minimum velocity in the x direction required for an electron to cross the barrier and is therefore given by;

$$\frac{1}{2} m^* v_{ox}^2 = q\,(V_{bi} - V) \tag{2.77}$$

where V_{bi} is the built-in potential at no applied bias. By substituting this into Equation 2.76 we have;

$$J_{s\rightarrow m} = A^* T^2 \exp\left(-\frac{q\phi_B}{k_B T}\right) \exp\left(\frac{qV}{k_B T}\right) \tag{2.78}$$

$$A^* = \frac{qm^* k_B^2}{2\pi^2\hbar^3} \tag{2.79}$$

where A^* is the effective Richardson constant for thermionic emission and ϕ_B is the barrier height and is equal to the sum of V_{bi} and V_n.

As the barrier height must be the same in both directions in equilibrium $J_{s\rightarrow m}$ must equal $J_{m\rightarrow s}$. Therefore, the current density of electrons from the metal into the semiconductor is derived from Equation 2.78 with $V = 0$;

$$J_{m\rightarrow s} = -A^* T^2 \exp\left(-\frac{q\phi_{Bn}}{k_B T}\right) \tag{2.80}$$

The total current density is therefore the sum of Equations 2.78 and 2.80;

$$J_n = J_s \left[\exp\left(\frac{qV}{k_B T}\right) - 1\right] \tag{2.81}$$

$$\text{where } J_s = A^* T^2 \exp\left(-\frac{q\phi_{Bn}}{k_B T}\right) \tag{2.82}$$

Therefore the current-voltage characteristics for a Schottky diode and a p-n junction are similar but with a very different form for the saturation current densities J_s.

2.3 Signal Generation in GaAs Detectors

The signal generated in a semiconductor particle detector is due to ionisation produced by the particle as it traverses the detector. The particle will knock electrons from the valence band into the conduction band, thereby creating an electron-hole pair. The number of electron-hole pairs generated depends on the energy deposited by the particle (which depends on the density of the material) and the energy required to create a pair. These numbers are tabulated in Table 1.1.

However, this is the number of carriers generated by the particle. The measured signal is related to this by Ramo's Theorem[13]. This theory, which has been shown to be applicable in semiconductor detectors[14, 15], states that;

$$i = E_v q v \tag{2.83}$$

where i is the instantaneous current induced on a strip electrode, E_v is the *equivalent* electric field, measured in m^{-1}, in the direction of v at the position of the electron and v is the velocity of the electron. This is the current due to a single electron. The *equivalent* field is found by placing the strip in question at 1V, grounding all other contacts and removing the electron.

To find the charge contribution from a single electron Equation 2.83 can be expressed for parallel electrodes - as is the case for semiconductor detectors - as;

$$dQ = \frac{q}{d} dx \tag{2.84}$$

where q is the charge on the electron, d is the separation of the electrodes and dx is the distance moved to induce the charge dQ on the electrodes.

However, there is an added complication in gallium arsenide detectors due to "traps". These are states which exist in the band gap that will "trap" free carriers and consequently these carriers will no longer contribute to the charge signal. In addition, not all of the detector's thickness will be active in general. There will be a "dead" layer (D) under the non-rectifying contact which will have a low electric field. In this region electron-hole pairs will recombine and free carriers will not have a large velocity. If we parameterise these effects with an active thickness (χ_A) for

the "active" layer (A) and mean free paths of carriers in the two regions ($\lambda_{[eh]}^{[AD]}$) we have the formulae;

$$
\begin{aligned}
Q_e &= \frac{q}{d}\left[\int_{x_o}^{\chi_A} \exp\left(-\frac{x-x_o}{\lambda_e^A}\right) dx + \exp\left(-\frac{\chi_A - x_o}{\lambda_e^A}\right)\int_{\chi_A}^{d} \exp\left(-\frac{x-\chi_A}{\lambda_e^D}\right) dx\right] \\
Q_h &= \frac{q}{d}\int_0^{x_o} \exp\left(-\frac{x_o - x}{\lambda_h^A}\right) dx
\end{aligned}
$$

where x_o is where the electron-hole pair is created. Figure 4.3 shows this configuration. It should be noted that holes will move towards the rectifying contact. These equations can be combined to determine the charge collection efficiency (ϵ) given the thickness, active thickness, mean free paths of the carriers and the depth at which electron-hole pairs are generated;

$$
\begin{aligned}
\epsilon\left(x_o, \chi_A, d, \lambda_{[eh]}^{[AD]}\right) = \frac{1}{d}\Bigg[&\int_0^{x_o} \exp\left(-\frac{x_o - x}{\lambda_h^A}\right) dx + \int_{x_o}^{\chi_A} \exp\left(-\frac{x-x_o}{\lambda_e^A}\right) dx \\
&+ \exp\left(-\frac{\chi_A - x_o}{\lambda_e^A}\right)\int_{\chi_A}^{d} \exp\left(-\frac{x-\chi_A}{\lambda_e^D}\right) dx\Bigg]
\end{aligned}
\tag{2.85}
$$

To determine the charge collected this quantity must be integrated through the detector depth multiplied by the number of electron-hole pairs created and the charge of an electron;

$$
Q = \frac{q\rho}{g}\int_0^d \epsilon\left(x, \chi_A, d, \lambda_{[eh]}^{[AD]}\right) \left.\frac{dE}{dx}\right|_x dx \tag{2.86}
$$

where ρ is the density of the material and g is the energy required to create an electron-hole pair.

2.4 Noise Sources in Semiconductor Detectors

In semiconductor detectors there are four classes of noise sources. These are thermal, shot, generation-recombination and modulation noise. The last of these is not as yet fully understood.

The first of these, thermal noise, is due to the random movement of carriers in the detector and its contacts. This noise is white and has a current spectral density given by[16];

$$S_i = \frac{4k_BT}{R} \tag{2.87}$$

where R is the resistance of the semiconductor.

The second form of noise is shot noise, which is due to the discrete flow of the charge carriers which constitute the leakage current of the detector.

Shot noise can be represented by adding a current source in parallel with the detector. The r.m.s. magnitude of this current, $\sqrt{\overline{i^2}}$, is given by[17]

$$\overline{i^2} = 2qI_{\text{leakage}}\Delta f \tag{2.88}$$

Due to the high levels of leakage current in gallium arsenide this term dominates and other noise sources are generally small in comparison.

The third classification, generation-recombination noise, is due to carriers being continually trapped and later de-trapped in the semiconductor.

The noise spectral density at low frequencies has a approximate 1/f dependence. This is known as modulation noise (or 1/f noise). The noise spectrum from a typical gallium arsenide detector pad is shown in Figure 2.10.

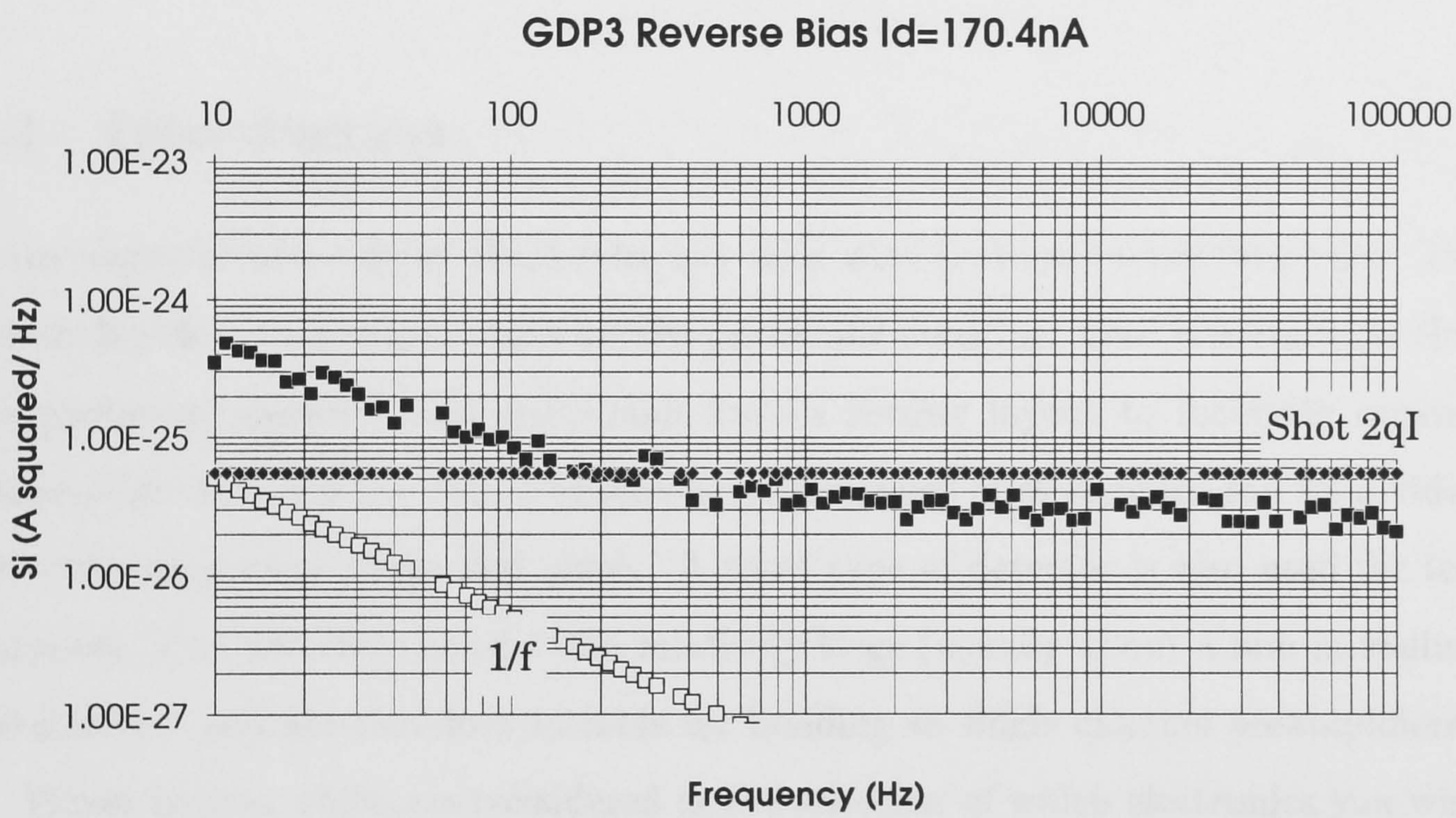

Figure 2.10: Noise Spectrum from a GaAs Detector which is a 7mm^2 pad detector with a thickness of 220μm

Chapter 3

Read-out Electronics

3.1 Introduction

Many varieties of read-out electronics are used with semiconductor detectors. The choice depends to a large extent on the particular detector. One constraint is that the particular detector and electronics have a similar layout to facilitate making connections between the two. Consequently, the types of electronics can be divided into two categories: strips and pixels. A third type of detector is also used for test purposes. Pad detectors consist of a relatively large (usually about a mm in radius) circular pad and are therefore suitable for bonding to single channel preamplifiers.

Other factors which are considered in the selection of which electronics you wish to use are noise, speed, power and architecture. The first of these is quite obvious: the noise of the electronics must be as low as possible in comparison with the signal to be measured.

Many applications also require fast electronics. For the LHC the shaping time of the electronics has been specified to be 50ns. This is due to the bunch crossing rate: which is to be 40MHz. The minimum time between (Level One) triggers will be 2 bunch crossings. Most other applications are not as stringent as this.

The heat generated by the electronics must also be at a manageable level. If there are going to be a very large number of channels then each channel must contribute a very small amount of heat. For example, ATLAS will have somewhere in the region of 10^7 micro strip detector channels and each electronics channel has been given the target of 1 mW, which adds up to 10kW for the inner detector.

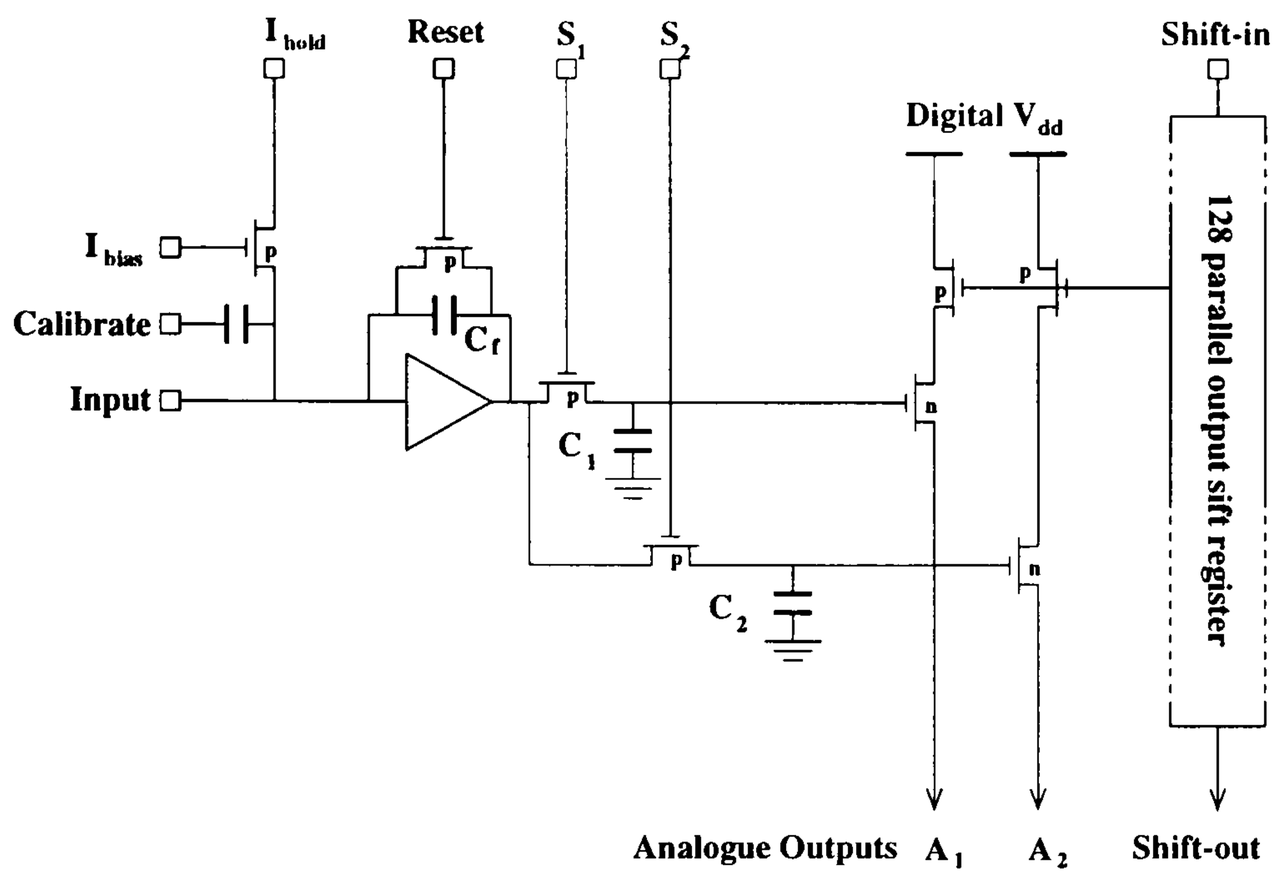

Figure 3.1: Basic MX Read-out Schematic

The architecture of the chip determines how easy or difficult it is to construct the system that will run the chip. The main architectural decision is what information the chip will produce: analogue, binary or digital. This choice is based on the application, for example for the measurement of an X-ray energy spectrum the choice would be limited to analogue or digital, (although presently available digital systems would not give adequate energy resolution to examine the features present in peaks, at the moment).

By using a binary system the amount of data to be moved around an experiment is reduced by an order of magnitude. The digital system has the advantage over a pure analogue system in removing the need for discrete ADCs. Analogue and digital systems allow on-line diagnostics of the detector system. Any drop in performance can become evident sooner. These systems can also use charge division to obtain a better position resolution with the same pitch of detector strips.

3.2 Microstrip Detectors

3.2.1 MX7-RH

The MX series of chips are 128 channel analogue pre-amplifiers. They use a multiplexed output so that all channels are read out using two cables. The output is the difference between the signals on these two cables.

The basic schematic for this chip is shown in Figure 3.1[18].

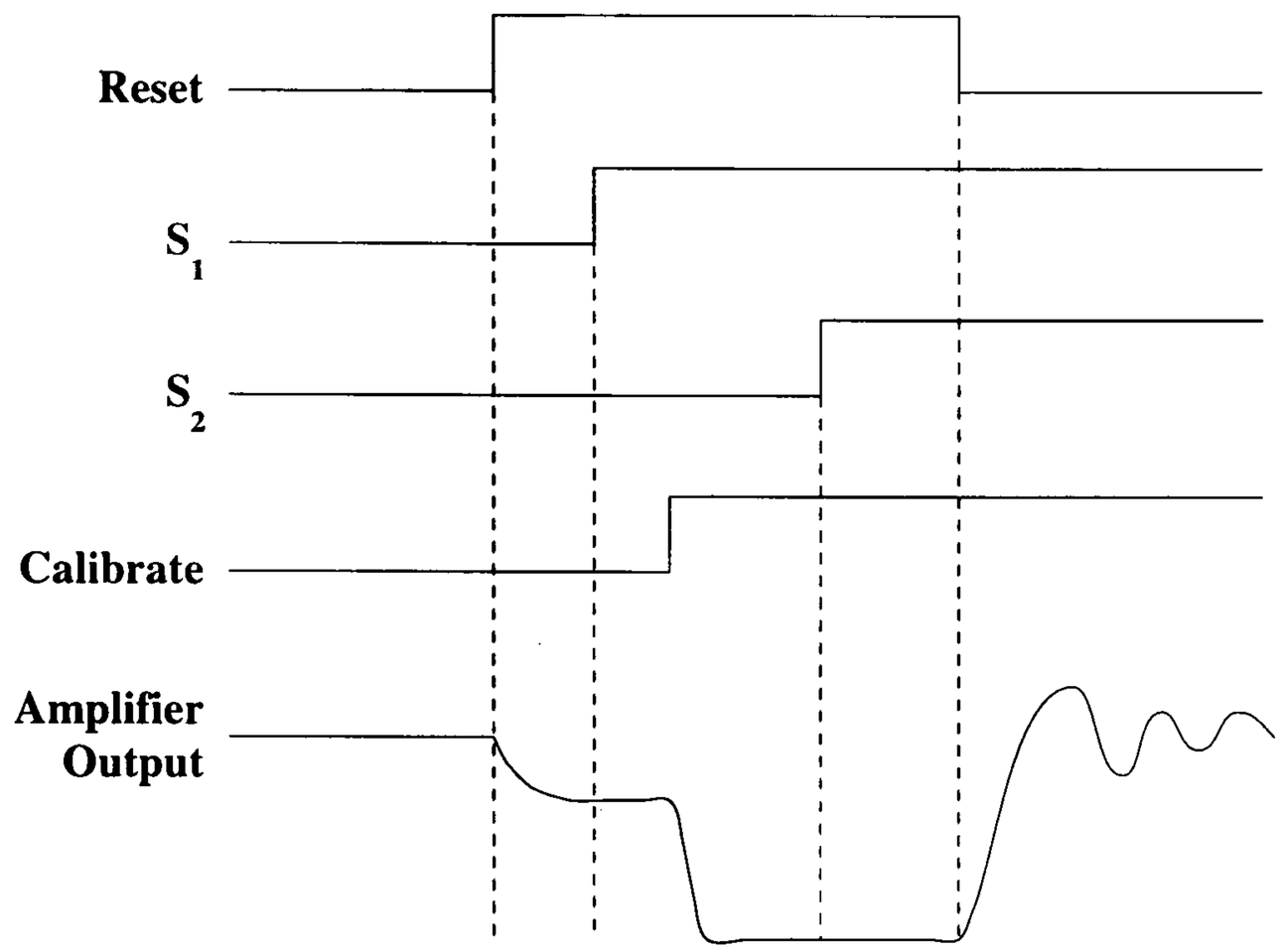

(a) Data Capture

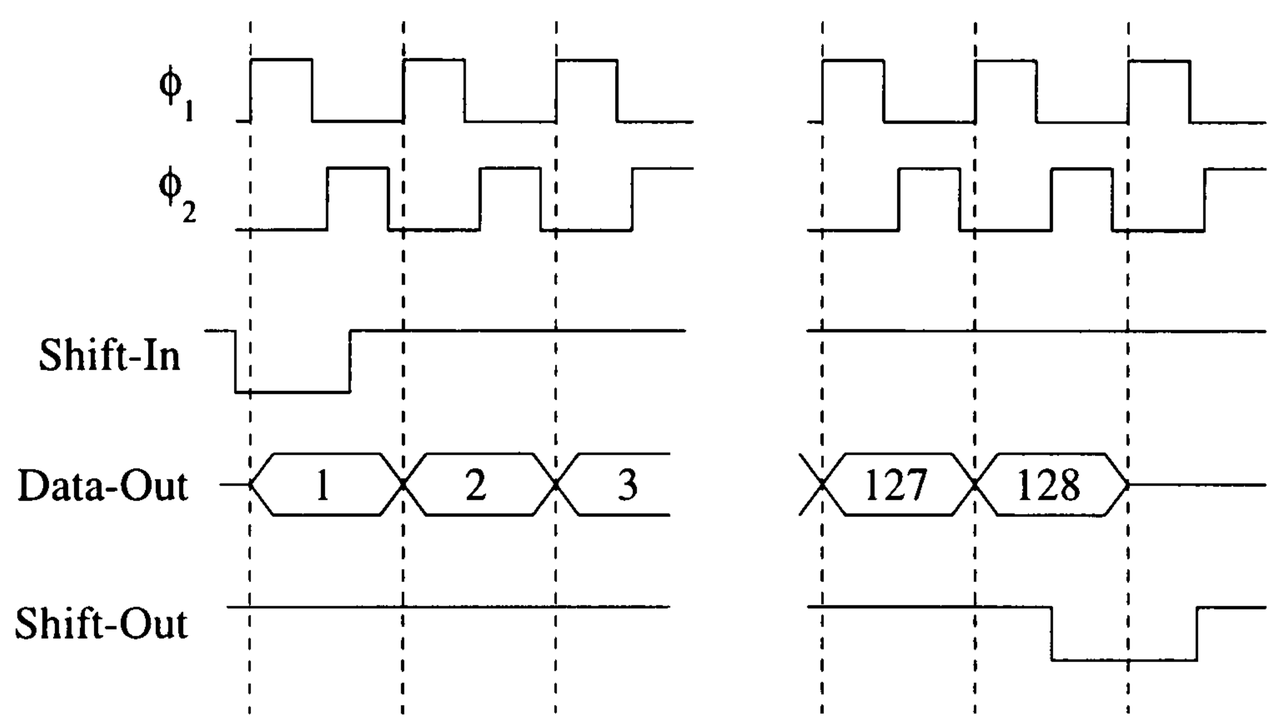

(b) Data Output

Figure 3.2: MX read-out sequence

Before the read-out phase, charge is built up on $C1$ to provide the background level of the pre-amplifier. During the read-out, charge from the event is built up on C_f and then the output level of the pre-amplifier is output to $C2$. Subtracting the signal on $C1$ from that on $C2$ should then eliminate common mode noise. The signals on these capacitors are read out when the SHIFT_IN signal has reached that channel in the shift register.

The read-out sequence is shown in Figure 3.2.

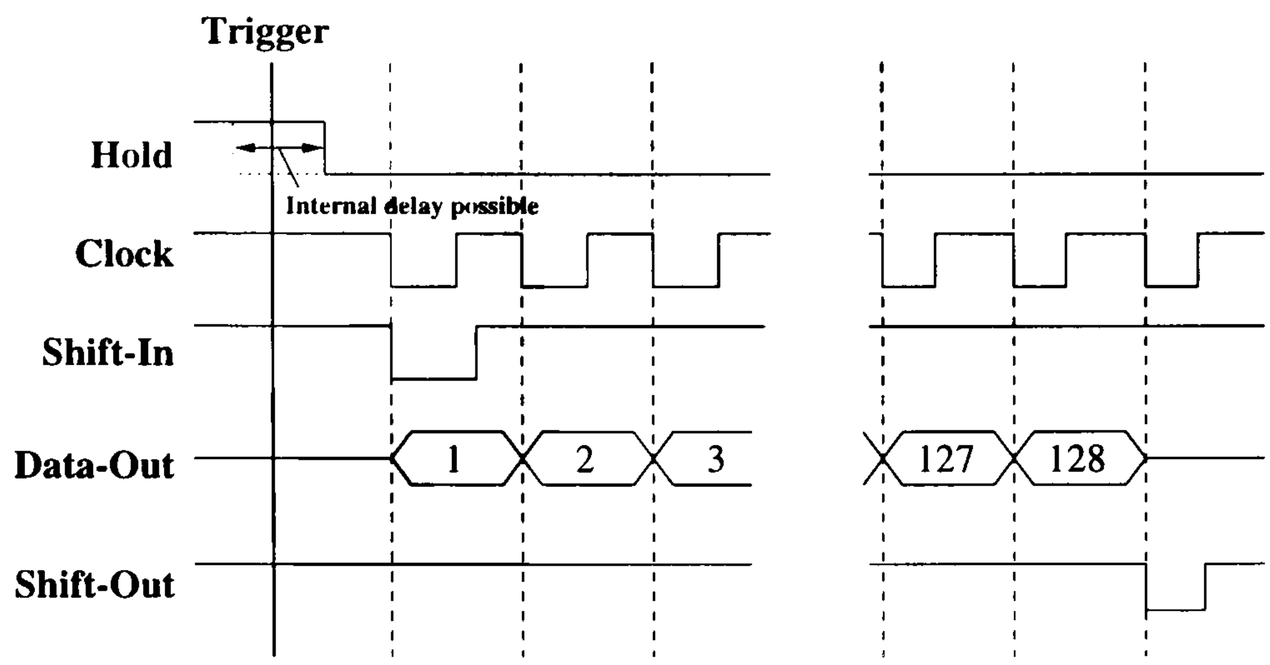

Figure 3.3: Viking read-out sequence

3.2.2 Viking

The Viking is also a 128 channel analogue output pre-amplifier. However, it uses a continuously sensitive amplifier in addition to being able to self trigger[19].

The read-out sequence of the Viking can be seen in Figure 3.3. The pre-amplifier of this chip has a 1.5μs shaping time with a noise performance of[20];

$$\mathrm{ENC_{preamp}} = 136e^- + 12C_{\mathrm{load}}[\mathrm{pF}]e^- \tag{3.1}$$

The noise due to the detector leakage current will be;

$$\mathrm{ENC_{leakage}} = \frac{e}{q}\sqrt{\frac{qI_{\mathrm{leakage}}\tau}{4}} \tag{3.2}$$

where τ is the shaping time of the pre-amplifier, e is the base of natural logarithms and q is the electronic charge. The noise due to the parallel resistance of the detector system is;

$$\mathrm{ENC_{resis}} = \frac{e}{q}\sqrt{\frac{\tau k_B T}{2R}} \tag{3.3}$$

where R is the parallel resistance.

3.2.3 APV5-RH

The APV5[21] read-out chip is designed to run at 40MHz so that it can be used at the LHC. However, due to a design flaw, the present version of the multiplexer only runs reliably at 20MHz.

This chip is also a 128 channel analogue read-out chip. It also incorporates a 160 event deep pipeline, to allow time for the trigger decision to be made. This trigger latency is programmable by the number of CLOCK cycles between the end of the RSTT and RSTP signals and should not exceed 128×25 ns. Once this latency time has passed the event will be read out through a multiplexer. To reduce noise and power consumption the channels are read out in Gray Code order. (This order allows only one bit to change state between channels).

While initial results from this chip are poor[22], an attempt is being made to rectify the problems identified in 1995 test beam running and a new revision (APV6) should be produced early in 1996.

3.2.4 FELIX

The FELIX[23] chip in an analogue read-out chip with 128 channels but at present it requires an external multiplexer. This chip has been used successfully in the 1995 test beam running[22]. The design will be transferred to rad-hard technology early in 1996.

3.2.5 AROW

The AROW read-out chip is a digital read-out chip incorporating the full architecture required for LHC operation, and is created from various subsystem designs incorporated into a single chip[24]. It will be a 128 channel, 7 bit digital read-out. The full scale value of the built-in ADC will be equivalent to the signal from 8 minimum ionising particles in 300μm of silicon (about 160,000 electrons). It will do pedestal subtraction and zero suppression before outputting data. A first (rad-soft) production run should supply chips for testing in March 1996.

3.2.6 The Binary Chip

Another read-out chip which is being evaluated for LHC experiments is the Binary Chip[25] incorporating a CAFE bipolar preamplifier stage. This chip uses an externally set comparator threshold to determine if there is a hit in a strip. If there is it will output the strip number of the hit strip. This approach reduces

the amount of data output by the detector but prevents the use of charge sharing information and the ability to use the data for online detector diagnostics.

3.3 Pixel Detectors

3.3.1 The PAC Family

A number of versions of the Pixel Array Chip have been designed at RAL. With the first version, PAC1, a pixel would register a hit if the signal passed a global threshold set using an external bias. The analogue preamplifier has a peaking time of 200ns. A block diagram of PAC1 and a schematic of one of the 200 μm square pixels in the 32 by 16 array can be seen in Figures 3.4(a) and 3.4(b). It utilises a token passing mechanism to ask each pixel in turn if it had been "hit". It also incorporates an encoder to turn the hit pixel into a 9 bit address so that only hit pixel addresses would be output.

The early tests of PAC1 prototypes revealed fundamental problems. Many investigations carried out at RAL with Martin Lovell, (the engineer at RAL who designed the chip), failed to produce any reason for the failure of the chip. All digital inputs were shown to work and draw the expected current. An attempt to probe the power rails on the chip proved unsuccessful as the passivation removal process usually resulted in the destruction of the underlying circuits.

The problem observed with PAC1 was finally identified [26] as due to a "bug" in the software used to design the electronics: when the design was checked for connectivity of power rails, a connection through the substrate which was thought to be acceptable by the software proved not to be so. During the search for the problem a fault in the digital logic of the pixel read-out was also discovered.

These problems have been rectified and PAC2, PAC3 and PAC4 produced. Instead of a 32 by 16 array of pixels as in PAC1, the new chips provide an 8 by 8 array. An additional change was increasing the size of the bond pad in the pixels to allow ultrasonic wire bonding to the pixels. This resulted in an increase in the pixel size to 300μm square.

PAC2 and PAC3 are almost identical. They differ in that PAC3[27] has the token passing and encoding logic integrated onto the chip. PAC2 has buffered outputs[28]

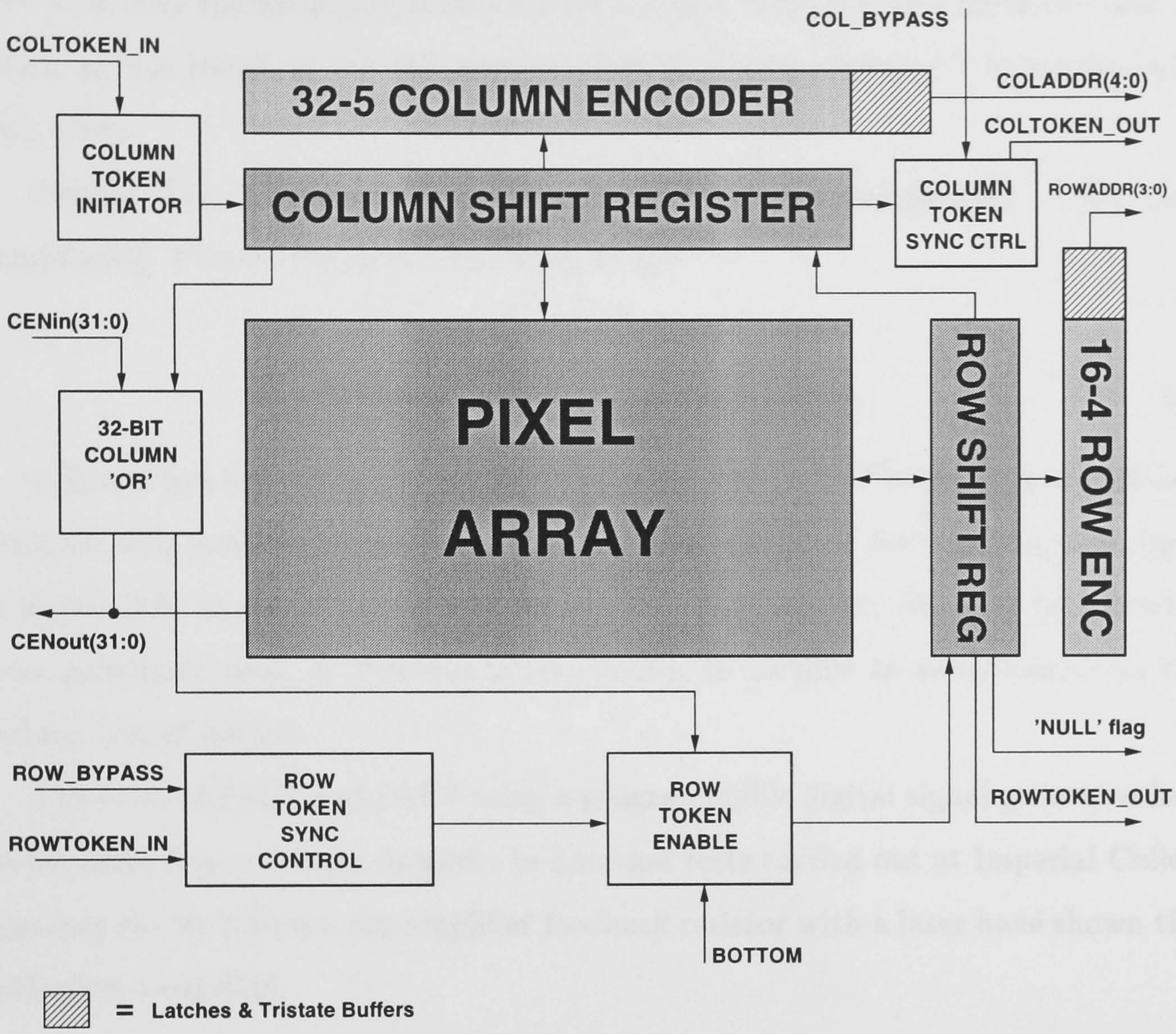

(a) Chip Block Diagram

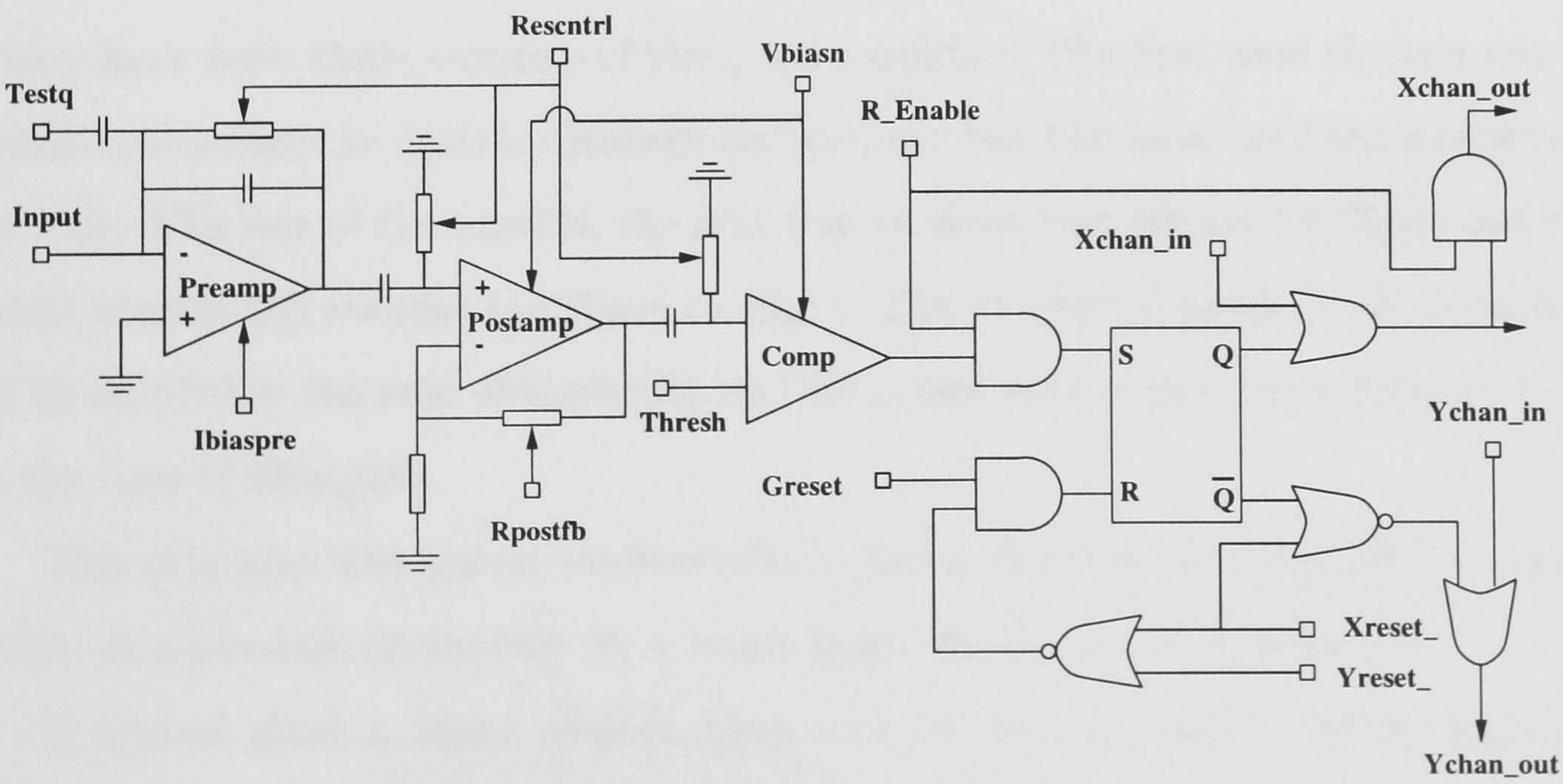

(b) Pixel Schematic

Figure 3.4: Pixel Array Chip 1

for each column and row which can be used to identify which pixel was hit and PAC3 encodes the hit position into a 6 bit address. PAC4 is very different from the others as it is based on the MX pre-amplifier. It has 64 analogue outputs, one from each pixel.

Results have already been presented on the noise performance of the pixel amplifier[9]. These have shown the noise to be;

$$\mathrm{ENC}_{\mathrm{preamp}} = 125e^- + 0.33C_{\mathrm{load}}[\mathrm{fF}]e^- \tag{3.4}$$

A board has been designed to allow the read-out of a PAC3 chip and an adjacent detector with several columns wire bonded. The schematic for this board is shown in Figure 3.5. It was required that the readout chip and the detector be placed in close proximity, and, as this was a test board, to be able to swap boards to test various sets of devices.

The tests of PAC2 and PAC3 using a programmable digital signal generator have shown their read out logic to work. In addition tests carried out at Imperial College injecting charge into the pre-amplifier feedback resistor with a laser have shown that each pixel works[29].

3.3.2 The Omega Family

There have been three versions of this pixel amplifier. The first used the last row of pixels to monitor the detector leakage current, the last two have used the guard ring for this. The size of the pixel in the first two versions was 500μm by 75μm but the latest version has reduced the 75μm to 50μm. The number of pixels in the layouts is 16 by 64 (128 in the case of Omega3), so that active area is 8mm by 4.8mm (6.4mm in the case of Omega3).

This chip also uses binary readout with a global threshold to determine if a pixel is hit. A schematic of the logic in a single pixel can be seen in Figure 3.6.

If a pixel gives a signal greater than that set by I_{dis2} and a Strobe signal is present, (after the delay), the D-type flip-flop will be set. Once a clock is applied and the strobe removed the flip-flop will be part of a 64-bit shift register spanning the column. All 16 columns are read out in parallel. The timing of the signals is illustrated in Figure 3.7.

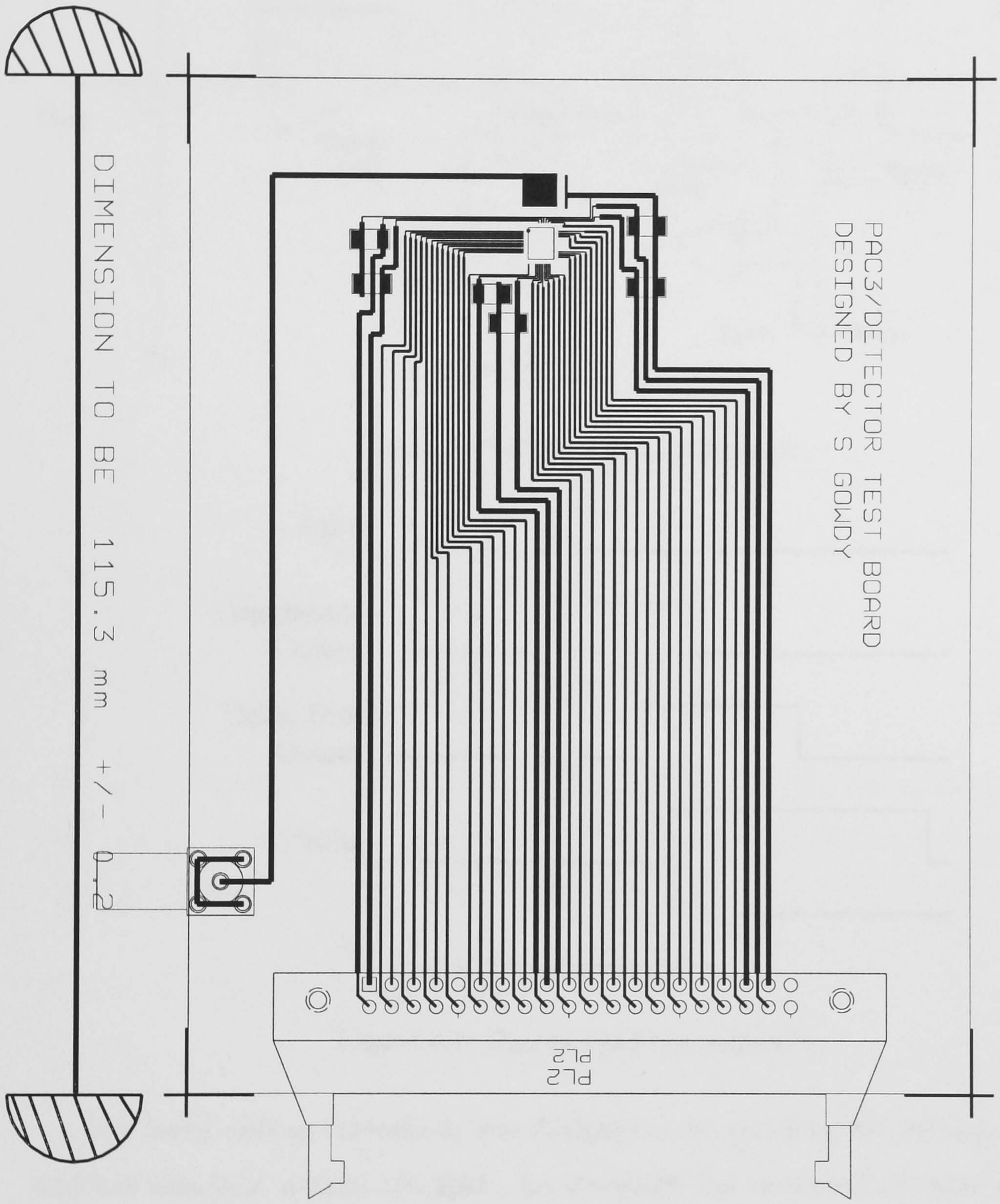

Figure 3.5: PAC3-Detector Readout Board

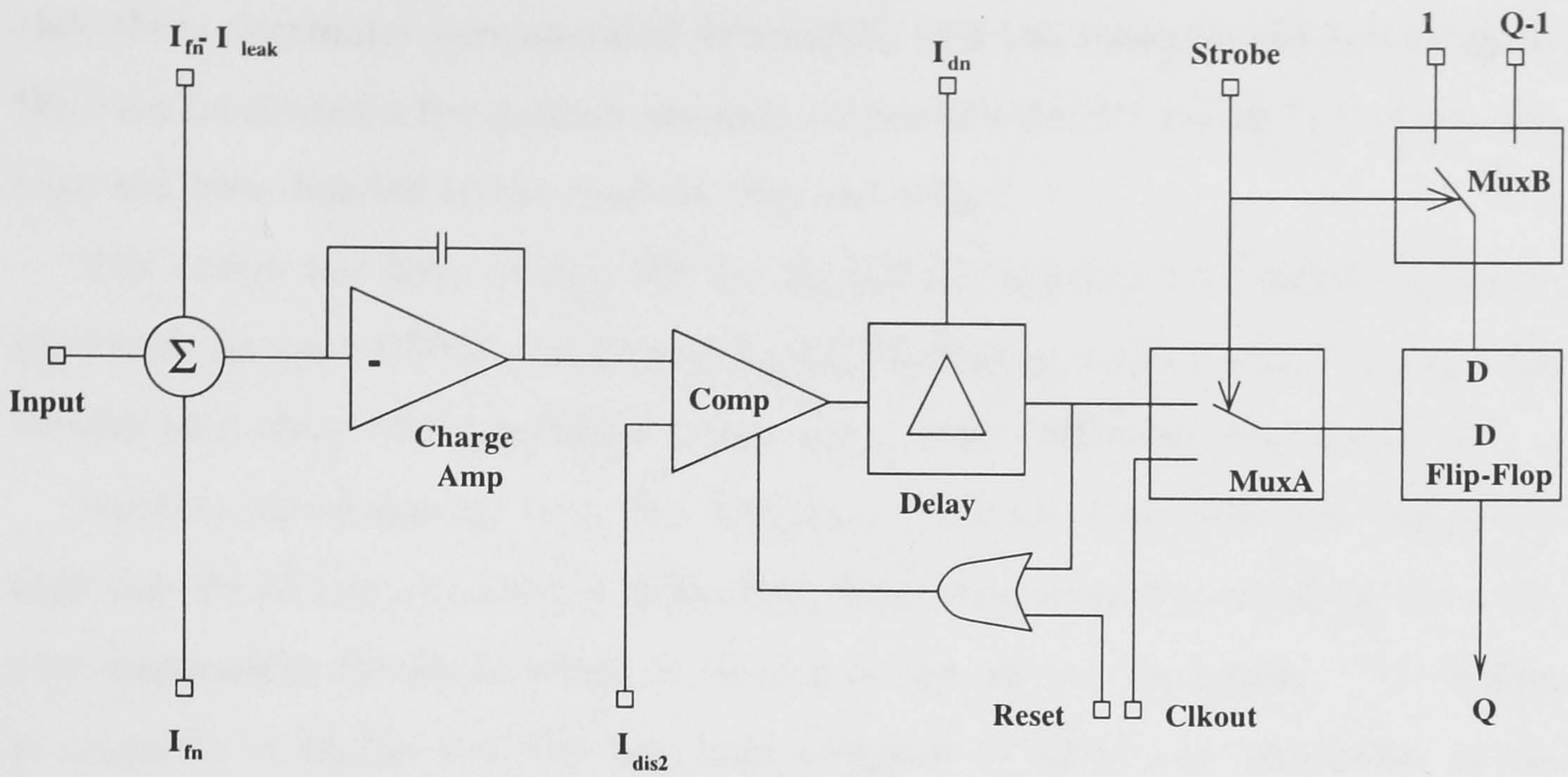

Figure 3.6: Omega pixel schematic

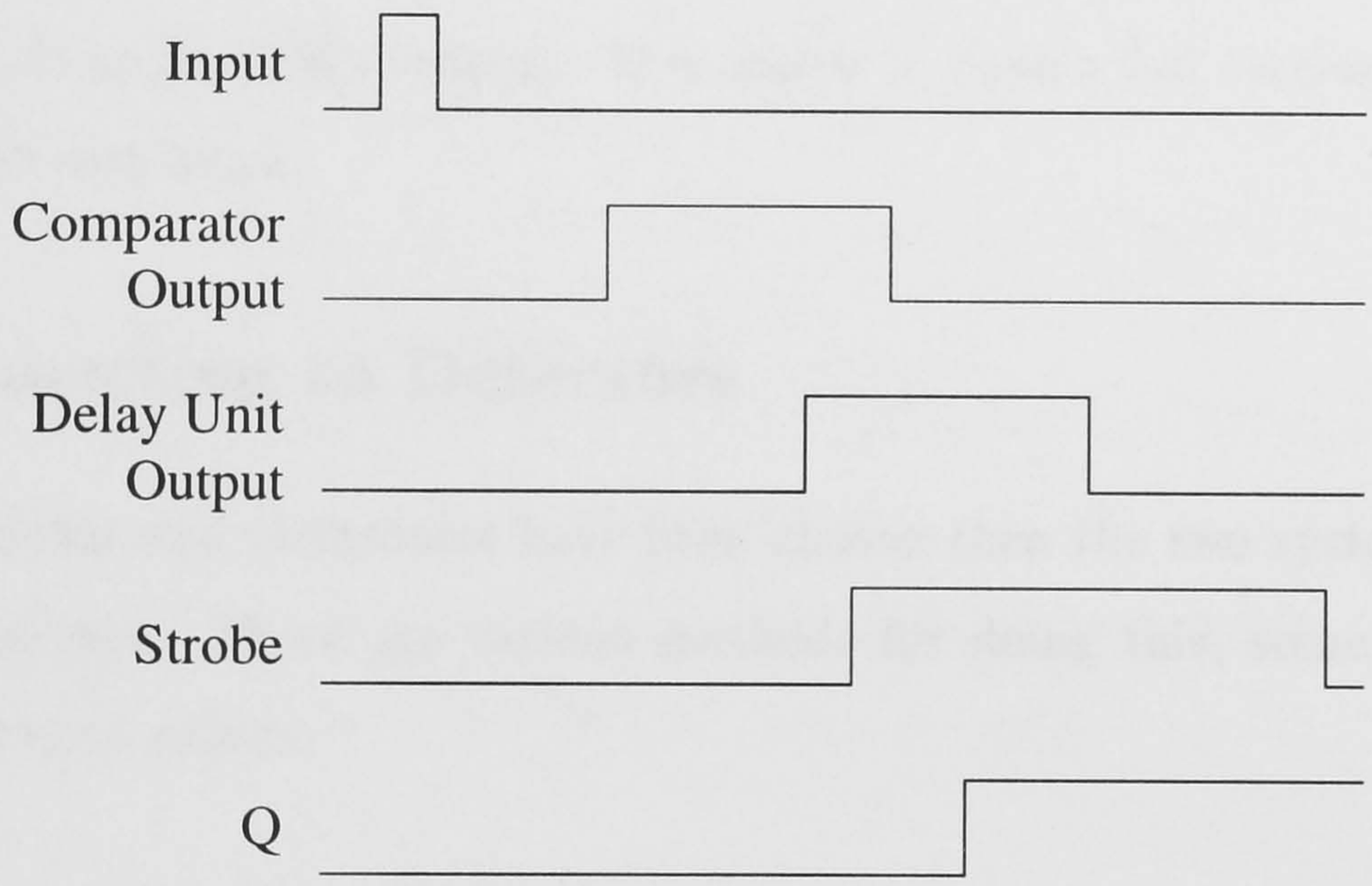

Figure 3.7: Omega read-out sequence

The latest version (Omega 3) was designed to be closer to ATLAS requirements and has also been named LHC1[30]. Its threshold can be varied between 3500 and 14000 electrons with a nominal ENC of 150 electrons. The threshold variation across the pixels has been measured to be 450 electrons (RMS) when set to 5000 electrons. The power required for each pixel pre-amplifier and discriminator is 34μW.

3.3.3 Other types

A third layout in development is based on read out electronics developed at CPPM, Marseilles for the Delphi silicon vertex detector's forward regions. In September of

1995 these electronics were operated successfully in a test beam for the first time[31]. We have fabricated a few gallium arsenide detectors with this layout but as yet they have not been bonded to the readout chip and tested.

The design has been refined for use at ATLAS and has been fabricated using the radiation hard DMILL[32] process by LETI, France. Early results[33] from this version have shown the possibility to operate it with a 2000 electron threshold.

Another development, from the Lawrence Berkeley Laboratory[34, 35] is the only chip which has an analogue capability. The measurement is based on the time-over-comparator-threshold which is related to the size of the signal. This design is currently radiation soft but has been designed to allow easy migration to the Honeywell radiation hard process.

The power required is expected to be less than 50μW per pixel and the minimum useful threshold to be 1000 electrons. It is hoped to have a full version of this chip ready for 1996 test beam.

3.4 Connecting to Detectors

Once the detector and electronics have been chosen then the two systems must be connected together. There are various methods for doing this, some more easily accomplished than others.

3.4.1 Ultrasonic Wire Bonding

This method is predominantly used to bond strip detectors to their electronics. This requires that the two semiconductor chips be placed close together and bonding is done between adjacent pads on the two chips. The bond pads on both chips are designed and arranged in an array to help automate this process.

The usual method is to bring a gold or aluminium wire into contact with the bond pad and then apply an ultrasonic signal to fuse the bond pad with the wire. This process is repeated on the appropriate pad of the other chip and the wire is then cut.

This form of bonding is carried out routinely at CERN and at the Rutherford Appleton Laboratory.

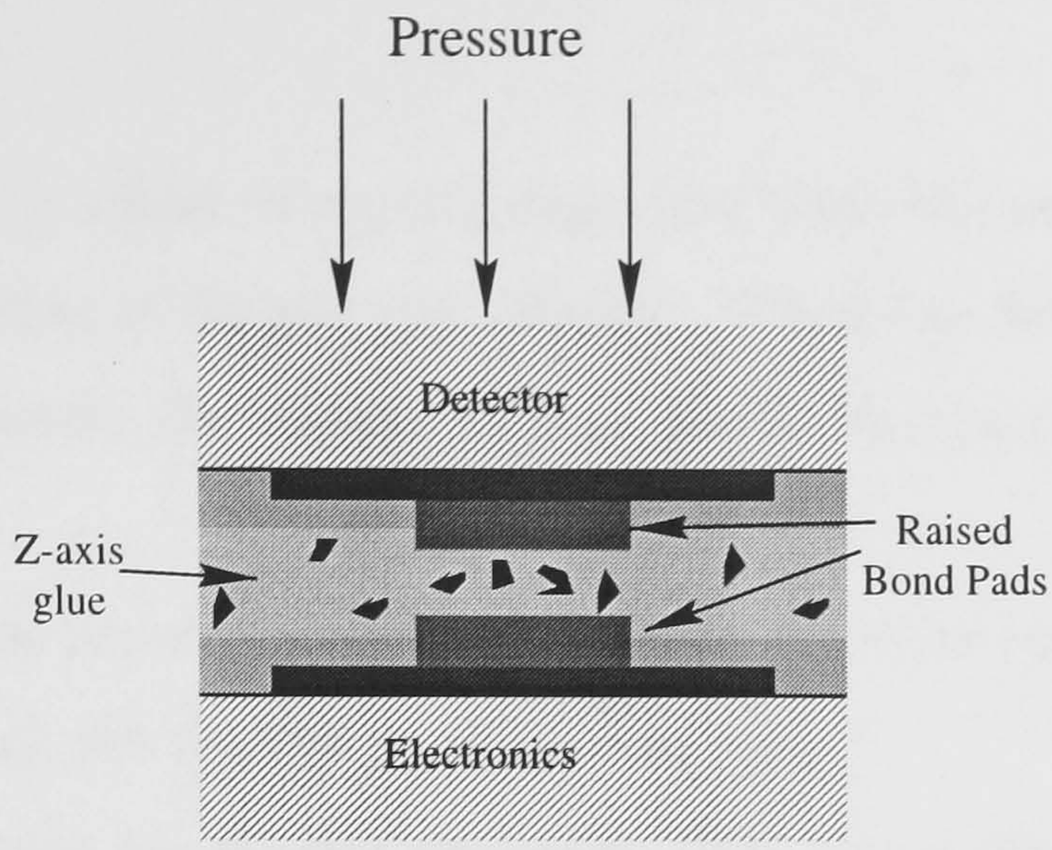

Figure 3.8: The z-axis glue principle

3.4.2 Flip Chip Bonding

In the case of pixel detectors and read-out a different method of bonding is required due to the high density of bonds required. To bond all of the pixels in the detector to the pixels on the electronics a two dimensional scheme must be used with the readout pixels on top of the detector pixel array.

All of the competing methods for doing this, however, face the same problem of alignment. When one chip is placed on top of the other it is no longer possible to see the contacts to align them before they are affixed. Depending on the materials used, one way of overcoming this is by using infrared light.

Z-Axis Glue

This method uses a "glue" which has some conduction particles in it with a size of around 5μm. The glue is sandwiched between the two devices and pressure and heat applied to cure the glue.

The basic idea is that the glue will be forced out from between the raised contacts faster than the particles and the particles will make connections between the adjacent contacts only. This process is illustrated in Figure 3.8.

Conducting Glue

A variation of the last method is to use small drops of accurately located glue. Then the devices can be aligned and placed together. This glue also needs to be cured.

Bump Bonding

This method utilises a solder bump[36] deposited onto the contacts of one of the devices. Then the other is flipped and aligned. When the devices are heated and the bump starts to melt, the surface tension of the bumps pulls the devices into better alignment.

This approach has proven very successful in early tests carried out by GMMT at Caswell for bonding the Omega pixel readout chip.

Other manufacturers use similar processes. IBM uses a simplified version which cuts down on the processing costs but is presently restricted to too coarse a pitch for the resolution required for ATLAS. However, it is foreseen that the latter will be attainable with further development[34]. This process is being used for the pixel detectors for the Delphi Vertex Detector where there are less strict requirements.

3.5 Conclusion

The low-speed Viking chips provide exceptionally low noise levels and ease of use and were chosen to be used in the test beams of 1994 (results described in Section 6.3) and 1995.

Although as yet there is no working version of the fast, radiation-hard electronics which will be required for the LHC experiments, it is hoped that these will soon be available. Currently the APV5 has been fabricated in radiation hard technology, but as indicated in Section 3.2.3 it is not operating as initially expected and a new, APV6, version is about to be produced. Other radiation-hard devices are developing and the final ATLAS choice will probably be made from;

- binary (CAFE+ADP[1]+MUX)
- digital (AROW)
- analogue (APV6, Felix-128)

This decision will be based on the choice of information required (for example detector problems are more easily identifiable with analogue or digital read-out),

[1] Provides comparator and binary pipeline

Architecture	Cost(kChF)
Binary	8,887.9
Digital	17,200.6
Analogue	16,225.2

Table 3.1: SCT Electronics Forecast Costs for ATLAS

power consumption and cost. Table 3.1 shows the current forecasts for the ATLAS SCT under the three architectures.

Another factor which will have a bearing on the decision is the short time-scale for this decision to be made. Full prototypes must be fabricated, tested and proved reliable and radiation-hard well in advance of production start-up in 1998.

There are various versions of pixel electronics which may meet LHC requirements. A major issue at the moment is to decide whether to choose an analogue or binary architecture. An additional important factor for pixel electronics will be a demonstration that the required power dissipation can be handled, given the very large number of pixels (about 1.6×10^8) in the restricted volume of the ATLAS inner tracker.

Chapter 4

X-ray Applications of GaAs Detectors

4.1 Introduction

As indicated in Chapter 1 gallium arsenide can be used to detect X-rays in the energy range 20–100keV very well. Due to the relatively large atomic numbers of gallium and arsenic, a large proportion of incident X-rays will be absorbed by a 200–300 μm thick detector.

Some of the many applications where the detection of X-rays is important are discussed in this Chapter and the merits of using gallium arsenide described.

The interaction of X-rays in gallium arsenide has also been studied by computer simulation. This also aims to aid in our understanding of the mechanisms which are responsible for the signal generated by our detectors.

4.2 X-ray Astronomy

The main reasons for the interest in gallium arsenide as an X-ray detector for Astronomy[5] are the much higher detection efficiency than silicon for energies greater than 20keV and the ability to operate at room temperature, thereby removing the requirement for cooling the detector.

Previously, space-borne X-ray telescopes could only focus an X-ray image below 10keV but it is now possible to do this up to 60keV[37]. Silicon CCD detectors which

have a very thin active region are unsuitable for use in future telescopes which will examine these higher energy sources, because of their low detection efficiency.

At present Si(Li) solid state detectors are widely used in X-ray astronomy. These detectors are suitable in similar rôles to silicon CCDs. The linearity of these detectors has been studied extensively[38].

A detector at the focal point of an X-ray telescope would have a required resolution of better than 500μm in all directions. This would be suited to a pixel detector and any of the three types of pixel read-out electronics described in Section 3.3 would perform well with a 200μm thick gallium arsenide detector.

4.3 Synchrotron Radiation

In the study of silicon detectors for synchrotron radiation the efficiency for 50μm and 300μm thick detectors, for a 17.04 keV X-ray beam, was measured to be 5.17% and 27.8% respectively[39] (c.f. Section 1.4). The time resolution was found to be very good at 0.5 ns[40].

Silicon CCDs have also been considered for this application, but in comparison with conventional techniques like photographic film they offer little gain except in speed of data acquisition[41]. In fact, the noise level is quite high in comparison. CCDs are limited in speed and sensitivity at higher energies. This is because the array reads out one row at a time. In a column each pixel must pass its charge on to the next pixel which takes typically $\approx$ 10μs[42]. A typical CCD has columns of around 1000 pixels in length. The limit to the sensitivity is due to CCDs only having a thin sensitive layer. An additional practical complication is the requirement that these detectors are operated below zero degrees Celsius.

Silicon strip detectors are also under investigation for this application. They have shown good performance for lower energy X-rays with very low noise levels[43] when cooled to below 0°C. For these lower energy X-rays, however, the metallic contacts of the detector affect the efficiency and, due to the poor electric field between the contacts, incomplete charge collection can be observed.

Another drawback with strip detectors is that their performance degrades at high fluxes[44]. However, by subdividing the strip into pixels the flux rate capability

increases dramatically as it is inversely proportional to the area of the detector element. This introduces another problem, however, namely that of read-out: the higher the number of channels, the more data that must be read out. This increases the "dead-time" of the detector. To get around this problem developments are under way to incorporate a counter in each pixel to obviate the need for read out during data capture[45].

The resolution requirements are varied, but a 200μm square pixel size would be sufficient for many applications. An asymmetric alternative is the Omega 3 electronics which provides 50μm pixel size in one direction and 500μm in the other. The 50μm would meet the requirement for resolving the detail in many currently-interesting diffraction patterns[44].

4.4 Medical & Dental Imaging

There are many applications in medical and dental fields for X-ray detectors. Many of these require X-ray energies greater than 20keV and are therefore well suited to gallium arsenide detectors[46, 47].

Two X-ray images have been taken using a pad detector fabricated in Glasgow. These are shown in Figures 4.1 and 4.2. The pad detector had a 2mm circular contact. The method to produce the image used two collimators of 1mm square on either side of the sample, to define the resolution of the images, with the source and detector on opposite sides of these collimators. Further investigations are now in progress using pixel detectors with Omega 3 read-out[48].

For dental applications the currently favoured technical solution is a silicon CCD with a scintillator placed in front of it. This system has a better detection efficiency than film and produces an "instantaneous" image. However, due to the image being produced from photons emitted from the scintillator rather than the X-ray photons themselves, the spatial resolution suffers.

Further development of the electronics to read out detectors for this application is desirable as the pixel size is required to be below 50μm to be competitive with current CCD systems. This may not be possible - due to the area per pixel required for the electronic read out - so other options are also being considered.

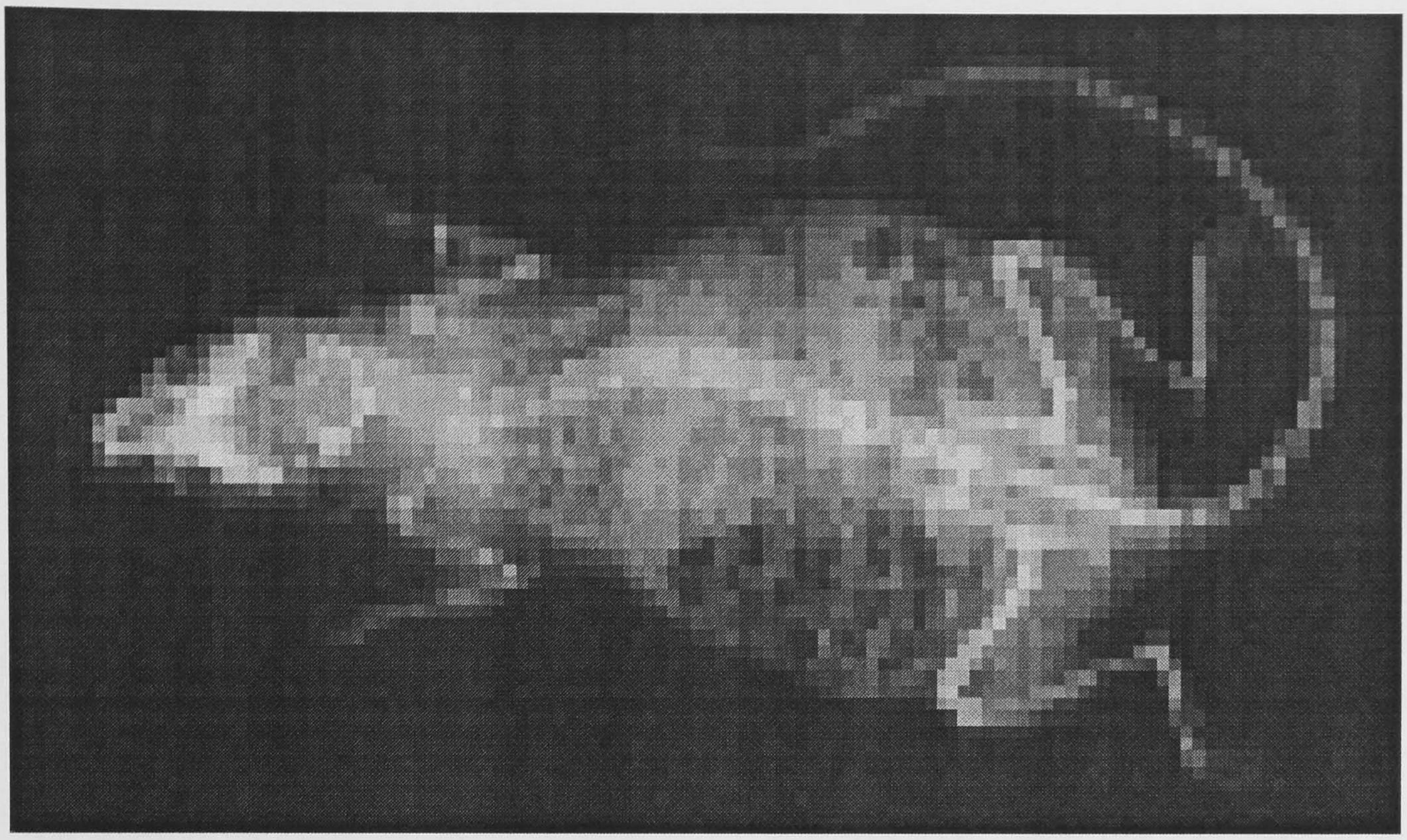

Figure 4.1: GaAs X-ray Image of Mouse

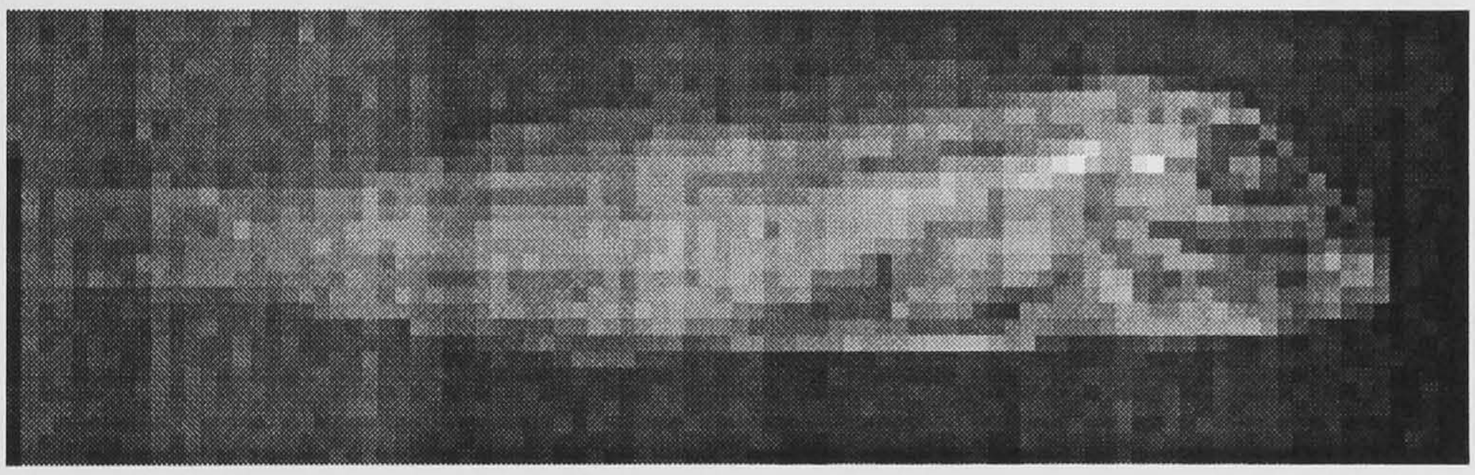

Figure 4.2: GaAs X-ray Image of Fish

As mentioned in the previous section, integrating a counter onto the pixel electronic element would aid in the data read out and minimise any dead-time in the system, thereby reducing the dose required. This would increase the area of the pixel, however, and may therefore, only be useful in applications where the resolution required is less demanding. Mammography, for example, would only require a pixel size of 200μm square.

4.5 Simulation of an X-ray Spectrum in GaAs

A better understanding of effects observed in GaAs detectors, including the reduced charge collection efficiency (see Sections 2.3 and 5.4.1 for further information), should be gained by a more comprehensive understanding of how signals are generated in

the devices.

To this end a model proposed by Toporowsky [49] (based on earlier studies by McGregor [50]) has proved successful in modelling detector response to minimum ionising particles and alpha particles.

This model has been adapted by the author and implemented in a program based on the GEANT detector simulation package to simulate the interaction of X-ray photons in gallium arsenide. This should provide complementary information with which to test the model, as the collection of the charge signal should be independent of the type of particle causing it.

4.5.1 The Model

At present the model is quite simplistic. It assumes that there are two regions in the detector, a high field (active) and low field (dead) region. The high field region can contribute to the signal in accordance with Ramo's Theorem but the low field region does not.

In addition to the division into high and low field regions, however, the electrons and holes in the active region undergo a trapping process. This is approximated by giving them a characteristic mean free path λ. It is assumed that the trapped charges are de-trapped so slowly that they do not contribute to the charge signal within the amplifier shaping time.

The simulation also includes a voltage sensitive active thickness χ_A, with the assumption that if the applied voltage across the detector is V volts:

$$\begin{aligned} \chi_A &= \alpha V \ \mu\text{m} \\ \alpha &\approx 1 \ \mu\text{m}\text{V}^{-1} \end{aligned}$$

Figure 4.3 gives a graphical representation, where the λs in this plot are defined in Equation 4.16.

4.5.2 Physics Processes in GEANT

For X-rays with energy E in the region 10keV to 100keV the two dominant interaction processes are Compton scattering (Figure 4.4) and the photoelectric

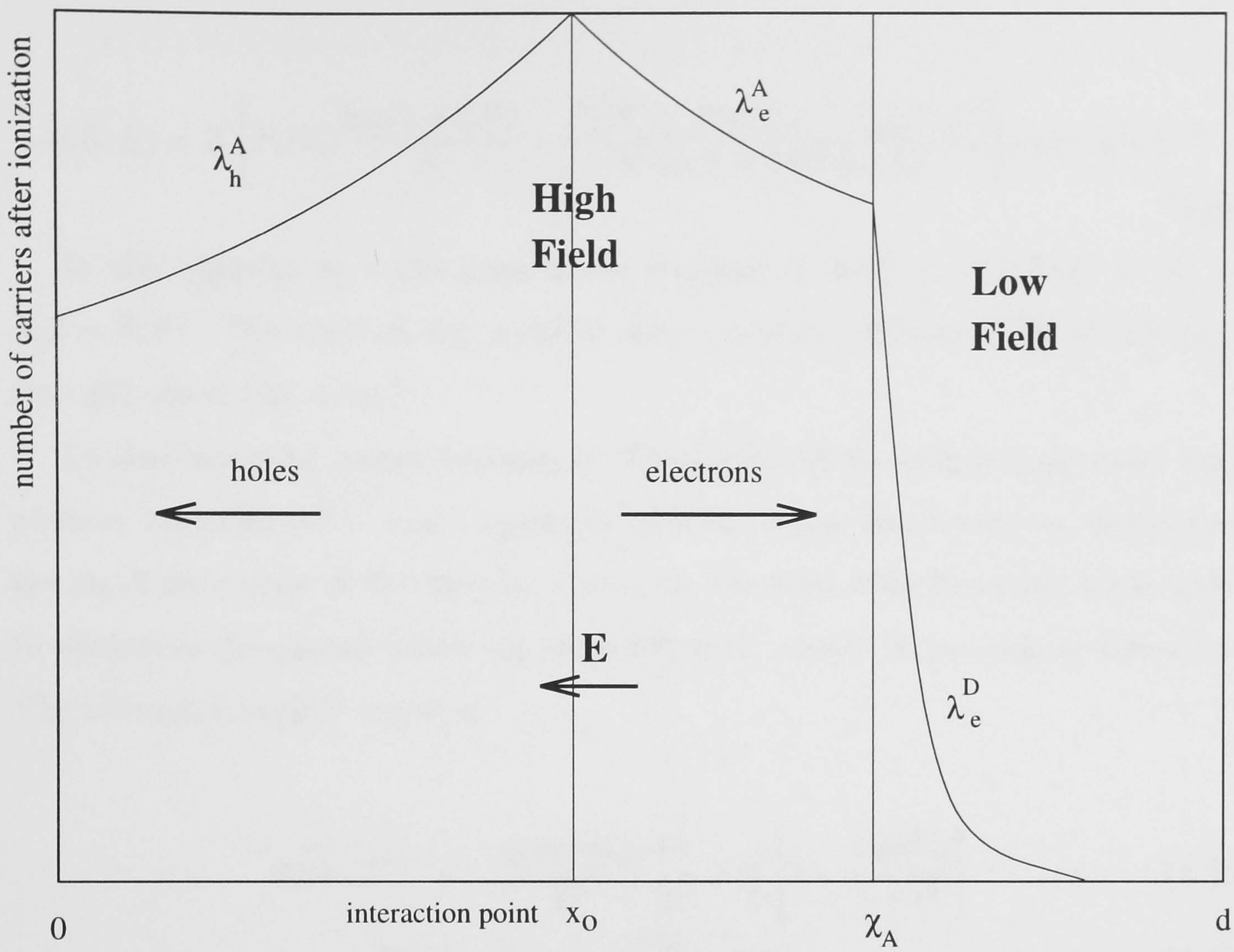

Figure 4.3: Toporowsky's model

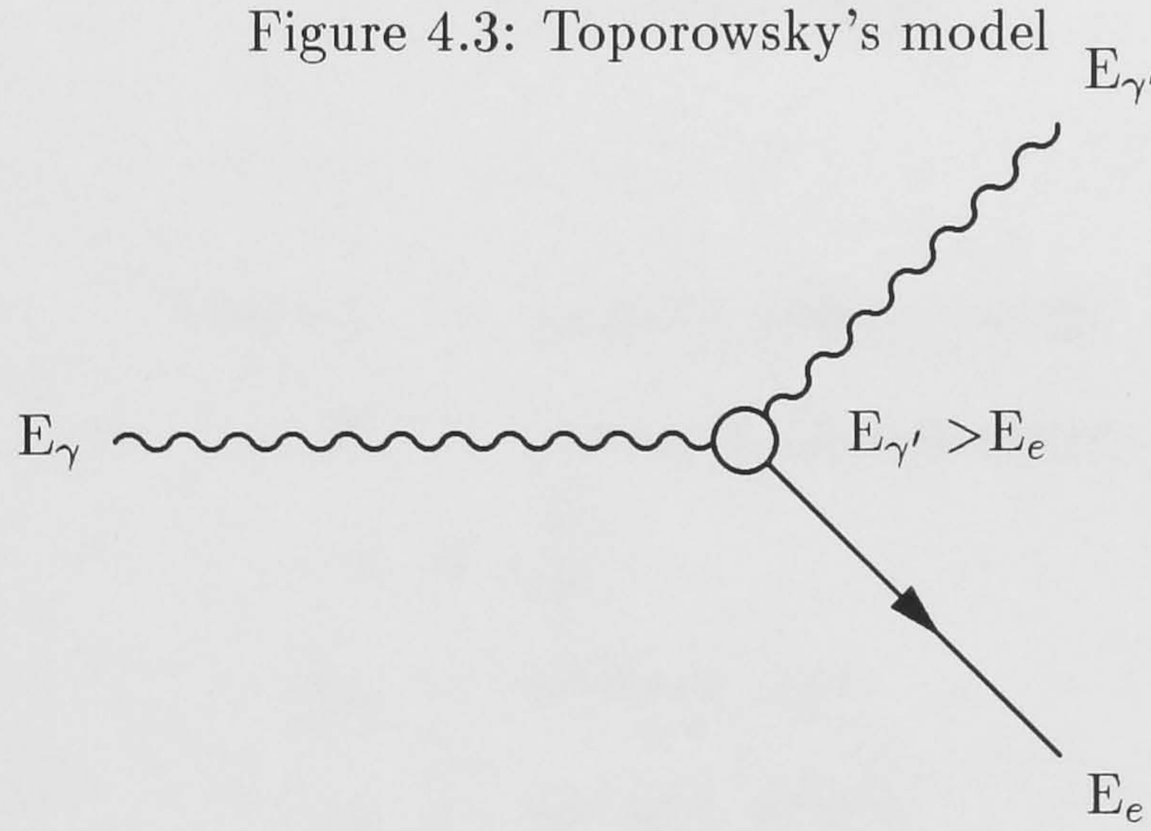

Figure 4.4: Diagram of Compton scattering event

effect.

Compton Scattering

The total cross-section used for this process is given by the empirical formula of Equation 4.1, taken from the GEANT manual[7]. The values of the coefficients were obtained from a fit over 511 experimental data points chosen in the region 10 keV $\leq E \leq$ 100 GeV and $1 \leq Z \leq 100$.

$$\sigma(Z,E) = Z\left[P_1(Z)\frac{\log(1+2X)}{X} + \frac{P_2(Z)+P_3(Z)X+P_4(Z)X^2}{1+aX+bX^2+cX^3}\right] \text{barn atom}^{-1} \tag{4.1}$$

In this equation m is the mass of the electron, X is E/m and $P_i(Z) = D_i + E_iZ + F_iZ^2$. The error on any point is approximately 10% below 20keV but less than 6% above this energy.

To determine the energy and angular distribution of the outgoing electrons and photons Equation 4.2 is used to generate a Monte-Carlo distribution to determine the resultant energy of the photon. Once this has been done Equation 4.3 is used to determine the photon scattering angle (ϑ) with respect to its original direction. The azimuthal angle is isotropic.

$$\Phi(E,E') = \frac{\chi_0 n\pi r_0^2 m_e}{E^2}\left[\frac{1}{\epsilon}+\epsilon\right]\left[1-\frac{\epsilon\sin^2\vartheta}{1+\epsilon^2}\right] \tag{4.2}$$

$$E' = E\frac{m_e}{m_e + E(1-\cos\vartheta)} \tag{4.3}$$

where E = incident photon energy

E' = scattered photon energy

$\epsilon = \frac{E'}{E}$

m_e = electron mass

n = electron density

r_0 = classical electron radius

χ_0 = radiation length

$c = 1$

The direction and energy of the electron are calculated from kinematics.

Photoelectric Effect

Again, an empirical formula, the SANDIA parametrisation [51], is used by GEANT for the photoelectric cross-section.

This is based on an expression for the mass absorption coefficient of the form;

$$\mu_{ij} = \frac{C_{1,ij}}{E_\gamma} + \frac{C_{2,ij}}{E_\gamma^2} + \frac{C_{3,ij}}{E_\gamma^3} + \frac{C_{4,ij}}{E_\gamma^4}\ cm^2 g^{-1} \tag{4.4}$$

In fitting measured mass absorption coefficients to this equation, the fits were performed in different energy ranges, denoted by the index j, for each element i.

For a mixture (as in gallium arsenide) the cross-sections are weighted by the mass fractions of the components, (f_k), as shown in Equations 4.5 and 4.6.

$$\mu_j = \sum_{k=1}^{N} f_k \mu_{j,k} \tag{4.5}$$

$$C_{i,total} = \sum_{k=1}^{N} f_k C_{i,jk} \tag{4.6}$$

Finally the macroscopic cross-section is calculated using equation 4.7.

$$\Sigma = \rho\mu\ cm^{-1} \tag{4.7}$$

In this equation ρ is the material density and μ is an appropriate mass absorption coefficient.

The energy of the photoelectron that is ejected from the atom is given by;

$$E_{photoelectron} = E_\gamma - E_{shell} + m_e \tag{4.8}$$

To determine which atomic sub-shell the electron occupied before the photoelectric interaction and the subsequent photoelectron angular distribution, the formulae of von Sauter [52, 53] and Gavrila [54, 55] are used. These are quoted in the GEANT manual [7]. The azimuthal angle is again isotropic. As the atom is now left in an excited state it must either emit a characteristic Auger electron or X-ray photon, with energies;

$$E_e = E_i - (E_j + E_k) \tag{4.9}$$

$$E_X = E_i - E_j \tag{4.10}$$

In these equations $E_{i|j|k}$ are sub-shell binding energies, with $E_i > E_j > E_k$.

To maintain conservation of energy, an additional photon is emitted with energy E_k for the Auger process and E_j for the fluorescence process. The choice between these processes is based on the compilation by Krause [56]. The angular distribution of the particles in each case is isotropic.

4.5.3 Simulation Input

The simulation program ran in one of two modes. One used GEANT to do all the tracking and generation (creation of the GEANT particles which will then be tracked) with the photon generated at the surface of the detector. In the other mode, which was used to allow easier probing of the features found in the output, it is assumed that the incident photon interacts with the detector exclusively through either the photoelectric or Compton scattering (see Figure 4.4) processes.

The cross-sections for both these processes are extracted from the GEANT 3.15 [7] detector simulation package using the method described in Section 4.5.2.

The secondary particles from these processes were then used as input into GEANT. They were generated at the appropriate depth into the material via a Monte-Carlo selection which used the cross-section data.

A further Monte-Carlo process was then used to derive the angular distribution of the secondary particles.

The differential cross-section for Compton scattering into the solid angle $d\Omega$ at an angle ϑ is given by[57];

$$d({}_e\sigma_s) = r_0^2 d\Omega \left[\frac{1}{1+\alpha(1-\cos\vartheta)}\right]^3 \left(\frac{1+\cos^2\vartheta}{2}\right) \left\{1 + \frac{\alpha^2(1-\cos\vartheta)^2}{(1+\cos^2\vartheta)[1+\alpha(1-\cos\vartheta)]}\right\} \tag{4.11}$$

where $\alpha = \dfrac{h\nu_0}{m_0c^2}$

Once this angle has been determined the new energy can be determined from;

$$h\nu' = \frac{m_0c^2}{1-\cos\vartheta + \left(\frac{1}{\alpha}\right)} \tag{4.12}$$

The new energy and direction of the Compton photon allows the evaluation of the energy (T) and direction (φ) of the electron with respect to the incident photon. This is shown in Equations 4.13 and 4.14.

$$T = h\nu_0 - h\nu' \tag{4.13}$$

$$\cot\varphi = (1+\alpha)\tan\frac{\vartheta}{2} \tag{4.14}$$

For the photoelectric effect the distribution of the electron relative to the direction of the incident photon was simulated using the distribution;

$$F(\vartheta) = \exp\left(-\frac{\left(\vartheta - \frac{\pi}{3}\frac{1}{a\alpha}\right)^2}{2\sigma^2}\right) \tag{4.15}$$

In the program a was chosen to be 20 and σ to be $\frac{\pi}{9}$ to approximate experimental measurements[57]. This distribution is shown in Figure 4.5 for a 60keV and 14keV photon.

The energy of the photoelectron is merely the energy of the incident photon reduced by the original binding energy of the electron.

After this electron has been emitted the atom is left in an excited state. One of two possible processes will then occur, in which a characteristic Auger electron or an X-ray can be emitted. The X-ray option was the only process used in this part of the simulation for simplicity.

This X-ray was given the equivalent of the binding energy of the photoelectron and a random direction.

4.5.4 Generation Of Signal

The actual generation of the signal is handled mainly by GEANT; in addition the program generated a Gaussian noise contribution for each event using a CERNLIB routine, RANNOR[58], which is added to the energy during analysis if required.

Once appropriate particles have been generated, GEANT tracks these and computes the energy deposited in each step of the particle trajectory. To determine the signal resulting from drift of the e-h pairs released by ionising particles, a weight

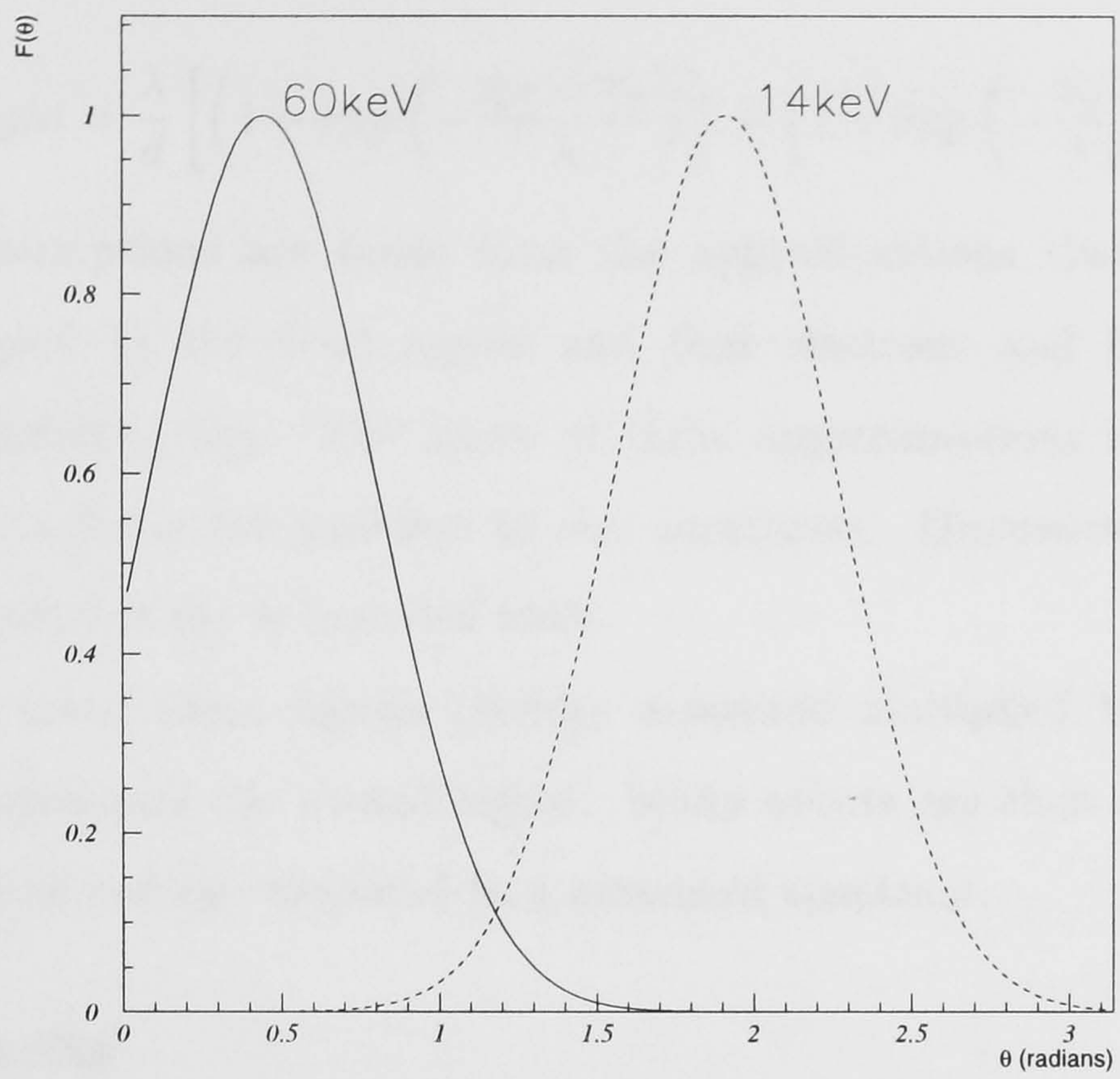

Figure 4.5: Assumed angular distribution of photoelectrons for a 60keV and 14keV incident photon

is placed on any charge signal generated via Ramo's Theorem [13] (see Section 2.3) using Equation 2.85;

$$\varepsilon\left(x_o, \chi_A, \lambda, d\right) = \frac{1}{d}\left[\int_0^{x_o} \exp\left(-\frac{x_o - x}{\lambda_h^A}\right) dx + \int_{x_o}^{\chi_A} \exp\left(-\frac{x - x_o}{\lambda_e^A}\right) dx + \exp\left(-\frac{\chi_A - x_o}{\lambda_e^A}\right) \int_{\chi_A}^{d} \exp\left(-\frac{x - \chi_A}{\lambda_e^D}\right) dx\right] \tag{4.16}$$

$\lambda_{h,e}$	-	characteristic free path
		- λ^A in "active" zone
		- λ^D in "dead" zone
d	-	detector thickness
χ_A	-	active thickness
x_o	-	depth of particle interaction point at which e-h pairs are created

A simplified version of this equation, assuming $\lambda_e^D \simeq 0$ and $\lambda_h^A \simeq \lambda_e^A = \lambda$, is

used in the simulation and the weight is then given by;

$$weight = \frac{\lambda}{d}\left[\left(1 - \exp\left(-\frac{\chi_A - x_o}{\lambda}\right)\right) + \left(1 - \exp\left(-\frac{x_o}{\lambda}\right)\right)\right] \tag{4.17}$$

These assumptions are made from the approximations that free carriers are quickly stopped in the dead region and that electrons and holes have similar transport characteristics. The latter of these approximations is clearly not very accurate but reduces the problem to one parameter. Discussion of varying these parameters individually is included later.

For each event these signals (energy deposited multiplied by the weight) are summed to produced the overall signal. Many events are then used to produce a spectrum which can be compared to a measured spectrum.

4.5.5 Results

The simulation program has been run for a 200μm thick detector measuring one centimetre square. The value used in the simulation for λ was 200μm, as determined from fitting to experimental data for α's and m.i.p.'s by Toporowsky[49].

The photon energies chosen for the simulation were 34keV and 60keV. The results presented show the active thickness varying from 25μm to 200μm in steps of 25μm.

For each energy three sets of spectra are shown;

- no noise
- 500e$^-$ ENC (equivalent noise charge)
- 1000e$^-$ ENC

The 34keV(60keV) results are shown in Figures 4.6, 4.7 and 4.8 (Figures 4.9, 4.10 and 4.11). In these plots the horizontal axis is energy in keV and the vertical axis is the number of counts.

In the spectra without noise it is possible to understand where the features of the spectra originate. There are four distinct features. There is a wide band just above zero pulse height with very few entries mainly due to Compton events. The peak

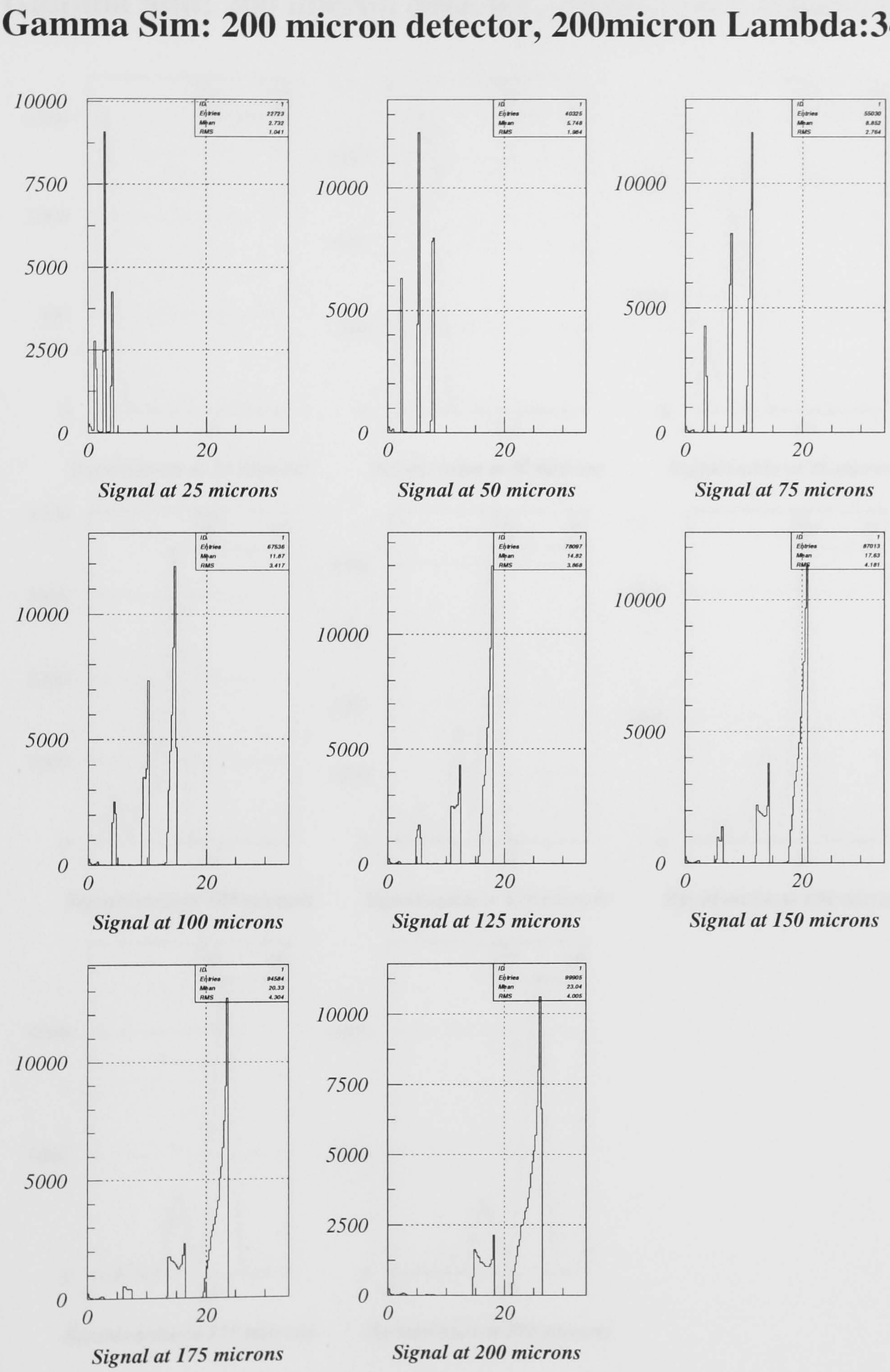

Figure 4.6: Simulated signal, measured in keV, with 34keV photons and no noise

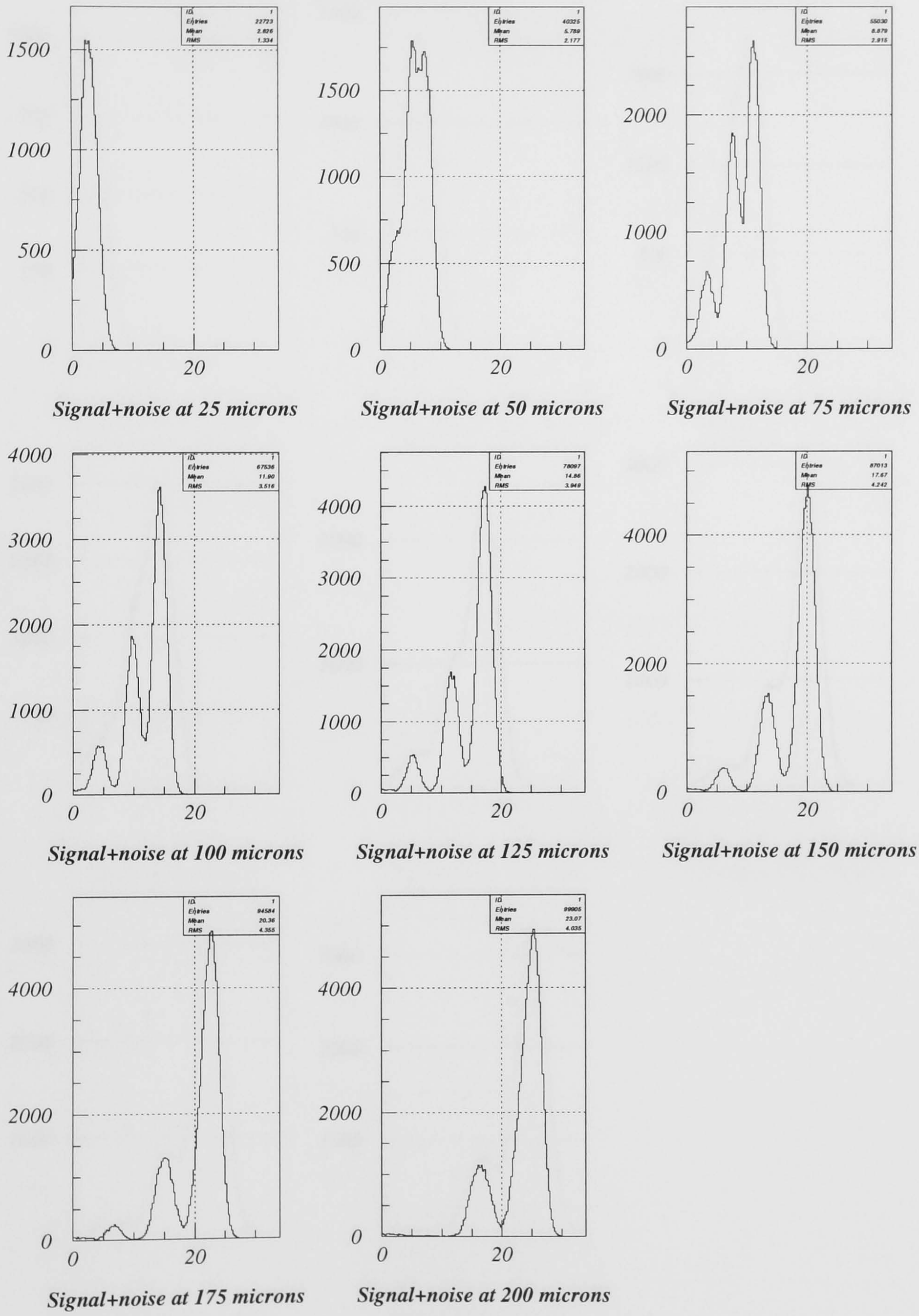

Figure 4.7: Simulated signal, measured in keV, with 34keV photons and 500 electrons ENC noise

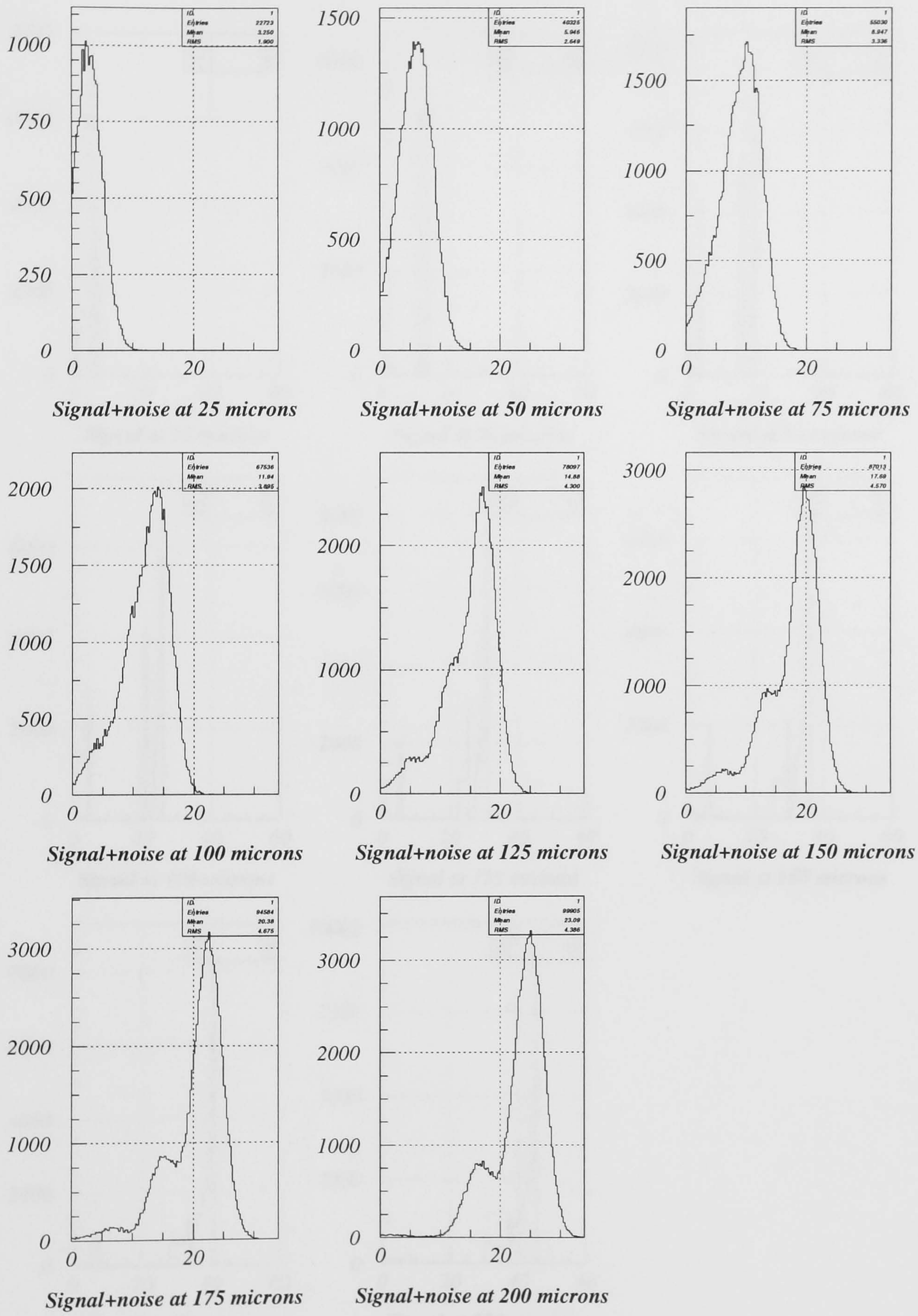

Figure 4.8: Simulated signal, measured in keV, with 34keV photons and 1000 electrons ENC noise

Gamma Sim: 200 micron detector, 200micron Lambda:60keV

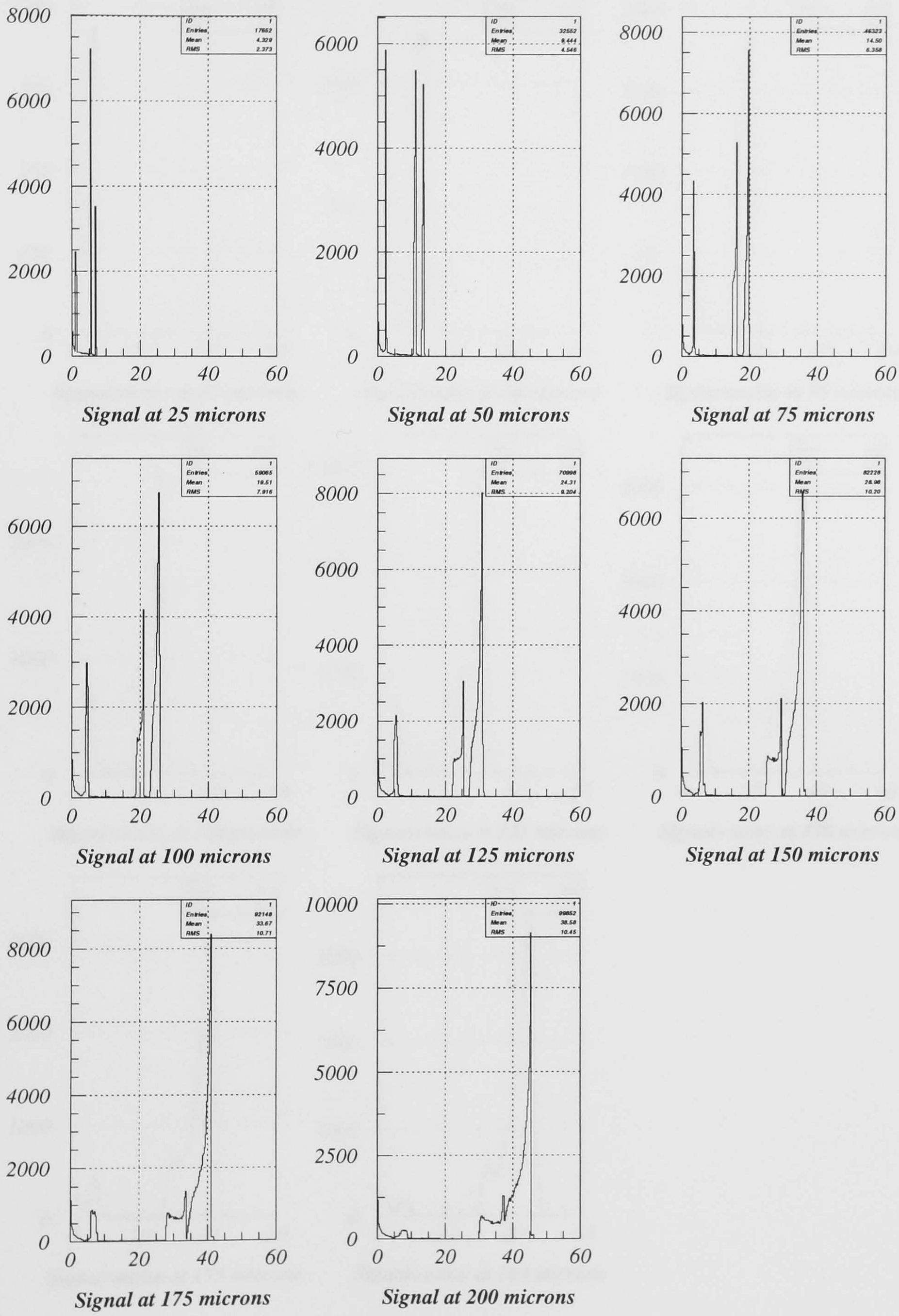

Figure 4.9: Simulated signal, measured in keV, with 60keV photons and no noise

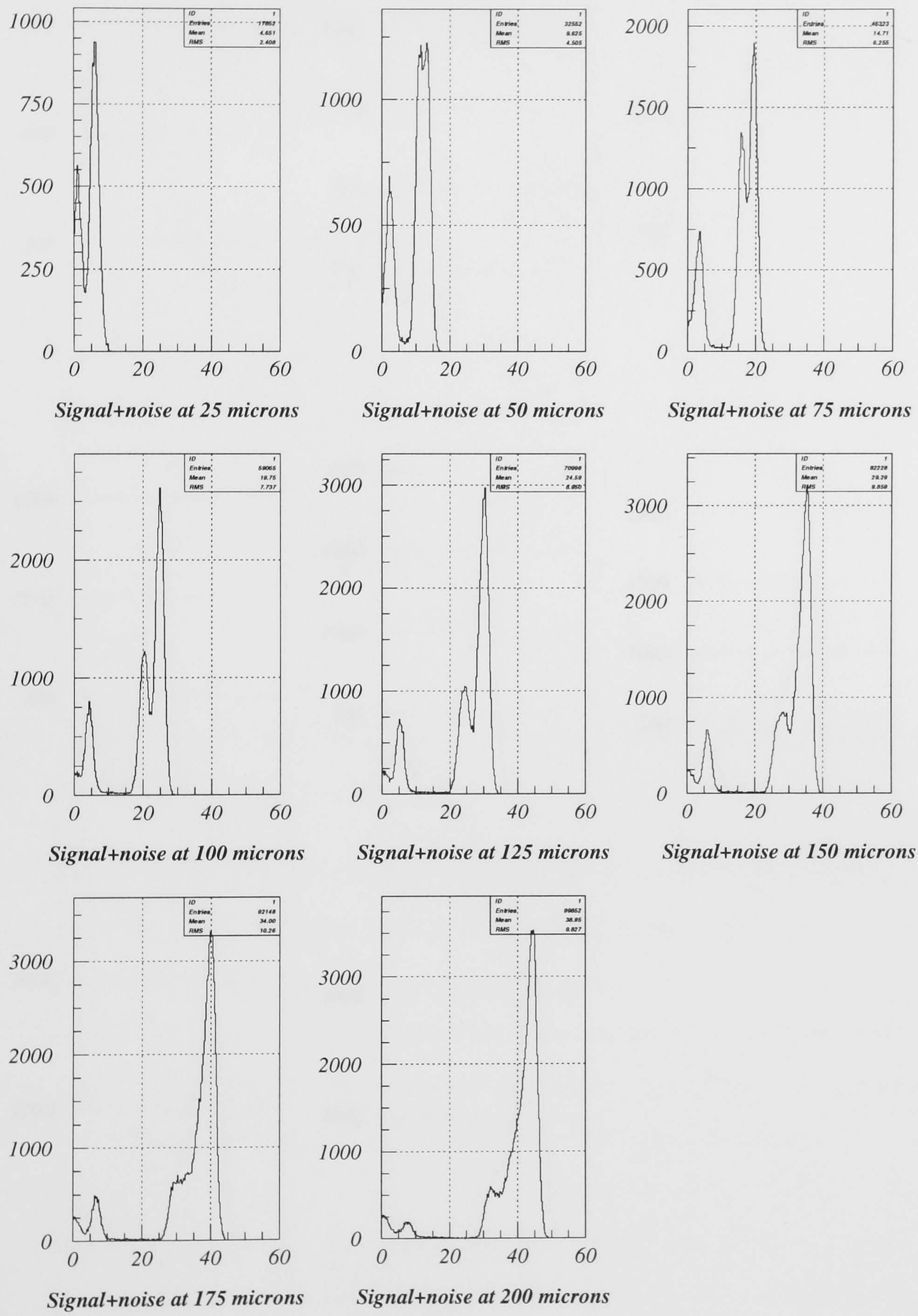

Figure 4.10: Simulated signal, measured in keV, with 60keV photons and 500 electrons ENC noise

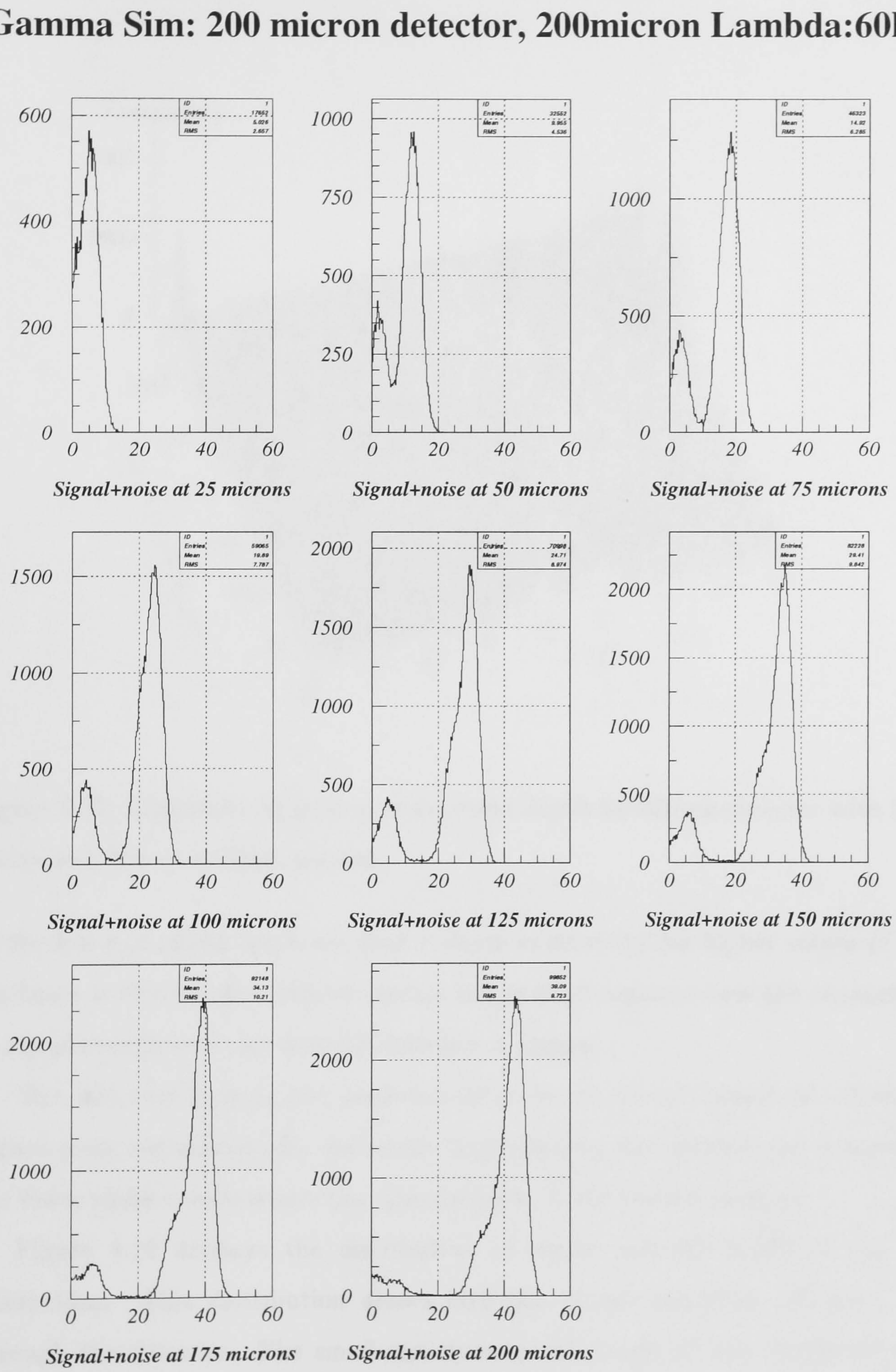

Figure 4.11: Simulated signal, measured in keV, with 60keV photons and 1000 electrons ENC noise

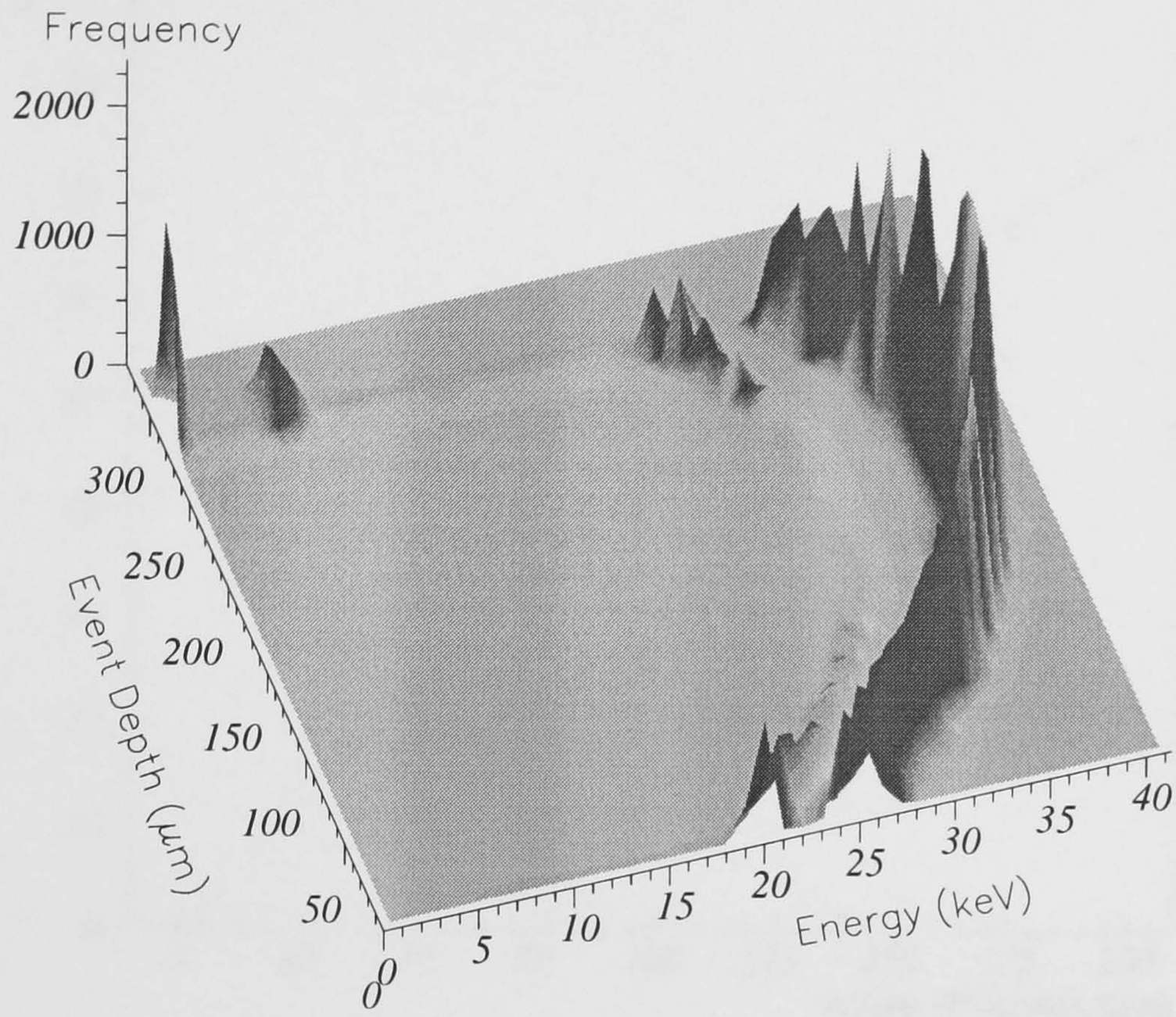

Figure 4.12: Simulated signal size verses event depth for 300μm detector with 280μm active and 60keV incident photon

at the low end of the spectrum that reduces in intensity for higher values of active thickness is due to photoelectric events in the dead region where the characteristic X-ray photon is emitted back into the active region.

The last two features are predominantly due to the photoelectric effect. The higher peak contains events for which both electron and photon are detected and the lower those events where the characteristic X-ray photon escapes.

Figure 4.12 displays the distribution of signal and the depth of the initial interaction. This distribution shows how the charge collection efficiency varies through the detector. The small structure in the height of the distribution is an effect of GEANT.

A graph of charge collection efficiency against active thickness can be seen in Figure 4.13, and a graph of the fraction of interactions against thickness in Figure 4.14. It should be noted that the fraction of interactions is proportional to the

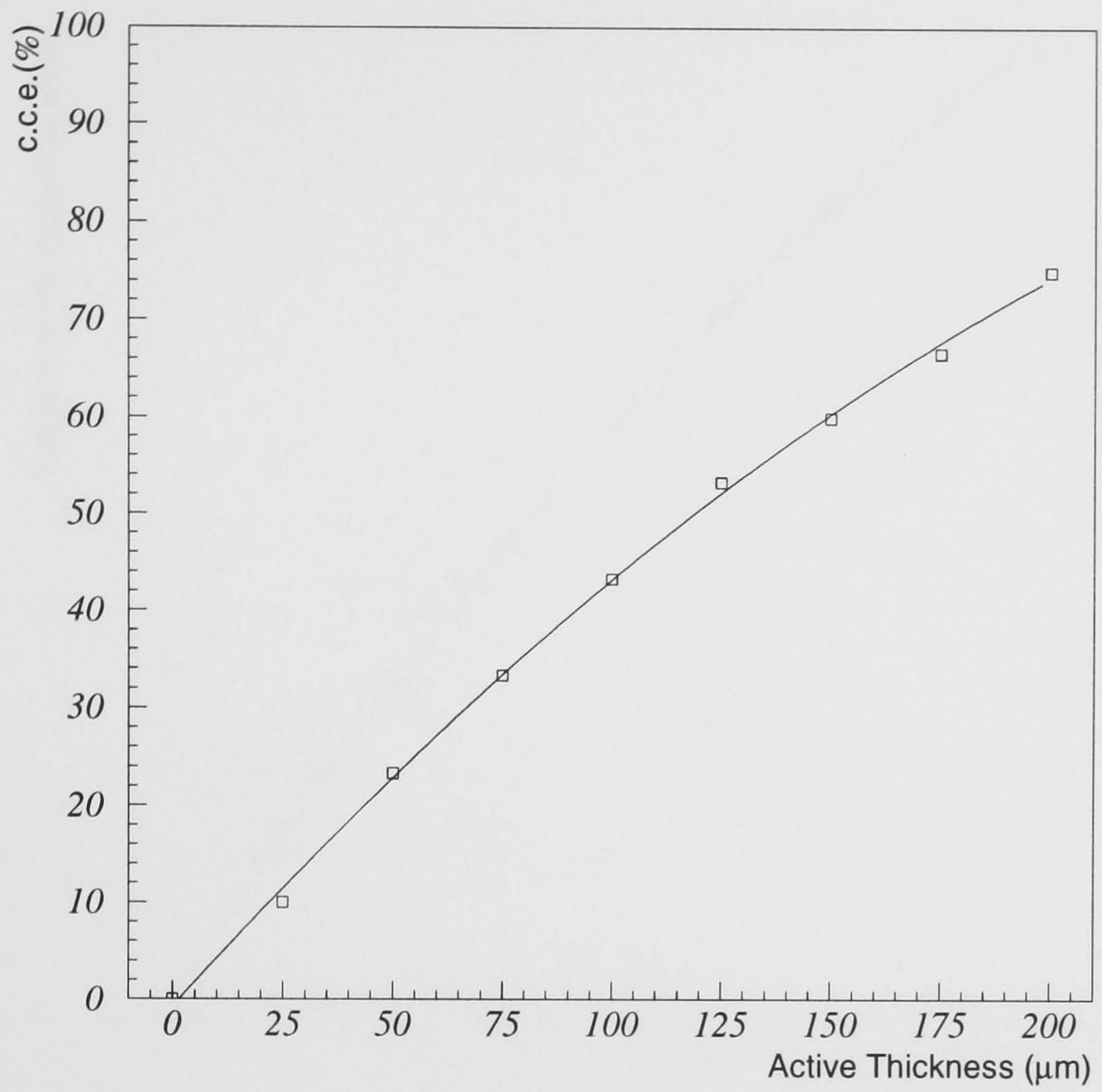

Figure 4.13: CCE(%) against active thickness for 60keV photons

counting rate expected in an experiment. Both these graphs are for the 60keV simulation. This shows that at full depletion (the whole device is active) 100% charge collection efficiency isn't reached, however, full detection efficiency is reached.

The program was further refined to have independent values for λ_h^A, λ_e^A and λ_h^D. A fuller form of Equation 4.17 was derived from Equation 4.16 for this purpose.

The simulation was then run for a 300 μm detector with 280 μm active. The values of the three λs were varied about the values λ_e^A=140 μm, λ_h^A=220 μm and λ_h^D=1 μm. These values are found to be most suitable for m.i.p. detection simulation[59]. The resulting spectra are shown in Figure 4.15.

As expected as the value of any of the λs increase the measured signal increases. In addition the shape of the spectrum changes.

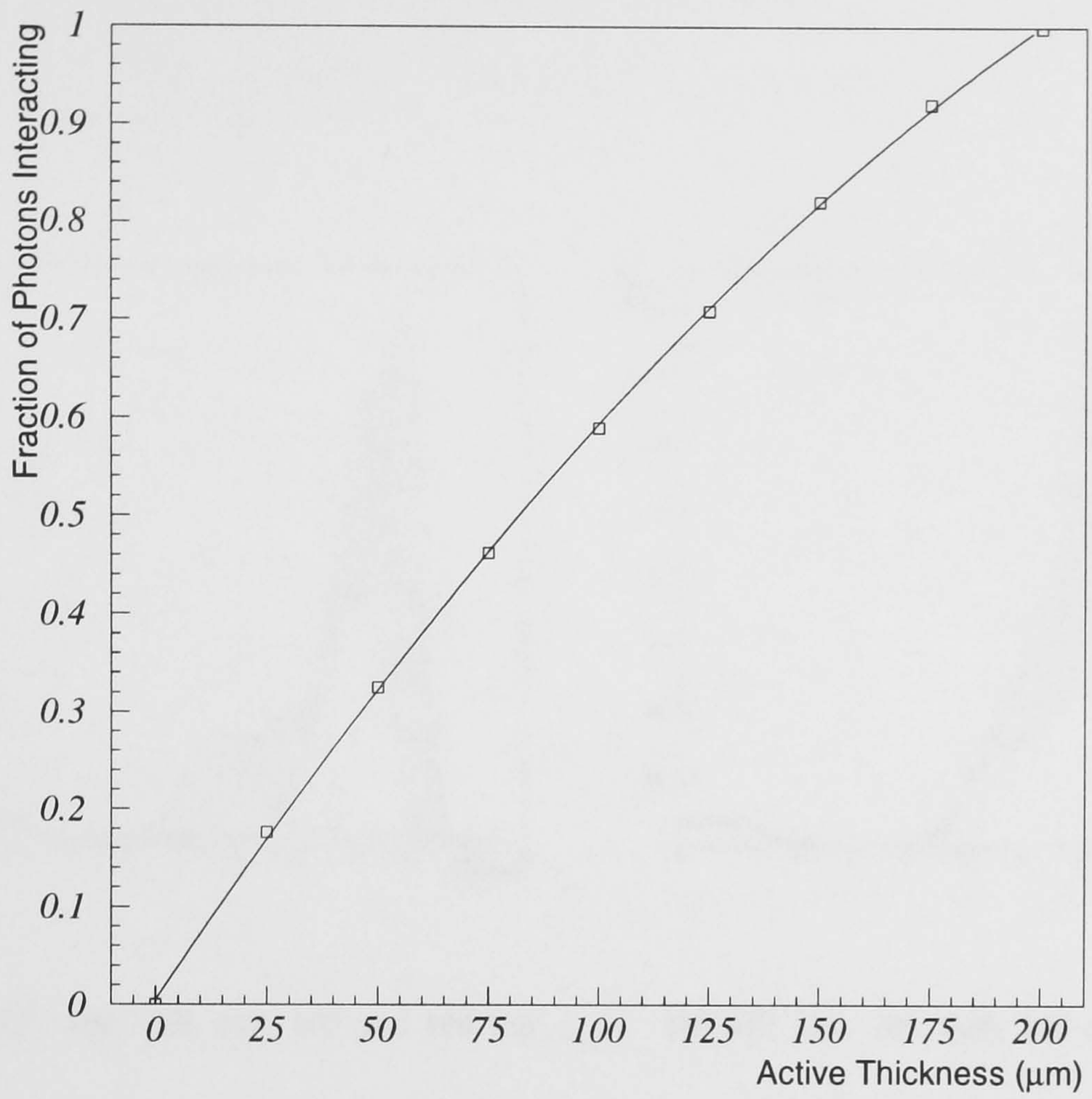

Figure 4.14: Fraction of photon interactions against active thickness for 60keV photons

4.5.6 Actual Spectrum

Figure 4.16 shows a low noise ^{241}Am spectrum [5] supplied by Andrew Holland from Leicester University, using a 300 μm thick Glasgow detector biased at 300 volts at -10°C. The measured spectrum displays the main features found in the simulation. (However, there is no "pedestal" generated in the simulation, so this is one source of difference between the experimental and simulated spectra. In addition, the ^{241}Am source emits Np L X-rays in the energy range 10–20 keV as well as 60 keV gammas.)

A simulated spectrum is shown in Figure 4.17 for a 300μm detector with 280μm active depth.

There is good agreement in the shape and features of spectra (cf Figure 4.16 and 4.17). Also, the original version of the simulation program, which treated a mono-energetic photon incident on the detector, has now been changed to allow

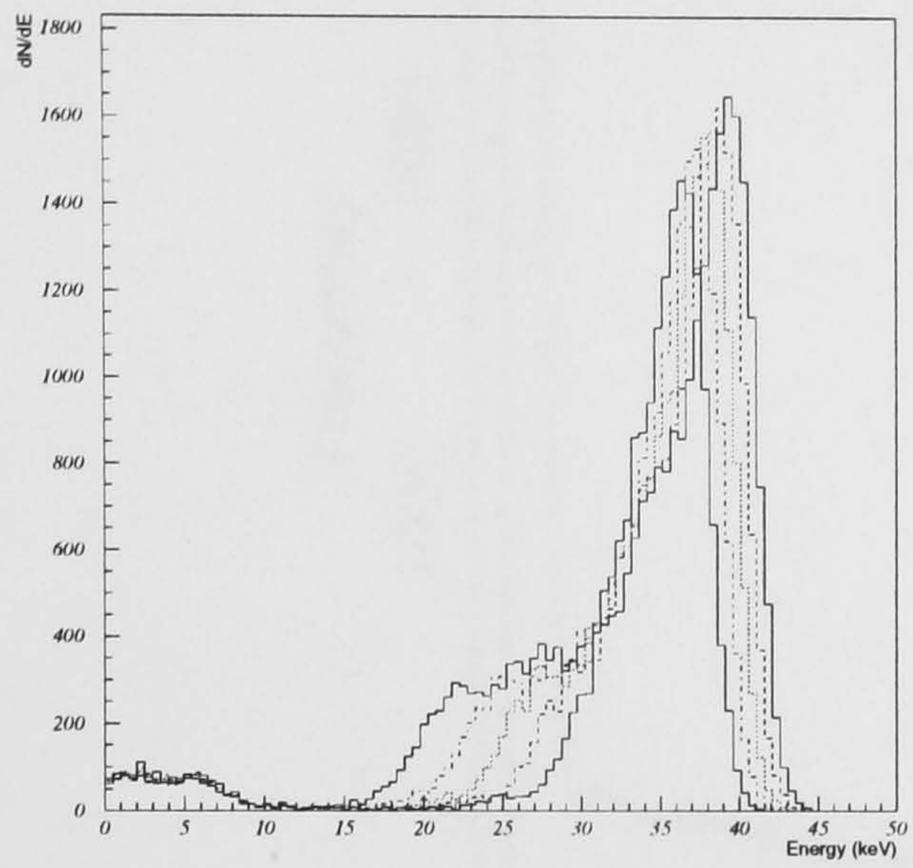

(a) λ_e^A: 100, 120, 140, 160 and 180 μm

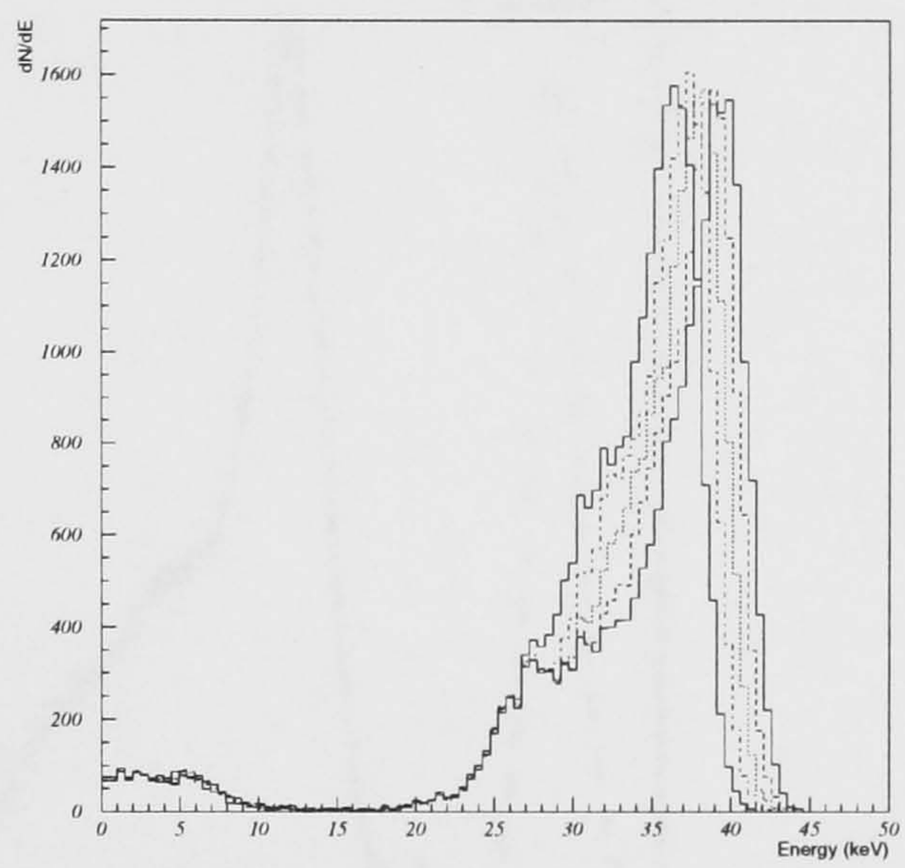

(b) λ_h^A: 180, 200, 220, 240 and 260 μm

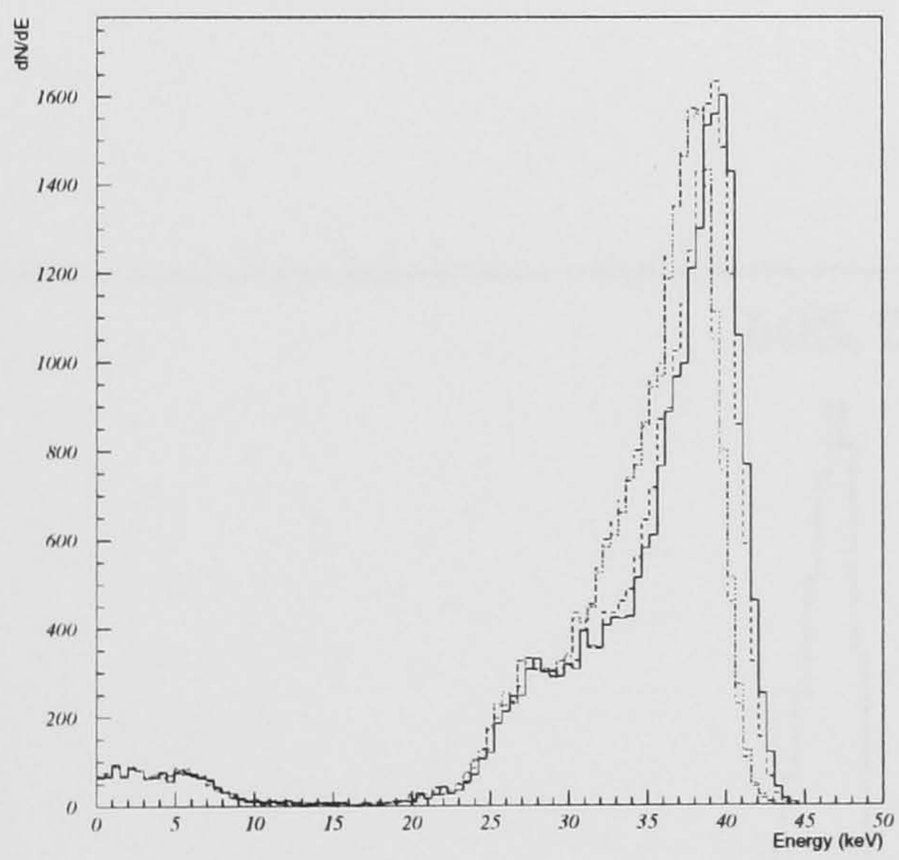

(c) λ_h^D: 0, 1, 20 and 40 μm

Figure 4.15: Variation in simulated signal from a 300μm detector. Increasing λ increases position of peak on all plots.

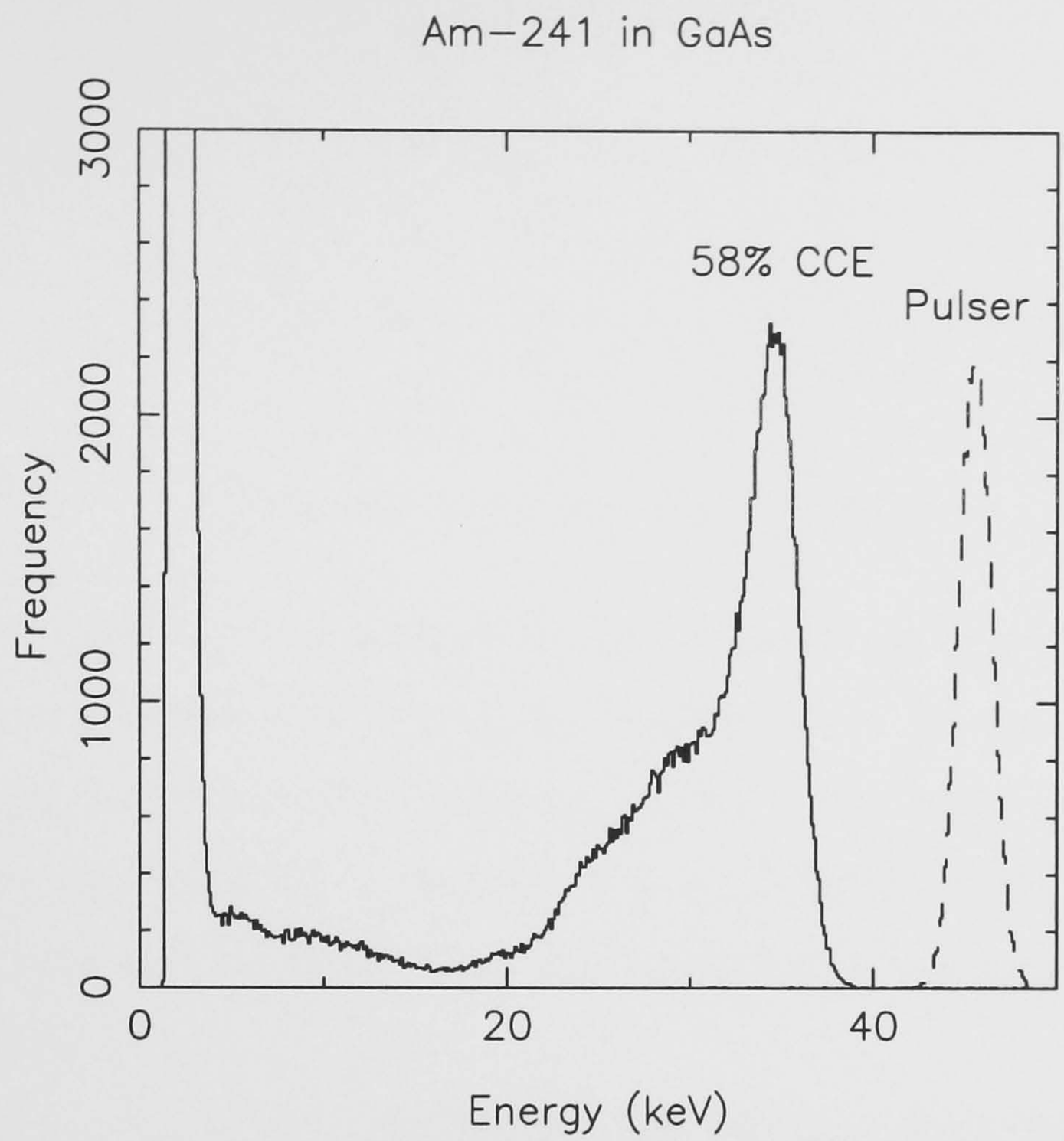

Figure 4.16: 60keV ^{241}Am Spectrum from 300 μm GaAs detector biased at 300V

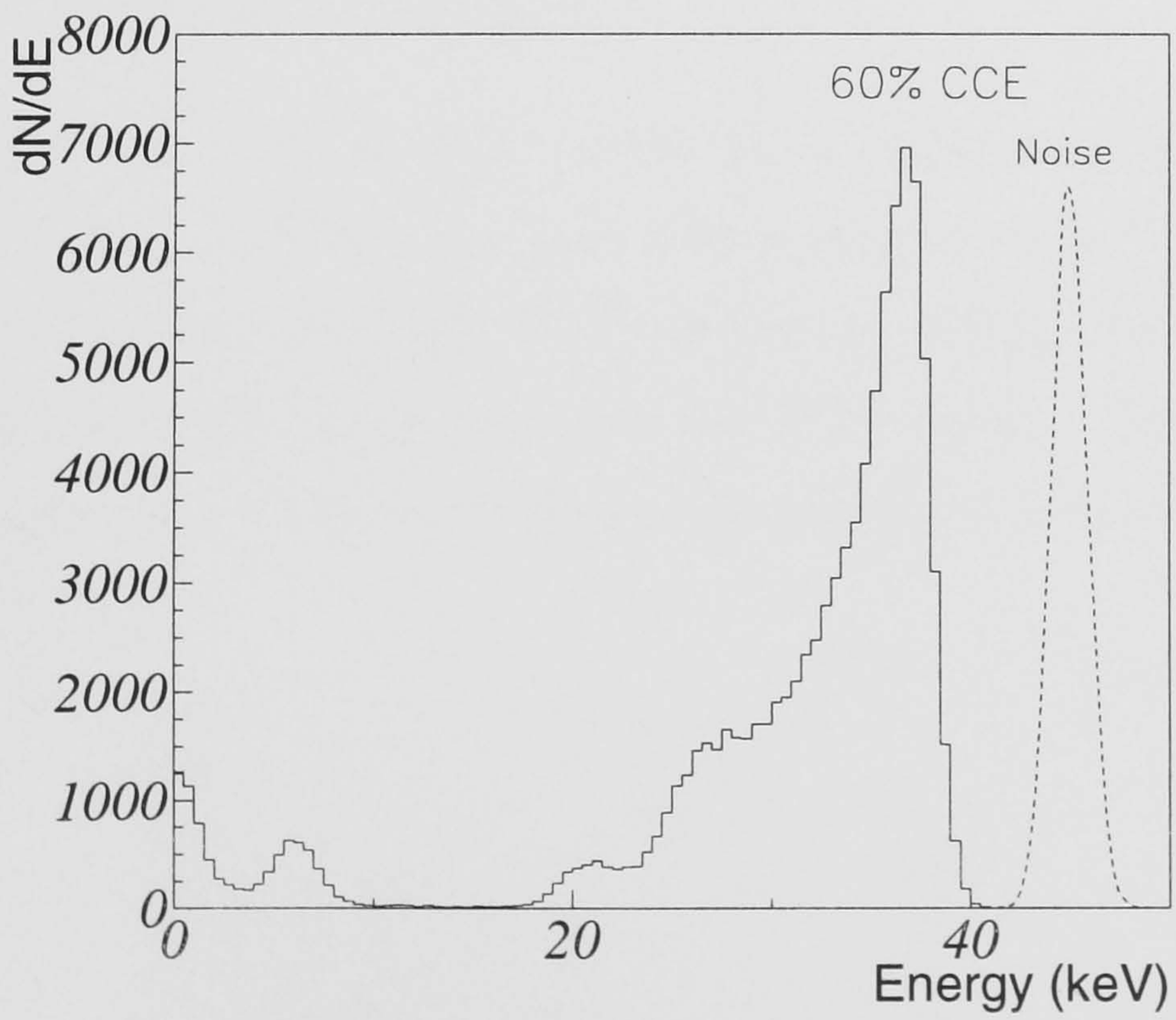

Figure 4.17: 60keV Spectrum simulation for a 300 μm GaAs detector biased at 300V

Line (keV)	% of activity
14	13.5
18	21.0
21	5.0
26	2.5
60	35.3

Table 4.1: Source data for ^{241}Am

the simulation to include a number of X-ray energies so as to simulate better an actual ^{241}Am source. The use of the relative magnitudes for the different lines given in reference [60] has led to other problems, however, due to the predominance of low energy photons which are attenuated in air (and indeed in the source) before reaching the detector. The source lines and their relative intensities are listed for reference in Table 4.1.

Figure 4.18(a) shows the signal without the addition of electronic noise, and Figures 4.18(b) and 4.18(c) show the contribution from Compton and Photoelectric events respectively.

4.6 Summary & Conclusion

The results presented in this Chapter show that is it possible to explain the features observed in an X-ray spectrum produced with a gallium arsenide detector as the model describes the data very well. This has been demonstrated without the need to simulate all the lower energy lines from the ^{241}Am source. These lines should produce the continuum which was lacking in the simulation below 17keV.

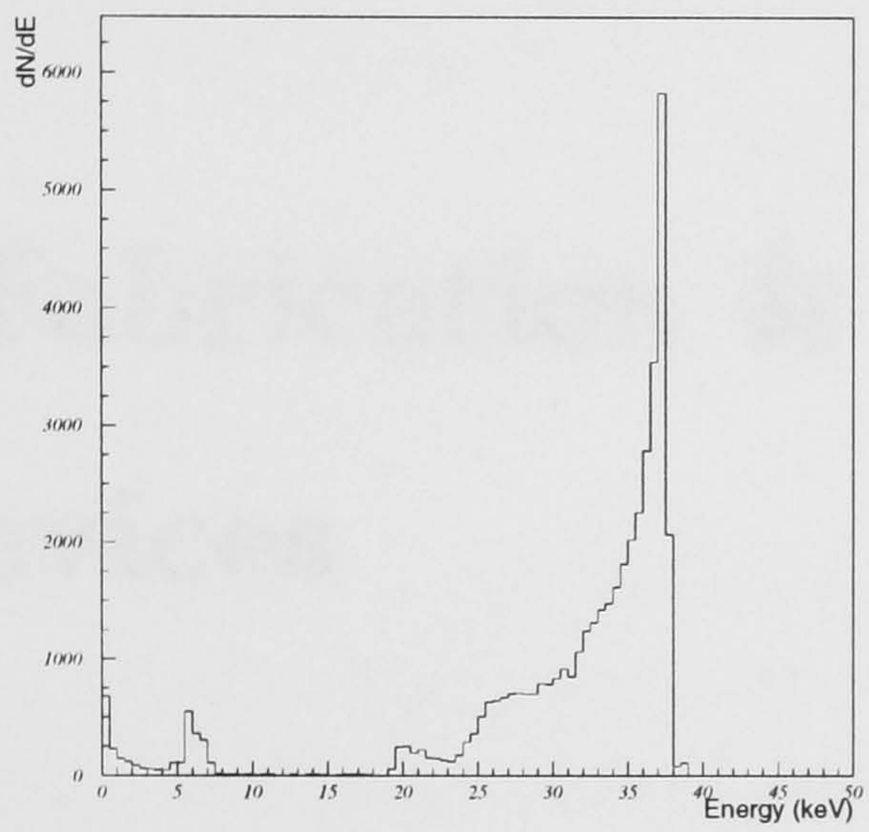

(a) All contributions

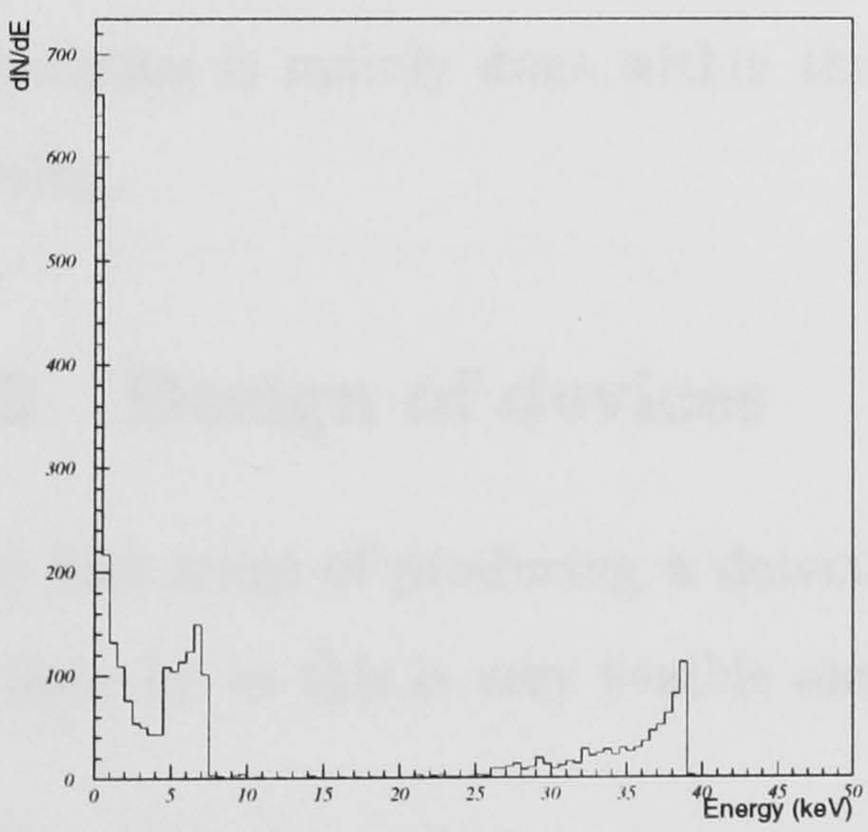

(b) Compton events

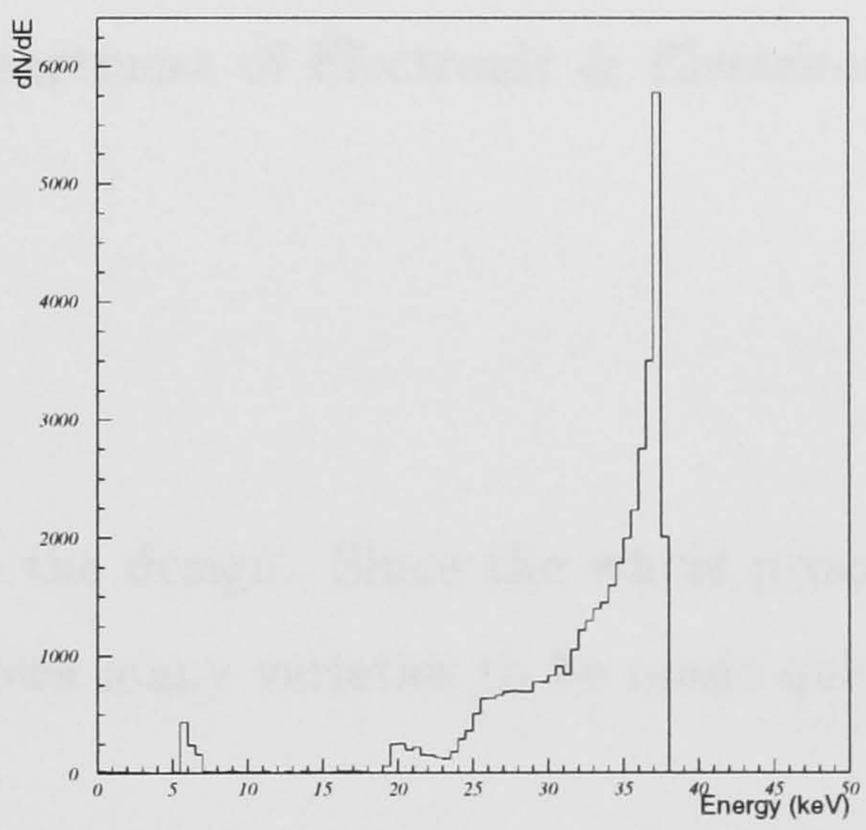

(c) Photoelectric events

Figure 4.18: 60keV Spectrum simulation for a 300 μm GaAs detector biased at 300V without electronic noise

Chapter 5

Design, Fabrication & Testing of GaAs Devices

5.1 Introduction

To succeed in making a working detector many prototypes have been produced. These prototypes were designed, produced and tested within the University. The fabrication is mainly done within the Department of Electronic & Electrical Engineering.

5.2 Design of devices

The first stage of producing a detector is the design. Since the whole process can be done by us this is very flexible and allows many varieties to be made quickly.

5.2.1 Design tools

The devices to be fabricated are designed using the WaveMaker package which runs on an IBM-PC compatible computer under DOS and allows the layout of a range of shapes on multiple layers. These shapes describe the metal contacts and passivation areas, generally with a new layer for each process step, although it is possible in some circumstances to use the same mask for two different processes.

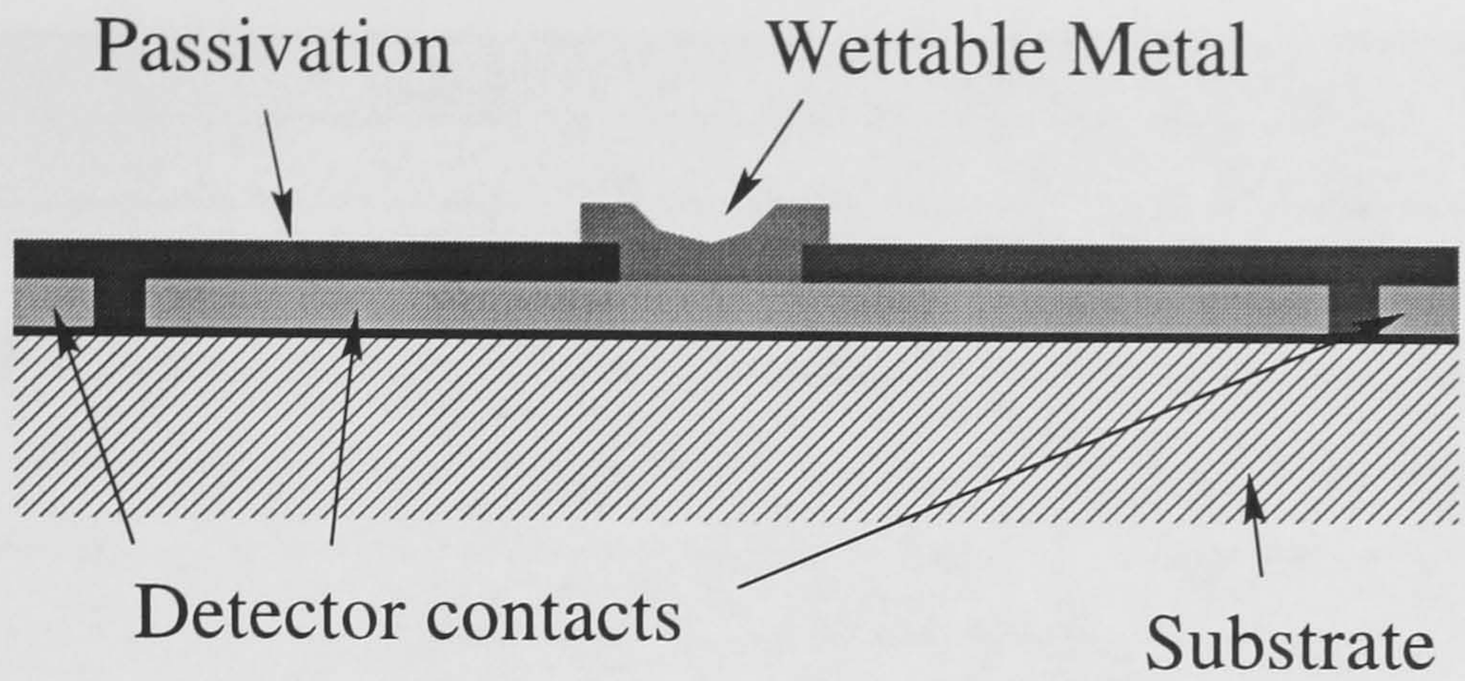

Figure 5.1: Pixel Detector bond pad cross-section

5.2.2 Design of Pixel Detectors

Pixel detectors have a two dimensional array of contacts which are flip-chip bonded to electronics (see Section 3.3). To do this each pixel incorporates a bond pad the structure of which is shown in cross-section in Figure 5.1.

From this cross-section, it can be deduced that five masks or layers are required, namely;

1. Front Metal Contact
2. Front Passivation Windows
3. Wettable Metal Windows
4. Rear Metal Contact
5. Rear Passivation Windows

These are all designed together, with the ability to view any number at the same time. The rear contact is a plane of metal directly beneath the front contact. A hole is required in the rear passivation to allow the connection of a bias supply to the detector. To allow testing of the individual pixels with a scanning laser beam a small (5μm square) hole is left in the rear metallisation of every pixel. One corner of the Omega 2 detector design is shown in Figure 5.2.

In order to cover large areas an array of detectors can be made. The method for doing this with the Omega type readout is to make long detectors, denoted "ladders". To allow room for the bonding of the individual electronic readout chips the length of the pixels at the ends of the electronics are extended to 1mm. A section

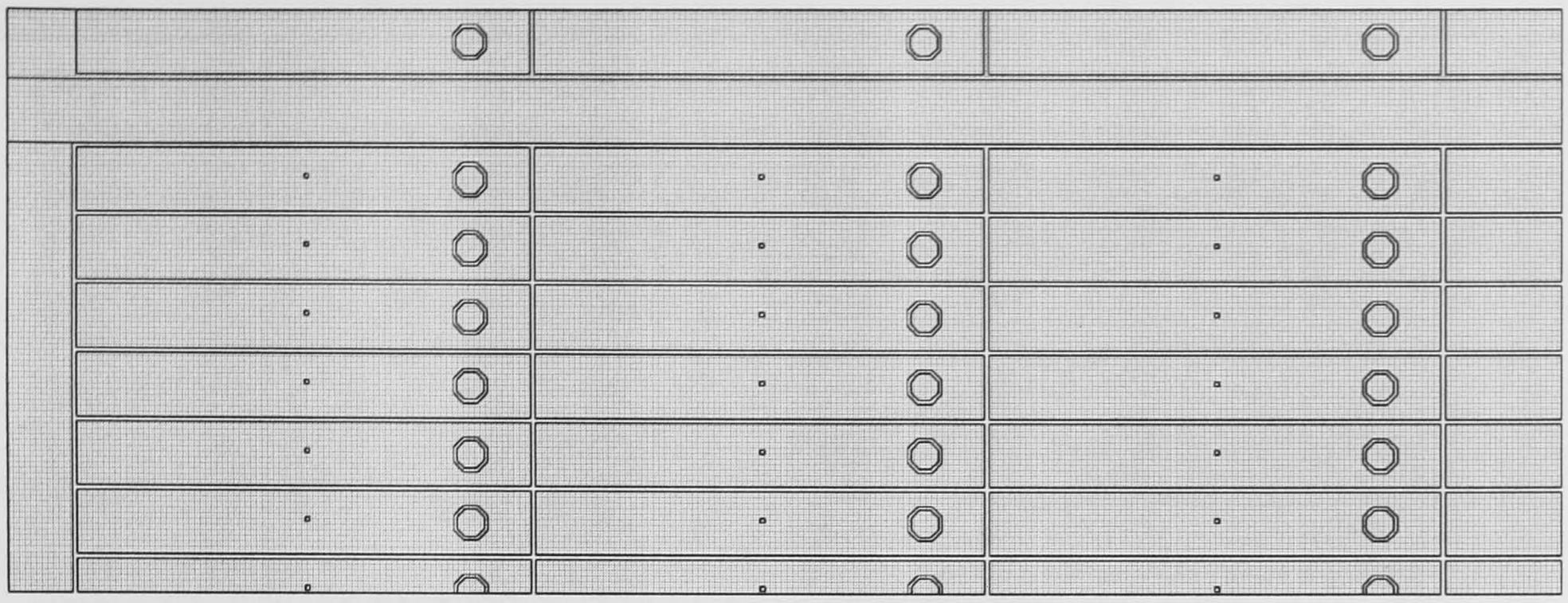

Figure 5.2: Corner of Omega 2 Detector Layout

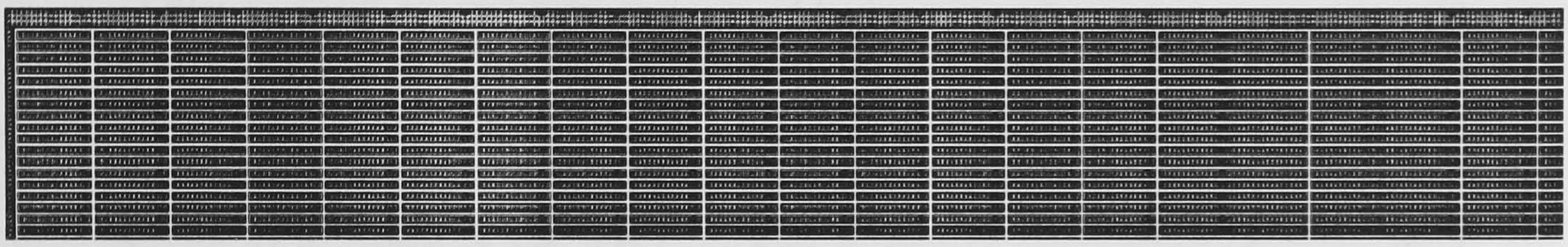

Figure 5.3: Section of Omega2 Detector Ladder with larger pixels on right hand side

of the detector layout for a ladder designed for gallium arsenide is shown in Figure 5.3 to illustrate this.

The next generation of Omega read-out will have a pixel size of $50\mu m \times 500\mu m$. The layout for this detector is shown in Figure 5.4. This design has 128×16 pixels inside a guard ring which has now been extended to imitate an adjacent pixel. The large rectangular area within the pixels is the hole in the rear passivation for biasing the detector.

5.2.3 Design of Microstrip Detectors

Microstrip detectors are constructed from long thin strips of metal on one side of the detector. The typical pitch of these strips is $50\mu m$. Various strip width configurations have been chosen to study systematically the effect of varying the width of the metal and the gap between the metal strips as this affects the field between the strips.

The bond pads required to wire bond to the detector must be wider than $50\mu m$ (to allow ultrasonic wire bonding) so they are staggered. There are two sets of bond pads to allow a detector to be reused in the event of a failure of the readout

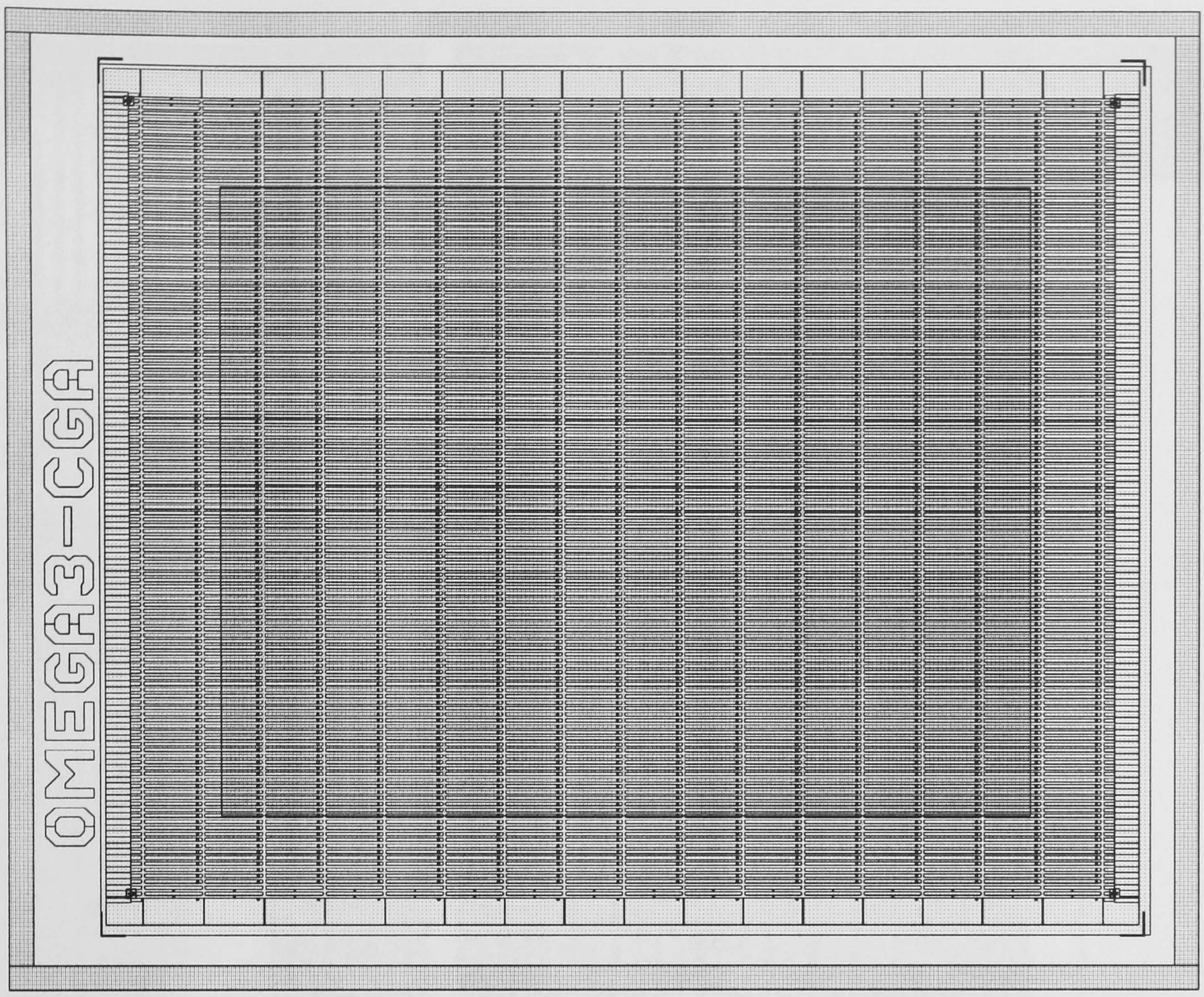

Figure 5.4: Omega3 Detector Layout

electronics. The layout at one end of a strip detector between two regions of different metal widths is shown in Figure 5.5(a). The area at the bottom where the strips widen is the back contact metallisation which is only under the strips and not the bond pads or the bias strip.

The bias strip (shown with its bond pad in Figure 5.5(b)) is used to ensure that the voltage on the detector strip bond pad is close to zero[61]. The voltage is required to be less than 20 volts across an external capacitor which AC couples the read-out electronics to the detector. This bias strip provides the DC path to ground for the leakage current. Some preamplifier chips require a low dark current, hence the need for the capacitor.

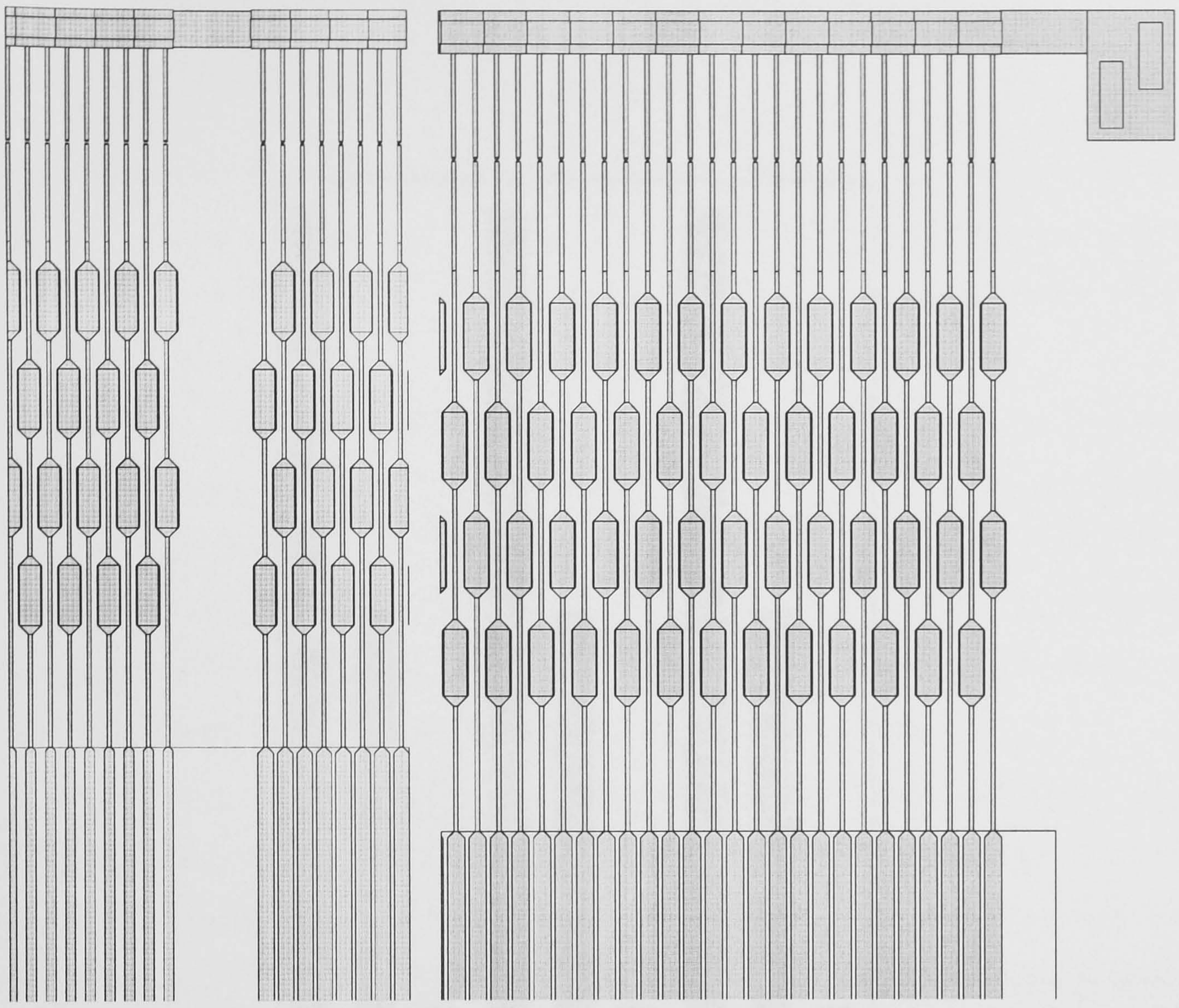

(a) Different Width Sections (b) Bias Strip Bond Area

Figure 5.5: Strip Detector Layout

5.2.4 Test Structures

Various test structures are also used to test the performance and characteristics of the detectors. One such device is to measure the capacitance of strips. This uses six strips with the first, third and fifth strip connected together. The capacitance can therefore be measured between any of the remaining strips and the three merged strips. These strips are fabricated in various lengths and widths, and are shown in Figure 5.6.

Circular pads are also used to test device performance and are used extensively in radiation tests due to the ease of use. These usually incorporate a guard ring on one side with a contact on the reverse side covering the area under the guard ring and detector pad.

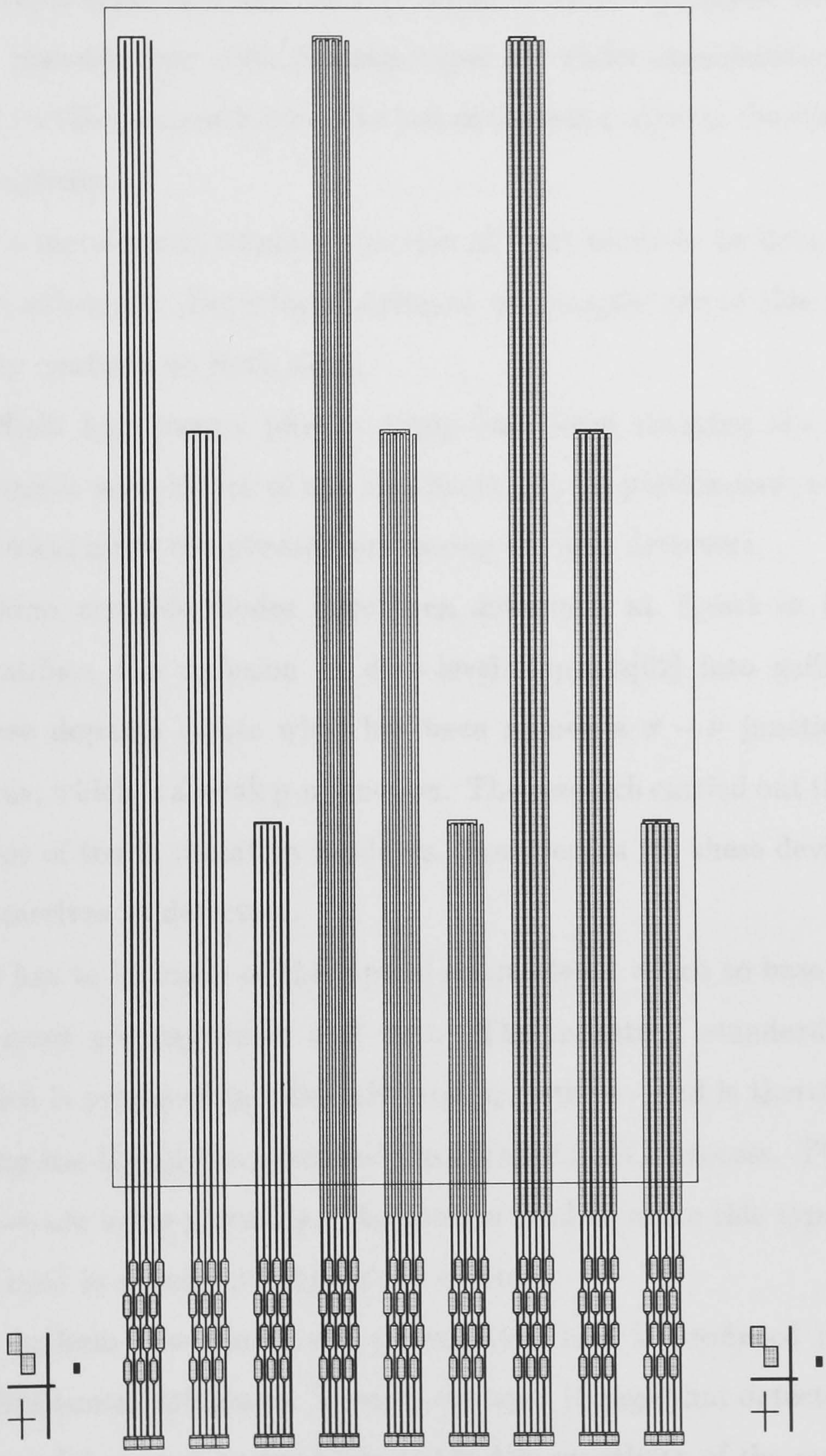

Figure 5.6: Strip Capacitance Test Structures

5.3 Fabrication

5.3.1 Substrate Choice & Preparation

There are various types of semiconductor diode detectors to choose from in gallium arsenide. At present three main junction types are under consideration, p-i-n type, π-ν type and metal-semiconductor. The last of these is currently the favoured option due to its simplicity.

To make a metal-semiconductor junction all that needs to be done is to deposit metal on the substrate. Detectors fabricated in Glasgow are of this type, usually with Schottky contacts on both sides.

The Sheffield high energy physics group have been studying the p-i-n variety, but as yet there is no evidence of any significant gain in performance to compensate for the somewhat more complicated processing of these detectors.

New gallium arsenide diodes have been developed at Tomsk in Russia. This technology utilises the diffusion of deep-level dopants[62] into gallium arsenide wafers. These dopants create what has been named a $\pi - \nu$ junction inside the semiconductor, which is a weak p-n junction. The research carried out there promises another factor of ten in radiation hardness. However, as yet these devices have still to prove themselves as detectors.

A choice has to be made of the type of substrate on which to base the detector. The main issues are impurities and cost. The industrial standard [63] gallium arsenide which is produced in relatively large quantities - and is therefore cheaper - is grown using the Liquid Encapsulated Czochralski (LEC) process. This is the type of material we are using presently. The process used to make this type is similar to the method used in manufacturing silicon crystals.

Another gallium arsenide crystal growth type that is produced in quantity in industry is Horizontal Bridgman. There is evidence though that detectors fabricated from this material are not as good due to the low resistivity of the material[64].

The RD8 collaboration has also been investigating GaAs layers prepared using Liquid Phase Epitaxy (LPE). This method is a slow and relatively expensive process and, until very recently, it was not possible to have LPE layers thicker than a few tens of microns. Now, however, it is becoming possible to have layers of up to 200μm.

The epitaxial layer is grown on top of a LEC wafer, then the wafer is thinned (see below for explanation) leaving just the LPE layer of about 200μm thickness. This material can be very pure (e.g. carrier concentrations of $\approx 10^{13}\text{cm}^{-3}$ have been achieved) and has demonstrated very good characteristics[65]. At present the cost would be prohibitively high for a large area ($> 1\text{m}^2$) detector constructed from this material.

In the past the wafers used to make our detectors have been processed with the polishing done by the manufacturer. Following the recent purchase by the group of a Wafer Thinning & Polishing Machine, we can now thin our wafers down using an abrasive process utilising 3μm particles of alumina in a solution. This allows us to choose the thickness of our wafer more freely. After the thinning stage both sides are polished with an ammonia and hydrogen-peroxide solution. This last process has improved the performance of our detectors measurably. We have seen that the charge collection efficiency (CCE) has improved to >=70% in most samples tested. Several samples have shown over 95% CCE and the first signs of a plateau in the curve of CCE vs reverse bias.

5.3.2 Photo-lithography

To define the areas on the detectors which have been designed masks are produced using a Leica EBPG 5-HR 100 electron beam writer. These masks are then used in a photo-lithography process.

The substrate is spun at 4000 RPM for 60s once the S1400 resist liquid has been applied. This is then baked in an oven for half an hour at 90°C. Usually, half way through the baking the substrate is immersed in Chlorobenzene for a short time ($\approx$ 10s) to aid in edge definition. Once this has been done the mask is placed in contact with the resist covering the substrate and then exposed to ultra-violet light[66] to which the photo-resist is sensitive. When the substrate is developed using a suitable solvent (Microposit 1400-31 developer) the exposed portion of the resist becomes soluble. Removal of this soluble portion leaves the area in the mask which was clear free from photo-resist on the substrate. This aspect of the process is shown in Figure 5.7.

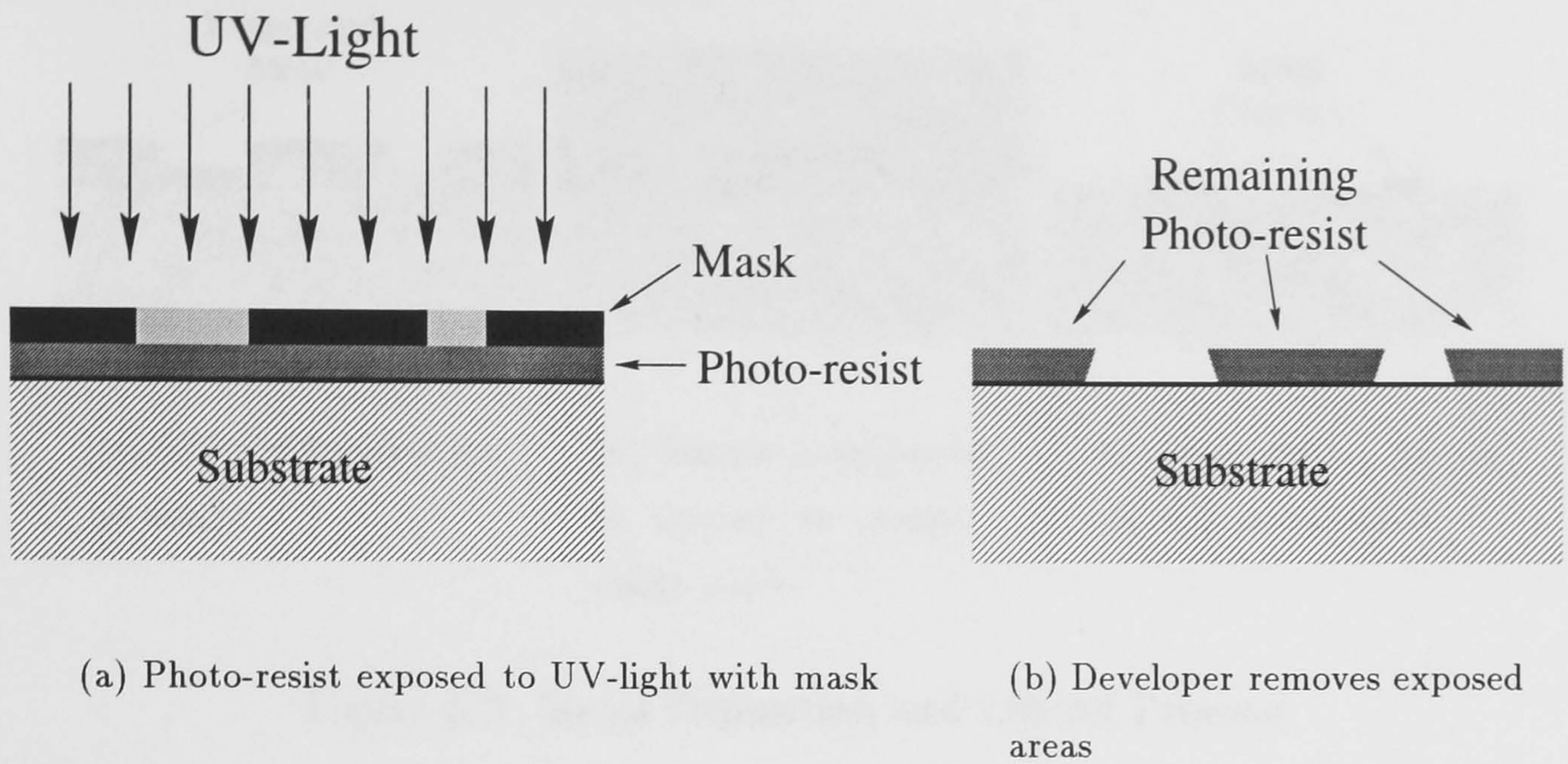

(a) Photo-resist exposed to UV-light with mask

(b) Developer removes exposed areas

Figure 5.7: Photo-lithography Process

5.3.3 Metal Deposition

Prior to metal deposition the substrate is deoxidised using a 1:1 hydrochloric acid and water solution. The substrate is immersed for 60s.

The metal can then be evaporated using an electron beam focused on a crucible of the require metal under vacuum. This is accomplished using a Plassys (France) Evaporator (model MB430) which automates the process. The sample is loaded into a entry chamber which is evacuated to less than 10^{-6} bar. Once this has been completed a shutter is opened to allow the sample to move into the main chamber which is always under vacuum.

Once the sample has been loaded a recipe is selected from a list which allows the choice of the type and thickness of the required metals for the contacts. Usually contacts are made of multiple layers of different metals.

Once the metal has been evaporated onto the sample and it has been brought back out of the evaporator, lift-off is performed. To do this the sample in immersed in acetone. To aid lift-off the acetone can be pre-heated in a bath of hot water. The sample is soaked for a while and if lift off is incomplete, it can be placed in an ultrasonic bath. By removing the sample from the acetone the lift-off process is ended so care must be taken to ensure that it is complete before doing so. Usually a microscope is used to view the sample while it is still immersed. This process is illustrated in Figure 5.8.

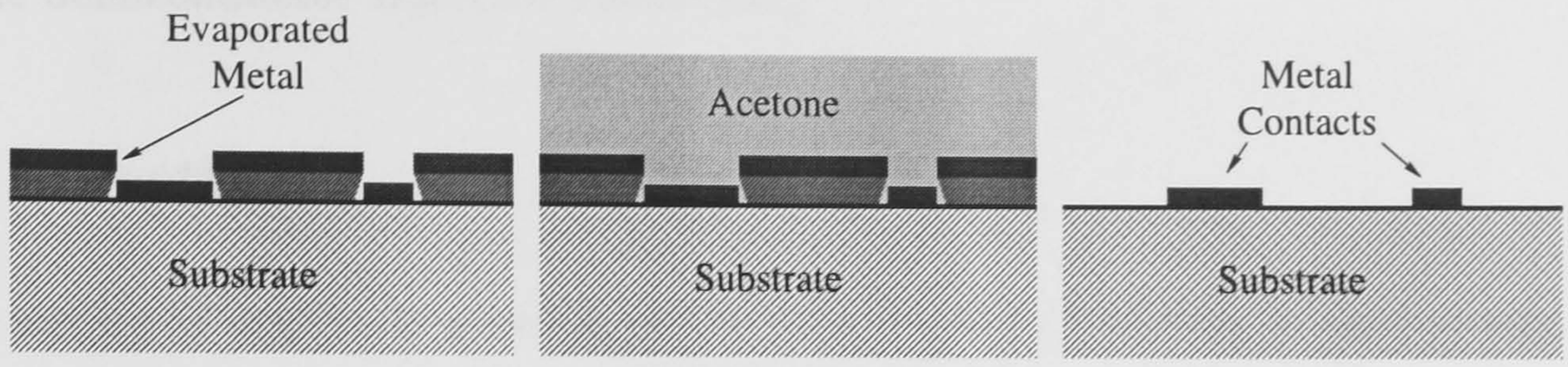

(a) Metal evaporated on to sample

(b) Sample is immersed in acetone to dissolve photo-resist

(c) Final result - metal contacts on substrate

Figure 5.8: Metal Deposition and Lift-off Process

5.3.4 Passivation & Etch

To protect the device from mechanical damage and to complete the crystal bonds on the outside of the detector, a passivation layer is used. Two forms are commonly used, silicon nitride and silicon oxide. The entire sample is coated with a layer, typically 1μm thick, by heating the sample to approximately 300°C in an atmosphere of the appropriate gas at pressure.

To make bonds to the detector contact holes must be made in this passivation at a later stage. To do this photo-resist is applied and holes made in it as described in Section 5.3.2. The sample is then placed in an atmosphere of CF_4 which is accelerated towards the sample using an electric field. This etches the passivation more readily than the photo-resist and, as a result, the holes in the photo-resist are duplicated in the passivation.

5.3.5 Commercial Prototypes

In 1994 the RD8 collaboration placed orders with two companies, Alenia in Italy and EEV in Britain, to produce prototype microstrip and pixel detectors.

The designs for these prototypes, produced in Glasgow, were sent to the companies for checking to see if anything needed to be added to aid processing. The modified designs were then returned and masks produced in the Ultra-Small Structures Laboratory in the Department of Electrical and Electronic Engineering.

Unfortunately only Alenia produced devices in time for the 1994 test beam periods. These detectors were subsequently brought back to Glasgow and tested

in the Semiconductor Detector Laboratory.

5.4 Testing

The testing of devices is possible in the Department of Physics & Astronomy. An area of laboratory space has been designated a clean area and steps have been taken to limit contamination in that area by partitioning a part of the lab and utilising a positive air flow out of this area. In addition, plastic strips have been put across door ways with a raised step to prevent dust entering the area.

5.4.1 Detector Tests

IV Tests

Before the detectors are tested in a beam they are characterised electrically. The basic test for a detector is to verify that it operates as a reverse-biased diode with acceptable current.

These tests are done using a Keithley 237 High Voltage Source Measurer, controlled by a Macintosh computer running a user application in LabView. The window used to control the Keithley is shown in Figure 5.9. These tests are typically carried out with up to a minute between successive measurement to allow the system to reach equilibrium, since very slow transients have been observed in gallium arsenide detectors.

A typical IV curve can be seen in Figures 5.10 and 5.11 for two Alenia detectors, which were later used in the test beam as reported in Section 6.3. These two detectors come from two different wafers which were also processed differently by Alenia.

A Glasgow fabricated detector has the reverse current plotted against voltage in Figure 5.12. The different curves correspond to the different $\frac{metal}{pitch}$ ratios.

VV Tests

To test the novel biasing structure the voltage on the detector strip was plotted against the voltage applied to the rear contact, using the circuit shown in Figure 5.13.

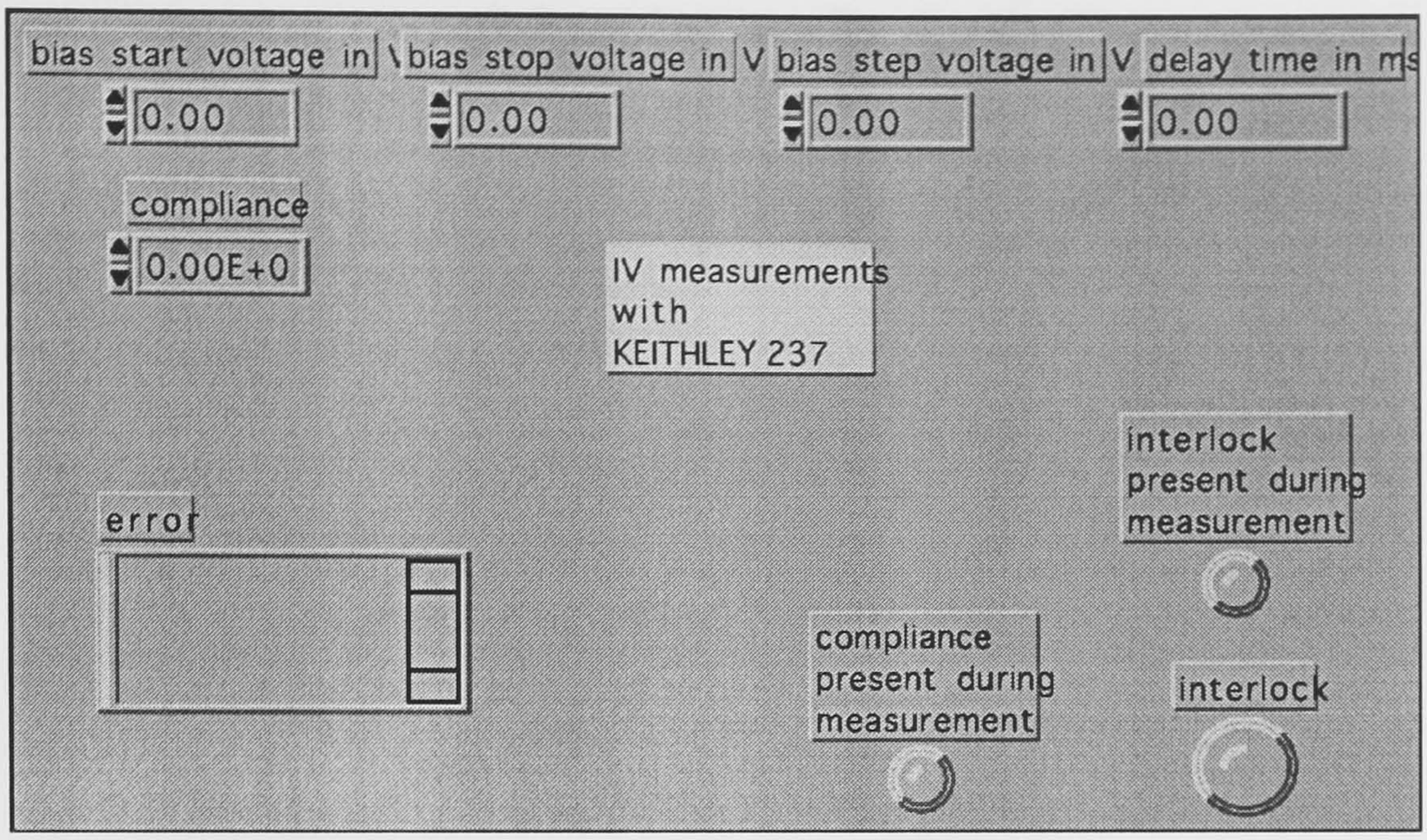

Figure 5.9: LabView Application for IV Tests

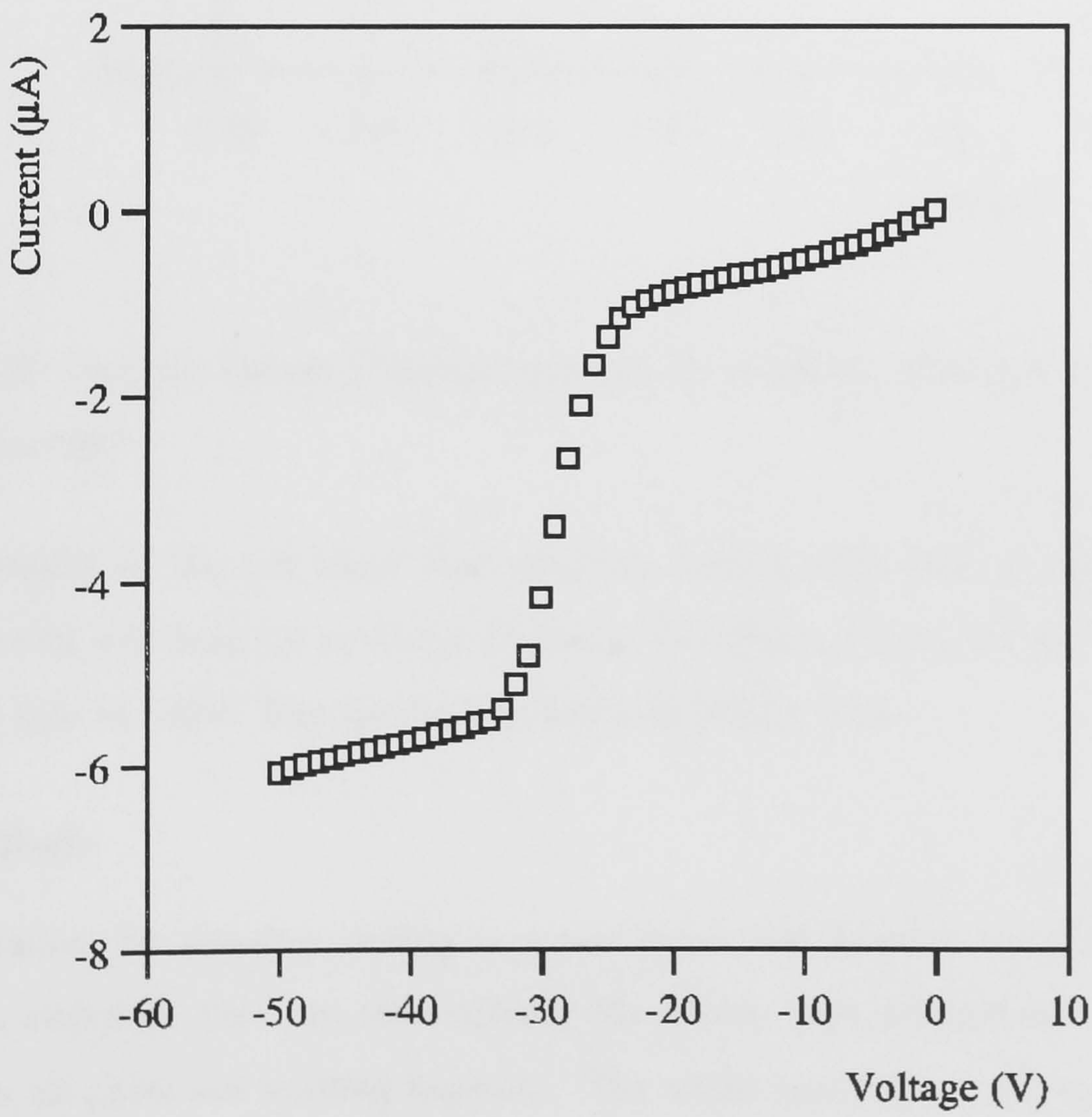

Figure 5.10: Current-Voltage Characterisation of AL-W3-7. This detector is $10cm^2$ and $200\mu m$ thick.

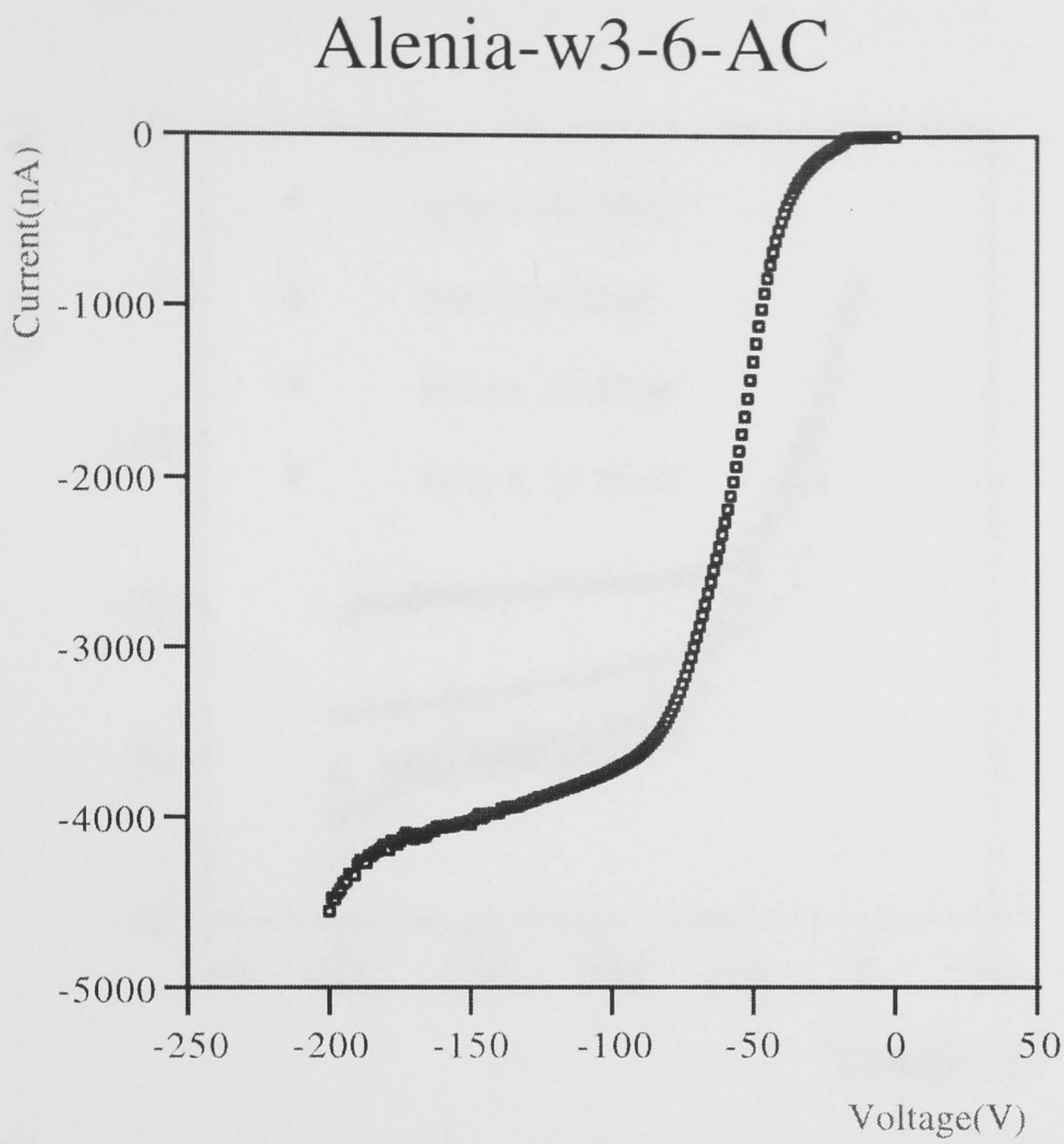

Figure 5.11: Current-Voltage Characteristics of AL-W3-6AC. This detector is 4.5cm^2 and 200μm thick.

The results of the test show that with the biasing strip held at zero volts the detector strip will float up to about 35 volts. Therefore, during the test beam this strip was held at -30V. The results are shown in Figure 5.14.

Source Tests

In preparation for detector testing in a test beam the detector can be proven to work. In addition, this can also validate the whole data acquisition system and show that all parts are working together. The whole readout system was therefore tested at CERN with the repeater card (which is the interface between the front-end electronic readout chip and the Data Acquisition system) to be used in the final test beam. These tests were done using a radioactive ^{90}Sr source.

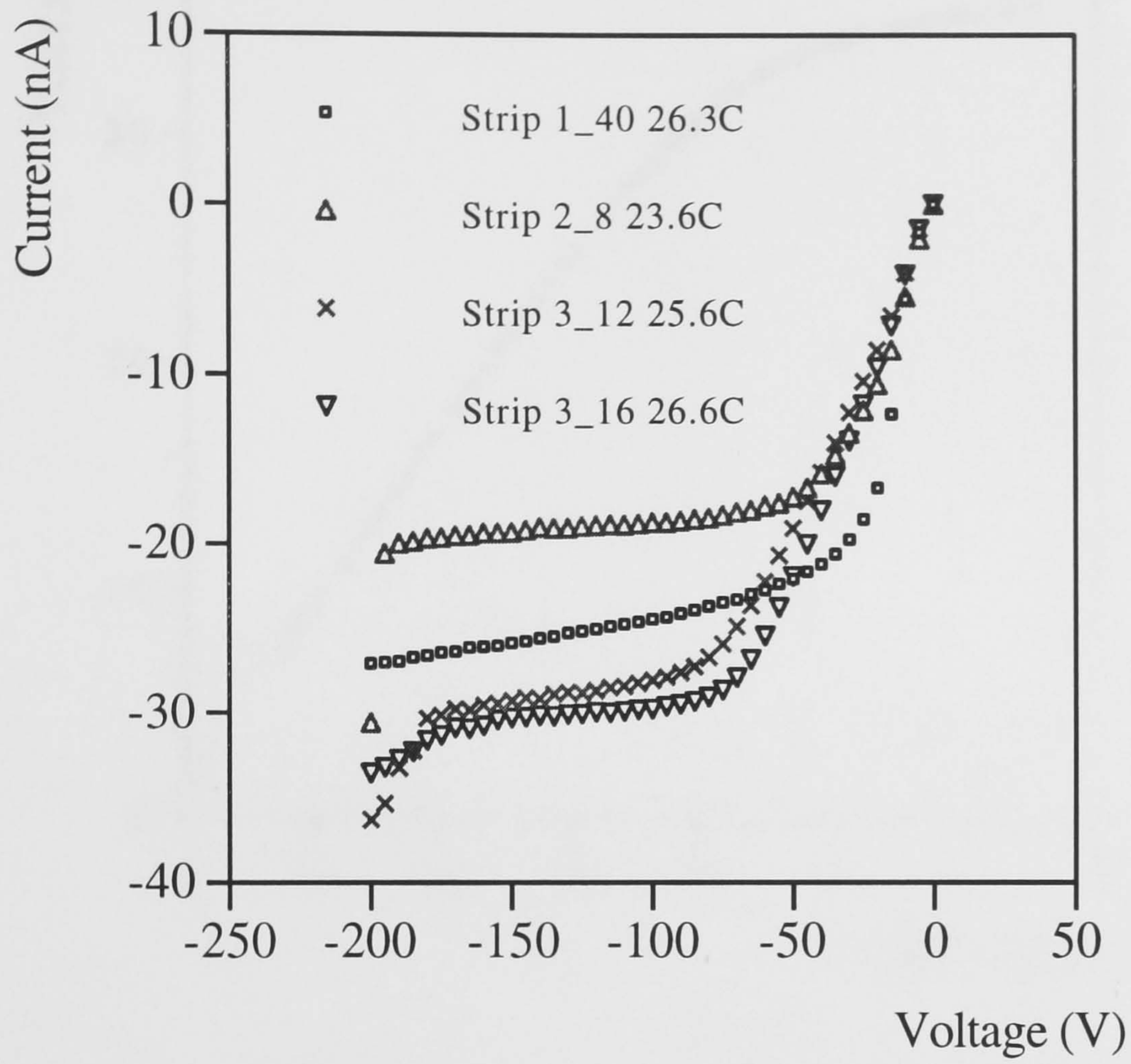

Figure 5.12: Current-Voltage characterisation of a Glasgow detector - GS196. This detector is 3.6cm^2 and 202μm thick. Each strip subtends an area of 0.925mm^2.

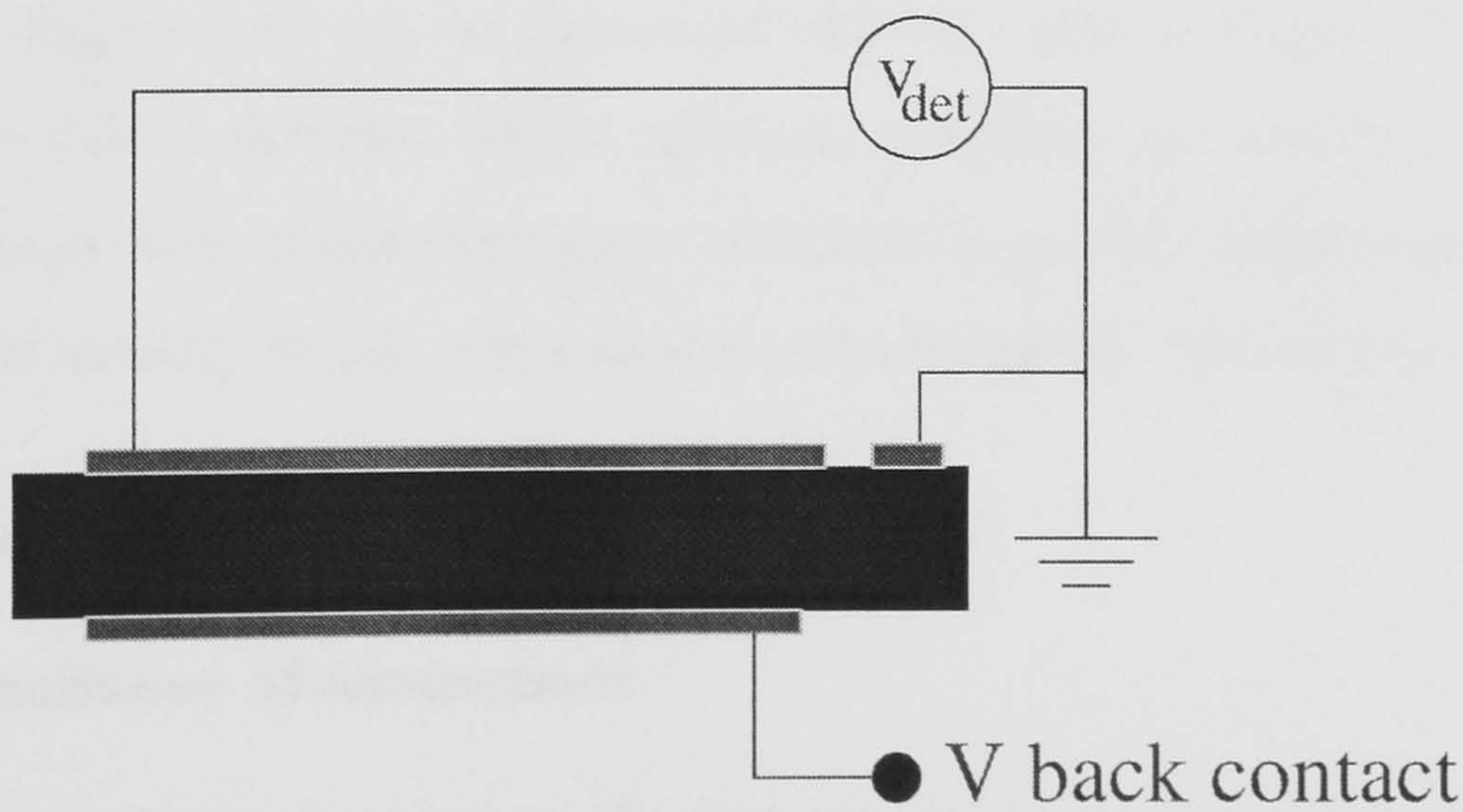

Figure 5.13: Schematic of VV Circuit

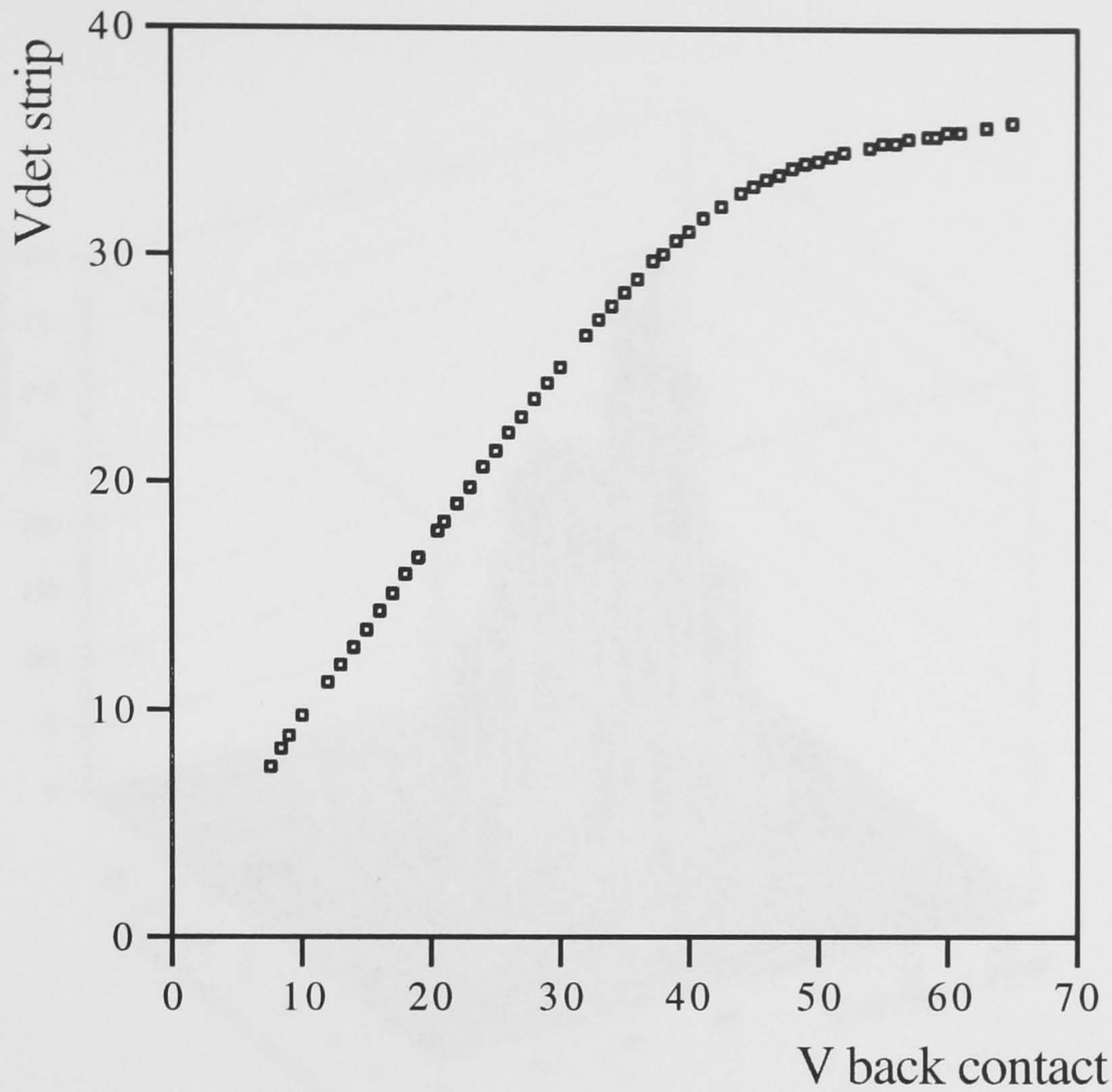

Figure 5.14: Voltage on detector strip vs voltage on back contact for DC coupled Alenia microstrip detector with 25μm wide strips at 50μm pitch

This process also saves time when setting up at the beam line. The allocation of time on a beam line is very tight and any delays can be very detrimental.

A ^{90}Sr beta source was also used to test the pixel detectors. A plot of the signal collected in Figure 5.15 can be compared with the plot in Figure 5.16 which was taken with a silicon detector. Some threshold problems are obvious in the gallium arsenide case as some pixels show large variations from their neighbours. This effect was observed in early silicon versions also and named the "Skyscraper" effect.

5.4.2 Test Structures

Strip Capacitance Measurement

The capacitance between strips on the test structure was measured and plotted for the three lengths of strips fabricated. This produces a line, the gradient of which gives the actual strip capacitance per unit length. This was done for all three widths

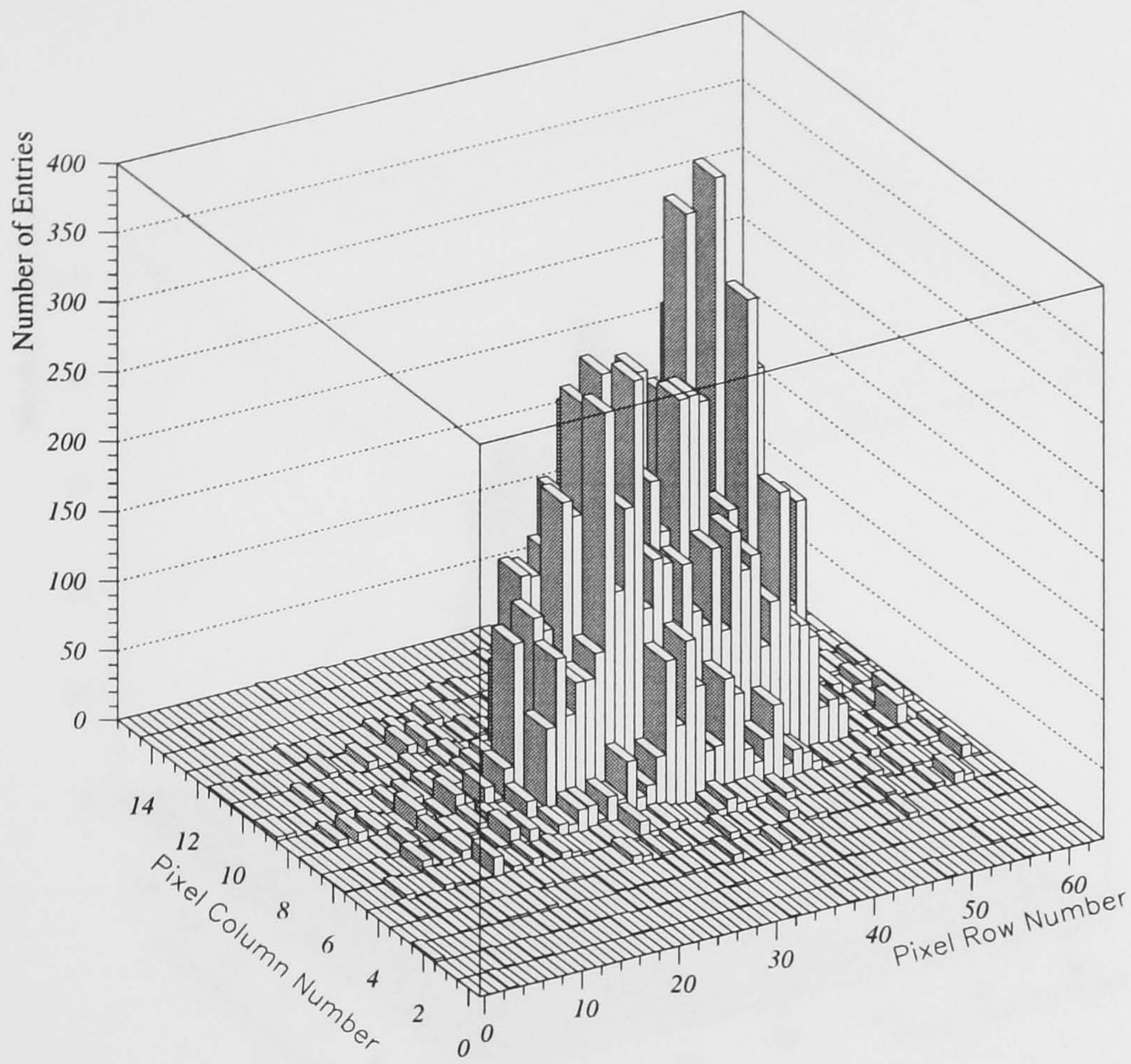

Figure 5.15: Signal measured in a gallium arsenide detector

of metal fabricated, 10μm, 25μm and 40μm.

To do the measurement a HP4274A LCR Meter is used. This can be controlled by a Macintosh running a user application in LabView. The control panel is shown in Figure 5.17. This is used to sweep the voltage and frequency used to measure the capacitance across the whole detector.

When measuring the inter-strip capacitance, however, a single value of 0V at 10kHz (results were identical at 100kHz) is used so there is no benefit in using the computer control. The results obtained are shown in Figure 5.18 together with a linear fit to the three points for each strip width.

5.4.3 Radiation Damage Tests

Gallium arsenide detectors are aimed at the high radiation areas of ATLAS. To prove their viability, radiation tolerance tests must be carried out on the various kinds of radiation that will be present in the experiment; neutrons, gamma-rays, protons

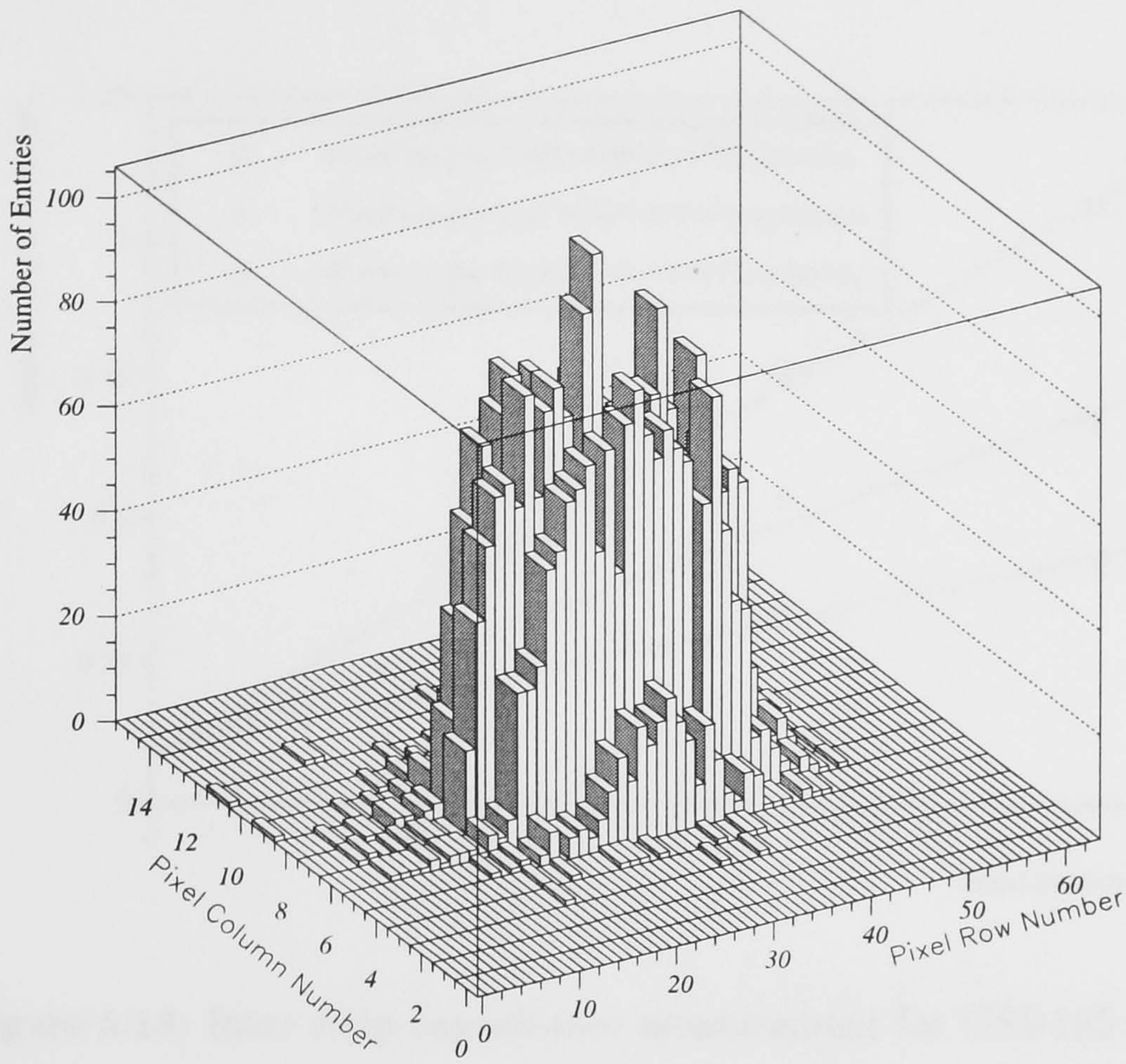

Figure 5.16: Signal measured in a silicon detector

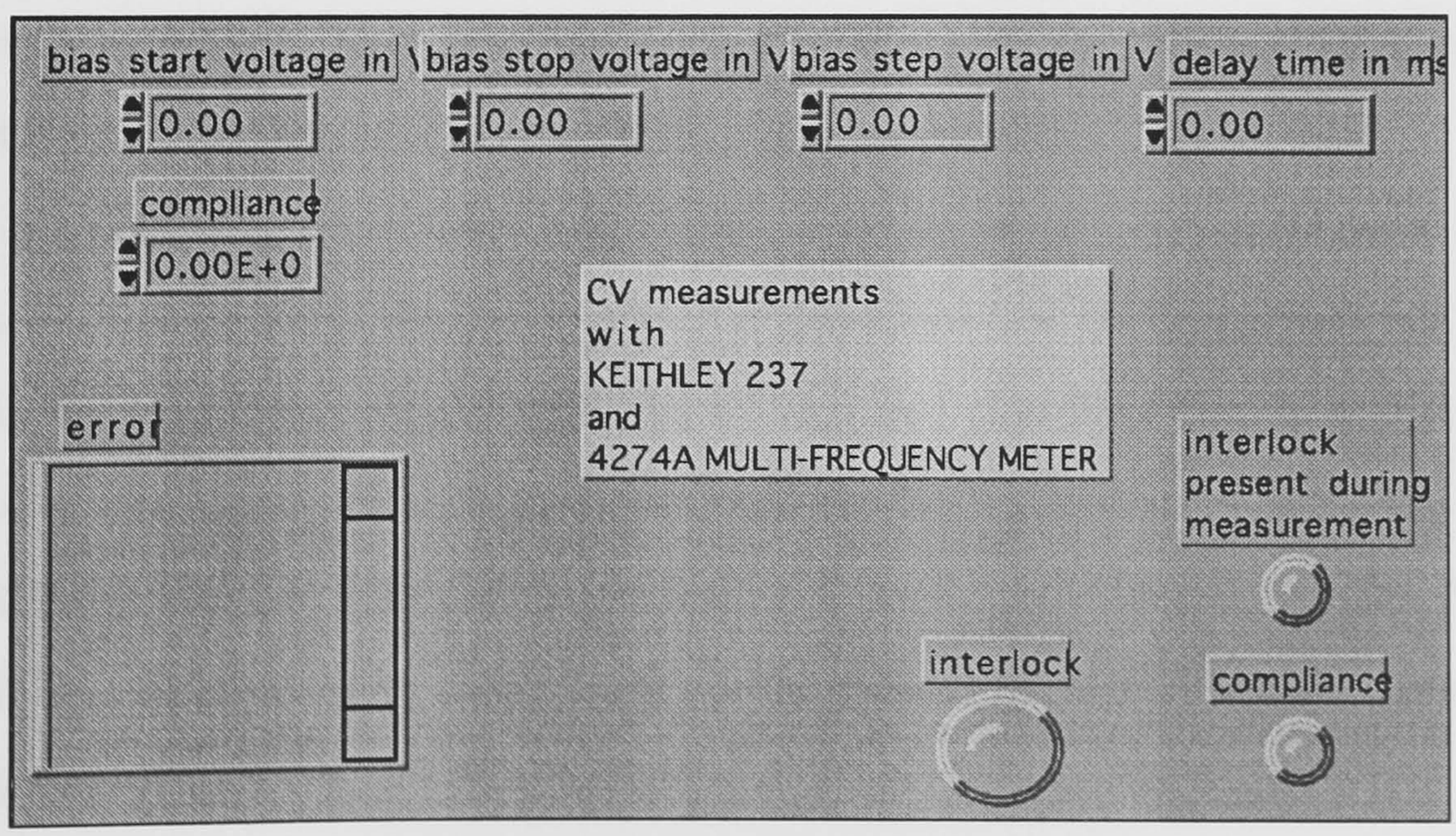

Figure 5.17: LabView Application for CV Tests

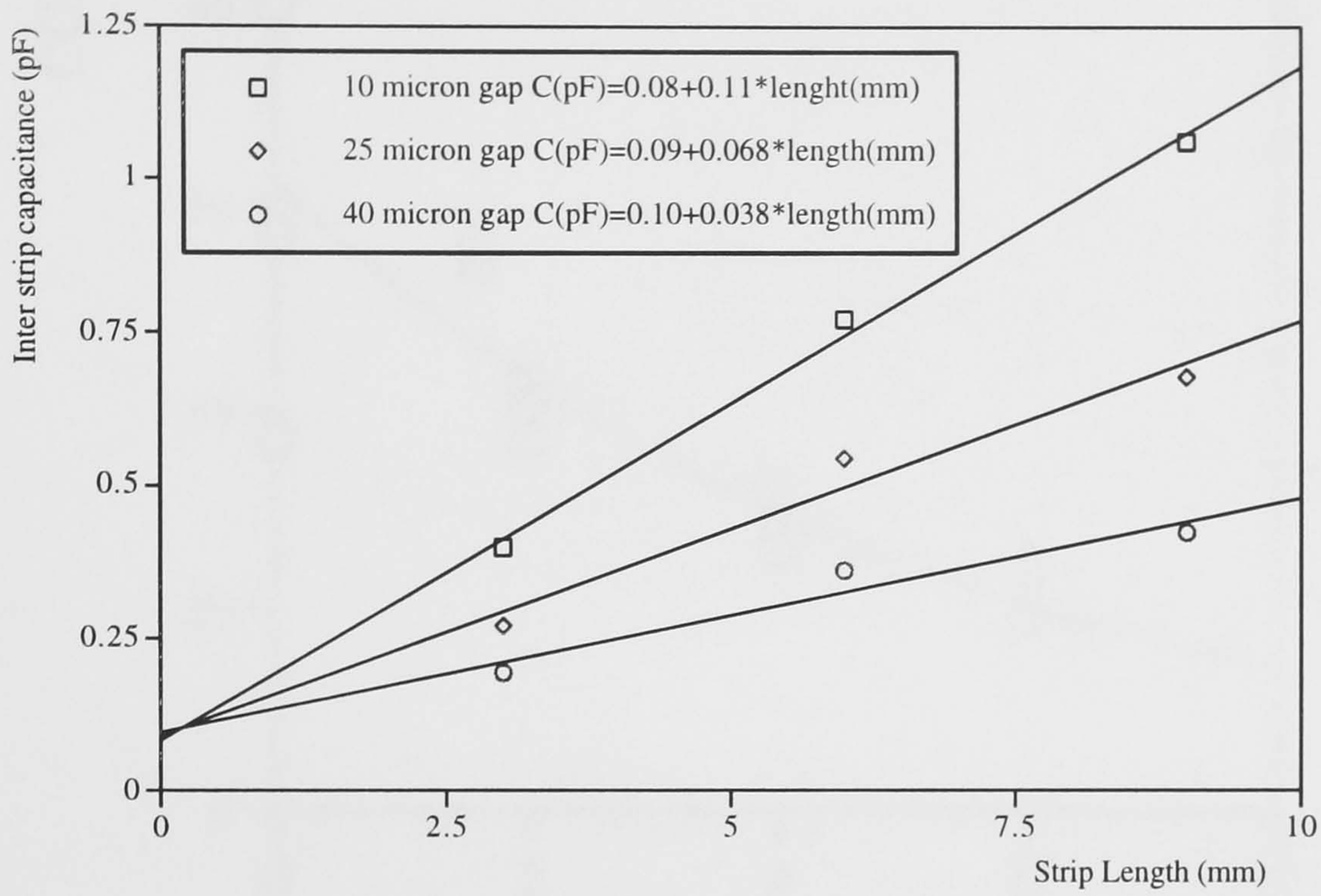

Figure 5.18: Inter-strip capacitance measurement for GSD185 device

and pions. The latter will be the most prolific, as discussed in Section 7.4 which presents Monte-Carlo predictions for pion and proton fluences in the region foreseen for gallium arsenide detectors in ATLAS.

Neutron irradiation has been carried out at the ISIS facility at the Rutherford Appleton Laboratory. This is a spallation source which delivers a similar spectrum of neutrons to that expected at the LHC, peaking at about 1MeV.

The results from these tests are shown in Figure 5.19. It can be seen that the signal from the detectors drops by a factor two after 3×10^{14} neutrons cm^{-2}. This dose is in excess of that expected[67] at ATLAS and therefore this is acceptable.

Another technology shows promise for even higher radiation hardness to neutrons. This is the $\pi - \nu$ diodes produced at Tomsk, described in Section 5.3. The results from radiation tests carried out on these detectors by Protvino are shown in Figure 5.20[68].

For testing detector hardness to protons, a 24 GeV proton beam from CERN's PS is used. During this irradiation measurements were made on the leakage current.

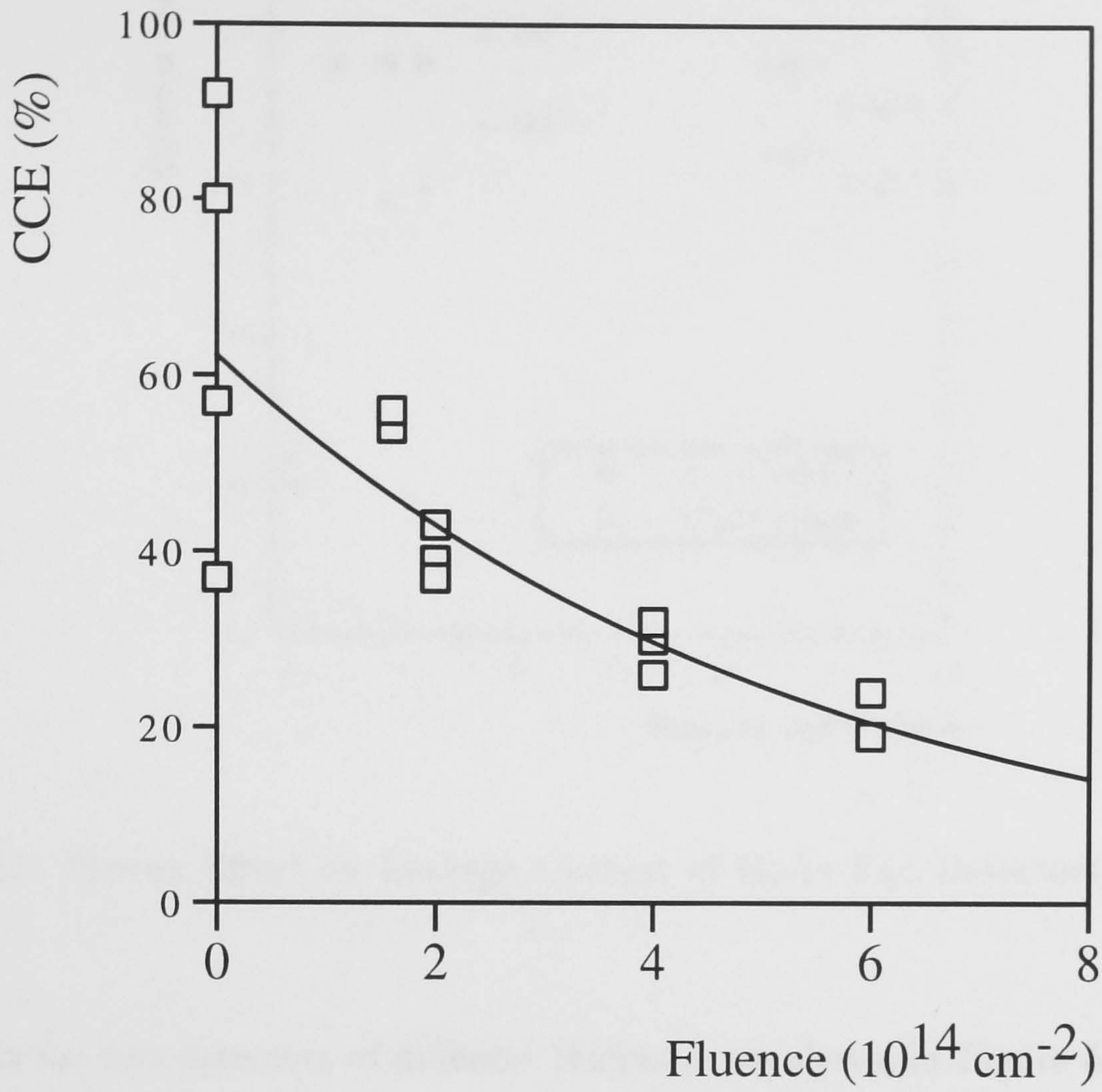

Figure 5.19: Variation of CCE with neutron dose at highest voltage possible. Measurements made at 20°C with a shaping time of 500ns.

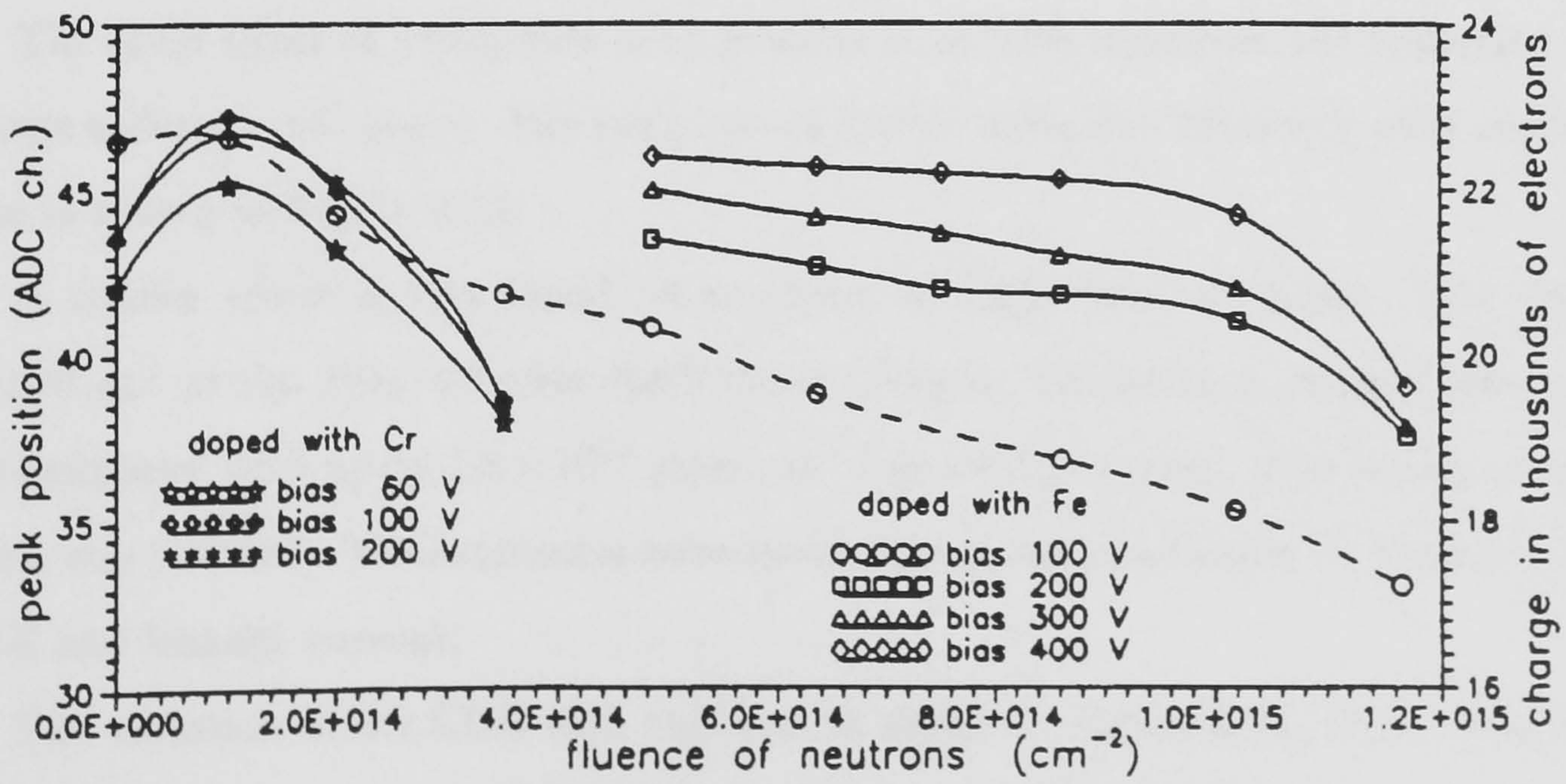

Figure 5.20: Variation of Collected Charge with Neutron Dose for Tomsk Detectors

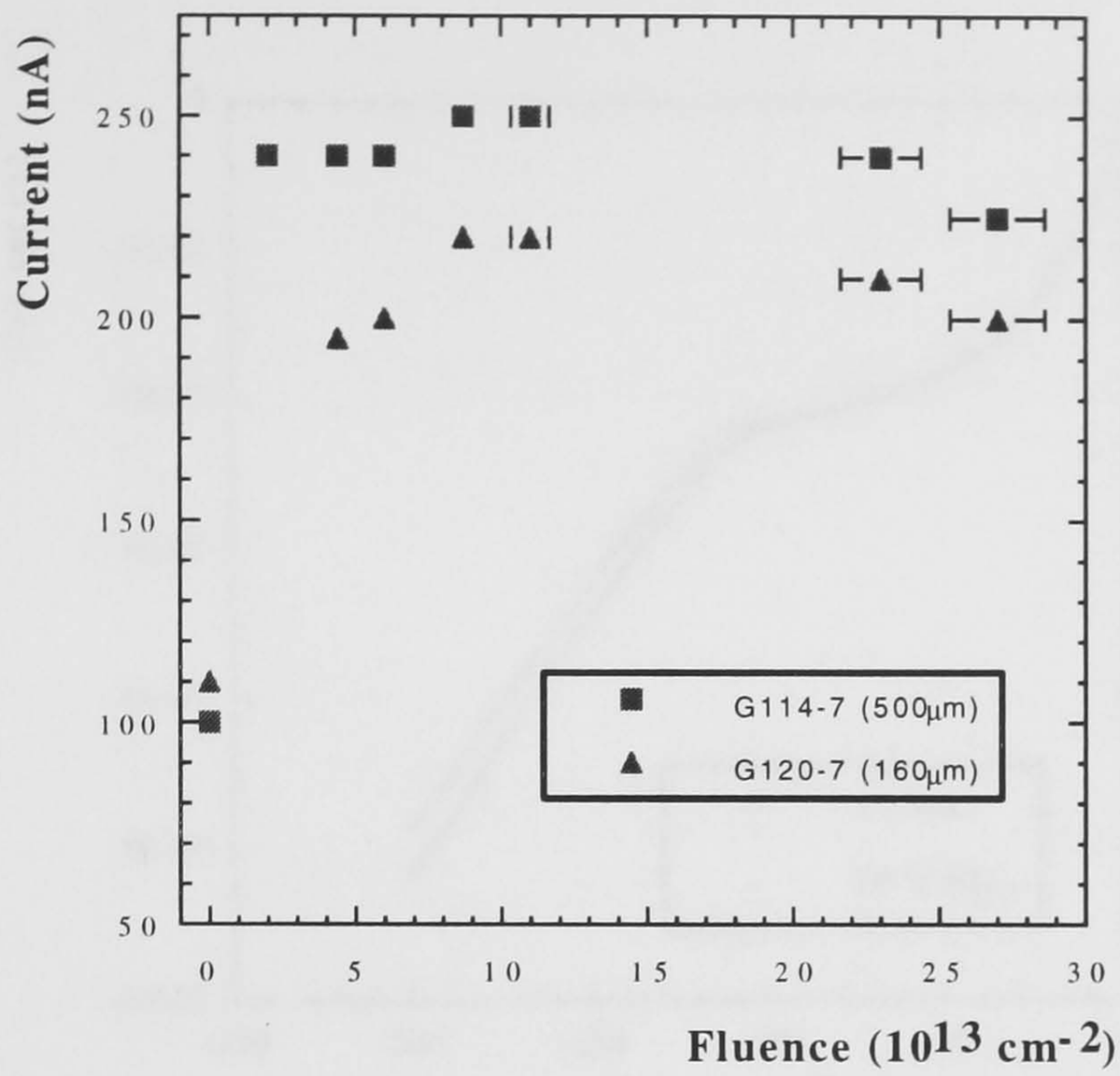

Figure 5.21: Proton Effect on Leakage Current of GaAs Pad Detectors with area 7mm^2

The results for two detectors of different thickness are shown in Figure 5.21.

In addition to this, some detectors were biased while receiving the proton dose. The IV curve for two detectors from the same wafer (which was processed as a wafer) are shown in Figure 5.22. This shows that there is no adverse effect on the reverse current of the detector due to the detector bias, as the leakage current is slightly lower for the biased detector at higher voltages.

The main effect of irradiation with protons is, as with neutrons, the reduction of charge collection efficiency. The variation of charge collection efficiency with proton dose is shown in Figure 5.23.

A similar effect is also found on exposure to high fluxes of pions. Test were carried out at the Paul Scherrer Institute in Villigen, Switzerland, where detectors were exposed with up to 1.8×10^{14} pions cm^{-2} in a 3 day period. The energy of the pions was 330MeV. Measurements were made during the irradiation to measure the CCE and leakage current.

The variation of the CCE with exposure is shown in Figure 5.24. Since the pion irradiation was conducted at the Δ resonance, where the total cross section is a factor of two higher there may be some enhancement of the damage. Investigations

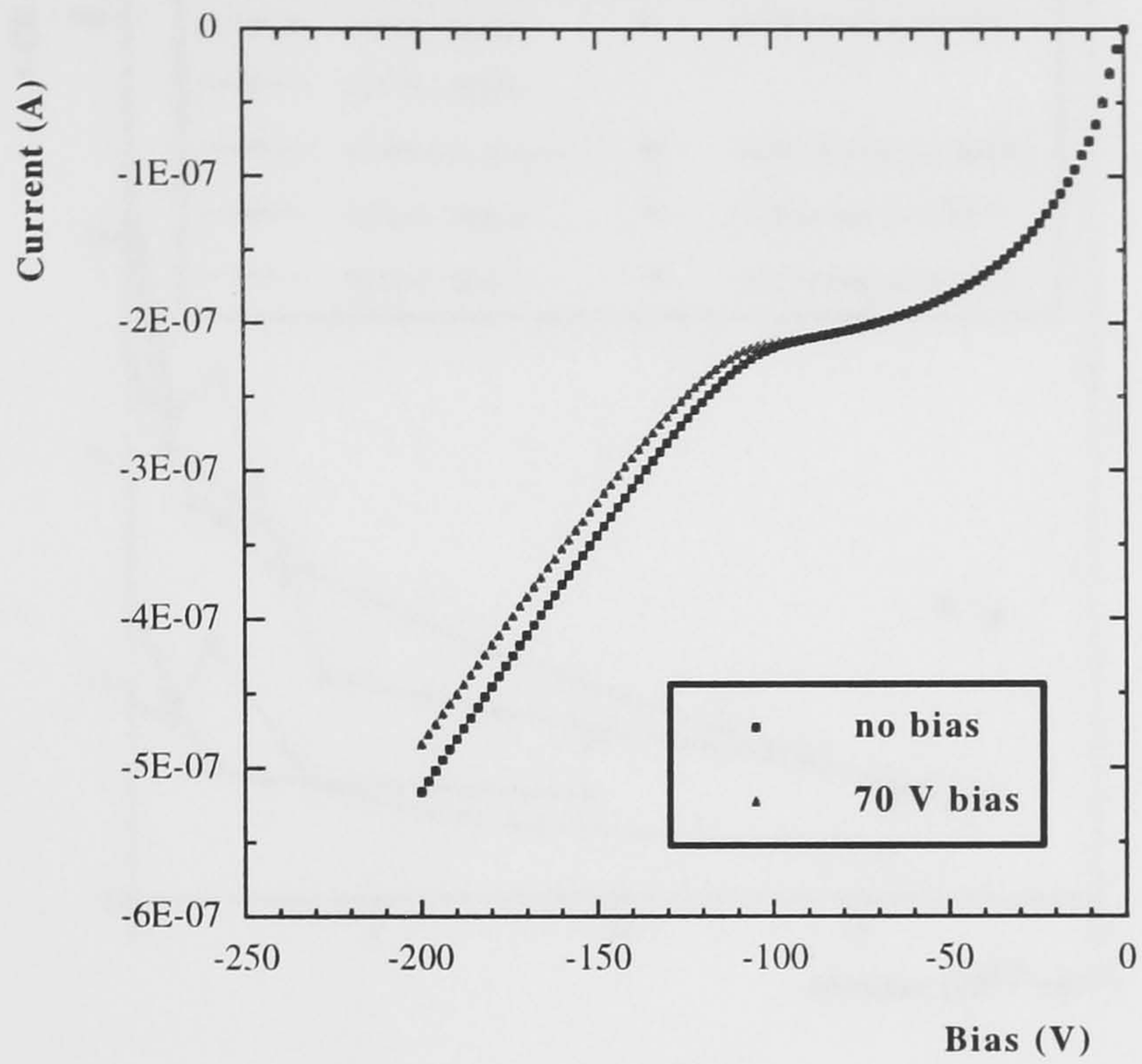

Figure 5.22: Effect of Bias during Irradiation with 10^{14} Protons cm^{-2} for pad detectors G120-1 and G120-8

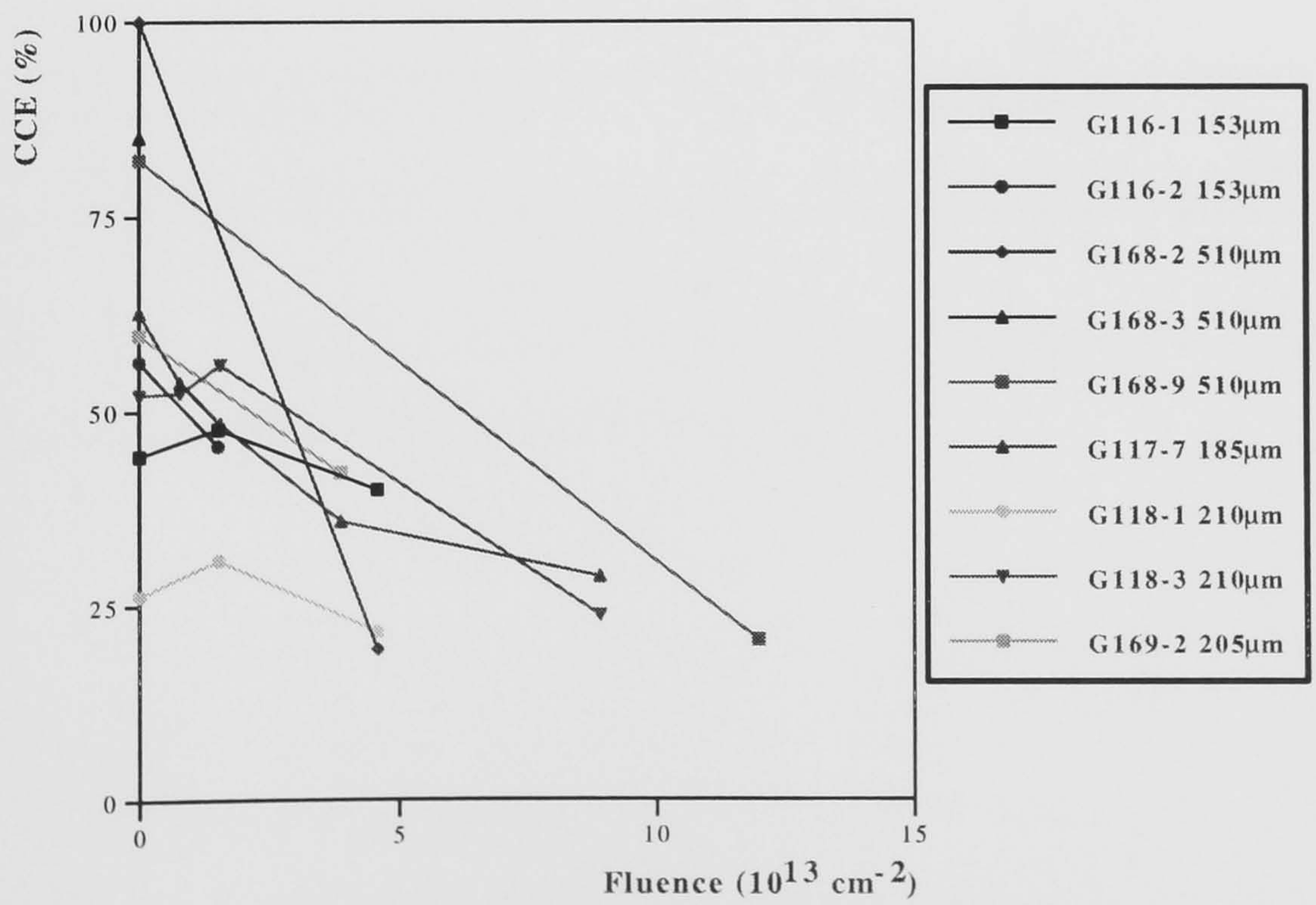

Figure 5.23: Variation of CCE with Proton Dose

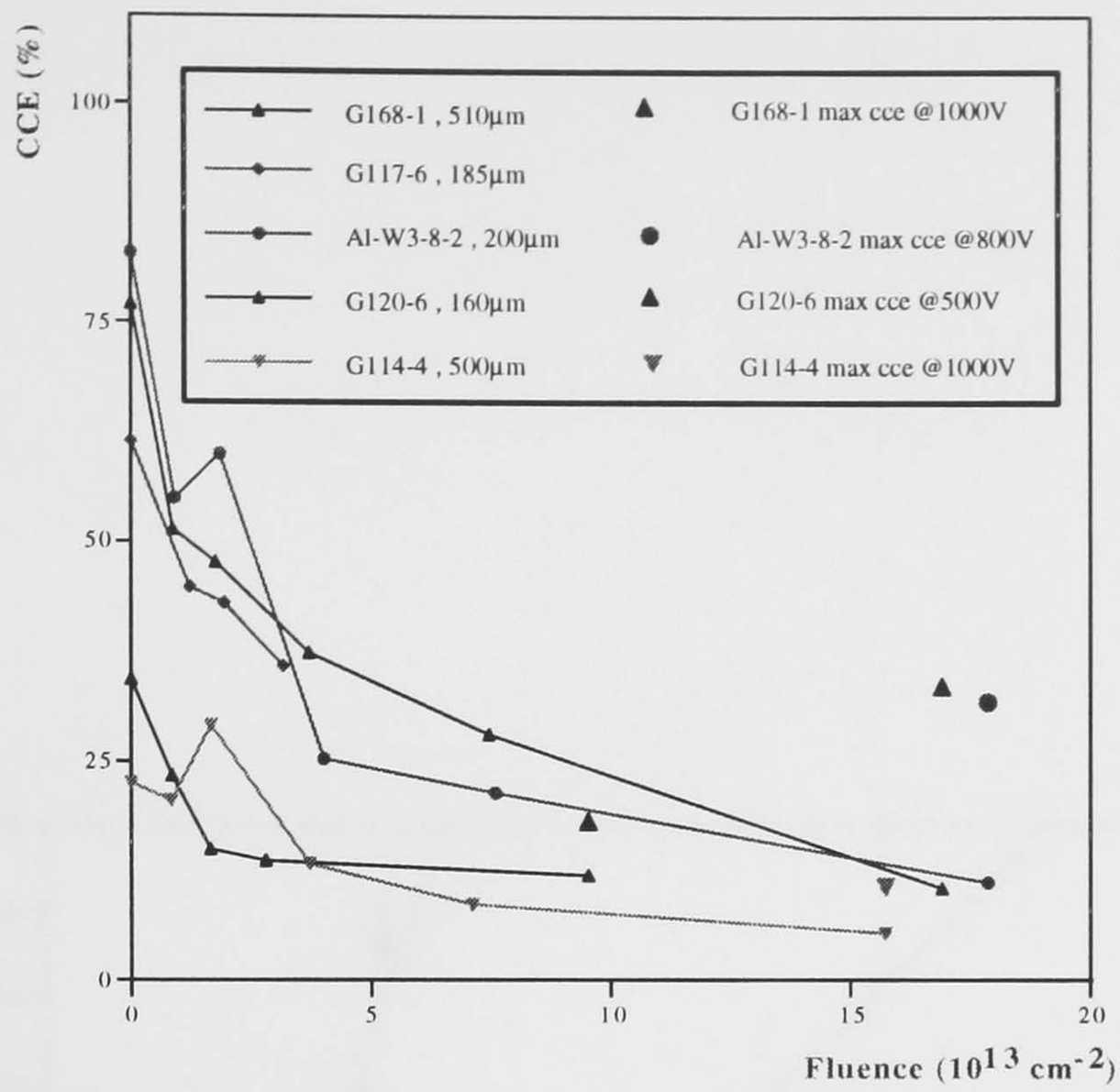

Figure 5.24: Variation of CCE with Pion Dose

are under way as to the nature of the damage and possible practices to repair it.

An indication that it may be possible to repair this damage has already been shown. Flash lamp annealing of an irradiated sample at 450°C for 2 minutes leads to a large recovery in the charge collection efficiency, as shown in Figure 5.25.

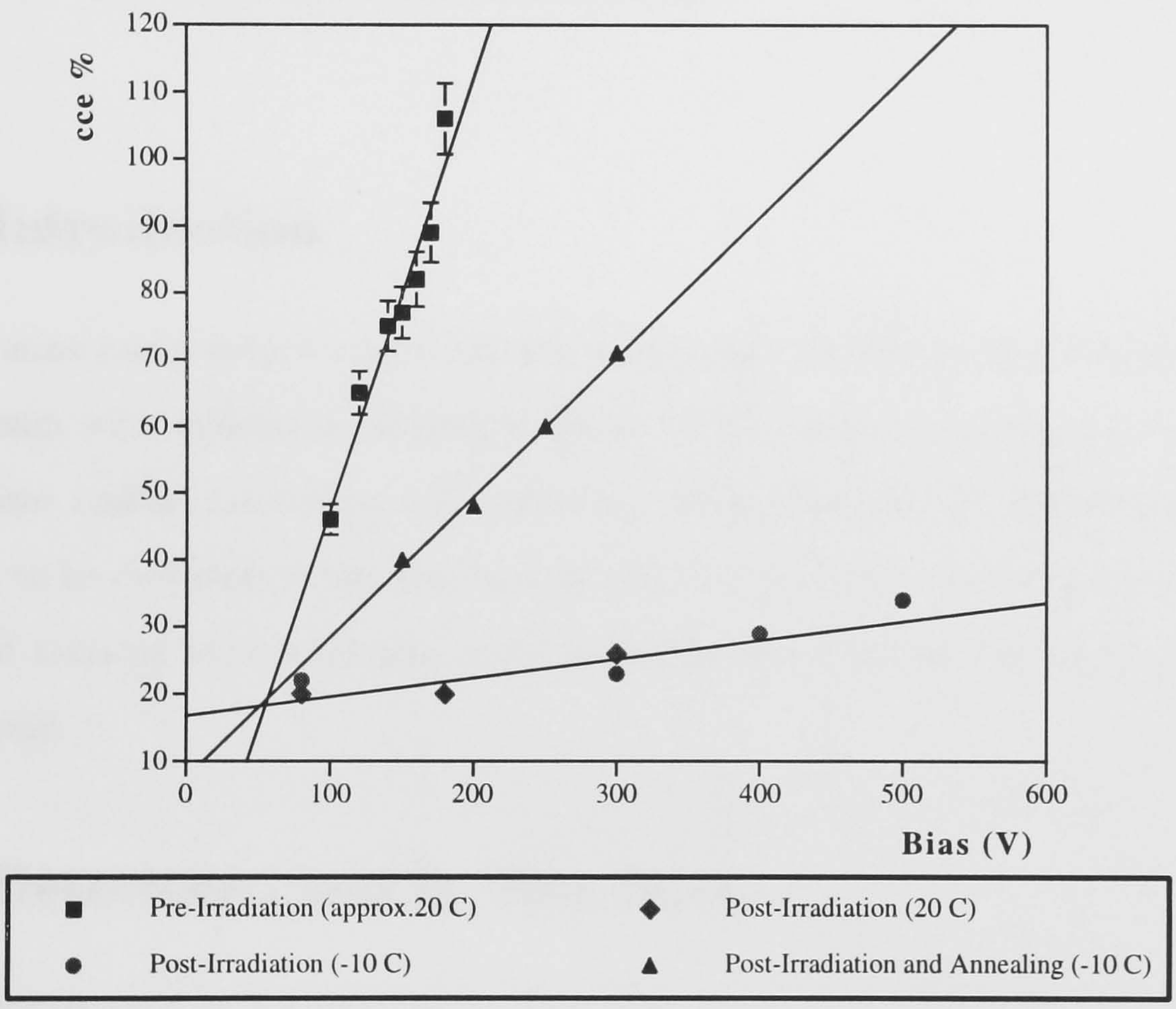

Figure 5.25: CCE vs Bias for G120-6 before and after irradiation of 1.7×10^{14} pions cm^{-2} and flash lamp annealing at 450°C for 2 minutes

Chapter 6

Test Beam Results

6.1 Introduction

To determine many detector performance parameters the detectors must be tested in a test beam with minimum ionising particles. This makes it possible, for example, to measure spatial resolution and detection efficiencies for the minimum ionising particles to be detected in the eventual ATLAS detector and other experiments. The results of tests of microstrip and pixel detectors are given in Sections 6.3 and 6.4 respectively.

6.2 Detectors Used in Test Beam

The detectors used in the test beams were first tested in the laboratory as described in Section 5.4.1.

The microstrip gallium arsenide detector tested was fabricated on a standard, undoped LEC substrate by Alenia SpA, Rome. It had both 50μm pitch and readout. The detector had an integrated, Si_3N_4 dielectric capacitor between two layers of metal, the lower in contact with the substrate and 30μm wide and the upper 20μm wide. A novel biasing scheme was used to keep the detector strips close to zero volts, since the integrated capacitors are only rated to operate with less than 10 volts across them by the manufacturer. The cross-section of a detector and a plan view of the detector are shown in Figure 6.1.

The gap between the biasing strip and the detector strip was 5μm long and 6μm

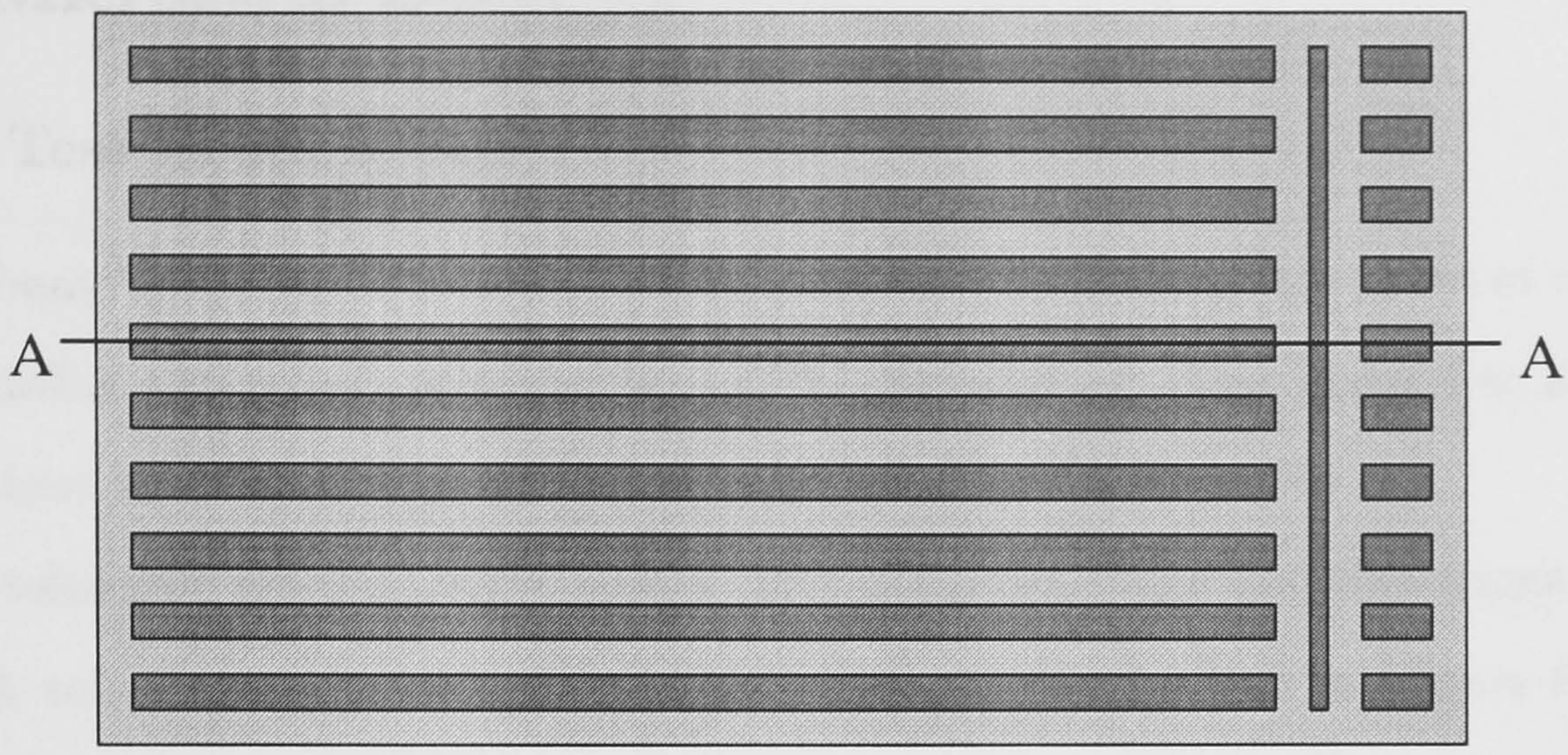

(a) Simplified plan of detector

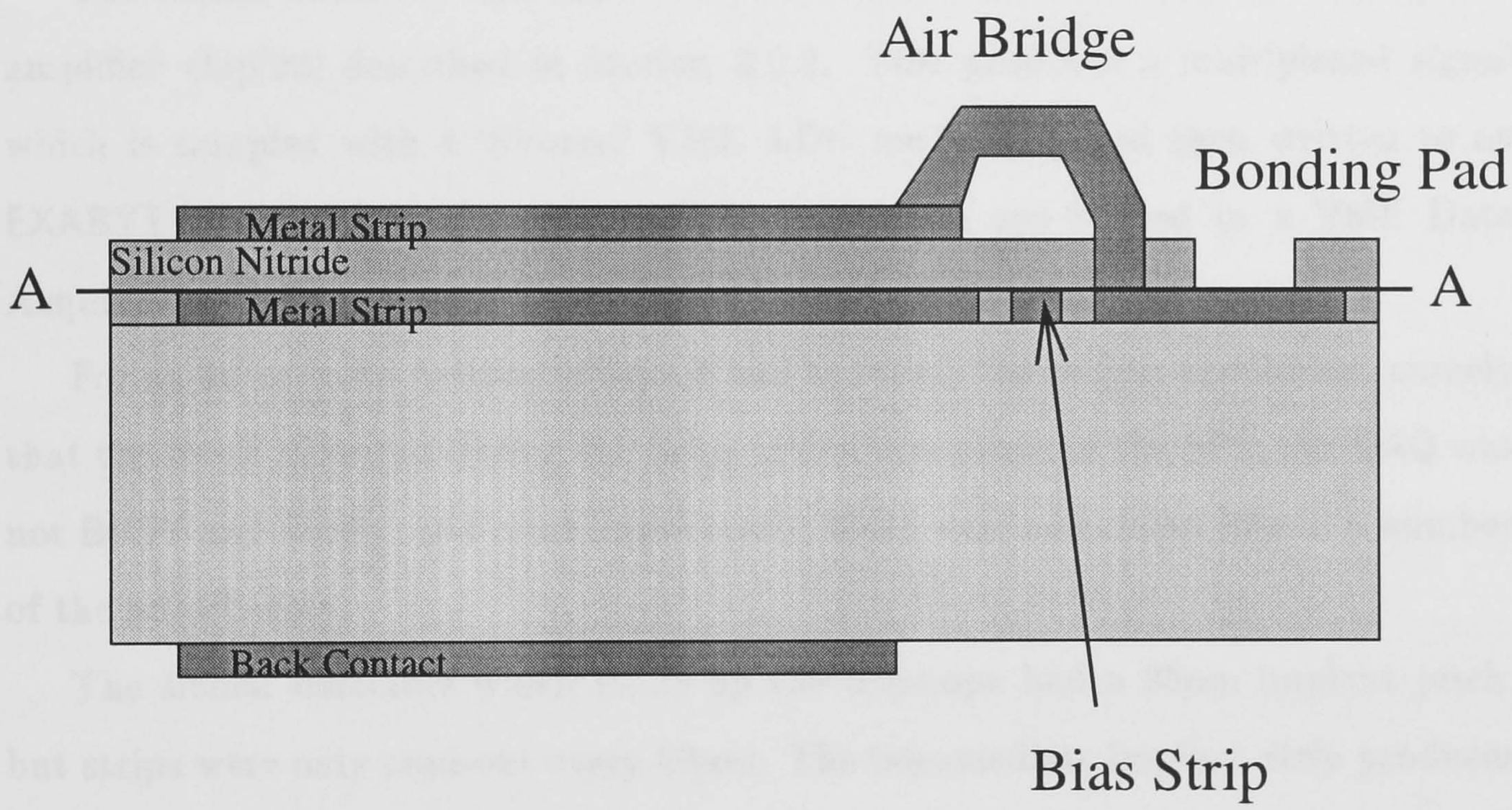

(b) Cross section of detector

Figure 6.1: Representation of an Alenia AC-coupled detector

wide. The thickness of the detector was 200μm.

Several pixel detectors fabricated (using the methods described in Section 5.3) in the Department of Electronic and Electrical Engineering by the author have been "bump bonded" to digital read-out front-end pixel electronics designed at CERN by the ECP [8] division microelectronics group: these have been described in Section 3.3.2. This bonding was carried out at GEC-Marconi Materials Technology (GMMT) at Caswell [36].

6.3 Microstrip Detector

6.3.1 Test Beam Setup

The X1 beam from the SPS at CERN was incident on the telescope (a set of detectors used to define the beam) provided by LEPSI, Strasbourg. This beam was a tertiary beam: pions with an energy of 70GeV were used for the test.

The telescope employs eight silicon microstrip detectors and five trigger scintillators. A schematic representation of the telescope can be seen in Figure 6.2. This system defines the point of intersection of the beam particles with the test detector to a precision of the order of 1μm[69].

The silicon detectors and the test detector were read out with the Viking preamplifier chip[20] described in Section 3.2.2. This produces a multiplexed signal which is sampled with a 'Sirocco' VME ADC module[70] and then written to an EXABYTE tape. The Siroccos and the tape drive are housed in a VME Data Acquisition (DAQ) system. This allowed limited on-line analysis.

For an event to be written to tape it had to satisfy the trigger conditions, namely that the event occurred during the beam extraction phase of the SPS, the DAQ was not BUSY and finally, and most importantly, there were coincident hits in a number of the scintillators.

The silicon detectors which made up the telescope had a 25μm implant pitch, but strips were only read-out every 50μm. The intermediate implant strip produces enhanced resolution between the strips. Each of these detectors was 300μm thick and operated fully depleted at a bias voltage of 50V.

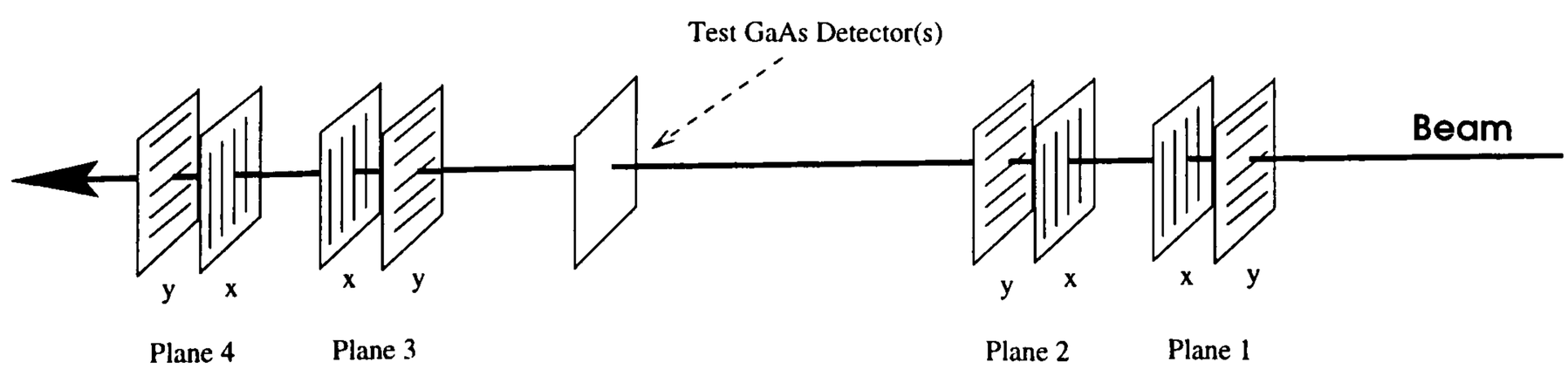

Figure 6.2: Strasbourg Telescope Layout

6.3.2 Off-line Analysis

The off-line analysis consists of two separate programs. The first program reads in the RAW data. The first 100 events are used to determine the pedestal levels of the data and the next 100 the noise. The pedestal and noise are stored on a channel by channel basis. The pedestal is the average value from the ADC and the noise is the root mean square of the ADC values after pedestal subtraction. This program also allows for a group of pedestals shifting coherently in what is known as Common Mode Shift(CMS). The groups of channels considered for CMS are one chip and a quarter chip which contain 128 and 32 channels, respectively.

After the initialisation phase the noise and pedestal values are continuously updated. This is done by multiplying the old value by a number (eg. 50) and adding the new value, then dividing by the number plus one. The larger this number the stronger the memory of the system. Increasing the memory will reduce the effect of signals from actual hits which are treated as noise because they fall below the $\frac{S}{N}$ cut, defined in detail below, where S is the signal, namely the ADC value with the pedestal subtracted, and N is the noise. The remaining data are then scanned for clusters.

A cluster is found if the $\frac{S}{N}$ value for any strip is above a certain value. A search is then made with a lower $\frac{S}{N}$ cut for any hits on adjacent strips . If found, these determine the width of the cluster; the cluster total signal and noise are then calculated using equations 6.1 and 6.2.

$$S = \Sigma S_{strip} \tag{6.1}$$

$$N = \sqrt{\frac{\Sigma N_{strip}^2}{\#strips}} \tag{6.2}$$

These cuts for the different detectors are tabulated in Table 6.1.

If the cluster is wider than a single strip, its η value is evaluated using equation 6.3. This is used to enhance the resolution using a non-linear charge sharing algorithm.

Cut Type	Si	GaAs
Centre Strip	4	3
Neighbour	2	1.5
Whole Cluster	4	3

Table 6.1: $\frac{S}{N}$ cuts used in offline analysis for silicon and gallium arsenide microstrip detectors

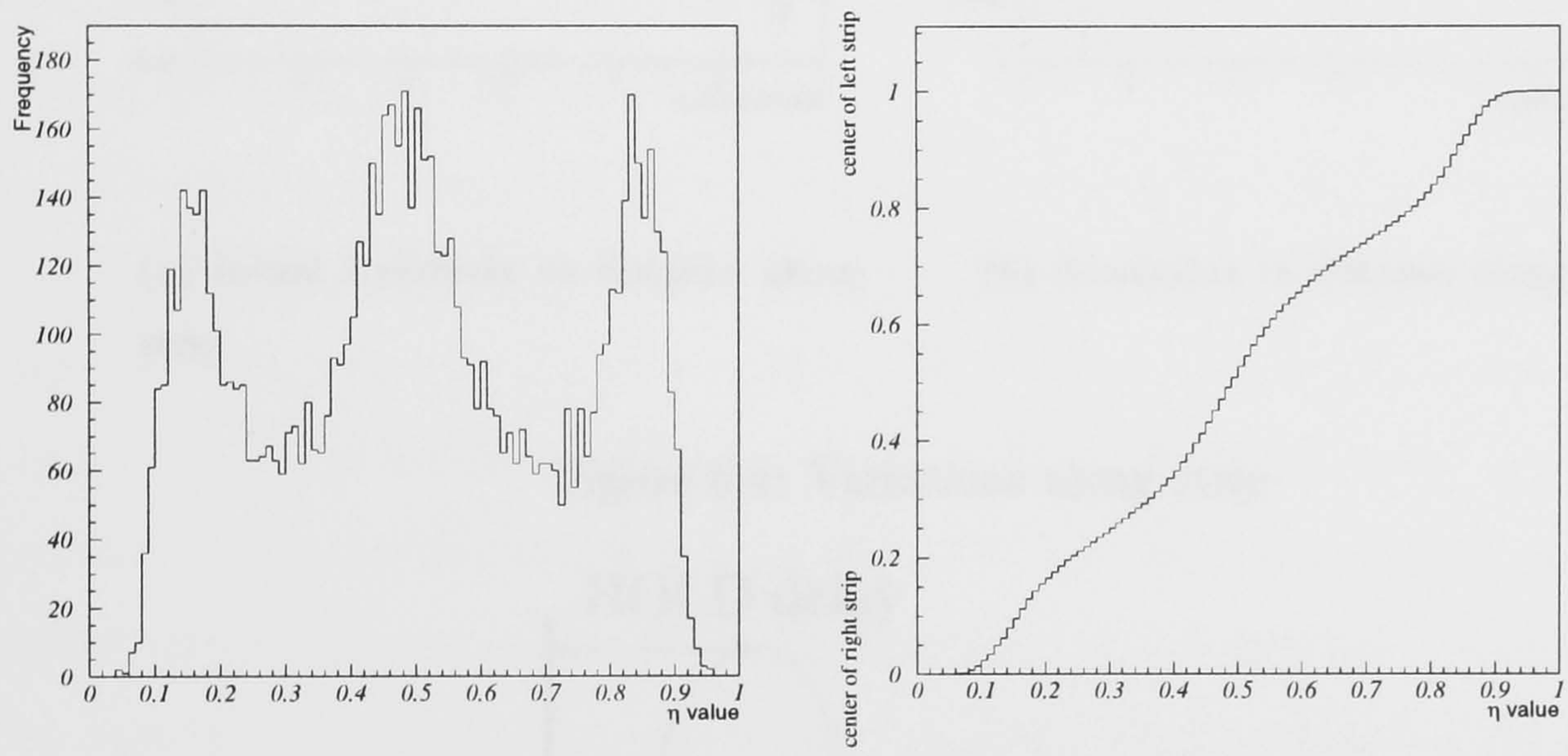

(a) η distribution (b) Integrated η distribution

Figure 6.3: η distributions in a silicon detector

$$\eta = \frac{S_L}{S_L + S_R} \tag{6.3}$$

In this equation $S_L(S_R)$ is the signal on the left(right) of the two maximum pulse height strips of a cluster. A typical η distribution from a silicon detector is shown in Figure 6.3(a).

By integrating the η distribution we define a look-up table for the position of a hit between the two strips. The integrated distribution is shown in Figure 6.3(b).

The cluster information is then written to a DST file together with the pulse height and noise values for the five strips on either side of the cluster centre.

This file is then read in by the track fitting program. It uses the hits in the DST file to determine the relative alignment of the detectors. Firstly, the telescope is self-aligned with its origin at the centre of the first detectors. Next the test detectors

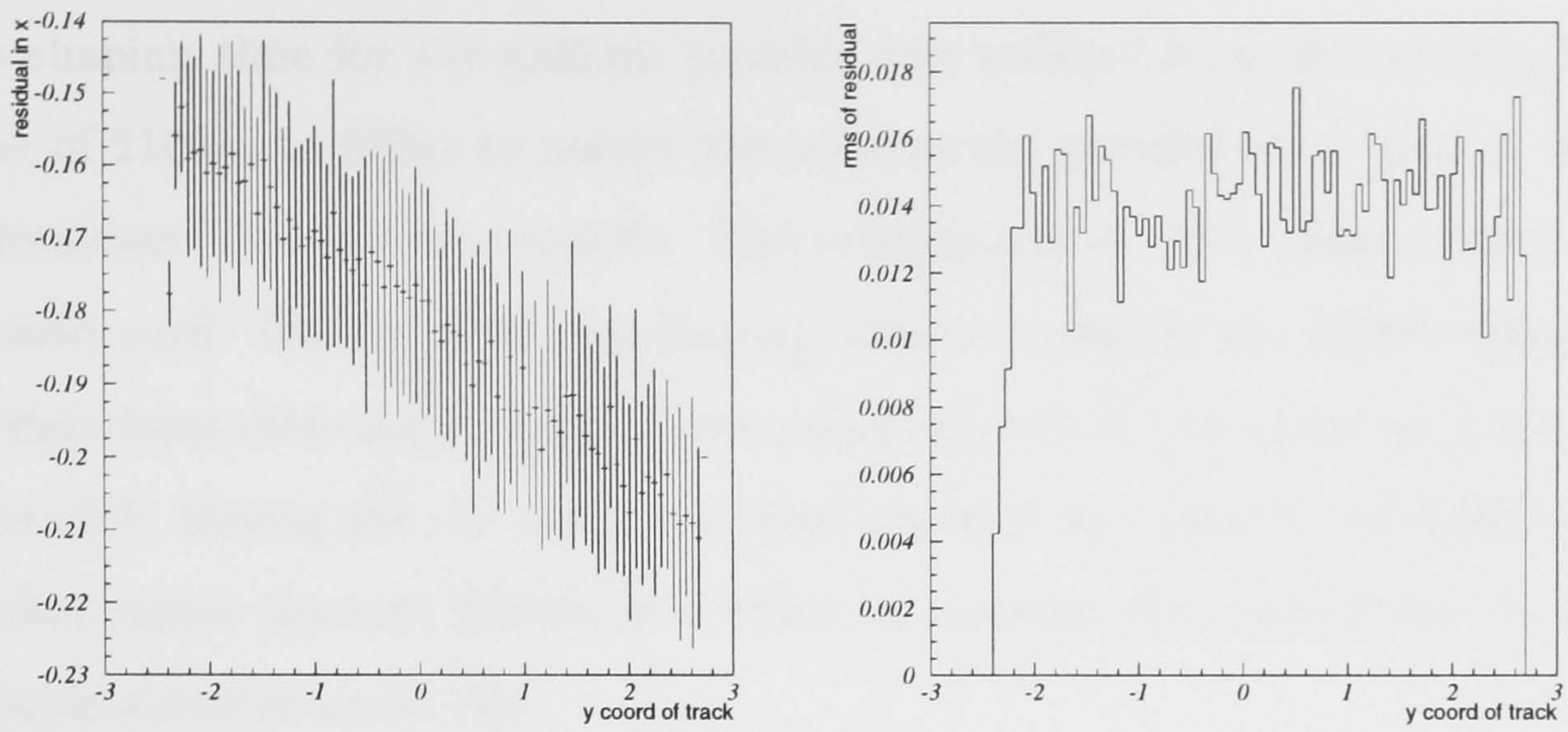

(a) Initial Residuals vs distance along strip

(b) Resolution vs distance along strip

Figure 6.4: Variations along strip

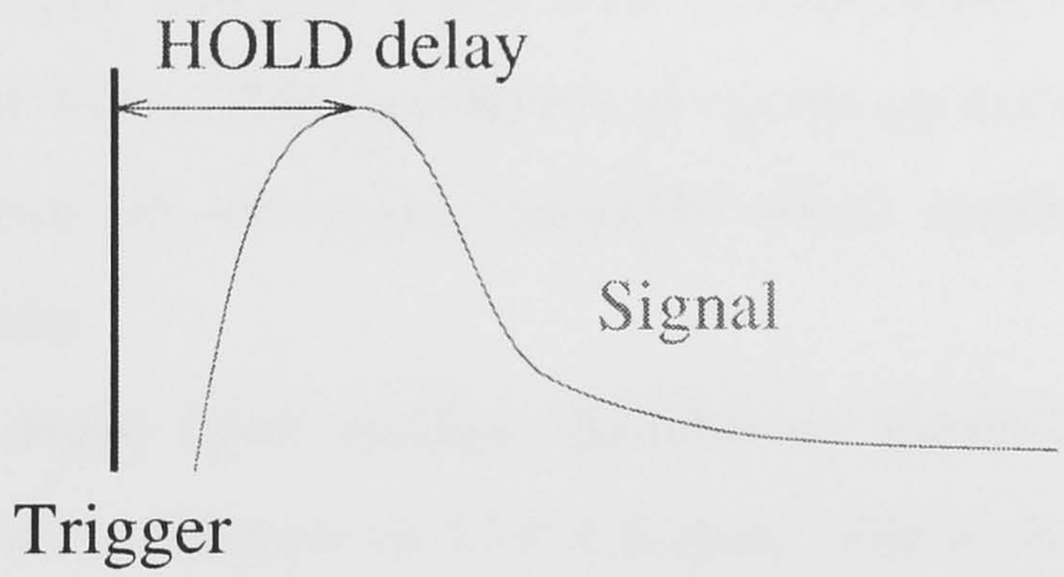

Figure 6.5: HOLD delay

are aligned in this reference frame. The first stage is carried out by centring the residual plot for the detector around zero. Then, to allow for the strips not being orthogonal to the reference frame, the residual in the detector is plotted against the position along the strip. This plot is shown in Figure 6.4(a). A linear fit is made to the data and the hits rotated to align the strips with the reference frame.

After this is complete the detector position along the beam line is adjusted so that the width of the residual distribution is minimised. The detector is then rotated by a small angle about an axis running through the central strip of the detector and the width of the residuals minimised again.

6.3.3 Results

The shaping time for the gallium arsenide was reduced from the standard silicon value of 2100ns to 680ns to reduce the noise as the parallel noise term is expected to dominate with gallium arsenide. This is implemented by a potentiometer on the repeater card. On the DAQ this shaping time is stored as the HOLD delay and is the time from receiving a trigger to the expected peak in the signal, as illustrated in Figure 6.5. During the test beam run there was only one value for all detectors: this number varied between 1000ns and 680ns to optimise the readout for the gallium arsenide detector under test.

The equivalent noise charge was measured to be $2000e^-$, to be compared with the expected $400e^-$ (cf Section 3.2.2[20]). The signal-to-noise from the data in all cases was very close to 6 (see Figure 6.6(b)). The signal was therefore $12000e^-$, which implies a charge collection efficiency(CCE) of 46%. This is in good agreement with tests made on pad diodes which have 60% CCE, but operating at 200V as opposed to 180V used in the test beam. The pad detectors can be operated at a higher voltage as they do not require the decoupling capacitor which requires a voltage of -20V across the biasing strip.

The rms of the fitted track residual distribution shown in Figure 6.6(c) corresponds to a detector resolution of $14.0 \pm 0.2\mu$m. Figure 6.4(b) shows that this is constant along the length of the strips. This compares well with the expected resolution from binary read out, that is without charge-sharing information, as given by equation 6.4.

$$\frac{pitch}{\sqrt{12}} = 14.43\mu m \tag{6.4}$$

Using only clusters with a width of two or more strips, the resolution improves to approximately 12μm. 50% of events have clusters of more than one strip, which is slightly more than expected from the gap to metal width ratio, indicating that a proportion are due to noise.

The detection efficiency at the shortest HOLD delay time was 47%. This was the highest value obtained. Various investigations were carried out on the data in an attempt to determine the source of this poor performance. A search was made

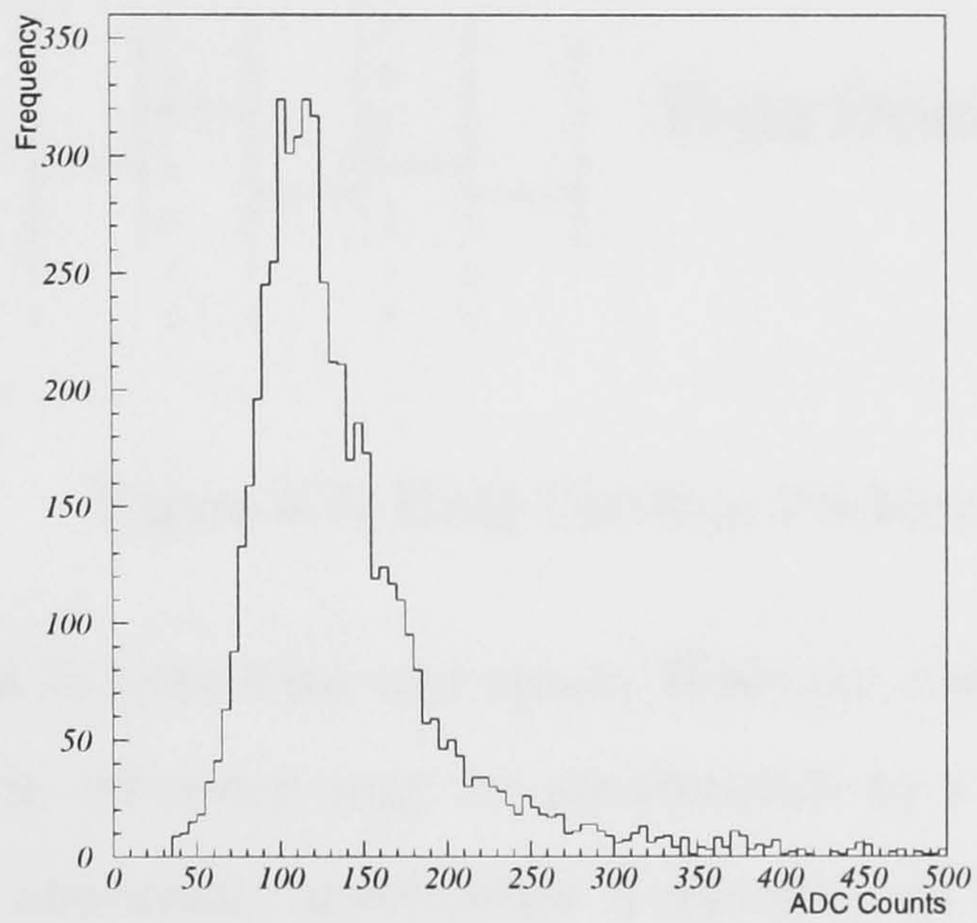

(a) Landau Distribution

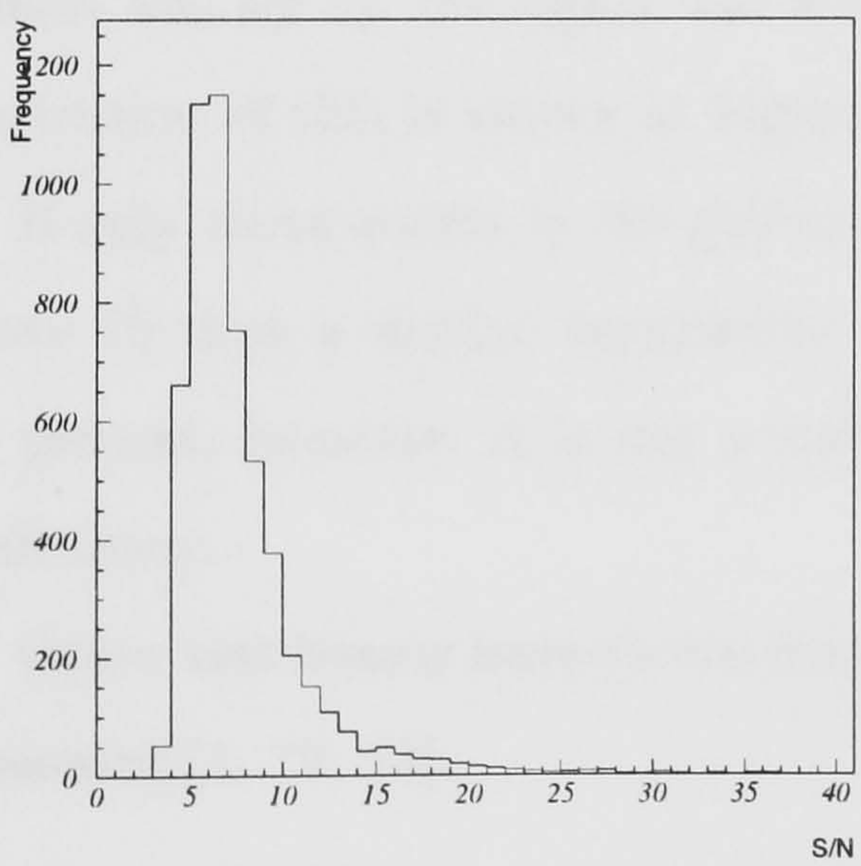

(b) $\frac{S}{N}$ Distribution

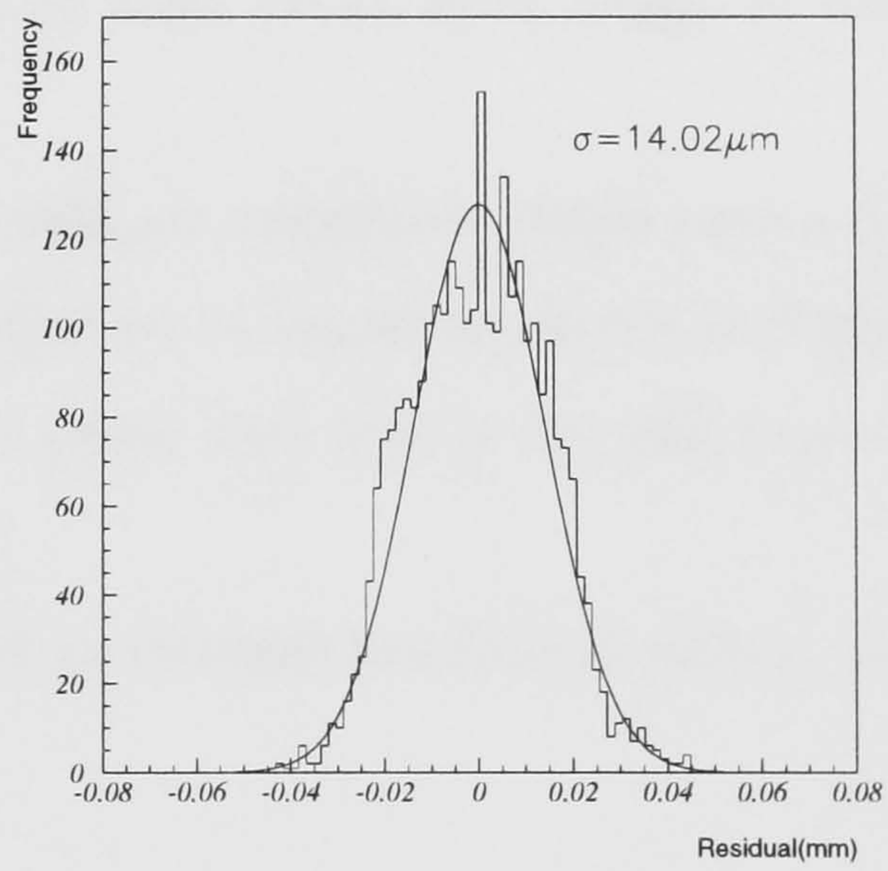

(c) Residual Distribution

Figure 6.6: Results for detector AL-W3-6AC

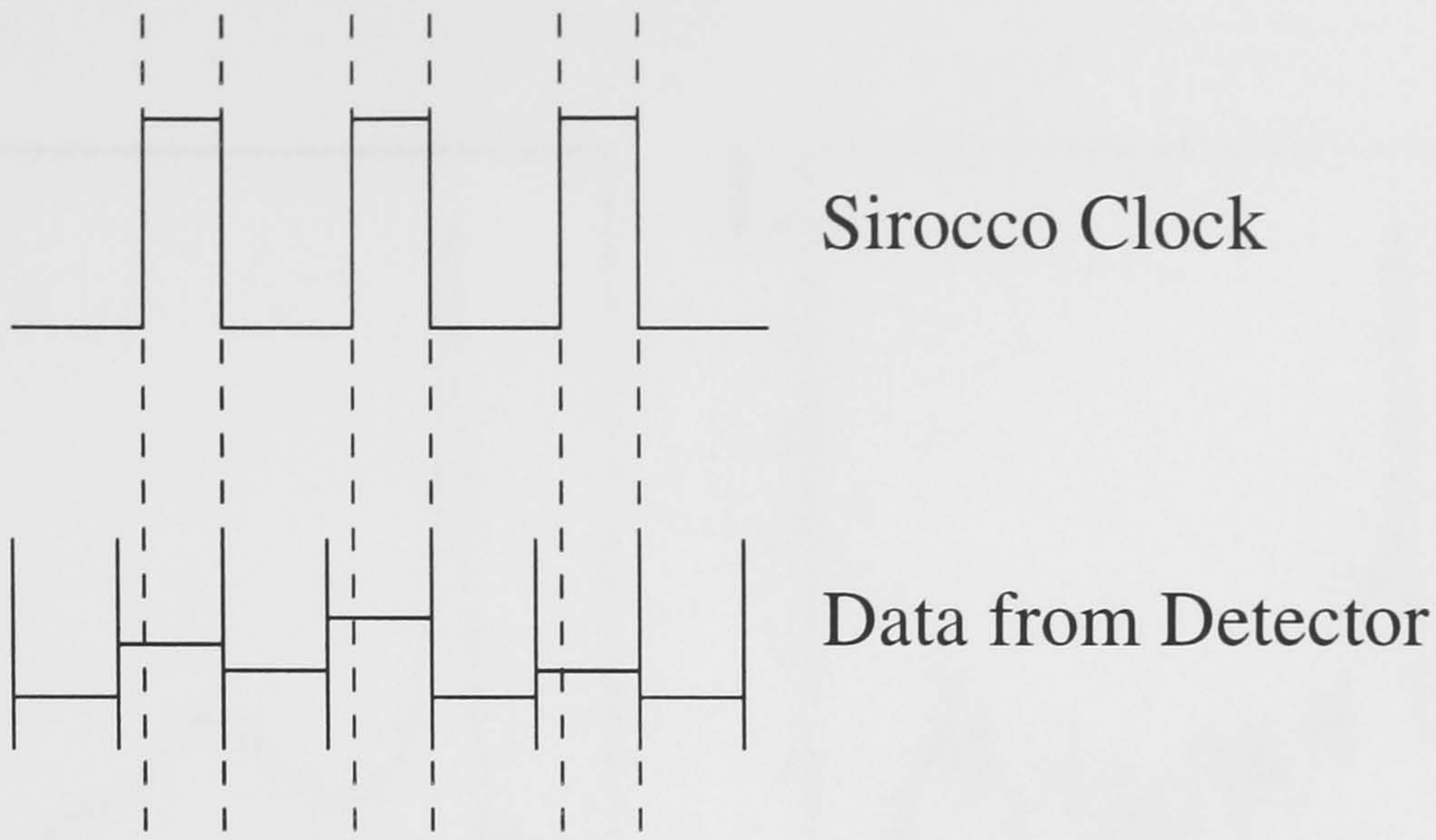

Figure 6.7: DAQ Clocking Problem

for inefficient regions in both time and space. However, none was found.

The low detection efficiency may be attributable to a problem with the DAQ which produced an abnormal, asymmetric η distribution for the silicon detectors of the telescope which had been normal before the test beam run. This could be produced by an observed problem with the clock signal used to inform the Siroccos to sample. The Siroccos sample every time this signal changes state, but when the system was set up the signal was not in each state for an equal length of time. An illustration of this is shown in Figure 6.7.

If only those events in the gallium arsenide are considered which have a $\frac{S}{N}$ value above 10 then a similar asymmetric distribution is found, as shown in Figure 6.8. At present, however, it is not possible to prove that this is the sole cause of the inefficiency.

Other test beams have shown this is not an intrinsic property of gallium arsenide detectors[71, 72, 73].

6.3.4 Simulation

To investigate other possible reasons for the poor detection efficiency, a computer simulation was carried out. The simulation program generated data in the same RAW format produced by the DAQ system, thus serving also as a test of our use of the software.

In the simulation, charge sharing is assumed to be linear in all detectors. The

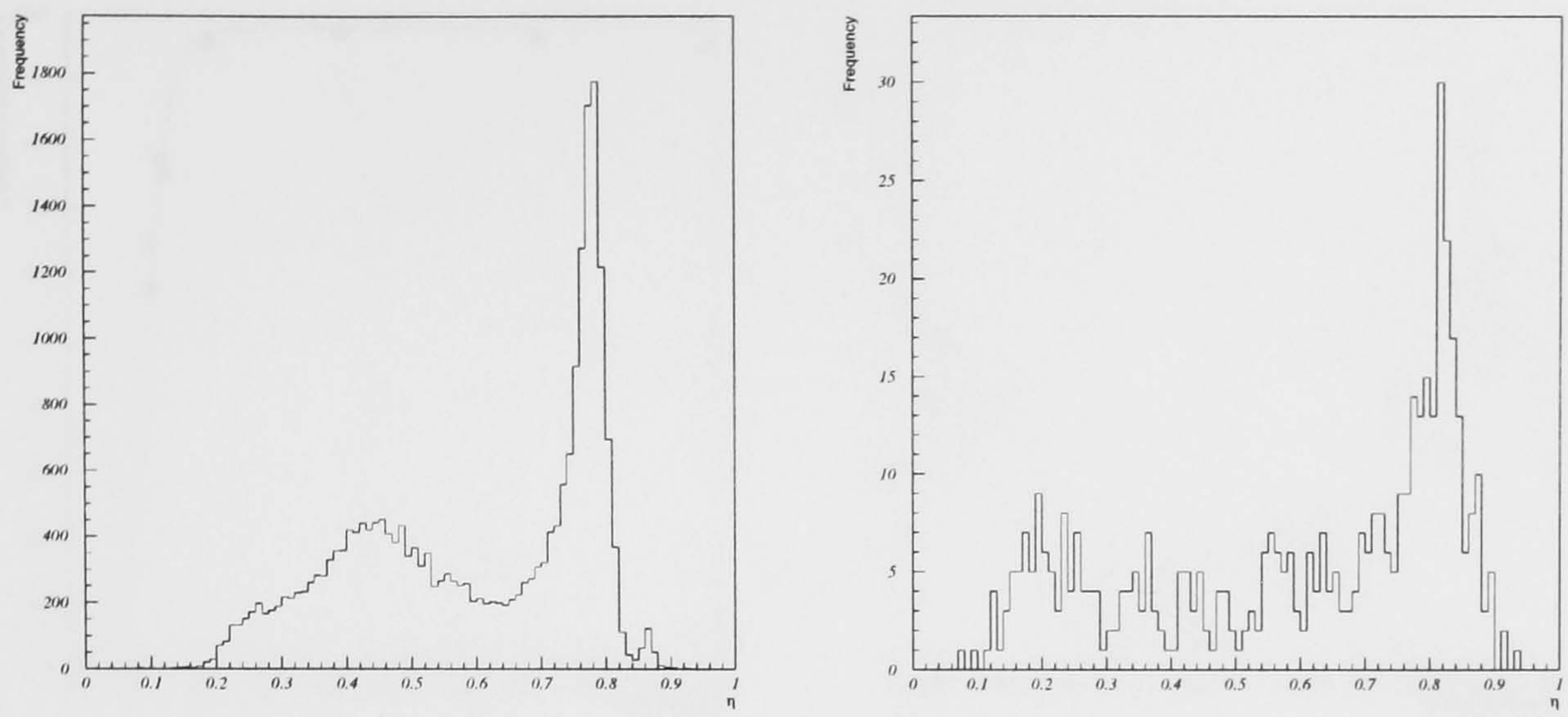

(a) η distribution in Silicon

(b) η distribution in gallium arsenide for $\frac{S}{N} > 10$

Figure 6.8: Asymmetric η distributions in test beam

charge deposited by a particle, determined from a function which produces a Landau distribution of signals, is shared between two strips. Once this sharing has been done, Gaussian noise is added to all strips.

The resulting $\frac{S}{N}$ is shown in Figure 6.9(a). It appears that, for a $\frac{S}{N}$ value below approximately ten, the detection efficiency drops dramatically. This is due to the charge sharing dividing the signal and a conspiracy of noise and Landau fluctuations pushing the signal below the threshold of $3\sigma_{(\frac{S}{N})}$.

The effect would be expected to occur more readily toward the centre of the gap between the strips, as observed in the simulation (shown in Figure 6.9(b)), however this effect was not observed in the actual data.

6.3.5 Conclusion

The noise observed in the test beam data and with the detector in the laboratory is over 5 times greater than expected. The source of this excess noise is currently under investigation by other members of the group.

By reducing the noise both resolution and detection efficiency will improve. The lack of resolution attainable with a given η algorithm is proportional to $\frac{N}{S}$ [74]. As seen in Figure 6.9(a), once the $\frac{S}{N} > 10$ detection efficiency should not be a problem.

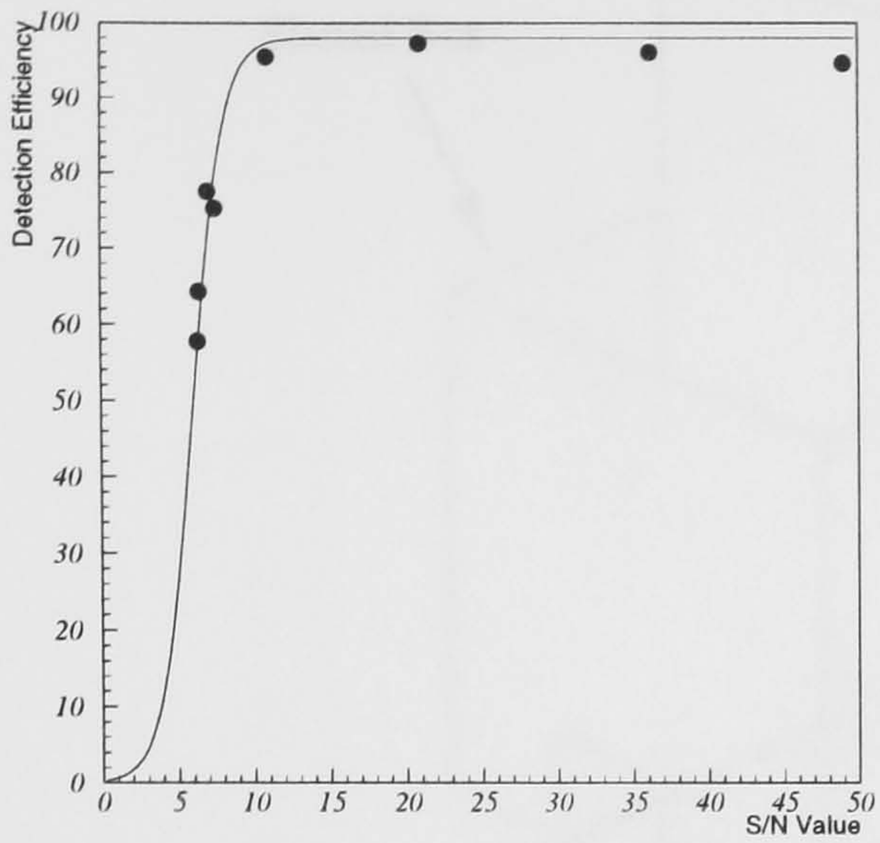

(a) Graph of $\frac{S}{N}$ and Detection Efficiency

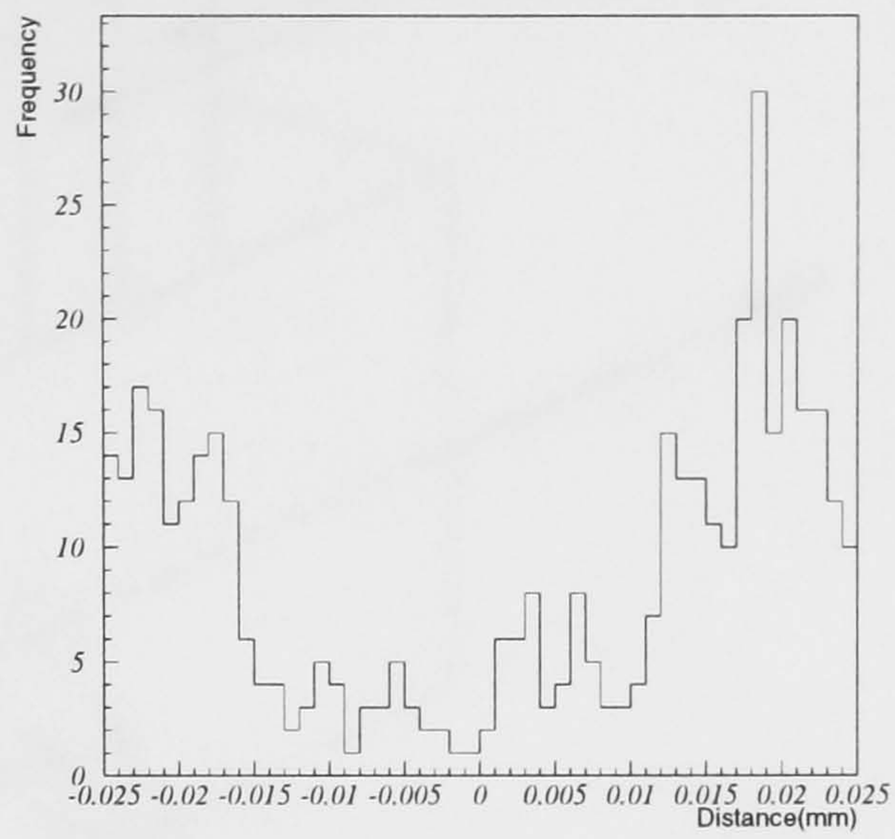

(b) Distribution of hits not seen wrt centre of strip

Figure 6.9: Results of test beam simulation

6.4 Pixel Detector

6.4.1 Test Beam Setup

The tests were made in the H6 test beam at CERN with a pion beam, using scintillators in coincidence and another with a hole - to supply a veto - as the trigger. The detector under test was placed in a slatted box equidistant from two silicon pixel detectors with similar read-out. Figure 6.10 depicts the setup used. We therefore had three planes of pixels constituting a pixel telescope.

The DAQ for this test beam was a Macintosh computer which ran a program written solely to read-out the Omega electronics. The DAQ software that was used displayed a selection of the events as they were acquired. It overlayed the three planes using a different colour for each plane or combination of planes.

Once the data had been acquired they were transferred to a VAX computer for analysis by a simple FORTRAN program (originally written by Peter Middelkamp).

6.4.2 Detection Efficiency

Following initial characterisation of the gallium arsenide pixel detector in Glasgow the detector telescope was tested in the H6 beam at CERN by M. Campbell and

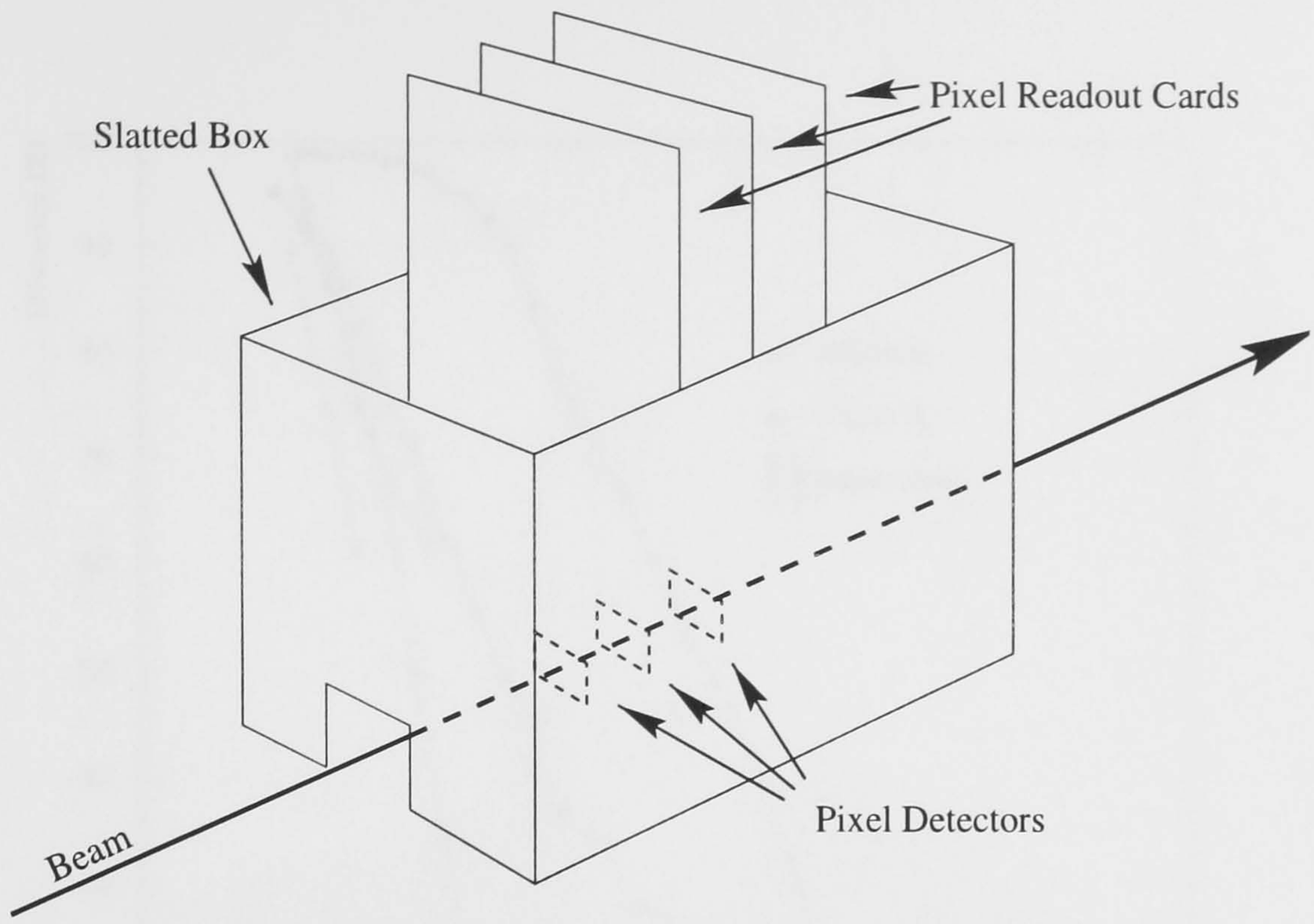

Figure 6.10: Pixel Detector Telescope Setup

C. da Via of the ECP division. For the runs described here a 110 GeV pion beam was used. Although the test proved to be generally successful, the gallium arsenide detector detection efficiency, defined as the number of hits observed in the gallium arsenide detector to the number of coincident hits in a reference silicon telescope apparently only reached 75%. From discriminator threshold scans, it seemed that the events were only generating charge signals of around 7000 electrons per minimum ionising particle.

Further testing was then carried out in Glasgow by Mr Kenneth Wyllie and the author which are described in Section 5.4.1.

At first the problem of reduced efficiency was thought to be due to a dead region between pixels where charge would not be efficiently collected. This area amounts to 30% of the total pixellated area. More recent measurements, however, have identified a problem with the particular read-out chip used which explains the difference in behaviour.

Subsequently a discriminator threshold scan was carried out, again in the H6 beam at CERN, for three 200μm thick gallium arsenide pixel devices. These are shown with the responses of 150μm and a 300μm thick silicon detectors for comparison in Figure 6.11, which illustrates how the detection efficiency varies when the size of signal required, (ie the comparator threshold), is increased. The gallium

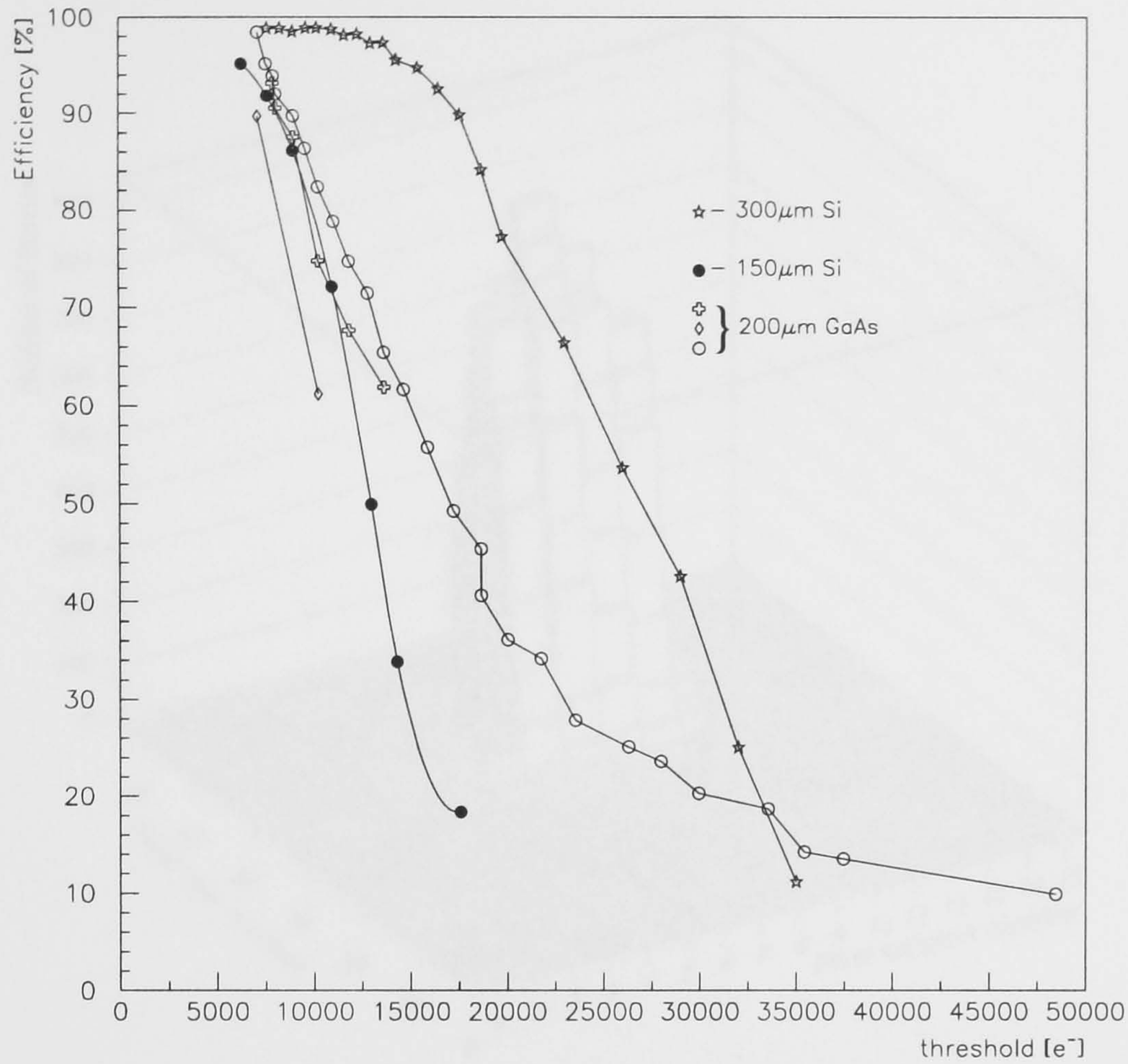

Figure 6.11: Detection efficiency versus discriminator threshold

arsenide results are highly satisfactory although the number of electrons collected is still below the expected value. There is no long plateau in the gallium arsenide curve due the broadening of the Landau distribution caused by the higher noise.

A beam profile from the gallium arsenide detector alone can be seen in Figure 6.12. A similar plot in Figure 6.13 contains only hits that are part of a track constructed from all telescope planes.

Compared to Figure 6.13, some additional events can be seen in Figure 6.12 due to interactions in the material of the first plane. This type of event is also observed in the on-line display.

6.4.3 Conclusion

This pixel test beam has shown for the first time the promise of gallium arsenide pixel detectors. The detection efficiency has been demonstrated to be close to 100%.

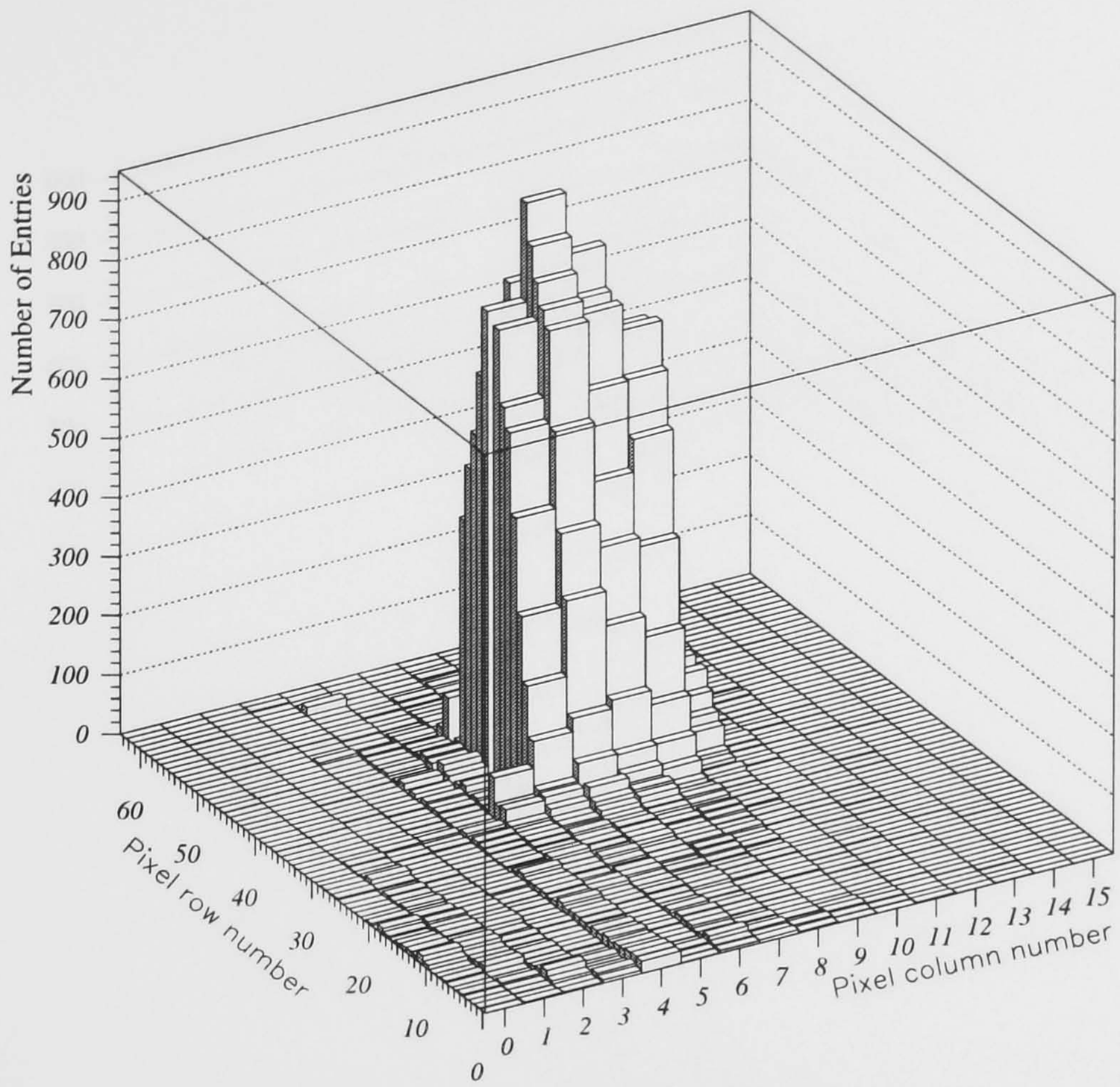

Figure 6.12: Beam profile in GaAs Pixel Detector

6.4.4 GaAs Pixel Telescope

A further test beam run carried out in 1995 implemented a three detector gallium arsenide pixel telescope. The setup was similar to the 1994 test beam of Section 6.4.1 but with a larger distance (5cm) between the planes. The beam profiles obtained in a preliminary analysis for each of the three planes are shown in Figure 6.14.

A single event is shown in Figure 6.15. In this event an interaction has occurred in the first plane resulting in two or three tracks in the second and third planes. This type of event displays the benefit of pixel detectors over strips: by providing two co-ordinates for hits, pattern recognition becomes much easier.

6.5 Overall Conclusions

Currently under investigation are non-injecting ohmic contacts which will enable detectors to be more easily "over-depleted". A higher bias voltage will increase the

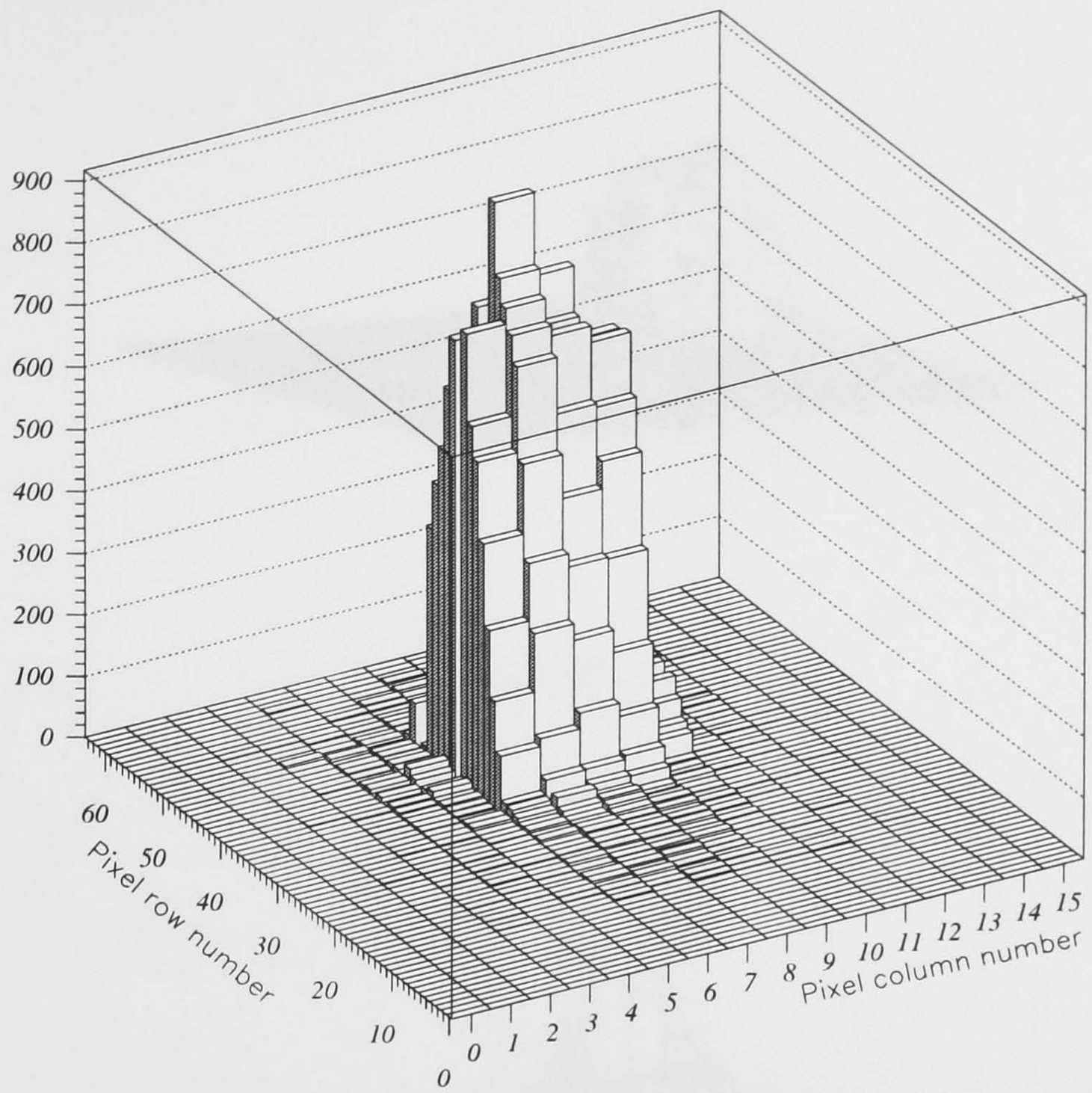

Figure 6.13: Hits in GaAs which are part of a reconstructed track

charge collection efficiency of the detectors and hence the signal produced.

Further studies beyond those reported here will include varying the microstrip detector gap/metal width ratio, evaluation of the response at lower temperatures and of a "keystone" strip detector geometry. In increasing the gap width for a given pitch in microstrip detectors the signal will decrease, (due to the poorer field), but the spatial resolution should improve. Since irradiated silicon detectors require an operating temperature of -10°C to prevent reverse annealing the gallium arsenide response at these temperatures needs to be checked. It is planned to use detectors with keystone geometry in the ATLAS forward region so detectors must be fabricated in this design to prove their viability and their ability to withstand non-uniform irradiation across their length in this high radiation environment.

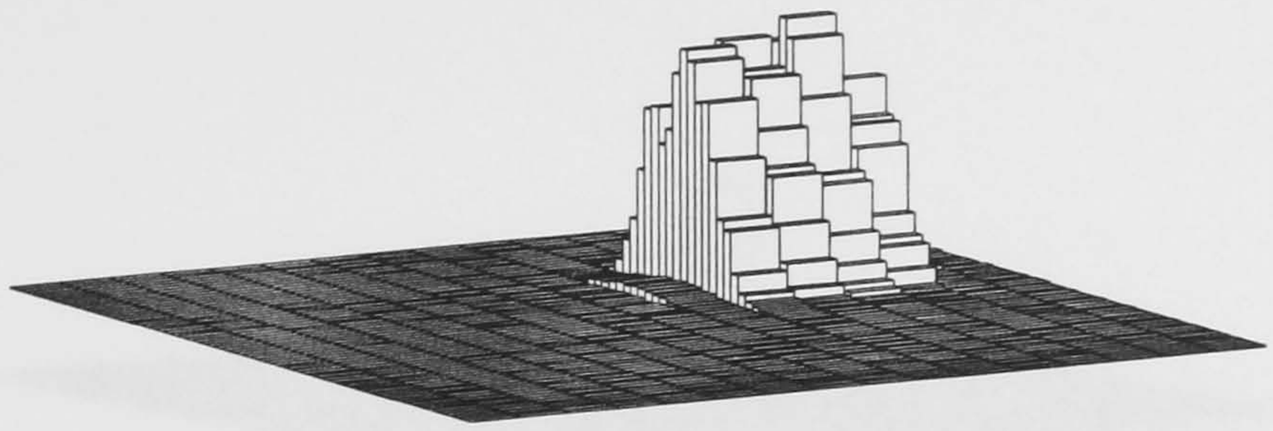

(a) Plane 0

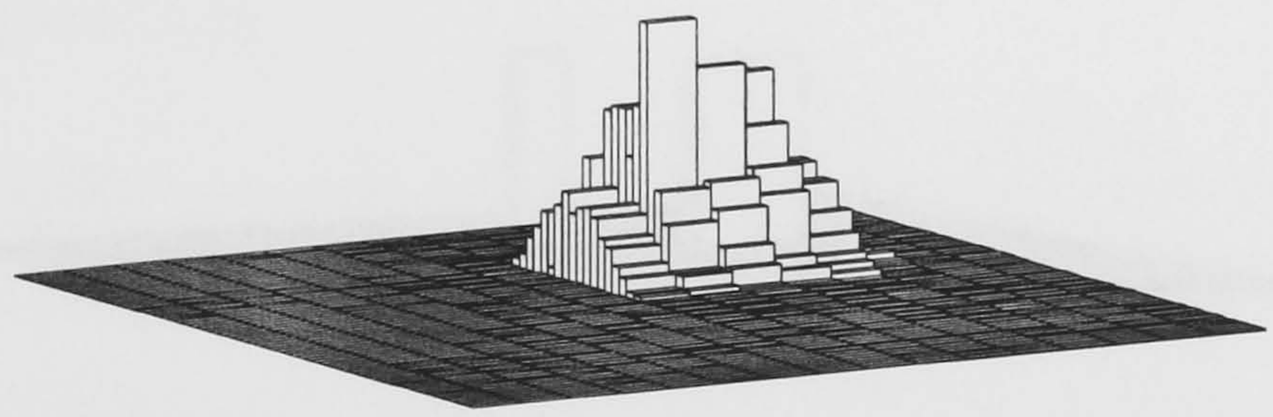

(b) Plane 1

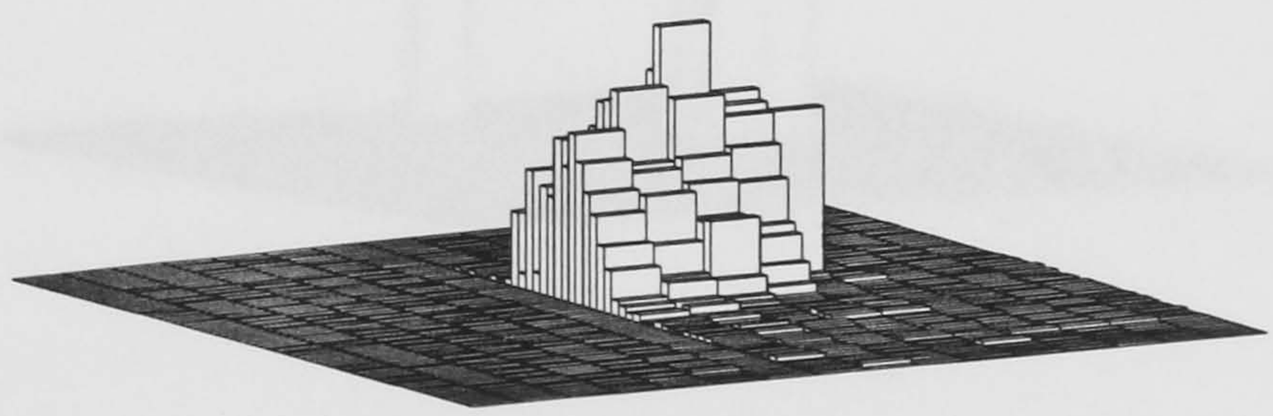

(c) Plane 2

Figure 6.14: Beam profiles in gallium arsenide pixel telescope

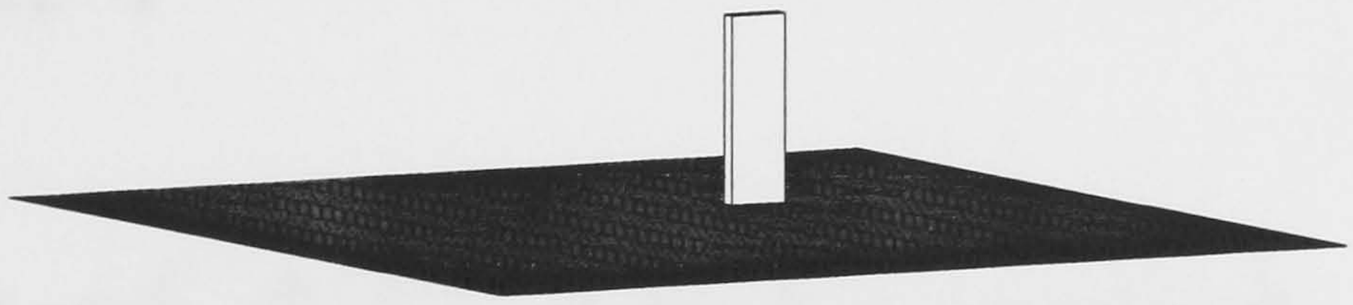

(a) Plane 0

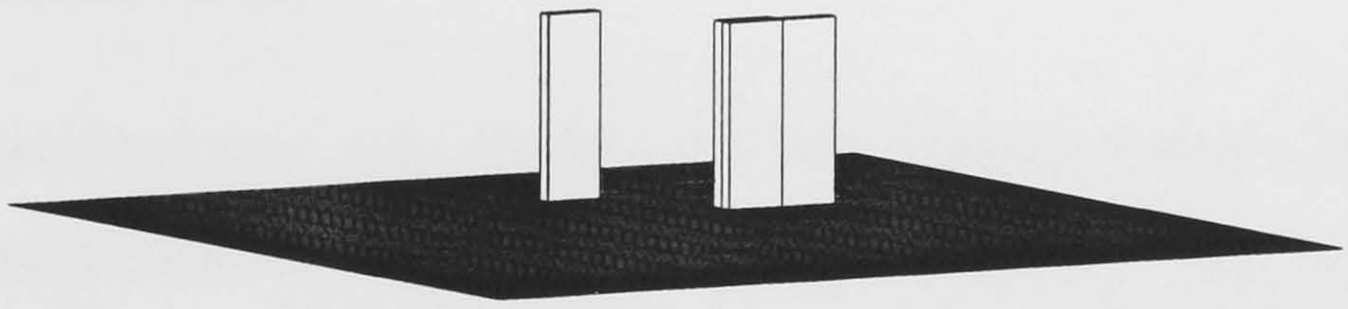

(b) Plane 1

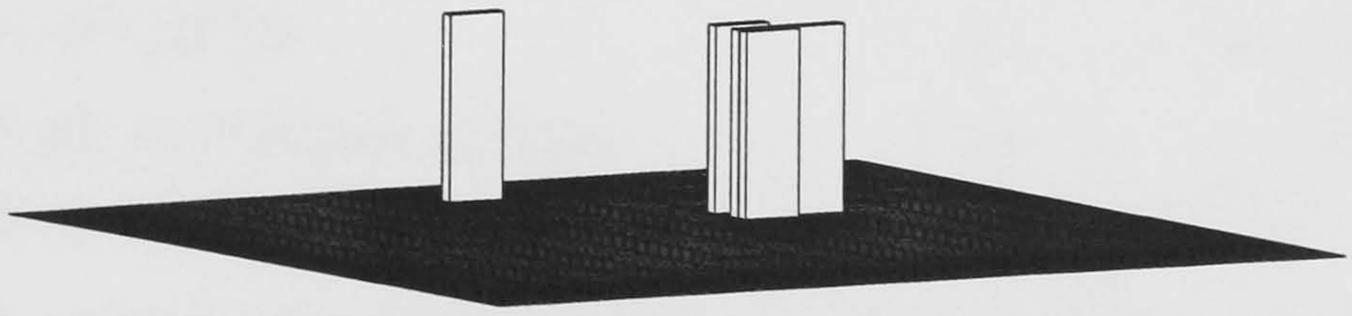

(c) Plane 2

Figure 6.15: Single event in gallium arsenide pixel telescope

Chapter 7

Study of ATLAS Forward Region

7.1 Introduction

ATLAS is a multipurpose experiment to study various aspects of the Standard Model. The major goal is to explore the origin of mass. This is thought to be provided by the Higgs mechanism. If this is the case a Higgs boson should be observable at ATLAS. The particle has different predicted decay modes depending on its mass.

$H \rightarrow b\bar{b}$	80	$<$	m_H	$<$	100 GeV
$H \rightarrow \gamma\gamma$	90	$<$	m_H	$<$	150 GeV
$H \rightarrow ZZ^* \rightarrow 4l^{\pm}$	130	$<$	m_H	$<$	$2m_Z$ GeV
$H \rightarrow ZZ \rightarrow 4l^{\pm}, 2l^{\pm}2\nu$			m_H	$>$	$2m_Z$ GeV
$H \rightarrow WW, ZZ \rightarrow l^{\pm}\nu 2\text{jets}, 2l^{\pm}2\text{jets}$			m_H	$<$	1 TeV

Many of these will involve the accurate and efficient detection of the b quark. To do this high precision tracking must be used as described in Chapter 1.

There are many limitations imposed in the design of a tracker which complicate the process. These include the requirement to make an accurate energy measurement outside the tracker and the cost constraints. These are two of the largest factors in limiting the performance of the tracker.

Monte-Carlo studies are carried out to understand and optimise the performance of the detector before it is built. These studies typically focus on certain important

interactions. This chapter contains information on the software used to describe the detector and then goes on to show the results from a b-jet study. An investigation into the expected particle fluxes of charged particles from the interaction point is also included, as this is relevant to the estimation of likely radiation doses in the ATLAS forward tracker.

7.2 DICE

This Detector Integration CodE is used to define the geometry and properties of the detector. It forms part of the SLUG software package which links together the various parts required to carry out a full simulation: the generator (usually Pythia[75, 76]), the detector simulation package (GEANT[7]), the detector description (DICE) and the user code to control the study and analyse the results.

The latest version of DICE[77] uses a GEANT language plus other extensions to FORTRAN to describe the detector elements. It also contains routines in a similar language to determine how energy deposited in the detectors is converted into measured signals.

The following is a example listing of a routine which defines the "mother volume" of the gallium arsenide tracker;

```
*********************************************************************
HODULE     GAASGEO  is the  Geometry of the GaArsenid forward tracker
*********************************************************************
Author     R.Brun, P.Nevski, Haya Stavrianakou, Stephen J. Gowdy
Created    23 august 95
* -------------------------------------------------------------------
+CDE,AGECOH,GCONST,GCKINE.
    Content   GAAS, GDSi, GSij, GDij, GSUB, GASS, GELE, GSUP, GFIX
    Structure GAAG { Version, Rmin, Rmax, Hlen, Ndisc, DrCounter, DfCounter,
                     DzCounter, TCKsubs, TCKsupp, Support,
                     DXele, DYele, Dzele,
                     Drfix, Dzfix, Nstereo, Nactive, Angle, DRactive,
                     DRdead, DFdead, DRoverlap }
    Structure GDSi { Disc, RIdisc, ROdisc, ZDisc }
    Real      Zdel,Rj,Zk,DR,DZmod,DRserv
    Real      xg1,xg2,zm,ym,f1,f2,f3,f4,f5,t
    Integer   Idisc,Ndv,j,N,m,m1,m2
* -------------------------------------------------------------------

 Fill  GAAG                        ! GAAS geometry definition
       version   = 2        !  Horges layout with keystones
       Rmin      = 19       !  overall min radius
       Rmax      = 50       !  overall max radius
       Hlen      = 200      !  overall half legth
       Ndisc     = 5        !  Nr. of discs (on each side)
       DrCounter = 6.0      !  DX (Dr) of a counter
       DfCounter = 2.1      !  DY (Dphi) of a counter
       DzCounter = .02      !  DZ (Thickness) of a counter
       TCKsubs   = .01      !  Thickness of the substrate
       TCKsupp   = 0.6      !  Thickness of the support area
       Support   = .2       !  Thickness of the support plane
       DXele     = 3.       !  DX (Dr) of the electronics board
       DYele     = 2.24     !  DY (Dphi) of the electronics board
       DZele     = .06      !  DZ (Thickness) of the electronics board
       Drfix     = 1.       !  DX (Dr) of the fixing board
       Dzfix     = .06      !  DZ (Thickness) of the fixing board
       Nstereo   = 2        !  2 stereo layers back to back (f/u or f/v)
       Nactive   = 1        !  1 active area on each side of a tile
       angle     = 3.10345  !  3.10345 degrees keystone(tile) angle
```

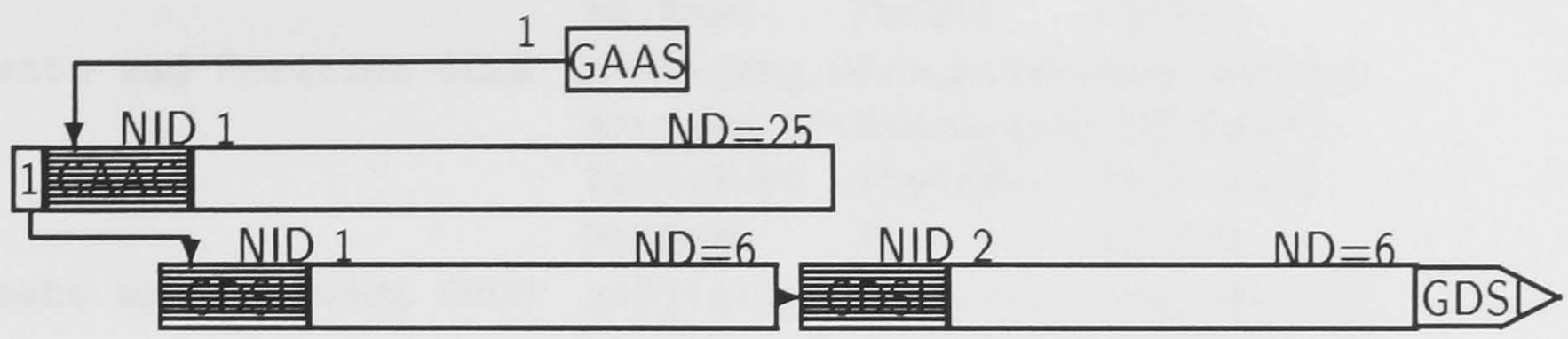

Figure 7.1: Data Banks of GaAs Detector in DICE

```
          DRactive  = 5.8      !  5.8 cm in r for each active area
          DRdead    = 0.0      !  0mm r-dead between the 2 areas in a tile
          DFdead    = 0.1      !  1mm phi-dead on each side of a tile
          DRoverlap = 0.0      !  2mm 2-tile overlap in r
Fill  GDSi                     ! GAAS disc parameters
          Disc = 1             !  disc  number
          RIdisc    = 26.      !  inner Radius
          ROdisc    = 32.      !  outer Radius
          Zdisc     = 84.0     !  Position along Z
Fill  GDSi                     ! same
          Disc = 2             !  second disc
          RIdisc    = 26.      !  inner Radius
          ROdisc    = 32.      !  outer Radius
          ZDisc     = 96.0     !  Position along Z
Fill  GDSi                     ! GAAS disc parameters
          Disc = 3             !  third disc
          RIdisc    = 26.      !  inner Radius
          ROdisc    = 32.      !  outer Radius
          Zdisc     = 120.1    !  Position along Z
Fill  GDSi                     ! same
          Disc = 4             !  fourth disc
          RIdisc    = 20.      !  inner Radius
          ROdisc    = 32.      !  outer Radius
          ZDisc     = 132.2    !  Position along Z
Fill  GDSi                     ! same
          Disc = 5             !  fifth disc
          RIdisc    = 26.      !  inner Radius
          ROdisc    = 32.      !  outer Radius
          ZDisc     = 168.5    !  Position along Z
*
    Use        GAAG   version=2
*   put calculations here to make the geometry better readable
    Dzmod  = gaag_TCKsubs+2*gaag_DzCounter ! module thickness in z
    DRserv = gaag_DXele+gaag_Drfix         ! electronics & fixing board in r
    t      = tan(gaag_angle/2*DegRad)
    f1     = t*gaag_DRcounter*2            ! used later
    f2     = t*gaag_DRactive*2
    f3     = t*gaag_DRdead*2
    f4     = t*gaag_DXele*2
    f5     = t*gaag_DRoverlap*2
    Zdel   = max(2*gaag_DZele+gaag_TCKsubs,Dzmod,gaag_Dzfix) ! max in z

    Create and position GAAS in INNER konly='HANY'

* ------------------------------------------------------------------
```

The FILL command creates a ZEBRA[78] bank and fills it with the information following the command for later use. If there are multiple FILLs then a new bank is chained on the end of the last one. A visualisation of this data bank structure is shown in Figure 7.1.

An individual module is defined by the following routine;

```
* ------------------------------------------------------------------
Block     GDij   is a sector containing one counter
   Shape                    DIVIsion   Iaxis=2  Ndiv=Ndv/2
   if (Rj>gdsi_RIdisc) m=m-1
   Create and Position GSUB  x=Rj+gaag_DRcounter/2,
                             ThetaX=90  ThetaY=0  ThetaZ=90,
```

```
                                PhiX=90    PhiY=0    PhiZ=0
Create and Position GELE  x=Rj+gaag_DRcounter+gaag_DXele/2,
                          z=-(gaag_TCKsubs+gaag_DZele)/2,
                          ThetaX=90  ThetaY=0  ThetaZ=90,
                          PhiX=90    PhiY=0    PhiZ=0
Create and Position GELE  x=Rj+gaag_DRcounter+gaag_DXele/2,
                          z=+(gaag_TCKsubs+gaag_DZele)/2,
                          ThetaX=90  ThetaY=0  ThetaZ=90,
                          PhiX=90    PhiY=0    PhiZ=0
Create and Position GFIX  x=Rj+gaag_DRcounter+gaag_DXele+gaag_Drfix/2,
                          ThetaX=90  ThetaY=0  ThetaZ=90,
                          PhiX=90    PhiY=0    PhiZ=0
endblock
* ------------------------------------------------------------------------
```

In both of these routines the information from the data bank is identified by variables of the form `<Bank>_<Variable>`.

The GDij routine creates as the module contents the two electronics boards back-to-back, a fixing board and the actual detector substrate. There are then further routines which define these elements in more detail.

Using this method the detector database is built up. It is possible to examine this database once it has been constructed. An interactive program called atlsim has been designed around GEANT and PAW++, it provides a display of the tree of detector elements and allows each to be viewed individually. The tree display is shown in Figure 7.2 and the module information in Figure 7.3.

There are therefore two sets of data banks, separate but linked by the DICE code, which contain complementary information.

7.3 b-jet Analysis

Pythia was used to study the type of b-jet produced from a 80GeV Higgs decay. The motivation for this study was the requirement for high b-tagging efficiencies and u,d,s-jet rejection factors at ATLAS. These are needed due to the channel $H \rightarrow b\bar{b}$ being the dominant decay channel for the Higgs particle with a mass in the range 80–120 GeV. This is below threshold for WW and ZZ decays of the Higgs.

The construction of algorithms to identify b-jets requires an initial evaluation of certain parameters including the angular size of the jets.

For this analysis only the process $f_i\bar{f}_j \rightarrow W^+H^o$ was allowed from pp collisions

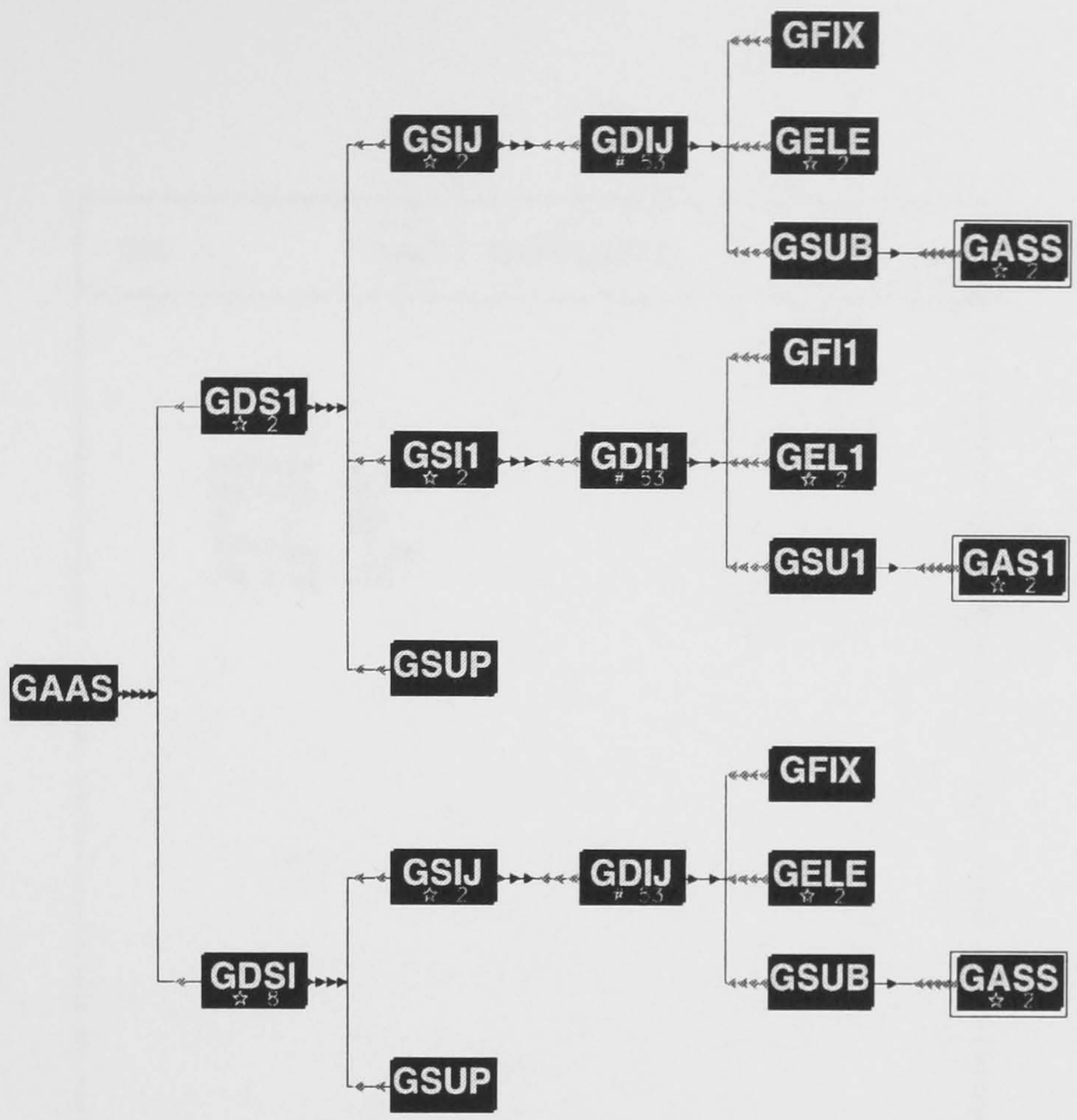

Figure 7.2: Tree Display of DICE Elements

with each beam having 7000GeV energy. The W^+ was forced to decay to a positron and an electron neutrino and the Higgs to a $b\bar{b}$ pair. This process is illustrated in Figure 7.4.

When trying to find a jet it is useful to find stiff tracks and then search around them for other tracks. Therefore, it is necessary to determine how closely the jet direction is correlated with the direction of the stiff track and how high a P_T this track actually has. The distribution of P_Ts of the stiffest track in a jet in each event in plotted in Figure 7.5 and the angle between this track and its parent quark is shown in Figure 7.6.

These distributions produce the results in Table 7.1, which has also been subdivided to show the difference as the energy of the B meson changes.

After finding the jet seed track it is necessary to search for the remaining tracks which are the remnants of the B. To aid in the speed of finding and reconstructing jets it is necessary to limit the search for tracks to a cone about this seed. The required size of this cone has been determined from the distribution of all tracks from the B. This is done both in ϕ and η and the size of the cone is expressed as

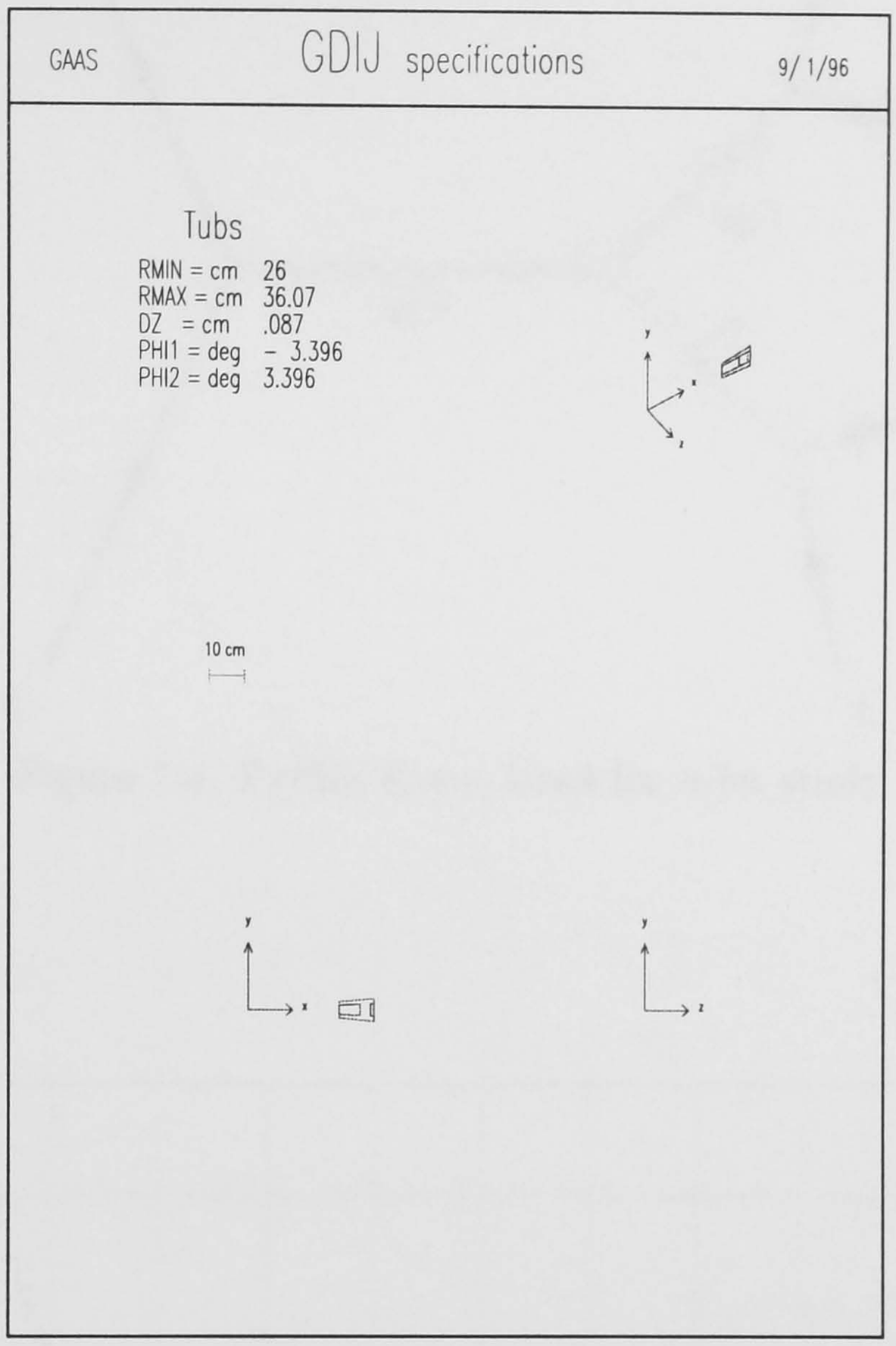

Figure 7.3: Module Information from atlsim

	P_T of B Hadron(GeV c^{-1})						
% of Jets to Pass	All	<10	10–20	20–30	30–40	40–100	>100
90	2.0	0.8	1.55	2.2	2.85	3.95	9.0
95	1.3	0.6	1.05	1.55	2.0	2.65	6.6
99	0.5	0.25	0.4	0.6	0.8	0.9	2.2

Table 7.1: P_T cut (GeV) to select jet from B

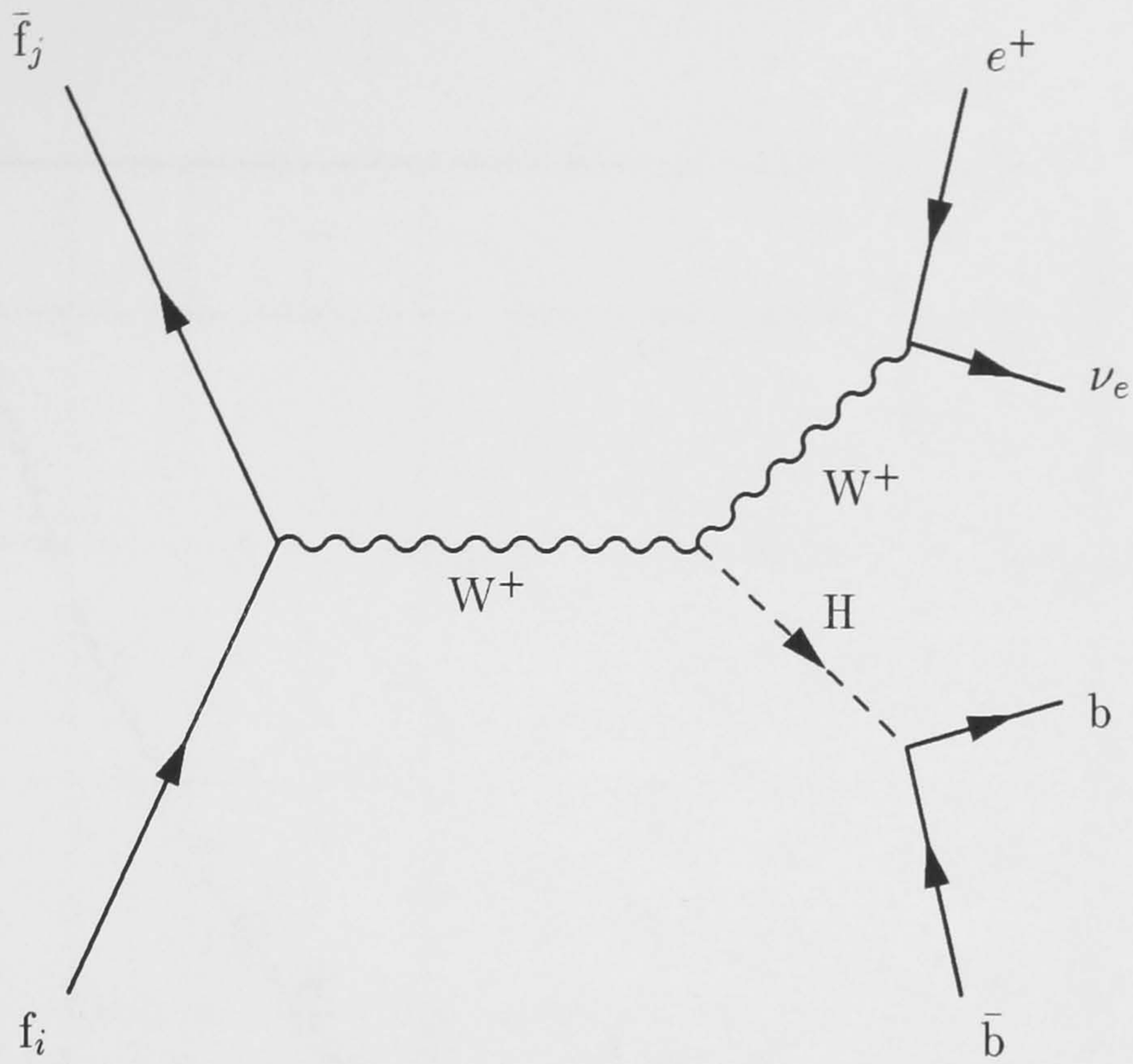

Figure 7.4: Pythia Event Used for b-jet study

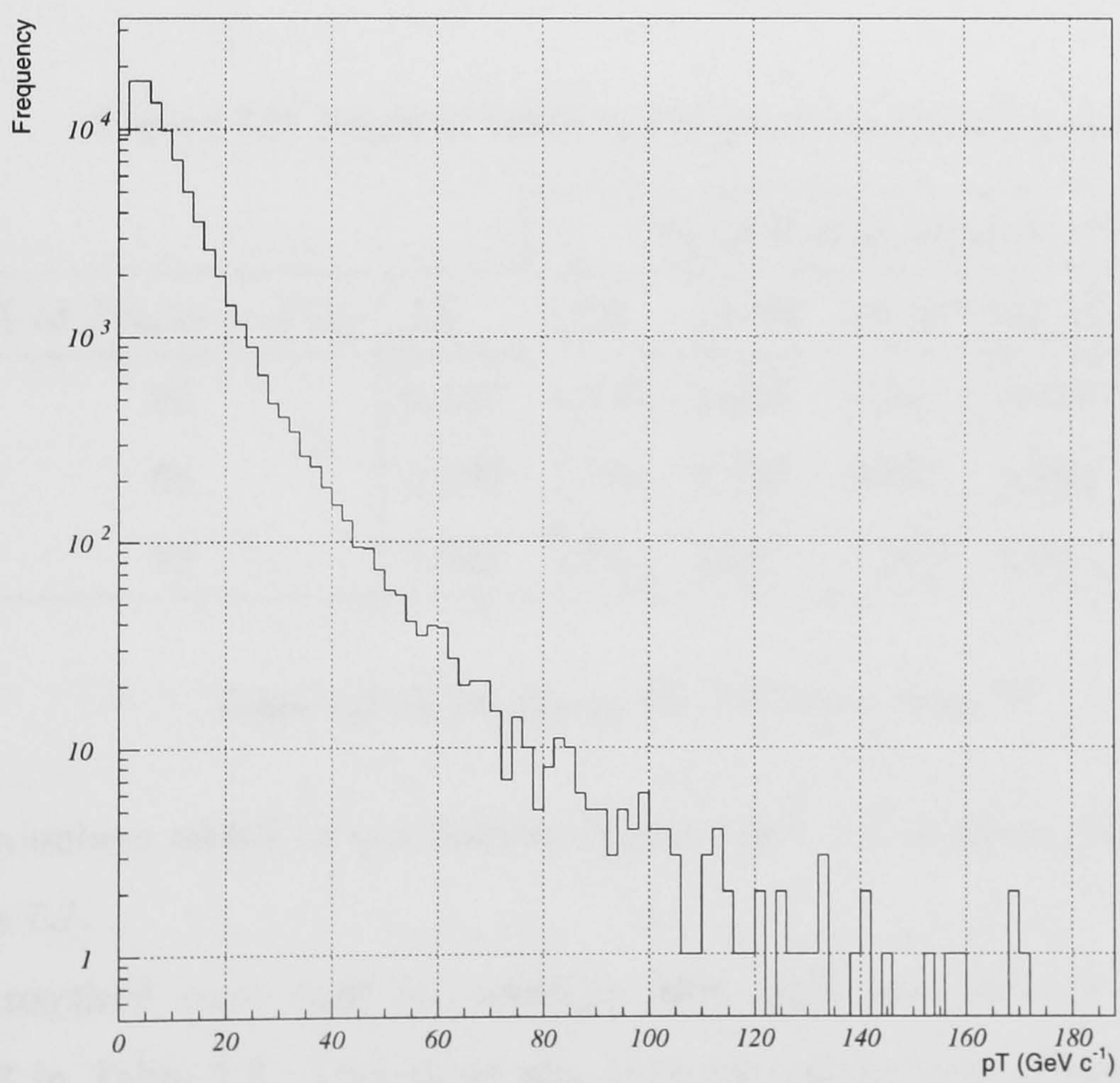

Figure 7.5: P_T of stiffest track from $H \rightarrow b\bar{b}$

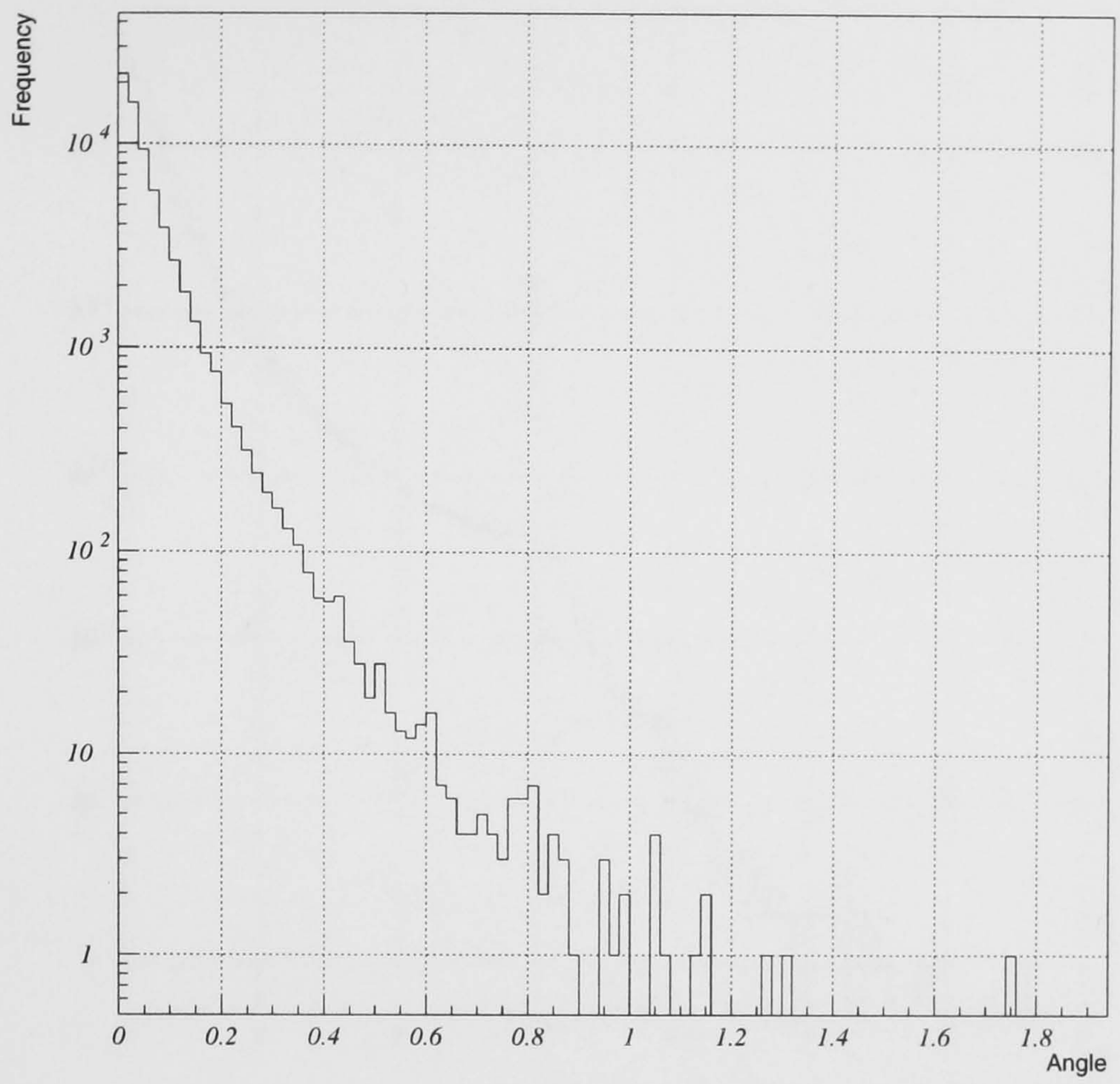

Figure 7.6: Angle of track in radians from parent quark

		P_T of B Hadron(GeV c^{-1})				
% of Tracks to Pass	All	<10	10–20	20–30	30–40	>40
90	0.548	1.450	0.612	0.447	0.418	0.447
95	0.806	1.732	0.837	0.632	0.592	0.671
99	1.761	2.915	1.597	1.265	1.275	1.533

Table 7.2: b-jet size in δR for tracks from B

the two numbers added in quadrature, denoted ΔR. All of these tracks are plotted in Figure 7.7.

The required cone sizes for selecting 90%, 95% and 99% of the tracks are presented in Table 7.2. This table also includes information of how the cone size varies with the energy of the B meson. These numbers are graphed in Figure 7.8.

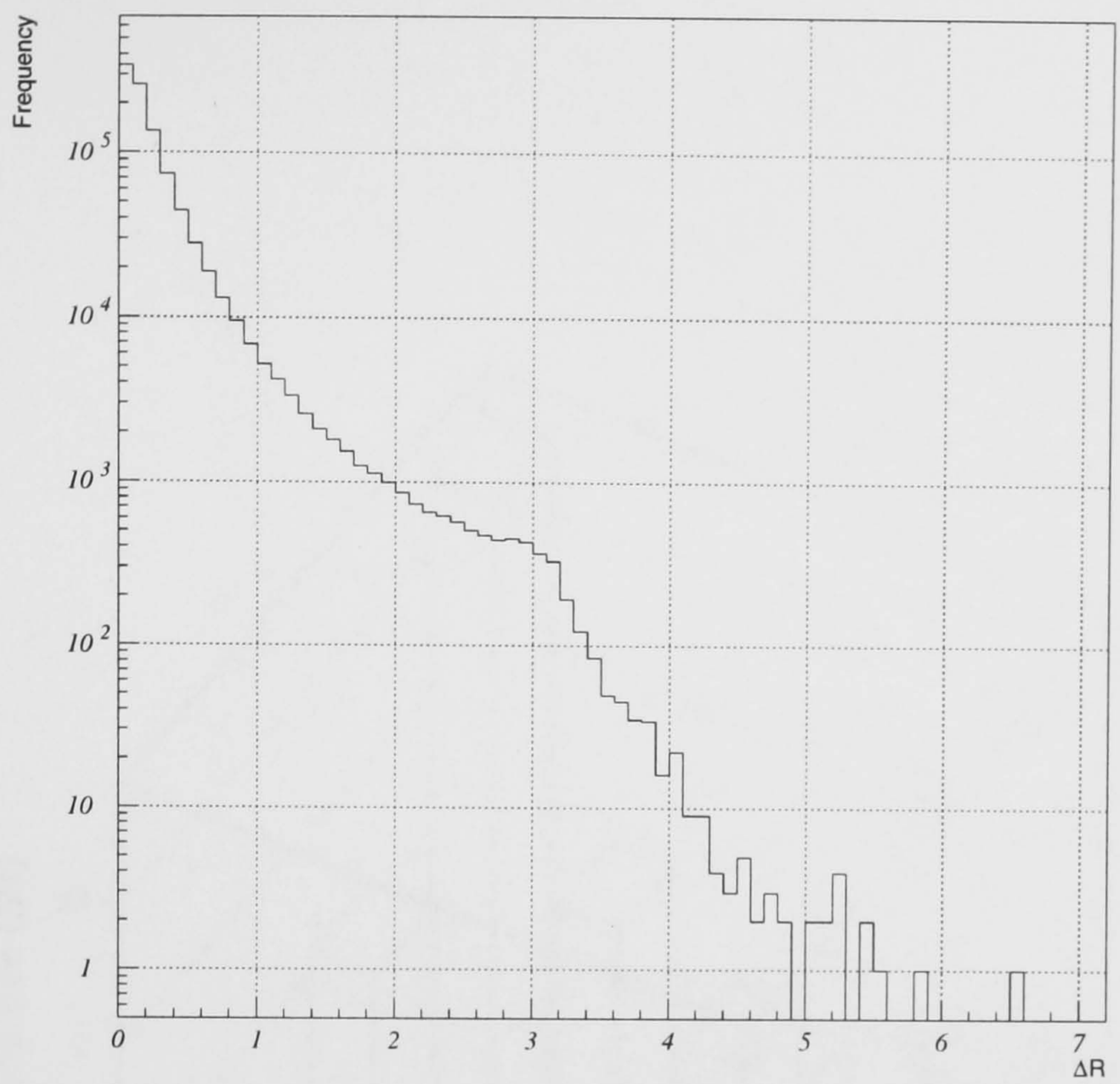

Figure 7.7: ΔR for each track with B as parent

7.4 Particle Flux Analysis

To determine the flux of charged particles expected from the interaction point in ATLAS a simulation was done using Pythia. This was run with the default processes turned on. The maximum cross-sections were due to low-P_T and semi-hard QCD scattering.

The simulation was run twice, once with 100,000 events searching for protons only and the other with a sample of 10,000 events looking for all "undecayed" charged particles.

Figure 7.9(a) shows the momentum spectrum for all protons from these events. Figure 7.9(b) shows this spectrum for those protons that would pass through the gallium arsenide detector defined by $2 < \eta < 2.5$. In addition the latter is also shown with only up to 20GeV protons in Figure 7.9(c).

Similar distributions are shown in Figures 7.10(a), 7.10(b) and 7.10(c) for all

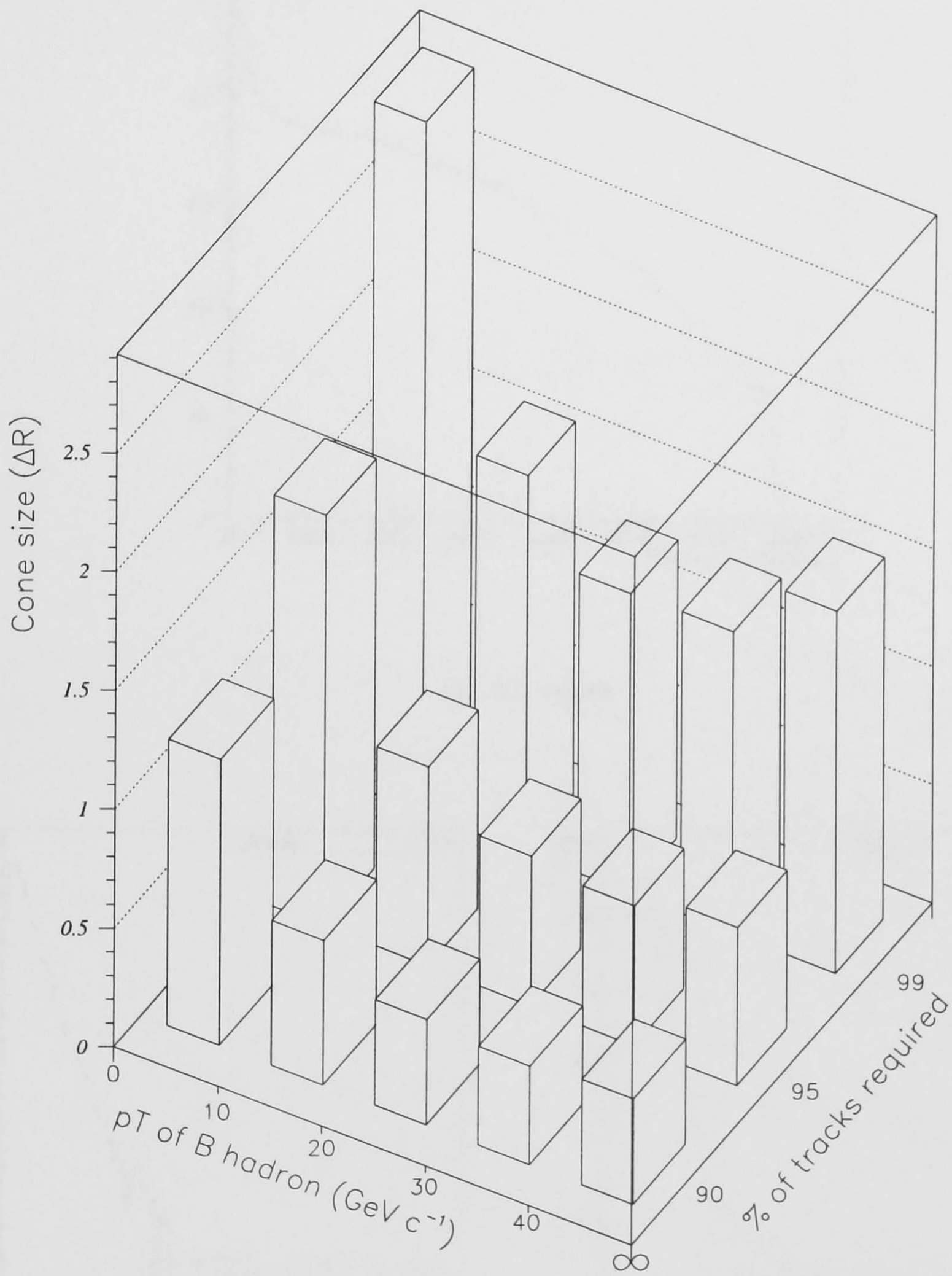

Figure 7.8: ΔR required to select % of tracks from B meson

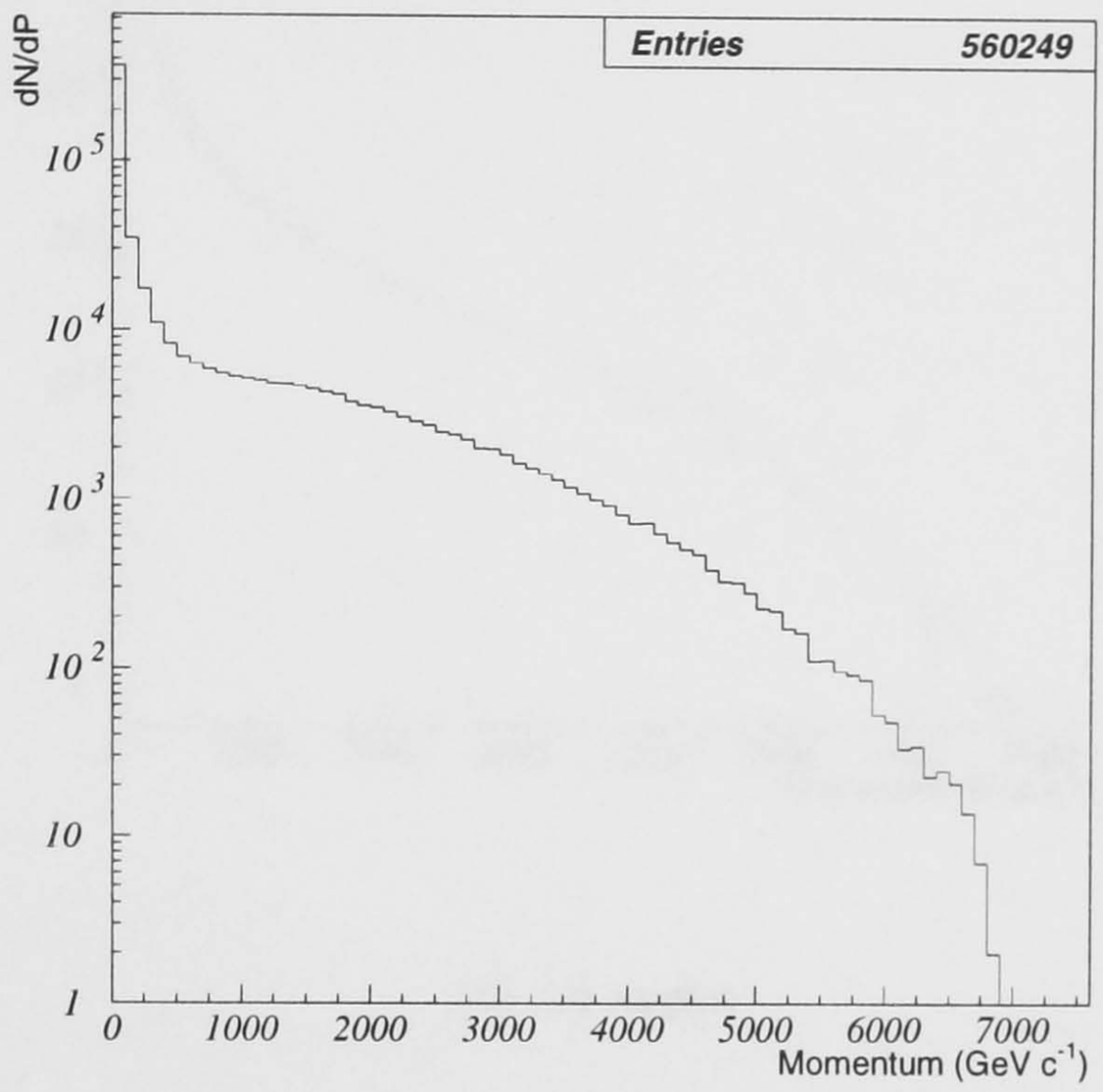

(a) All angles

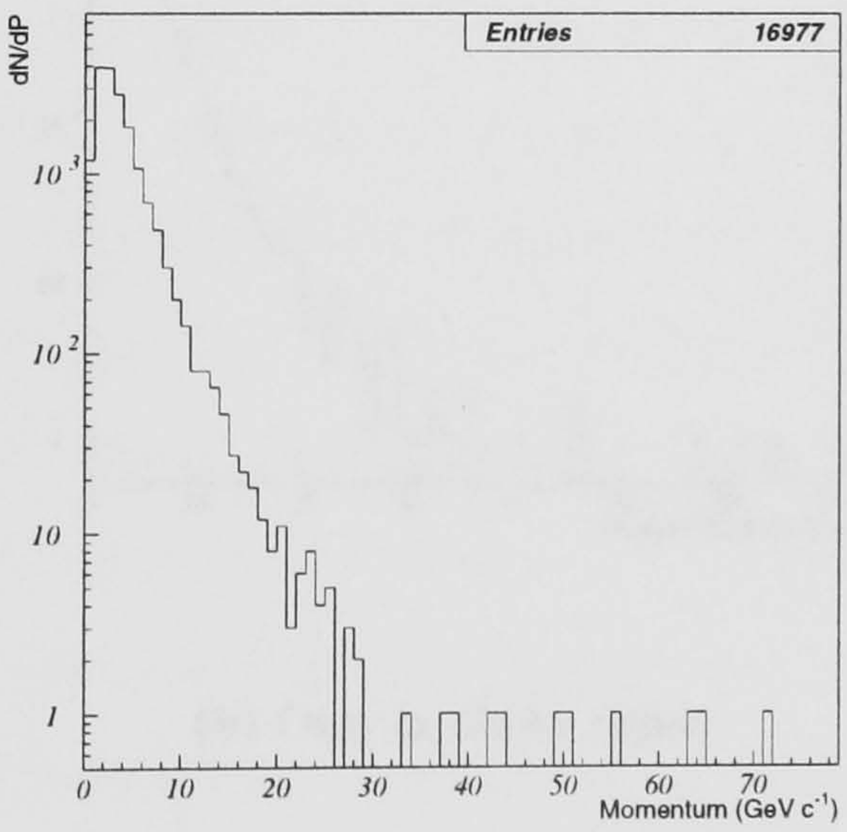

(b) Only in GaAs region

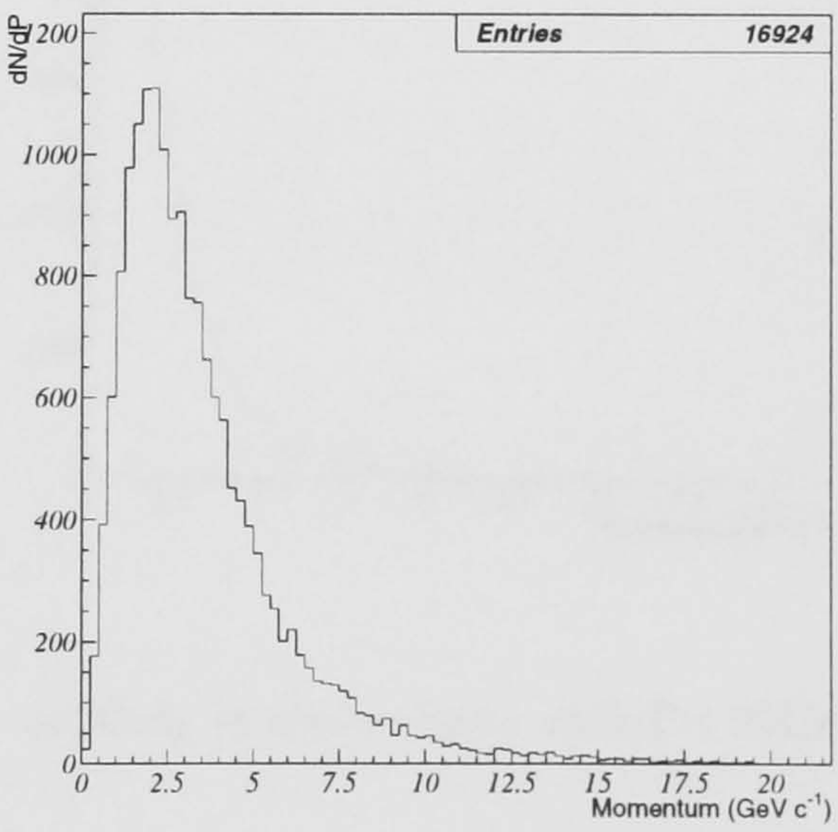

(c) Only in GaAs region with P< 20GeV

Figure 7.9: Proton momentum spectra from pp collisions at 14TeV

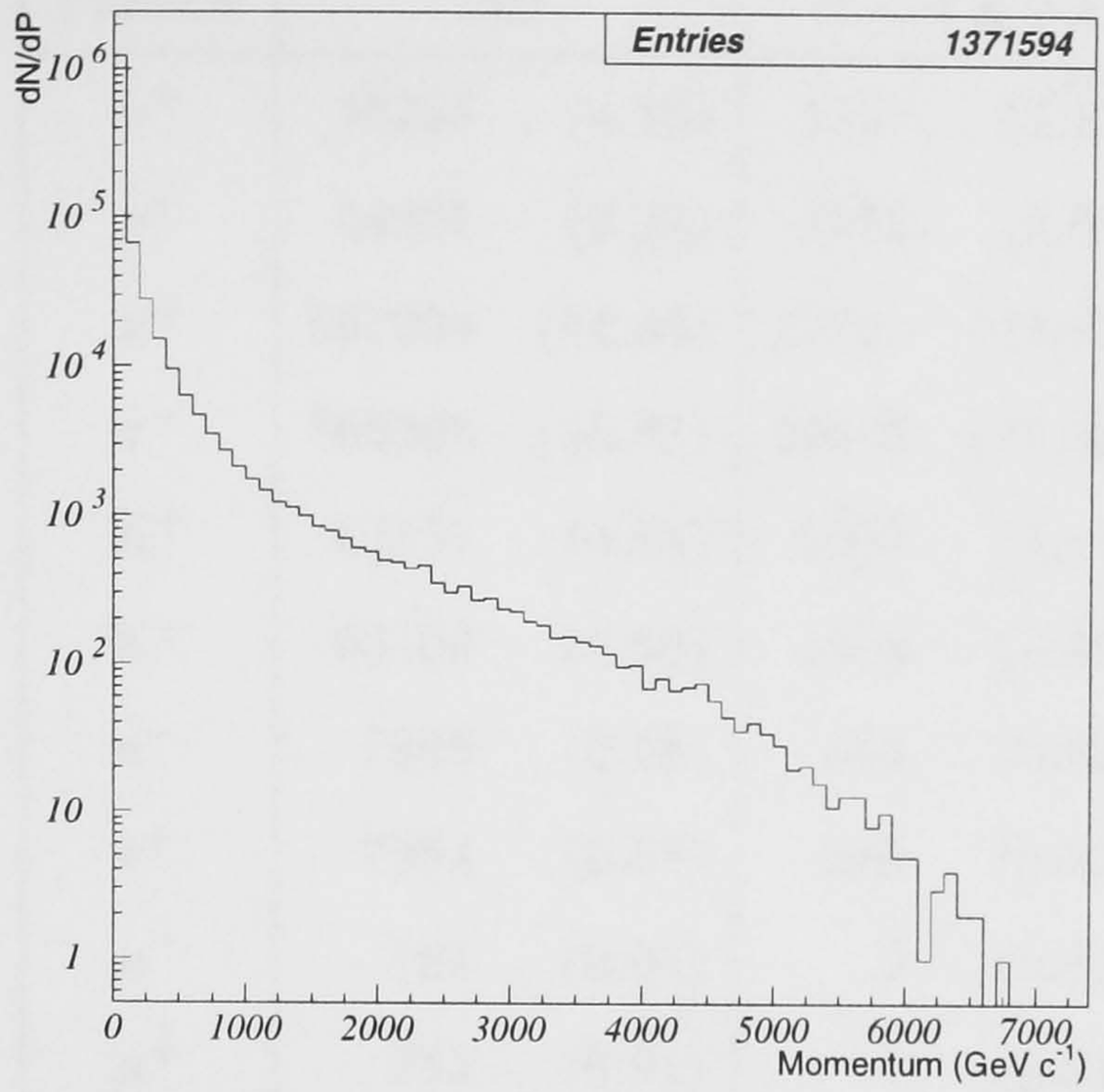

(a) All angles

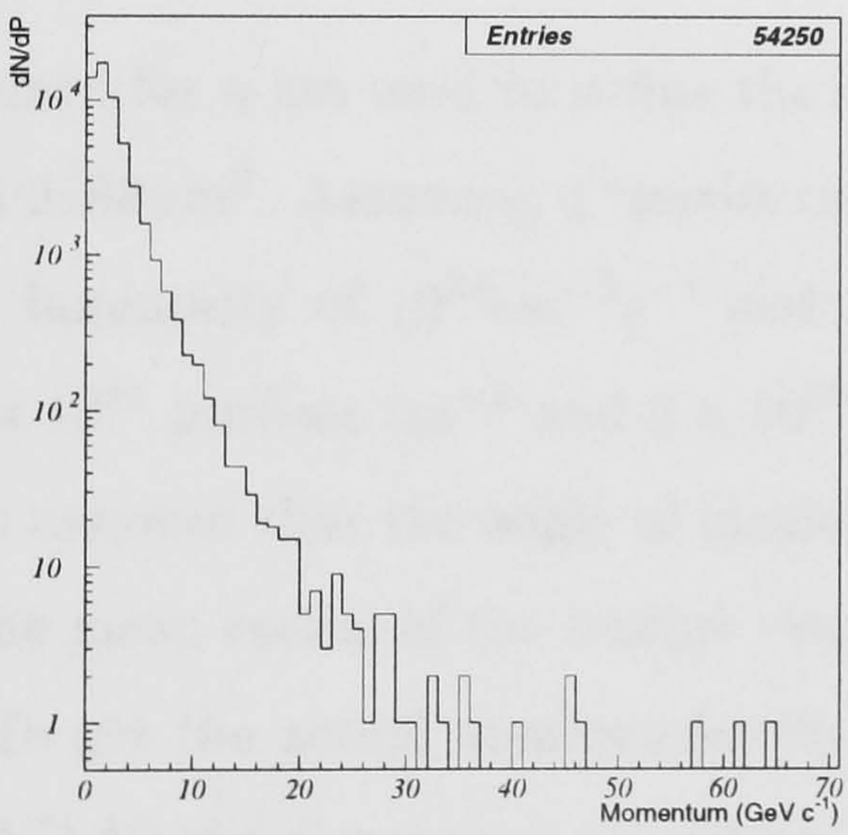

(b) Only in GaAs region

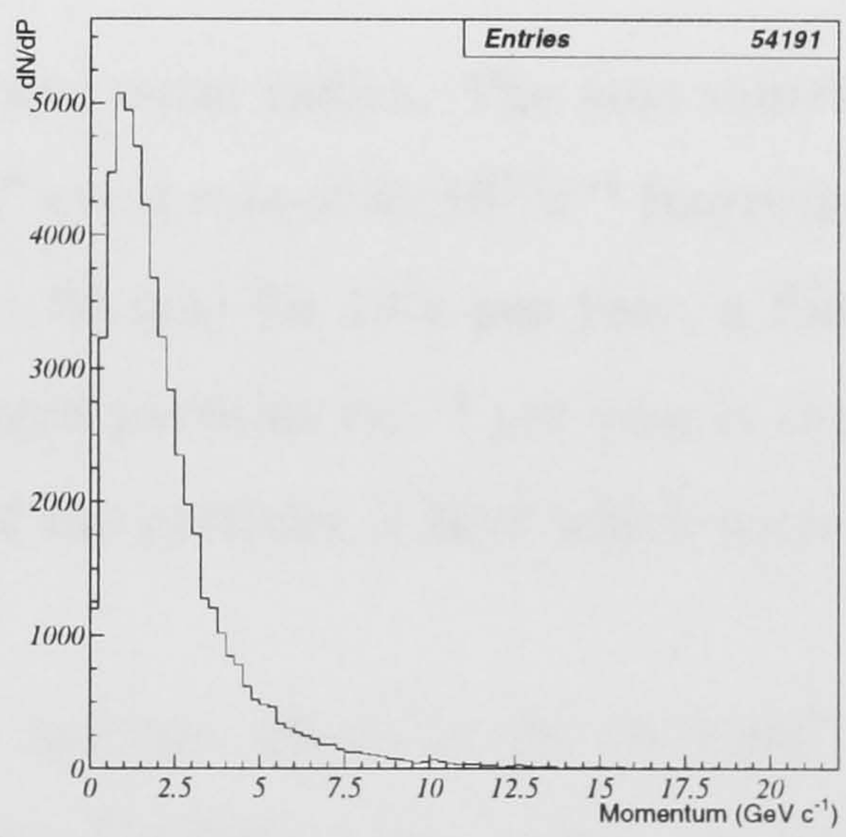

(c) Only in GaAs region with P< 20GeV

Figure 7.10: Charged particle momentum spectra from pp collisions at 14TeV

charged particles. The composition of these particles is listed in Table 7.3.

To work out the particle flux the area of the detector is required. This can be determined from the z distance of the detector from the interaction point along the beamline. The detector will be a wheel at this z value and the limiting values

Particle	Area of interest			
	All		$2 < \eta < 2.5$	
p^+	56254	(4.10)	1707	(3.15)
p^-	44291	(3.23)	1652	(3.05)
π^+	567299	(41.36)	22721	(41.88)
π^-	560308	(40.85)	22400	(41.29)
K^+	64157	(4.68)	2628	(4.84)
K^-	63109	(4.60)	2468	(4.55)
e^-	7985	(0.58)	324	(0.60)
e^+	7984	(0.58)	339	(0.62)
μ^-	104	(0.01)	3	(0.01)
μ^+	103	(0.01)	8	(0.01)
Total	137159		54250	

Table 7.3: Number (and percentage) of undecayed charged particles listed by type from 10000 events

assumed for η are used to define the inner and outer radius. The area subtended is then 2188 cm^2. Assuming a "minimum bias" event rate of $8 \times 10^{15} s^{-1}$ (corresponding to a luminosity of $10^{34} cm^{-2} s^{-1}$ and $\sigma_{tot} = 80$ mb) for 10^7s per year, a fluence of 6.2×10^{11} protons cm^{-2} and 2×10^{13} charged particles cm^{-2} per year is expected. This assumes that the angle of incidence of the particles is that which corresponds to the mean radius of the tracker element.

To get the actual numbers for the first and last wheels in the "Morges" layout for ATLAS the dimensions are extracted from DICE95. These results are presented in Table 7.4. Figure 7.11 shows how the fluence will vary across the first wheel.

These fluxes show the effect of the magnetic field in the inner detector which will cause low momentum particles to loop around the magnetic field lines. This effect of "loopers" has not been included for the figures quoted in the text which are derived only from a range of η.

Wheel	Radius (η)		Z [cm]	Fluence [cm^{-2} per year]	
	Inner [cm]	Outer [cm]		Protons	All Charged
First	26 (1.89)	32 (1.69)	84.0	6.00×10^{11}	2.30×10^{13}
Without B-Field				4.72×10^{11}	1.65×10^{13}
Last	26 (2.57)	32 (2.36)	168.5	6.95×10^{11}	2.46×10^{13}
Without B-Field				5.25×10^{11}	1.65×10^{13}

Table 7.4: Dimensions and radiation levels in first and last wheels of ATLAS very forward tracker

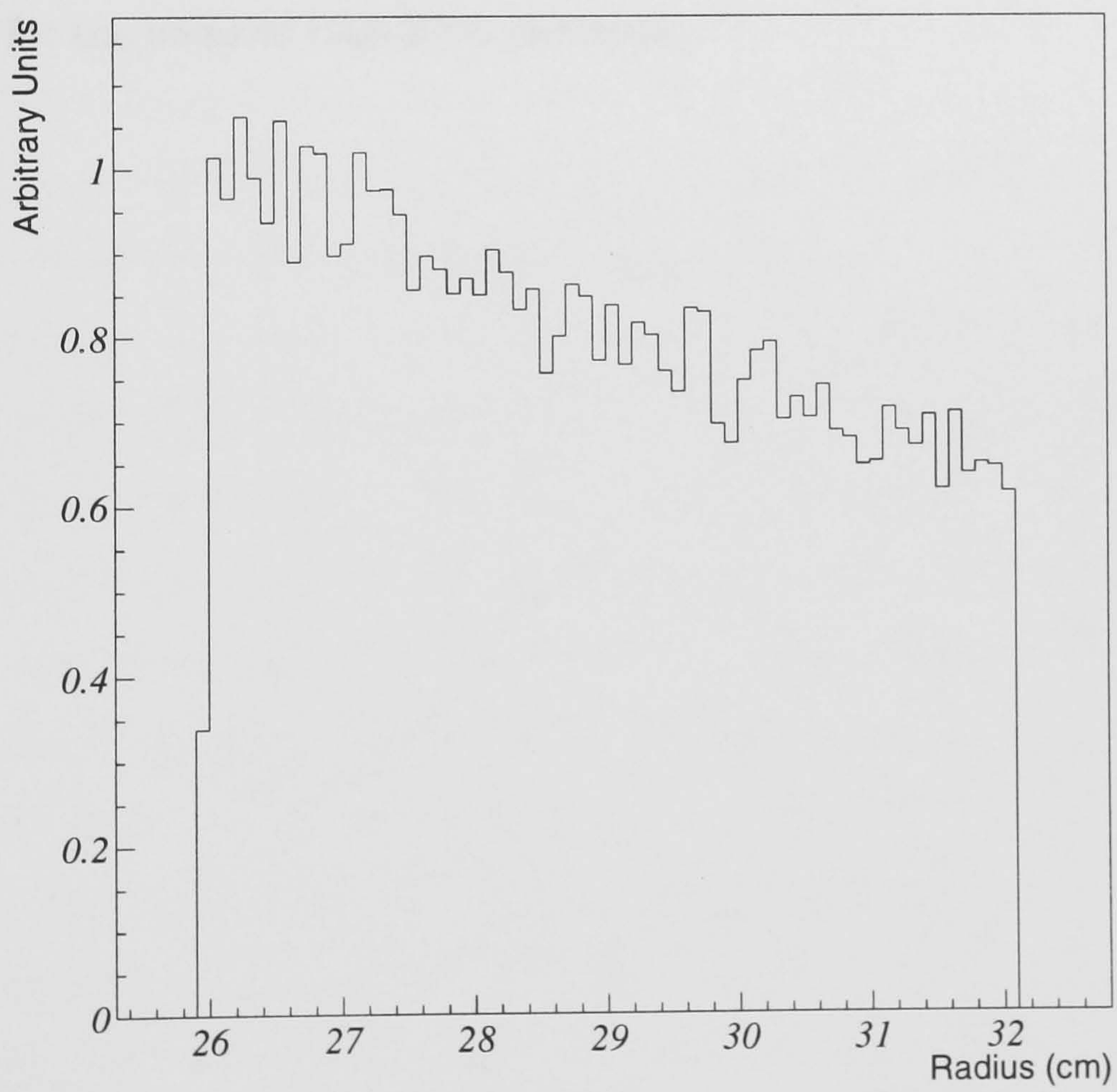

Figure 7.11: Variation of fluence across first wheel in ATLAS

7.5 Conclusion

The detector simulation for ATLAS now includes many effects which have previously been neglected or only roughly approximated. The creation of DICE95 has helped this greatly and allowed detector developers to modify the layouts of their detectors with relative ease.

The information gained from the b-jet study has guided the development of the ATLAS pattern recognition package iPatRec.

The fluences expected from the results of Section 7.4 are in close agreement with those of earlier studies[67]. They should be compared with those in Section 5.4.3. It is clear that the radiation effects on detectors need to be investigated further. The radiation hardness of gallium arsenide detectors for charged particles at the LHC needs to be examined closely as these two sets of results imply that forward detector will generate a signal of about 5000 electrons after three years running (at full luminosity) which will probably be within 3σ of the noise (assuming a realistic estimate for the noise of 1500 ENC electrons).

Chapter 8

Conclusions

This thesis has presented work done within the ATLAS and RD8 collaborations. It has described the current status of gallium arsenide detectors and some aspects of the ATLAS experiment.

Pad detectors, used predominantly in testing, now show charge collection efficiencies approaching 100%. Microstrip detectors have also proven successful, with measured spatial resolutions better than 14 μm with a 50 μm pitch. Pixel detectors have shown $\approx$ 100% detection efficiency. All types of detectors agree on charge collection efficiency when taken from the same wafer.

There does seem to be a problem, however, with radiation hardness to pions. Pions damage gallium arsenide at a faster rate than originally anticipated. Some tentative explanations have now been developed for this[79]. As previously mentioned, studies are under way to investigate whether suitable annealing can recover some of this damage in the irradiation tests. Another possibility is that due to the very high flux rates during testing damage measured could be higher than will actually be found in long term operation at the LHC. Further tests are planned in which the detectors are irradiated at lower rates to verify this.

Another factor evident in the test beam analysis is the unexpectedly large noise. The biasing strip is only one possible source of this additional noise which will be investigated further, using detectors with alternative bias arrangements.

Latest test beam results have reinforced the results presented in this thesis. By using only hits which produce two strip wide clusters it is possible to push the resolution below 10μm, as shown in Figure 8.1. The noise problem, however,

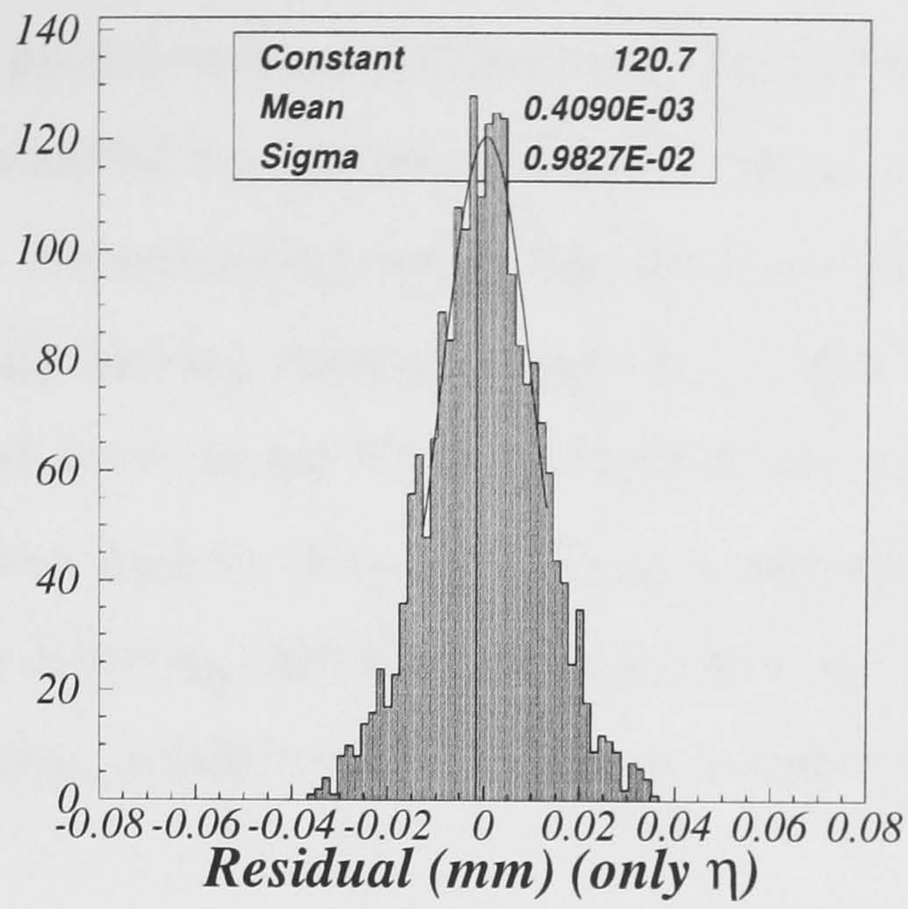

Figure 8.1: Optimum resolution of GaAs microstrip detector achieved to date. Detector is AL-W3-6AC biased at 180V (rear) and -30V (bias strip)

remains.

The material used to construct the detectors has undergone a great deal of development. The choice for ATLAS is driven largely by cost, however, and therefore industry standard LEC material will most probably be used. Other applications which have less sensitivity to cost could consider LPE or VPE epitaxial material which can have much better characteristics due to less trapping of charge carriers.

What has been developed in Glasgow is a greater understanding of the processing of gallium arsenide detectors. Through the better preparation of the surface of the detectors, better charge collection efficiencies and smaller leakage currents have been obtained. Various metal contact recipes have also been evaluated.

Charge transport in our detectors is now thought to be well understood. By comparing data and simulation of X-ray signals it has been possible to strengthen the model of signal generation in gallium arsenide. A method has been proposed[80] which explains the electric field profile observed experimentally[81].

For the ATLAS semiconductor tracker modules should be tested which include fan-shaped detectors. The GaAs Forward Tracker elements will adopt the same mechanical, cooling and read-out solutions as the Silicon Forward Tracker. In addition to the layout of the detector/module, studies will be performed to evaluate the performance of gallium arsenide detectors using the fast electronics required for

ATLAS. No degradation is expected in the signals from these faster electronics.

Gallium arsenide pixel detectors have shown great promise. There is a possibility that they could be adopted for the less hospitable areas of ATLAS, depending on the progress make in understanding the details of their radiation hardness.

These detectors are making strong progress in the field of medical imaging. A gallium arsenide pixel detector for X-ray imaging would require approximately an order of magnitude less dose to the patient than a photograph or silicon detector. A European network involving the Glasgow group has very recently been set up to investigate the practical details and to prototype a new sensor for applications in dentistry.

In a more ambitious development project, another member of the group, V O'Shea, is investigating the possibility of incorporating a multi-quantum well opto-electronics modulator on each pixel of the detector. This could cut down a great deal on the required read-out electronics and, in the case of medical imaging, allow the effective conversion of an X-ray image to one involving optical photons, modulated in intensity by the signals produced by the X-rays in a gallium arsenide detector.

References

[1] P13. Proposal to Develop GaAs Detectors for Physics at the LHC. CERN. DRDC 90-58, 1990.

[2] P22. Development of Hybrid and Monolithic Silicon Micropattern Detectors. CERN, DRDC 90-81, 1990.

[3] CERN-RD2 Collaboration. Recent results of radiation studies in silicon. *Nuclear Instruments and Methods in Physics Research*, A344(1)(1994):228–236.

[4] W. Bencivelli et al. Evaluation of elemental compound semiconductors for X-ray digital radiography. *Nuclear Instruments and Methods in Physics Research*, A310(1991):210–214.

[5] A. D. T. Short A. D. Holland and T. Cross. X-ray Detection using Bulk GaAs. Submitted to Nuclear Instruments and Methods in Physics Research, March 1994.

[6] H. Hirayama W. Nelson and D. Rogers. The EGS4 Code System. SLAC, Report 265, 1985.

[7] Application Software Group. GEANT - Detector Description and Simulation Tool. CERN, Long Writeup W5013, June 1993. Online manual available at http://wwwcn.cern.ch/asdoc/geant_html3/geantall.html.

[8] M. Campbell et al. Design and performance of the Omega-ion hybrid silicon pixel detector. CERN, ECP 92-6, 1992.

[9] M. Raymond et al. A 2-D amplifier array chip for pixel detector readout. *Nuclear Instruments and Methods in Physics Research*, A348(1994):673–677.

[10] S. M. Sze. *Semiconductor Devices: Physics and Technology.* John Wiley & Sons, 1985.

[11] H. P. Myers. *Introductory Solid State Physics.* Taylor & Francis, 1990.

[12] S. M. Sze. *Physics of Semiconductor Devices.* John Wiley & Sons, 2nd edition, 1981.

[13] S. Ramo. Currents Induced By Electron Motion. *Proc. of the I.R.E.*, pages 584–585, September 1939.

[14] G. Cavalleri et al. Extension Of Ramo's Theorem As Applied To Induced Charge In Semiconductor Detectors. *Nuclear Instruments and Methods in Physics Research*, 92(1970):137–140.

[15] R.N. Williams and E.M. Lawson. Formation Of Current Pulses In Semiconductor Nuclear Radiation Detectors. *Nuclear Instruments and Methods in Physics Research*, 113(1973):597–598.

[16] R. Bates et al. Noise Spectra of SIU-GaAs Pad Detectors With Guard Rings. In J. Ludwig et al. [82]. Also GLAS-PPE/95-06.

[17] A. van der Ziel. Semiconductor Noise. In L.D. Smullin and H.A. Haus, editors, *Noise in Electron Devices*, chapter 6, pages 311–343. John Wiley & Sons & Tech. Press of MIT, 1959.

[18] J. Stanton. An Introduction To The MX Chip. Rutherford Appleton Laboratory, RAL 89-028, 1989.

[19] E. Nygård et al. CMOS Low Noise Amplifier for Microstrip Readout Design and Results. CERN, PPE 90–142, 1990.

[20] O. Toker et al. Viking, A CMOS Low Noise Monolithic 128 Channel Frontend For Si-strip Detector Readout. CERN, PPE 93-141, July 1993.

[21] M. French. APV5-RH Operation Manual. Rutherford Appleton Laboratory, Technical report, October 1994.

[22] S. Roe. Test Beam Results. *Proc. of the ATLAS SCT Workshop* [83].

[23] T.Akesson et al. Silicon/GaAs/MSGC Front-end Electronics Review. ATLAS Internal Note, INDET NO-074, November 1994.

[24] E. Evans. Digital Readout Status. *Proc. of the ATLAS SCT Workshop* [83].

[25] ATLAS. Minutes of SCT Electronics Review Meeting. Available from ATLAS secretariat, December 1995.

[26] M. Lovell. Private communication, November 1993.

[27] M. Lovell. PAC3 Specification. Rutherford Appleton Laboratory, Technical report, October 1994.

[28] M. Lovell. PAC2 Specification. Rutherford Appleton Laboratory, Technical report, October 1994.

[29] M. Lovell. Private communication, May 1995.

[30] E.H.M. Heijne. LHC1/Omega3 Readout: preliminary results. *Proc. of the ATLAS Inner Detector Electronics Meeting* [84].

[31] V. Bonzom. CPPM LHC Test Beam Results/Plans. *Proc. of the ATLAS SCT Workshop* [83].

[32] P. Abbon et al. DMILL, a mixed analog-digital radiation hard technology for high energy physics electronics. CERN, LHCC 95-13, 1995.

[33] V. Bonzom. Test results from prototype pixel chips in DMILL & HSOI3HD rad. hard technologies. *Proc. of the ATLAS Inner Detector Electronics Meeting* [84].

[34] G. Hallewell. Present Development Status of "Active" Pixel Detectors. *Proc. of the 2nd International Symposium on Development & Application of Semiconductor Tracking Detectors*, Hiroshima, October 1995.

[35] K. Einsweiler. Status of LBNL pixel electronics effort. *Proc. of the ATLAS Inner Detector Electronics Meeting* [84].

[36] D.J. Warner et al. Flip chip-bonded GaAs MMIC's compatible with foundry manufacture. *IEE Proceedings-H*, 138(1)(1991):74–78.

[37] D. Alexiev T.J. Sumner, S.M. Grant and K.S.A. Butcher. LPE GaAs as an X-ray detector for astronomy. *Nuclear Instruments and Methods in Physics Research*, A348(1994):518–521.

[38] K. Torii et al. Some characteristics of a solid state detector in the soft X-ray region. *Nuclear Instruments and Methods in Physics Research*, A361(1,2)(1995):364–371.

[39] I.P. Dolbnya et al. Measurements of absolute sensitivity of semiconductor detectors for 7–20keV X-rays using synchrotron radiation of VEPP-3 storage ring. *Review of Scientific Instruments*, 63(1)(1992):685–688.

[40] I.P. Dolbnya et al. Measurement of time parameters of X-ray semiconductor detectors using synchrotron radiation of the VEPP-3 storage ring. *Nuclear Instruments and Methods in Physics Research*, A359(1,2)(1995):432–436.

[41] J. Partanen T. Tuomi and K Simomaa. Direct X-ray sensitive charged-coupled device (CCD) as a detector in the study of synchrotron section topographs. *Nuclear Instruments and Methods in Physics Research*, B61(1991):569–574.

[42] R. Clarke et al. Synchrotron radiation applications of charge coupled device detectors. *Review of Scientific Instruments*, 63(1)(1992):784–789.

[43] B. Ludewigt et al. A High Rate, Low Noise, X-ray Silicon Strip Detector System. *Proc. of the IEEE Nuclear Science Symposium and Medical Imaging Conference*, San Francisco, CA, November 1993.

[44] G. Hall. Silicon pixel detectors for X-ray diffraction studies at synchrotron sources. *Quarterly Reviews of Biophysics*, 28(1)(1995):1–32.

[45] E.H.M. Heijne. Pixel detector review. *Proc. of the 4rth International Gallium-Arsenide Workshop*, Aberfoyle, 1996.

[46] T.J. Sumner et al. GaAs revisited as a room temperature X-ray detector. *Nuclear Instruments and Methods in Physics Research*, A322(1992):514–517.

[47] W. Bencivelli et al. Some new results on semi-insulating GaAs detectors for low energy X-rays. *Nuclear Instruments and Methods in Physics Research*, A355(2,3)(1995):425–427.

[48] S. D'Auria. Private Communication, December 1995.

[49] M. Toporowsky. Status report on detectors. *Proc. of the International Gallium-Arsenide Workshop*, Jostal, 1993. (unpublished).

[50] D.S. McGregor et al. *IEEE Transactions on Nuclear Science*. NS-39(1226)(1992).

[51] F. Biggs and R. Lighthill. Analytical approximations for X-ray cross sections 3. Sandia National Lab., SAND 87-0070 UC-34, 1987.

[52] F Sauter. *Ann. Physik*, 9(217)(1931).

[53] F Sauter. *Ann. Physik*, 11(454)(1931).

[54] M. Gavrila. Relativistic K-shell photoeffect. *Phys. Rev.*, 113(514)(1959).

[55] M. Gavrila. Relativistic L-shell photoeffect. *Phys. Rev.*, 124(1132)(1961).

[56] M.O. Krause. Atomic radiative and radiationless yields for K and L shells. *J. Phys. Chem. Ref. Data*, 8(307)(1979).

[57] R. D. Evans. *The Atomic Nucleus*. McGraw-Hill, 1955.

[58] Application Software Group. CERN Program Library. CERN, Short writeups, March 1995. Online manual available at http://wwwcn.cern.ch/asdoc/shortwrups_html3/crnfinal.html.

[59] M. Toporowsky. Properties of GaAs Particle Detectors. *Proc. of the 2nd International Gallium-Arsenide Workshop* [85].

[60] The Radiochemical Centre, Amersham. *Gamma reference source set*. Data sheet 11188.

[61] S. D'Auria. Development Of Biasing Structures For AC-Coupled Detectors And Related Contacts. *Proc. of the 2nd International Gallium-Arsenide Workshop* [85].

[62] A.Vorobiev. Radiation Resistance of GaAs Structures Based on $\pi - \nu$ Junction. ATLAS Internal Note, INDET NO-036, February 1994.

[63] I.R. Grant. Bulk growth of gallium arsenide. ICI Wafer Technology Ltd, Technical report, 1989.

[64] R.Bertin et al. A Preliminary study of GaAs solid-state detectors for High-Energy Physics. *Nuclear Instruments and Methods in Physics Research*, A294(1990):211–218.

[65] K.S.A. Butcher D. Alexiev. High purity liquid epitaxial gallium arsenide nuclear radiation detector. *Nuclear Instruments and Methods in Physics Research*, A317(1992):111–115.

[66] J. Pacansky and J.R. Lyerla. Photochemical Decomposition Mechanisms for AZ-Type Photoresists. *IBM Journal of Research & Development*, 23(1)(1979):42–55.

[67] ATLAS Collaboration. ATLAS Technical Proposal for a General-Purpose pp Experiment at the Large Hadron Collider at CERN. CERN, LHCC 94-43, 1994.

[68] V.B. Chmill et al. Radiation Resistance of GaAs Structures. ATLAS Internal Note, INDET NO-143, 1996.

[69] C. Colledani et al. A Submicron Precision Silicon Telescope for Beam Test Purposes. LEPSI, Preprint 95–03, 1995. accepted for publication in Nuclear Instruments and Methods in Physics Research A.

[70] A. Lang and J.P. Vanuxem. Sirocco II: A Silicon Strip Read-out CAMAC Controller with Flash ADC Input. CERN, EP-ELECTRONICS 90-01, 1990.

[71] S.P. Beaumont et al. First results from GaAs double-sided detectors. *Nuclear Instruments and Methods in Physics Research*, A348(1994):514–517.

[72] J. Chen et al. Beam Tests of GaAs Strip Detectors. ATLAS Internal Note, INDET NO-98, 1995.

[73] P.J. Sellin et al. Spatial Resolution Measurements of Gallium Arsenide Microstrip Detectors. ATLAS Internal Note, INDET NO-123, 1996.

[74] R. Turchetta. Spatial resolution of silicon microstrip detectors. *Nuclear Instruments and Methods in Physics Research*, A335(1993):44–58.

[75] Application Software Group. Pythia 5.7 and Jetset 7.4 - Physics and Manual. CERN, Long Writeup W5035/W5044, February 1994. Online manual available at http://wwwcn.cern.ch/asdoc/pythia_html3/pythia57.html.

[76] T. Sjöstrand. Pythia 5.7 and Jetset 7.4. *Computer Physics Commun.*, 82(1994):74.

[77] K. Bos. ATLAS Detector Simulation Package. World Wide Web. WWW:ATLAS → Software → Dice Manual.

[78] Application Software Group. ZEBRA - Memory and File Management System. CERN, Long Writeup Q100/Q101, February 1995. Online manual available at http://wwwcn.cern.ch/asdoc/zebra_html3/zebramain.html.

[79] J.S. Meyer A. Chilingarov and T. Sloan. Radiation Damage due to NIEL in GaAs Particle Detectors. ATLAS Internal Note, INDET NO-134, 1996.

[80] S. D'Auria et al. Model of charge transport in Semi-Insulating Undoped GaAs microstrip detectors. In J. Ludwig et al. [82]. Also GLAS-PPE/95-05.

[81] K.Berwick et al. Studies of charge collection in GaAs radiation detectors. *Mat. Res. Soc. Symp.*, 302(1993):363–368.

[82] J. Ludwig et al., editor. *3rd International Gallium-Arsenide Workshop*, San Miniato, March 1995. World Scientific. ISBN 981-02-2393-5.

[83] CERN. *ATLAS SCT Workshop*, Oxford, September 1995.

[84] *ATLAS Inner Detector Electronics Meeting*. September 1995. Minutes are available online at WWW:ATLAS → Working Groups → Inner Detector → Electronics.

[85] *2nd International Gallium-Arsenide Workshop*, Jostal, 1994.

GLASGOW
UNIVERSITY
LIBRARY